SISSA
Scuola
Internazionale
Superiore di
Studi Avanzati

Physics Area - PhD course in
Theory and Numerical Simulation of Condensed Matter

Dissipative and Measurement-Induced Phases in Many-Body Quantum Systems

Thesis submitted for the degree of
Doctor Philosophiae

Candidate:
Anna Delmonte

Advisors:
Prof. Rosario Fazio
Prof. Giuseppe Santoro

Academic Year 2024-2025



Abstract

Open quantum many-body systems are an important setting that allows us to study the interplay between dissipation and interactions, contributing to a more accurate description of real-life phenomena and experiments, and providing new features to be exploited both on theoretical and technological grounds. This thesis deals with the study of such systems across a wide range of settings. Beyond providing the theoretical tools to analyze and understand this framework, the thesis also addresses some important and modern concepts. A key goal is to show how dissipation enables the realization of new phases of matter, such as quantum synchronization and time-crystal phases. To achieve this, various theoretical tools will be employed, ranging from path integral formalism to a Lindblad master equation approach. These same tools will also allow us to pursue another important goal: studying the dynamics of many-body systems subject to continuous measurements. This will lead to observing the emergence of a recently discovered phenomenon, known as measurement-induced phase transitions, and will provide a natural framework for addressing the complexity arising from the stochastic nature of quantum measurements. This thesis constitutes a modern and comprehensive view of the field of open quantum many-body systems, with a special focus on novel phases of matter emerging from interactions with an external environment or with a measuring device.

Acknowledgements

I would like to start by expressing my deepest gratitude to my supervisors: Rosario Fazio, whose patience, support, experience, and irony have helped me grow over these four years, both as a physicist and as a person; and Giuseppe Santoro, who welcomed me warmly from my very first day at SISSA and has offered insightful advice, support, and kindness throughout my PhD.

A big thank-you goes to Alessandro Romito, who has followed my PhD journey from the very first project to the very last. I am especially grateful for the time and attention he has given me, treating me as one of his own students and always encouraging me.

I am also deeply grateful to my closest collaborator, Zejian Li, with whom I have shared most of the challenges of recent years — including Duolingo Friends Quests. My gratitude also goes to all those who contributed to the works presented in this thesis and helped deepen my understanding of these topics: Gianluca Passarelli, Giulia Salatino, Alberto Biella, Xhek Turkeshi, Eric Yilun Song, Diego Barberena, and Ana Maria Rey.

These years at SISSA would not have been the same without all my colleagues in condensed matter — Alessio, Matteo, Samuele, Davide, and Luca — and everyone at SISSA and ICTP who, through their friendship, have made life in Trieste easier and more enjoyable, turning it into a very special place. The list of names would be far too long, but I will thank, though unfairly and incompletely, Zeno, officemate and companion of coffee breaks from the first to the last day; Clemente and Shreyansh, the best flatmates in Trieste; and Alfredo, Michele, Cecilia, Elaheh, Freya, Emanuele, and Stefania for sharing so many moments together.

I would also like to thank my family, especially my grandmother, Nonna Pina, who did not want me to leave but who, I am sure, would have been proud of what I have achieved here.

Lastly, my gratitude goes to Cristiano, simply for being there with me through every single moment of these years (perhaps a bit too much — you could have found another office!).

Publications

Journal papers

- Delmonte, A., Romito, A., Santoro, G. E., and Fazio, R. *Quantum effects on the synchronization dynamics of the Kuramoto model*, Phys. Rev. A 108 (3), 032219 (2023)
- Delmonte, A., Li, Z., Passarelli, G, Song, E.Y., Barberena, D., Rey, A.M., and Fazio, R. *Measurement-induced phase transitions in monitored infinite-range interacting systems*, Phys. Rev. Research (7) 023082 (2025)
- Li, Z., Delmonte, A., Turkeshi, X, and Fazio, R. *Monitored long-range interacting systems: spin-wave theory for quantum trajectories*, Nat. Comm. (16) 4329 (2025)

Preprints

- Li, Z., Delmonte, A., and Fazio, R. *Emergent deterministic entanglement dynamics in monitored infinite-range bosonic systems*, arXiv:2506.18624

In preparation

- Delmonte, A., Li, Z., Fazio, R., and Romito, A. *Measurement-induced phase transition in interacting bosons from most likely quantum trajectory*

Contents

1. Basic concepts of open quantum systems and measurements **3**

1.1. Open Quantum Many-Body systems . . . 3

1.1.1. Caldeira-Leggett Model . . . 8

1.1.2. Lindblad master equation . . . 12

1.2. Quantum Measurements . . . 15

1.2.1. Weak and Gaussian Measurements or Homodyne detection . . . 16

1.2.2. Counting events, or quantum jump measurements . . . 21

2. Critical Phenomena in Open Quantum Systems **25**

2.1. Dissipative phase transitions . . . 25

2.1.1. Persistent oscillations and Time Crystals . . . 27

2.1.2. Bistability . . . 29

2.2. Measurement-induced phase transitions . . . 31

2.2.1. The complexity of monitored systems . . . 34

3. Quantum Synchronization **37**

3.1. Classical Synchronization . . . 38

3.1.1. Basics of synchronization: phase locking . . . 38

3.1.2. The Kuramoto-Sakaguchi model . . . 39

3.2. From Classical to Quantum synchronization . . . 42

3.2.1. The Quantum Kuramoto model . . . 42

3.2.2. Self-consistent equation for the order parameter . . . 45

3.2.3. Properties of the steady state . . . 48

3.3. Conclusions to the Chapter . . . 52

4. Monitored infinite- and long-range systems **55**

4.1. Infinite- and Long-Range models, and the post-selection problem . . . 55

4.2. The Tavis-Cummings model . . . 57

4.2.1. Dissipative phase transition . . . 59

4.2.2. Measurement-induced phase transitions in the entanglement entropy . . . 61

4.2.3. Experimentally-relevant details . . . 69

4.3. Long-Range models . . . 75

4.3.1. The spin-wave theory for quantum trajectories . . . 78

4.3.2. A benchmark: the infinite range case . . . 82

4.3.3. MIPTs and Post-Selection in long-range systems 85
4.4. Comments on the results 88
4.5. Conclusions to the Chapter 89

5. Monitored interacting bosonic models **91**
5.1. The most likely trajectory 92
5.1.1. How to build the most-likely trajectory 95
5.2. A benchmark: the Free Bosons CFT 98
5.3. The monitored Sine-Gordon Model 101
5.3.1. Dynamics 104
5.3.2. Steady state properties 106
5.4. Conclusions to the Chapter 109

6. Conclusions **111**

A. Appendix to Chapter 1 **115**
A.1. Keldysh field theory for Caldeira-Leggett's bath 115

B. Appendix to Chapter 3 **119**
B.1. Path integral formulation for the classical stochastic process 119
B.2. First order expansion of the self-consistent equation 120
B.3. Solutions to the saddle point equations 122

C. Appendix to chapter 4 **123**
C.1. Saturation time 123

D. Appendix to chapter 5 **125**
D.1. Saddle-Point procedure for Measurements Path Integrals 125
D.2. Exact results for the Free Bosons CFT 126
D.3. The Self-Consistent-Time-Dependent Harmonic Approximation For the Sine-Gordon model 128

Introduction

A good description of quantum phenomena inevitably has to deal with the fact that real systems might not be closed and isolated, and thus must take into account not only the system at the center of our study but also all the other effects that arise from the surrounding environment [1–3]. This necessity arises in order to make contact with real systems, ranging from natural to synthetic ones, which cannot be properly described on their own.

The theory of open quantum systems has been developed over the past 70 years, starting from simple systems [4–8], and is still evolving today to enable the description of many-body quantum problems. This has become crucial to theoretically understand the physics observed with quantum simulators and quantum computers [9–14], which, in general, cannot be fully described as isolated systems. Additionally, these studies have shown that the effects of working with an open system, especially in a many-body setting [14, 15], not only represent challenges to overcome but can also serve as a resource for realizing peculiar states and phases of matter. Many examples stand out in this context, ranging from entangled states [16, 17] to topological states [18–20]. Among these intriguing phases are time-crystal [21] phases of matter, which cannot be realized at equilibrium [22] and thus benefit from an open quantum system setting [23, 24], and quantum-synchronized phases [25–27], both of which will be thoroughly studied throughout this thesis [28–31].

A natural extension of the field of open quantum systems is the theory of quantum measurement [32, 33]. Measurements involve coupling to an external degree of freedom, which suddenly changes the structure of the state in a way that cannot be described by the Schroedinger or von Neumann equation, and which can often be recast in the language of open quantum systems. This connection began years ago with the study of measurements on small systems [34–39] and has recently been extended to many-body physics. This crucial step has enabled the discovery of critical phenomena that require full knowledge of measurement statistics to be unveiled [40], known as measurement-induced phase transitions (MIPTs).

Measurement-induced phase transitions have represented a significant portion of recent research in quantum statistical mechanics and condensed matter, initially to identify, characterize, and describe the emergence of these phases of matter in various contexts (from quantum circuits [40–42] to Hamiltonian systems [43–45]), and subsequently to understand under which circumstances they can be observed experimentally [46–48].

A fundamental problem related to this exciting new critical phenomenon is the requirement for experimentalists not only to fully characterize a quantum state but also to do so while conditioning the state on all possible realizations of the stochastic measurement process. The study of this fundamental issue, known as the post-selection problem, will occupy a large part of this thesis [29, 30], along with the necessity to tackle the numerical and analytical complexity involved in studying stochastic systems.

The thesis is organized as follows: Chapter 1 introduces in detail the formalism and concepts used to study open quantum systems, considering both the path integral formalism and the master equation approach. We then extend the formalism to incorporate quantum measurements under different measurement settings and analyze connections and differences between standard dissipation and monitoring. This leads to Chapter 2.1 which presents the critical phenomena induced by the interplay between unitary dynamics and dissipation or quantum measurements, along with providing some examples.

Chapter 3 focuses on dissipative phase transitions involving temporal ordering. Specifically, we extend a paradigmatic classical model of synchronization, the Kuramoto model, to the quantum domain, demonstrating the power of the path integral formalism in describing open quantum systems and their non-Markovian dynamics as well as the emergence of quantum synchronization.

Chapter 4 is entirely devoted to the complexity of studying measurement-induced phase transitions. We address the post-selection problem by carefully analyzing an experimentally relevant model, the Tavis-Cummings model, to identify key experimental challenges and propose possible resolutions. This analysis is then extended to a long-range setting, where we must first handle the complexity of stochastic many-body simulations. This leads us to devise a new method based on spin-wave theory, able to account for the stochastic nature of the dynamics and well represent the measurement process.

Chapter 5 deals again with the monitored dynamics of many-body systems, using this time an analytical perspective. Analytical calculations also suffer from the stochastic complexity of studying measurement-induced phase transitions. Additional challenges in this context arise from dealing with interacting models, which usually require approximations or must be treated in specific regimes, even outside the quantum measurement setting. The chapter shows how to overcome both challenges through a deterministic description based on the most likely realization of the measurement process and on well-known many-body techniques, unveiling analytically the emergence of an MIPT in an interacting bosonic model.

The final chapter, Chapter 6, presents the conclusions drawn from this original study of open quantum many-body systems, which encompasses diverse but interconnected phenomena.

1. Basic concepts of open quantum systems and measurements

In this first Chapter, the main theoretical concepts and tools used throughout the thesis will be introduced in detail.

Section 1.1 will deal with the theoretical description of open many-body quantum systems, which consist of a system interacting with an environment that cannot be accessed, probed, or modified. We will introduce two connected but distinct tools to describe the dynamics of such systems: a more general and complex path integral formalism, and a more intuitive and specific Markovian approach through the Lindblad equation. This will also lead us to describe steady-state properties, which will be of great interest for the thesis, and which will be described in the second introductory Chapter, Chap. 2.

The second part of this Chapter, in Section 1.2, will instead focus on quantum measurements and the monitored dynamics of many-body systems. After introducing different types of quantum measurements and their effects on the system's state, we will frame the measurements description within the language of open quantum systems introduced in the first part. We will explore connections with both the path integral formalism and the Lindblad equation approach. This Chapter lays the foundations for Chap. 2, which will explore the steady state properties emerging from this type of dynamics, introducing the concept of measurement-induced phase transitions.

1.1. Open Quantum Many-Body systems

Describing how the properties of a system change when it is influenced by interaction with an external environment has always attracted significant interest in quantum mechanics [4–6, 8] as it is usually quite difficult to completely isolate a system [49–54]. In this context, the usual description of the system through pure states evolving according to the Schrodinger equation is no longer sufficient. As we will see, interactions tend to correlate the system with the environment, generally making the system's state a mixed one and producing dissipative or decoherence effects that cannot be captured by unitary Hamiltonian evolution [1–3], going beyond the Schroedinger and von Neumann equations.

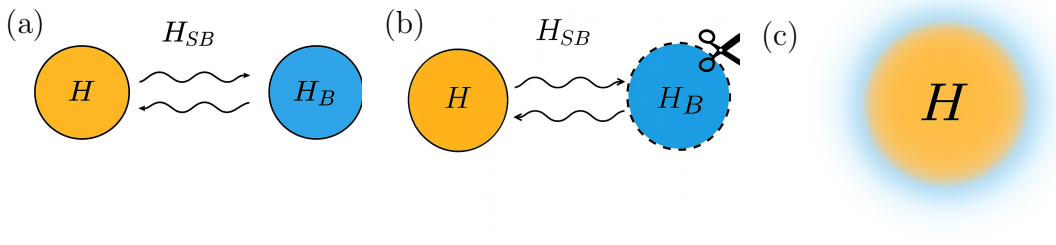

Figure 1.1.: (a) Pictorial representation of a system interacting with a bath. When the degrees of freedom of the bath are traced out in the equations for the dynamics, as depicted in (b), one gets an effective description for an open quantum system, as in panel (c).

This section will focus on different ways to derive and characterize the evolution of an open quantum system. The idea behind these methods is very simple and is briefly illustrated in Fig. 1.1. The system we would like to study, represented as an orange circle in the figure, interacts with a bath, or environment, represented as a blue circle. The bath cannot be accessed or controlled in our study; its presence is only evident through the effects it has on our system. The theoretical description, therefore, starts from the broader picture of an isolated global system comprising both the bath and the system of interest. Since the global system is isolated and closed, we can describe its evolution using standard quantum mechanics techniques, such as the Schrodinger or von Neumann equations (if we are interested in master equations), or through a Feynman path integral formalism. To obtain a complete description in terms of the system alone, we need to eliminate the bath's degrees of freedom from the full description of the global system.

This idea is both powerful and general, and will be developed in the first part of the thesis through a path integral formalism. Within this framework, we will encounter an important object: the influence functional, which precisely captures the effects of the system-bath interaction without requiring a description of the bath's evolution.

Baths can have very different natures and structures, which shape the way their effects manifest on the system. We will explore several forms of the influence functional corresponding to baths with various characteristics. First, in Sec. 1.1.1, we will introduce a Caldeira-Leggett type of bath composed of collections of harmonic oscillators at thermal equilibrium, which will be particularly useful for Chap. 3. Then, in Sec. 1.1.2, we will consider a very special type of bath and connect its effects to those described by the Lindblad master equation, one of the main tools for describing Markovian dynamics in open quantum systems, as we will see in Chap. 4. This will also lead us to a discussion of the properties of the Lindblad equation.

We are now ready to start describing in a quantitative way how the interaction with a bath deeply modifies the evolution of a many-body system.

From now on, we will set $\hbar = 1$ unless otherwise stated.

Consider a many-body system described by a Hamiltonian

$$\hat{H} = \frac{\hat{\mathbf{p}}^2}{2m} + V(\hat{\mathbf{x}}). \tag{1.1}$$

The system is composed of N objects with canonically conjugate variables $\hat{\mathbf{x}} = (\hat{x}_1, .., \hat{x}_N)$ and $\hat{\mathbf{p}} = (\hat{p}_1, .., \hat{p}_N)$ such that $[\hat{x}_i, \hat{p}_j] = i\delta_{i,j}$.

Suppose the system is in contact with another system, the bath. The bath has Hamiltonian

$$\hat{H}_{\mathrm{B}} = \frac{\hat{\mathbf{P}}^2}{2m} + V_{\mathrm{B}}(\hat{\mathbf{X}}). \tag{1.2}$$

We can keep the structure of the bath general, and only assume it is composed of M objects having canonically conjugated variables $\hat{\mathbf{X}} = \left(\hat{X}_1, .., \hat{X}_M\right)$ and $\hat{\mathbf{P}} = \left(\hat{P}_1, .., \hat{P}_M\right)$ such that $\left[\hat{X}_i, \hat{P}_j\right] = i\delta_{i,j}$.

The system and the bath interact via an interaction Hamiltonian, having a structure

$$\hat{H}_{\mathrm{SB}} = V_{\mathrm{SB}}(\hat{\mathbf{x}}, \hat{\mathbf{X}}). \tag{1.3}$$

The global Hamiltonian is thus given by

$$\hat{H}_{\mathrm{tot}} = \hat{H} + \hat{H}_{\mathrm{B}} + \hat{H}_{\mathrm{SB}}. \tag{1.4}$$

The global system is represented in Fig. 1.1(a).

The work presented in this Thesis will aim to describe the dynamical and steady state properties of this kind of system supposing we can access only the system's degrees of freedom and not the bath's. In the next paragraphs, we will see how it is possible to achieve this, without discarding any important information about the system and the bath as a whole.

In general, we will always suppose to start the dynamics from an initial state separable between the degrees of freedom of the bath and the system, i.e.

$$\hat{\rho}_{\mathrm{tot},0} = \hat{\rho}_0 \otimes \hat{\rho}_{\mathrm{B},0}, \tag{1.5}$$

where $\hat{\rho}_0$ and $\hat{\rho}_{\mathrm{B},0}$ are respectively the system's and the bath's initial state, which can be taken as mixed states to keep full generality.

As standard in quantum mechanics, the evolved state is obtained through the application of the evolution operator $\hat{\mathfrak{U}}(t, t_0) = \exp\left\{-i\,(t - t_0)\hat{H}_{\mathrm{tot}}\right\}$. Supposing the evolution starts at $t_0 = 0$, we can express the evolution of the position representation of the state up to time t,

$$\hat{\rho}_{\mathrm{tot}}(t) = \int d\mathbf{x}\, d\mathbf{x}' \int d\mathbf{X}\, d\mathbf{X}' \rho_{\mathrm{tot}}(\mathbf{x}, \mathbf{X}, \mathbf{x}', \mathbf{X}'; t) \left|\mathbf{x}, \mathbf{X}\right\rangle \left\langle \mathbf{x}', \mathbf{X}'\right|, \tag{1.6}$$

through a path integral formalism [7, 55]. Notice that we have used the short-hand notation $\rho_{\rm tot}(\mathbf{x},\mathbf{X},\mathbf{x}',\mathbf{X}';t) = \langle \mathbf{x},\mathbf{X}|\,\hat{\rho}_{\rm tot}(t)\,|\mathbf{x}',\mathbf{X}'\rangle$. The time-evolved density matrix reads

$$\begin{aligned}\rho_{\rm tot}(\mathbf{x},&\mathbf{X},\mathbf{x}',\mathbf{X}';t) = \\ &= \langle \mathbf{x},\mathbf{X}|\,\hat{\mathcal{U}}(t,0)\,\hat{\rho}_{\rm tot,0}\,\hat{\mathcal{U}}^\dagger(t,0)\,|\mathbf{x}',\mathbf{X}'\rangle \\ &= \int d\mathbf{x}_0\,d\mathbf{x}'_0\int d\mathbf{X}_0\,d\mathbf{X}'_0\,\rho_{\rm tot,0}(\mathbf{x}_0,\mathbf{X}_0,\mathbf{x}'_0,\mathbf{X}'_0) \\ &\int_{\mathbf{x}_1(0)=\mathbf{x}_0}^{\mathbf{x}_1(t)=\mathbf{x}}\mathcal{D}\mathbf{x}_1\int_{\mathbf{x}_2(0)=\mathbf{x}'_0}^{\mathbf{x}_2(t)=\mathbf{x}'}\mathcal{D}\mathbf{x}_2\int_{\mathbf{X}_1(0)=\mathbf{X}_0}^{\mathbf{X}_1(t)=\mathbf{X}}\mathcal{D}\mathbf{X}_1\int_{\mathbf{X}_2(0)=\mathbf{X}'_0}^{\mathbf{X}_2(t)=\mathbf{X}'}\mathcal{D}\mathbf{X}_2\,e^{i\left(S_{\rm tot}[\mathbf{x}_1,\dot{\mathbf{x}}_1;\mathbf{X}_1;\dot{\mathbf{X}}_1]-S_{\rm tot}[\mathbf{x}_2,\dot{\mathbf{x}}_2;\mathbf{X}_2;\dot{\mathbf{X}}_2]\right)}.\end{aligned} \tag{1.7}$$

To define the evolution through path integrals, we have introduced the action associated with the Hamiltonian $\hat{H}_{\rm tot}$

$$\begin{aligned}S_{\rm tot}[\mathbf{x}_a,\dot{\mathbf{x}}_a;\mathbf{X}_a;\dot{\mathbf{X}}_a] &= S[\mathbf{x}_a,\dot{\mathbf{x}}_a] + S_{\rm B}[\mathbf{X}_a;\dot{\mathbf{X}}_a] + S_{\rm SB}[\mathbf{x}_a,\mathbf{X}_a] \\ &= \int_0^t dt'\left[\frac{m\dot{\mathbf{x}}_a^2}{2} - V(\mathbf{x_a}) + \frac{m\dot{\mathbf{X}}_a^2}{2} - V_{\rm B}(\mathbf{X_a}) - V_{\rm SB}(\mathbf{x_a},\mathbf{X_a})\right],\end{aligned} \tag{1.8}$$

and we have used the fact that the Feynman propagator associated to $\hat{\mathcal{U}}^\dagger(t)$ is given by the complex conjugate of the propagator generated by $\hat{\mathcal{U}}(t)$, yielding the minus sign in front of $S_{\rm tot}[\mathbf{x}_2,\dot{\mathbf{x}}_2;\mathbf{X}_2,\dot{\mathbf{X}}_2]$ in Eq. (1.7). The fields we have introduced in the path integral are labeled by $a = 1,2$ and correspond respectively to variables on the *forward* path — associated to the $\hat{\mathcal{U}}(t)$ propagator— and on the backward path — associated to $\hat{\mathcal{U}}^\dagger(t)$. This is the typical structure of Path Integrals in the Keldysh formalism, which is often used to describe non-equilibrium settings [56–59].

So far, the time evolution we have considered is unitary, as the global system comprising the system and the bath is closed and isolated. Typically, we don't have access to the bath's degree of freedom and we can only see how its coupling with the system affects the system itself. It is then interesting to describe these conditions starting from our equation. This will allow both to understand how some typical behaviors of our system are enhanced or hindered by the presence of an environment, and to have a description closer to what can effectively be observed in real-life experiments.

In order to have a description of the dynamics in terms of the system's degrees of freedom only, we can trace over the bath's degrees of freedom as represented in

Fig 1.1(b):

$$\begin{aligned}
\rho(\mathbf{x},\mathbf{x}';t) &= \qquad (1.9)\\
&= \int d\mathbf{X}\, \rho_{\mathrm{tot}}(\mathbf{x},\mathbf{X},\mathbf{x}',\mathbf{X}'=\mathbf{X};t)\\
&= \int d\mathbf{x}_0\, d\mathbf{x}'_0\, \rho_0(\mathbf{x}_0,\mathbf{x}'_0) \int_{\mathbf{x}_1(0)=\mathbf{x}_0}^{\mathbf{x}_1(t)=\mathbf{x}} \mathcal{D}\mathbf{x}_1 \int_{\mathbf{x}_2(0)=\mathbf{x}'_0}^{\mathbf{x}_2(t)=\mathbf{x}'} \mathcal{D}\mathbf{x}_2\, e^{i(S[\mathbf{x}_1,\dot{\mathbf{x}}_1]-S[\mathbf{x}_2,\dot{\mathbf{x}}_2])}\\
&\qquad \Bigg[\int d\mathbf{X}_0\, d\mathbf{X}'_0\, d\mathbf{X}\ \rho_{\mathrm{B},0}(\mathbf{X}_0,\mathbf{X}'_0)\\
&\qquad \int_{\mathbf{X}_1(0)=\mathbf{X}_0}^{\mathbf{X}_1(t)=\mathbf{X}} \mathcal{D}\mathbf{X}_1 \int_{\mathbf{X}_2(0)=\mathbf{X}'_0}^{\mathbf{X}_2(t)=\mathbf{X}} \mathcal{D}\mathbf{X}_2\, e^{i\left(S_{\mathrm{B}}[\mathbf{X}_1;\dot{\mathbf{X}}_1]+S_{\mathrm{SB}}[\mathbf{x}_1,\mathbf{X}_1]-S_{\mathrm{B}}[\mathbf{X}_2;\dot{\mathbf{X}}_2]-S_{\mathrm{SB}}[\mathbf{x}_2,\mathbf{X}_2]\right)}\Bigg]\\
&= \int d\mathbf{x}_0\, d\mathbf{x}'_0\, \rho_0(\mathbf{x}_0,\mathbf{x}'_0) \int_{\mathbf{x}_1(0)=\mathbf{x}_0}^{\mathbf{x}_1(t)=\mathbf{x}} \mathcal{D}\mathbf{x}_1 \int_{\mathbf{x}_2(0)=\mathbf{x}'_0}^{\mathbf{x}_2(t)=\mathbf{x}'} \mathcal{D}\mathbf{x}_2\, e^{i(S[\mathbf{x}_1,\dot{\mathbf{x}}_1]-S[\mathbf{x}_2,\dot{\mathbf{x}}_2])}\Phi[\mathbf{x_1},\mathbf{x_2}].
\end{aligned}$$

The path integration over the bath's degrees of freedom generates, through the interaction with the system, a functional $\Phi[\mathbf{x}_1,\mathbf{x}_2]$ of the system's degrees of freedom. The **influence functional** [7, 55, 60]

$$\begin{aligned}
\Phi[\mathbf{x}_1,\mathbf{x}_2] = &\int d\mathbf{X}_0\, d\mathbf{X}'_0\, d\mathbf{X}\ \rho_{\mathrm{B},0}(\mathbf{X}_0,\mathbf{X}'_0) \qquad (1.10)\\
&\int_{\mathbf{X}_1(0)=\mathbf{X}_0}^{\mathbf{X}_1(t)=\mathbf{X}} \mathcal{D}\mathbf{X}_1 \int_{\mathbf{X}_2(0)=\mathbf{X}'_0}^{\mathbf{X}_2(t)=\mathbf{X}} \mathcal{D}\mathbf{X}_2\, e^{i\left(S_{\mathrm{B}}[\mathbf{X}_1;\dot{\mathbf{X}}_1]+S_{\mathrm{SB}}[\mathbf{x}_1,\mathbf{X}_1]-S_{\mathrm{B}}[\mathbf{X}_2;\dot{\mathbf{X}}_2]-S_{\mathrm{SB}}[\mathbf{x}_2,\mathbf{X}_2]\right)}
\end{aligned}$$

modifies the dynamics of the system by incorporating the effects resulting from the interaction between the bath and the system itself, as shown in Fig. 1.1(c). Notice how the influence functional depends on both branches of the path integral, and in general, introduces interaction between them.

The structure of the influence functional can be very complicated, depending on the architecture of the bath. One can however rely on some properties which naturally follow from its definition. The most prominent and useful in the cases we will consider are:

- it's Hermitian $\Phi[\mathbf{x}_1,\mathbf{x}_2] = \Phi^*[\mathbf{x}_2,\mathbf{x}_1]$
- Independent baths have factorizing influence functionals $\Phi[\mathbf{x}_1,\mathbf{x}_2] = \prod_{j=1}^{N_{\mathrm{b}}} \Phi_j[\mathbf{x}_1,\mathbf{x}_2]$ if $\hat{H}_{\mathrm{B}} + \hat{H}_{\mathrm{SB}} = \sum_{j=1}^{N_{\mathrm{b}}} \hat{H}_j$

Moreover, there are cases in which the influence functional has a particularly simple shape. Considering, for example, a quadratic Hamiltonian for the bath along with a linear interaction between the system and the bath, yields a Gaussian influence functional for the system.

In general, considering Gaussian influence functionals is a good approximation of some complex cases, just as Gaussian noise in classical statistical mechanics, as it can

model, for example, the interaction with many baths being weakly coupled to the system of interest [55].

For this reason, from now on we will only consider Gaussian influence functionals, whose most general form is

$$\Phi[\mathbf{x}_1, \mathbf{x}_2] = \exp\left\{-\int dt'\, dt''\ [\boldsymbol{\alpha}(t', t'')\mathbf{x}_1(t'') - \boldsymbol{\alpha}^*(t', t'')\mathbf{x}_2(t'')]\,[\mathbf{x}_1(t') - \mathbf{x}_2(t')]\right\} \quad (1.11)$$

Some comments are in order. The presence of the influence functional can be recast into an effective action for the system, living on both forward and backward branches:

$$S_{\text{eff}}[\mathbf{x_1}, \dot{\mathbf{x}}_\mathbf{1}; \mathbf{x_2}, \dot{\mathbf{x}}_\mathbf{2}] = S[\mathbf{x_1}, \dot{\mathbf{x}}_\mathbf{1}] - S[\mathbf{x_2}, \dot{\mathbf{x}}_\mathbf{2}] - i \log \Phi[\mathbf{x_1}, \mathbf{x_2}]. \quad (1.12)$$

The effective action, due to the presence of $\boldsymbol{\alpha}(t, t') \in \mathbb{C}$ coefficients coming from the influence functional, is no longer necessarily real. The imaginary part of the effective action now describes dissipation processes arising due to the interaction with the bath:

$$e^{-\text{Im}S_{\text{eff}}[\mathbf{x_1}, \dot{\mathbf{x}}_\mathbf{1}; \mathbf{x_2}, \dot{\mathbf{x}}_\mathbf{2}]} \sim \exp\left\{-\int dt' dt''\, (\mathbf{x}_1(t') - \mathbf{x}_2(t'))\, \text{Re}\,\{\boldsymbol{\alpha}(t', t'')\}\, (\mathbf{x}_1(t') - \mathbf{x}_2(t'))\right\}.$$

The effect arising from this part is essentially decoherence: the off-diagonal elements are exponentially suppressed by $\text{Re}\,\{\boldsymbol{\alpha}\}$. Dissipation processes do not appear only in the imaginary part of the action, but can also affect the real part. A typical example is the appearance of friction effects, as we will see in the next Section. The imaginary part of the influence functional can involve both diagonal and off-diagonal elements [2, 61].

In the next Section, we will consider a specific type of bath's structure, leading to the famous Caldeira and Leggett model for baths, which will provide further explanations about the influence functional and dissipation terms arising from it. Then we will consider a special case of the influence and, without digging into its specific derivation, we will link it to Lindblad theory and the Markovian Lindblad master equation.

1.1.1. Caldeira-Leggett Model

We now introduce a specific architecture of a bath, to show how it shapes and defines the structure of the influence functional and the effects it can cause on the dynamics of the system coupled to it.

We will consider our system to be coupled to a collection of independent harmonic oscillators, each coupled linearly to the system's degrees of freedom. This specific architecture has been introduced by Caldeira and Leggett and is named after them [62]. As already discussed, this type of bath leads to a Gaussian influence functional and will give us the chance to explore the structure of the coefficients $\boldsymbol{\alpha}$ naturally emerging from this picture.

Performing all the steps of the calculation to derive the Caldeira and Leggett's influence functional requires some technical points. We will not explore them in this Section, as the aim is mainly to understand the properties of this architecture of bath and its effects on the system. However, some details can be found in Appendix A, where Caldeira and Leggett's simple setting is used to introduce some important concepts of Keldysh Field theory, such as the Keldysh rotation and the Keldysh Green's functions. We refer the readers to this Appendix if interested in these technical details and concepts.

The structure of Caldeira and Leggett's bath can be introduced in this simplified setting. We consider a single particle system with Hamiltonian

$$\hat{H} = \frac{\hat{p}^2}{2m} + V(\hat{x}), \tag{1.13}$$

in interaction with a bath composed of a set of N_b harmonic oscillators:

$$\hat{H}_\mathrm{B} = \sum_{j=1}^{N_\mathrm{b}} \hat{H}_\mathrm{B}^j = \sum_{j=1}^{N_\mathrm{b}} \left(\frac{\hat{P}_j^2}{2M} + \frac{1}{2} M \Omega_j \hat{X}_j^2 \right), \tag{1.14}$$

such that all the harmonic oscillators have the same mass, and different frequencies Ω_j. We also suppose the initial state to be separable, with each harmonic oscillator being in a thermal state at inverse temperature β,

$$\hat{\rho}_{\mathrm{B},0} = \bigotimes_{j=1}^{N_\mathrm{b}} \hat{\rho}_{\mathrm{B},0}^{(j)} = \bigotimes_{j=1}^{N_\mathrm{b}} \frac{e^{-\beta \hat{H}_\mathrm{B}^j}}{Z}. \tag{1.15}$$

We take the interaction Hamiltonian to be

$$\hat{H}_\mathrm{int} = C \sum_{j=1}^{N_\mathrm{b}} \hat{x}\, \hat{X}_j, \tag{1.16}$$

where C is the interaction strength between each harmonic oscillator and the system.

Since the bath is made of a composition of independent elements, we can exploit the factorization property of the influence functional

$$\Phi[x_1, x_2] = \prod_{j=1}^{N_\mathrm{b}} \Phi_j[x_1, x_2] \tag{1.17}$$

$$= \prod_{j=1}^{N_\mathrm{b}} \int dX_0^j\, dX_0'^j\, dX^j\ \mathcal{F}(X^j, X^j, t; X_0^j, X_0'^j, 0) \tag{1.18}$$

where we have defined

$$\mathcal{F}(X^j, X^j, t; X_0^j, X_0'^j, 0) = \int_{X^j{}_1(0)=X^j{}_0}^{X^j{}_1(t)=X^j} \mathcal{D}X_1^j \int_{X^j{}_2(0)=X^j{}_0'}^{X^j{}_2(t)=X^j} \mathcal{D}X_2^j\, \rho_{\mathrm{B},0}^{(j)}(X_0^j, X_0'^j) \tag{1.19}$$

$$\exp\left\{ i \int_0^t dt \left(\frac{M(\dot{X}_1^j - \dot{X}_2^j)}{2} - \frac{1}{2} M \Omega_j^2 (X_1^{j^2} - X_2^{j^2}) - C\left(x_1 X_1^j - x_2 X_2^j\right) \right) \right\}$$

The calculation of the jth influence functional requires some technical steps, and is reported in App. A. Although technical, the calculation relies on a simple idea: the influence functional is quadratic, as well as the initial state. Thus, one can exploit standard Gaussian integration techniques to identify the structure of the influence functional. We report the result in a matrix form, in frequency space, i.e. in order to find the time structure of the result we are presenting, one should perform the inverse Fourier transform $x_{1,2}(t'-t'') = \int \frac{d\omega}{2\pi} e^{-i\omega(t'-t'')}\, x_{1,2}(\omega)$. The jth influence functional reads

$$\Phi[x_1,x_2] = \prod_{j=1}^{N_{\text{b}}} e^{\frac{iC^2}{2}\int\frac{d\omega}{2\pi}\left(x_1(\omega)-x_2(\omega),\quad \frac{x_1(\omega)+x_2(\omega)}{2}\right)\mathbb{G}^j(\omega)\begin{pmatrix} x_1(-\omega)-x_2(-\omega) \\ \frac{x_1(-\omega)+x_2(-\omega)}{2}\end{pmatrix}}, \tag{1.20}$$

where we have introduced the matrix $\mathbb{G}(\omega)$ which contains the Green's function for the jth harmonic oscillators at temperature $T = 1/\beta$, introduced in App. A.

In the case of the equilibrium harmonic oscillator baths, we have the specific forms:

$$\mathbb{G}^j(\omega) = \begin{pmatrix} G_K^j(\omega) & G_R^j(\omega) \\ G_A^j(\omega) & 0\end{pmatrix} = \begin{pmatrix} \coth\frac{\omega}{2T}\left[G_R^j(\omega)-G_A^j(\omega)\right] & \frac{1}{M\left((\omega+i\epsilon)^2-\Omega_j^2\right)} \\ \frac{1}{M\left((\omega-i\epsilon)^2-\Omega_j^2\right)} & 0\end{pmatrix} \tag{1.21}$$

The full influence functional is given by the product of all the Q harmonic oscillators' contribution, as in Eq. (1.17). This means that the couplings between the system's fields x_1, x_2 will not be determined by G_K^j, G_R^j, G_A^j alone, but rather by the sum over all of them:

$$\begin{aligned}\Phi[x_1,x_2] &= \\ &= \exp\left\{\int\frac{d\omega}{2\pi}\left[(x_1(\omega)-x_2(\omega))\left(\frac{iC^2}{2}\sum_{j=1}^{Q}G_K^j(\omega)\right)(x_1(-\omega)-x_2(-\omega))\right]\right\}\cdot \\ &\cdot\exp\left\{i\int\frac{d\omega}{2\pi}\left[(x_1(\omega)-x_2(\omega))\left(\frac{C^2}{4}\sum_{j=1}^{Q}(G_R^j(\omega)+G_A^j(-\omega))\right)(x_1(-\omega)+x_2(-\omega))\right]\right\}\end{aligned} \tag{1.22}$$

Thus, the only step remaining to identify the structure of the influence functional for Caldeira and Leggett's bath model is to sum

$$\begin{aligned}\mathcal{A}_{R/A}(\omega) = i\frac{C^2}{2M}\sum_{j=1}^{Q}G_{R/A}^j(\omega) &= i\frac{C^2}{2M}\sum_{j=1}^{Q}\frac{1}{(\omega\pm i\epsilon)^2-\Omega_j^2} \\ &= i\int\frac{d\Omega}{2\pi}\frac{\Omega\, J(\Omega)}{(\omega\pm i\epsilon)^2-\Omega^2},\end{aligned} \tag{1.23}$$

where we have introduced the distribution $J(\Omega)$, such that

$$J(\Omega) = \frac{\pi C^2}{2M\Omega}\sum_{j=1}^{Q}\left[\delta(\Omega-\Omega_j)-\delta(\Omega+\Omega_j)\right]. \tag{1.24}$$

This distribution is the only information we need to know about the structure of the collection of harmonic oscillators. The specific parameters C, M, Ω_j do not enter independently in the influence functional but only through their combination in $J(\Omega)$.

A typical choice for the distribution $J(\Omega)$ is the *Ohmic Bath* [61–63]. In this case

$$J(\Omega)\Big|_{\text{Ohmic}} = m\gamma\Omega, \tag{1.25}$$

where m is the mass of the particle in $\hat{H}$ and the meaning of γ will be clear in a few lines.

This choice yields $\mathcal{A}_{R/A}(\omega) = \mp\frac{i}{2}m\gamma\omega$, and

$$\mathcal{A}_K(\omega) = i\frac{C^2}{2}\sum_{j=1}^{Q} G_K^j(\omega) = \frac{m\gamma\omega}{2}\coth\frac{\omega}{2k_BT}$$

With these steps we have fully specified the influence functional for an Ohmic Caldeira-Leggett bath, and we can gain some insight into the coefficient $\alpha(t,t')$, which defines the general form of a Gaussian influence functional, which now reads:

$$\begin{aligned}&\Phi[x_1,x_2] = \\ &= \exp\left\{-\frac{m\gamma}{2}\int\frac{d\omega}{2\pi}\left[(x_1(\omega)-x_2(\omega))\,\omega\,\coth\frac{\omega}{2k_BT}\,(x_1(-\omega)-x_2(-\omega))\right]\right\}\cdot \\ &\cdot\exp\left\{i\,\frac{m\gamma}{2}\int\frac{d\omega}{2\pi}\left[(x_1(\omega)-x_2(\omega))\,\omega\,(x_1(\omega)+x_2(\omega))\right]\right\}.\end{aligned} \tag{1.26}$$

From this, we can identify the α coefficients from Eq. (1.11) which characterize this peculiar influence functional and some of their properties. Specifically:

$$i\text{Im}\alpha(t-t') = \int\frac{d\omega}{2\pi}\,e^{-i\omega(t-t')}\,\mathcal{A}_R(\omega), \tag{1.27}$$

$$\text{Re}\alpha(t-t') = -\int\frac{d\omega}{2\pi}\,e^{-i\omega(t-t')}\,\mathcal{A}_K(\omega). \tag{1.28}$$

For an Ohmic bath, we get in particular:

- An imaginary part $\text{Im}\alpha(\omega) \propto \gamma\omega$ which leads to a friction effect. Fourier transforming to real time, we get a term in the action of the form

$$-m\gamma\int dt'\,(\dot{x}_1(t)+\dot{x}_2(t))\,(x_1(t)-x_2(t)) \tag{1.29}$$

  In this context, γ can be regarded as a friction coefficient.

- A real part $\text{Re}\alpha(t-t')$ with a memory Kernel, as the Fourier transform of $\omega\coth\frac{\omega}{2k_BT}$ does not lead in general to time local terms. This is a non-Markovian

effect coming from the dynamics of the bath itself. In the infinite temperature limit, the real part of the α coefficient can be approximated as a constant ($\omega \coth \frac{\omega}{2k_BT} \sim 2k_BT$), leading to a time-local term and restoring Markovianity [61].

All these concepts will be used in the exploration of quantum synchronization in Chap. 3, and we will see how they also apply in the realm of quantum measurements in Chap. 4.

1.1.2. Lindblad master equation

In this subsection, we will explore another very special case of the influence functional, which can describe Markovian dynamics.

Suppose, for example, to have a Gaussian influence functional, as in Eq. (1.11) with

$$\alpha(t,t') = \gamma\,\delta(t-t'), \tag{1.30}$$

such that the effective action contains only a dissipative term, which is time-local and doesn't contain memory effects.

The system's state $\hat{\rho}$, restoring the many-body formalism, evolves like

$$\rho(\mathbf{x},\mathbf{x}';t) = \int d\mathbf{x}_0\, d\mathbf{x}'_0\, \rho(\mathbf{x}_0,\mathbf{x}'_0) \int_{\mathbf{x}_1(0)=\mathbf{x}_0}^{\mathbf{x}_1(t)=\mathbf{x}} \mathcal{D}\mathbf{x}_1 \int_{\mathbf{x}_2(0)=\mathbf{x}'_0}^{\mathbf{x}_2(t)=\mathbf{x}'} \mathcal{D}\mathbf{x}_2\; e^{i\,S_{\text{eff}}[\mathbf{x}_1,\dot{\mathbf{x}}_1,\mathbf{x}_2,\dot{\mathbf{x}}_2]}, \tag{1.31}$$

$$S_{\text{eff}}[\mathbf{x}_1,\dot{\mathbf{x}}_1,\mathbf{x}_2,\dot{\mathbf{x}}_2] = \int_0^t dt' \left[\frac{m(\dot{\mathbf{x}}_1^2-\dot{\mathbf{x}}_2^2)}{2} - V(\mathbf{x}_1) + V(\mathbf{x}_2) + i\gamma\,(\mathbf{x}_1-\mathbf{x}_2)^2\right]. \tag{1.32}$$

We are now interested in obtaining the evolution over the time slice $t = \delta t$, i.e., over a short time step. This allows us to approximate the path integral as the simpler integral [55]

$$\rho(\mathbf{x},\mathbf{x}';t) = \left(\frac{2\pi}{m}\right) \int d\mathbf{x}_0\, d\mathbf{x}'_0\, \rho(\mathbf{x}_0,\mathbf{x}'_0)\, e^{i\,S_{\text{eff}}[\mathbf{x},\mathbf{x}_0,\mathbf{x}',\mathbf{x}'_0]}, \tag{1.33}$$

$$\begin{aligned} S_{\text{eff}}[\mathbf{x},\mathbf{x}_0,\mathbf{x}',\mathbf{x}'_0] = \delta t \Bigg[& \frac{m((\mathbf{x}-\mathbf{x}_0)^2-(\mathbf{x}'-\mathbf{x}'_0)^2)}{2\delta t^2} - V\Big(\frac{\mathbf{x}+\mathbf{x}_0}{2}\Big) + V\Big(\frac{\mathbf{x}'+\mathbf{x}'_0}{2}\Big) + \\ & + i\frac{\gamma}{4}\,(\mathbf{x}+\mathbf{x}_0-\mathbf{x}'-\mathbf{x}'_0)^2\Bigg]. \end{aligned} \tag{1.34}$$

Performing now the change of variables $\mathbf{x}_0 \to \boldsymbol{\eta} = \mathbf{x}-\mathbf{x}_0$, and $\mathbf{x}'_0 \to \boldsymbol{\varepsilon} = \mathbf{x}'-\mathbf{x}'_0$ we notice that the highly oscillating kinetic term ($\propto \delta t^{-1}$), allows for non-zero contribution to the integral only when $\boldsymbol{\eta},\boldsymbol{\varepsilon} \sim \sqrt{\delta t}$ [55]. Thus, we expand the above evolution equation up to first order in δt, and second order in $\boldsymbol{\eta},\boldsymbol{\varepsilon}$, one obtains

$$\begin{aligned} \frac{\partial\rho(\mathbf{x},\mathbf{x}')}{\partial t} = -i\Bigg(& -\frac{1}{2m}\frac{\partial^2\rho(\mathbf{x},\mathbf{x}')}{\partial\mathbf{x}^2} + \frac{1}{2m}\frac{\partial^2\rho(\mathbf{x},\mathbf{x}')}{\partial\mathbf{x}'^2} + \\ & + V(\mathbf{x})\rho(\mathbf{x},\mathbf{x}') - \rho(\mathbf{x},\mathbf{x}')V(\mathbf{x}')\Bigg) + \gamma\left(\mathbf{x}\rho(\mathbf{x},\mathbf{x}')\mathbf{x}' - \frac{\mathbf{x}^2\rho(\mathbf{x},\mathbf{x}') + \rho(\mathbf{x},\mathbf{x}')\mathbf{x}'^2}{2}\right). \end{aligned} \tag{1.35}$$

Remembering that the $\mathbf{x}$ variables come from the forward path (and thus lie on the left of the $\hat{\rho}$ operator), while the $\mathbf{x}'$ variables come from the backward path (and thus lie on the right of the $\hat{\rho}$ operator), we can rewrite the master equation in operatorial form

$$\partial_t \hat{\rho} \;=\; -i\left[\hat{H},\hat{\rho}\right] + \gamma \sum_{i=1}^{N}\left(\hat{x}_i\,\hat{\rho}\,\hat{x}_i - \frac{1}{2}\left\{\hat{x}_i^2,\hat{\rho}\right\}\right). \tag{1.36}$$

The equation we just wrote has exactly the shape of a **Lindblad master equation** [64, 65], which describes Markovian dissipative dynamics [1–3]. The structure of the equation we have obtained from this very special influence functional is very suggestive. The first term, containing the commutator of the density matrix with the Hamiltonian, corresponds to unitary dynamics and is essentially the Von-Neumann master equation. The second part, real and multiplied by γ corresponds to the action that the bath has on the system, and inserts non-unitarity in the evolution, preserving the trace of the initial state.

We have obtained the Lindblad master equation in a very specific setting, but it represents a very general form of master equation to generate Markovian quantum dynamics [64–67].

The most general (diagonal) form we can derive for the Lindblad equation, is

$$\partial_t \hat{\rho} = -i\left[\hat{H},\hat{\rho}\right] + \sum_{i=1}^{M}\gamma_i\left(\hat{L}_i\,\hat{\rho}\,\hat{L}_i^\dagger - \frac{1}{2}\left\{\hat{L}_i^\dagger\hat{L}_i,\hat{\rho}\right\}\right), \tag{1.37}$$

where the dissipation is due to the action of the **jump operators** $\hat{L}_i$, directly coming from the interaction with the environment. In this case, the equation contains M jump operators, describing M independent types of interaction with the environment (or environments).

The Lindblad equation has several important properties, such as the **linearity** in the system's state $\hat{\rho}$, and **complete positivity**. The Lindblad equation is also **trace preserving**, as can be easily checked directly from Eq. (1.37) using the cyclic properties of the trace. Altogether, these properties ensure that the reduced density matrix of the system's state $\hat{\rho}$ has all the good properties of density matrices preserved at any time step despite dissipation.

Notice that the Lindblad master equation can be written introducing the Liouvillian $\mathcal{L}$, as

$$\dot{\rho}(t) = \mathcal{L}(\rho), \tag{1.38}$$

which allows for the suggestive description of the dynamics (for a time-independent Liouvillian) as

$$\rho(t) = e^{\mathcal{L}t}\hat{\rho}(0). \tag{1.39}$$

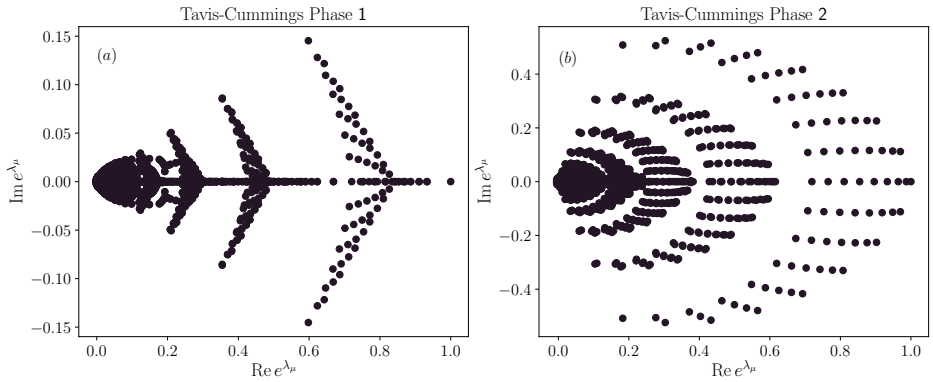

Figure 1.2.: Examples of Lindbladiand spectra. The two pictures show the exponentiation of the eigenvalues λ_μ for the Tavis-Cummings model for $N = 8$ spins, which will be discussed in detail in Sec.4.2. The two panels show the spectrum in the two phases of the Tavis-Cummings model (stationary in panel (a) and time-crystal in panel (b)), which present a totally different structure of the eigenvalues.

The integrated form of the Lindblad master equation, Eq. (1.39) reveals some important properties of the dynamics of Markovian open quantum systems. This can be easily uncovered through the process of vectorization [68, 69], which generalizes density matrices to superstates (and rewrites it as a vector) and the Liouvillian to a superoperator (becoming a symmetric non-Hermitian matrix).

$$\hat{\rho} \to |\rho\rangle\!\rangle, \qquad \mathcal{L} \to \hat{\hat{\mathcal{L}}}. \tag{1.40}$$

The vectorization process takes the problem to a higher dimensionality: given that the density matrix has size $D \times D$ (with D being the dimension of the Hilbert space), the vector $|\rho\rangle\!\rangle$ will have size D^2, while the Liouvillian superoperator will be a $D^2 \times D^2$ matrix. Although computationally expensive, this formalism allows for the diagonalization of the Liouvillian and offers a powerful theoretical insight. Being a symmetric non-Hermitian matrix, the diagonalization provides both left eigenvectors $\langle\!\langle l_\mu|$ and right eigenvectors $|r_\mu\rangle\!\rangle$ along with complex eigenvalues λ_μ in conjugate pairs:

$$\hat{\hat{\mathcal{L}}}\,|r_\mu\rangle\!\rangle = \lambda_\mu\,|r_\mu\rangle\!\rangle, \qquad \langle\!\langle l_\mu|\,\hat{\hat{\mathcal{L}}} = \lambda_\mu\,\langle\!\langle l_\mu|\,. \tag{1.41}$$

Examples of Liouvillian spectra are shown in Fig.1.2, the plots are drawn from the Tavis-Cummings model, discussed in Sec.4.2.

A few properties of the spectrum of the Liouvillian, assuming bi-orthogonality $\langle\!\langle\, l_\mu \,|r_\nu\,\rangle\!\rangle = \delta_{\mu,\nu}$, will be now listed. The trace preservation property of the Lindblad equation implies that the identity $\langle\!\langle \mathbb{I}| = \langle\!\langle l_0|$ is always a left eigenvector, with relative eigenvalue $\lambda_0 = 0$; This means that there must be (at least) one right eigenvector $|r_0\rangle\!\rangle$ with $\lambda_0 = 0$. If it is unique, then it is trace one $\langle\!\langle\, \mathbb{I}\,|r_0\,\rangle\!\rangle = 1$ and all the other right eigenvectors are traceless $\langle\!\langle\, \mathbb{I}\,|r_\mu\,\rangle\!\rangle = 0, \mu \neq 0$. In Fig. (1.2), $|r_0\rangle\!\rangle$ is identified by the point $(\mathrm{Re}e^{\lambda_\mu}, \mathrm{Im}e^{\lambda_\mu}) = (1, 0)$.

This is particularly useful for dynamics and identification of the steady state, as we can rewrite the evolution equation in terms of overlaps of the left eigenvectors with the initial state $|\rho(0)\rangle\!\rangle$, the right eigenvectors, and the eigenvalues.

$$\mathscr{C}_\mu = \langle\!\langle\, l_\mu \,|\rho(0)\,\rangle\!\rangle, \qquad\qquad |\rho(t)\rangle\!\rangle = \sum_\mu \mathscr{C}_\mu\, e^{\lambda_\mu\, t}\ |r_\mu\rangle\!\rangle. \tag{1.42}$$

The structure of the dynamics is clear from this equation: the real part of the eigenvalues (always negative) determines an exponential decay with time, while the imaginary part yields oscillations.

Let us assume for a moment that there is only one eigenvalue with $\mathrm{Re}\lambda_\mu = 0$. It is then evident that for long times $t \to \infty$ the eigenvalue which dominates the dynamics is $\lambda_0 = 0$, giving the non-decaying steady state $|r_0\rangle\!\rangle = |\rho_{\mathrm{SS}}\rangle\!\rangle$.

The relaxation dynamics is instead determined by the eigenvalue with the smallest real part $\Gamma = -\mathrm{Re}\tilde{\lambda} = \min_{\mu\neq 0}\{-\mathrm{Re}\lambda_\mu\}$, which is denominated **Liouvillian Gap**. From now on, we will label the eigenvector relative to $\tilde{\lambda}$ as $|\tilde{r}\rangle\!\rangle$ (notice that if $\mathrm{Im}\tilde{\lambda} \neq 0$, also $\tilde{\lambda}^*$ and its eigenvector should be considered).

Thus, as presented, the Liouvillian spectrum defines not only the dynamical features of many-body open quantum systems, but also the structure of the steady state. The intriguing properties of steady states and the possibility of witnessing dissipative phase transitions due to the interplay of dissipation and unitary dynamics are key concepts in this Thesis, and will be discussed in general in Chap. 2. Concrete examples of dissipative phase transitions will then be studied in Chaps. 3 and 4, not only through the Lindblad formalism but also through the more general path integral one.

1.2. Quantum Measurements

Measurements represent one of the most peculiar effects in quantum mechanics, as they modify the system state in a unique way that goes beyond the description that unitary operations can offer [70–73]. In general, measuring a system requires coupling it to a measurement device, which is responsible for extracting information from the system and in turns irreversibly modifies the system's state. This picture connects directly to the open-quantum system setting and this Section will be devoted to expanding this connection.

The most typical example of how drastically a system's state is changed by measurements is given by the application of projective measurements. This shows how the domain of quantum measurements goes beyond the natural framework of closed and isolated systems as they cause the system's state to collapse on one of the eigenvectors of the measured operator $\hat{R}$ (with $\hat{R}\,|R\rangle = R\,|R\rangle$):

$$|\psi'\rangle \to \hat{\Pi}_R\,|\psi\rangle \propto |R\rangle\,. \tag{1.43}$$

happening with a probability,

$$P(R) = \langle\psi|\hat{\Pi}_R|\psi\rangle\,. \tag{1.44}$$

Thus, performing a projective measurement of the $\hat{R}$ operator abruptly changes the state to one of the eigenvectors of the observable we are measuring, $|R\rangle$, selected according to Born's rule i.e. with a probability $P(R)$.

Projective measurements let us gain complete information about the post-measurement state, but dramatically change the shape of the pre-measurement state. It is possible to monitor the system through the so-called weak measurements, which allow access to little information about the system's state, but at the same time perturb it as little as possible. These types of measurements will be central in our discussion.

Specifically, this Section will describe the continuous monitoring of many-body systems by means of weak measurements. As in laboratories, one has several possibilities for measuring the system under consideration, hence, we will introduce several methods that correspond to different ways of probing and, inevitably, modifying the system's state. In Sec. 1.2.1, Gaussian weak measurements will be introduced. This setting is particularly important because it allows for a picture similar to the one introduced in Sec. 1.1 of system-bath interactions, which directly connects to the path integral formalism already introduced. Sec. 1.2.2, will instead introduce the concepts of measurements by counting events and the idea of quantum jumps, creating further connection with the language of open quantum systems.

As Sec. 1.1 has laid the foundations to thoroughly characterize the effects induced by dissipation on the structure of the steady-state of the system, this section will offer a discussion to handle the long-time properties of monitored systems. In particular, we will be interested in the introduction of the concept of measurement-induced phase transitions, which are critical phenomena emerging only from the monitoring of many-body systems. This will be the content of the next Chap. 2.2, which deals with critical phenomena.

1.2.1. Weak and Gaussian Measurements or Homodyne detection

A first example of weak measurements was proposed in the 80s in Refs. [74, 75].

In this context, weak measurements are obtained by weakly coupling our system to a measurement device - the *meter*, which is projectively measured.

For simplicity, we will picture this framework using a single-body system, $\hat{x}, \hat{p}$ with $[\hat{x}, \hat{p}] = i$, and a single-body meter with $\hat{X}, \hat{P}$ and $\left[\hat{X}, \hat{P}\right] = i$. We focus on position measurements $\hat{x}$. Following Cave's implementation [75] the interaction between the system and the meter is determined by

$$\hat{H}_{\text{int}} = g\,\hat{x}\,\hat{P}. \tag{1.45}$$

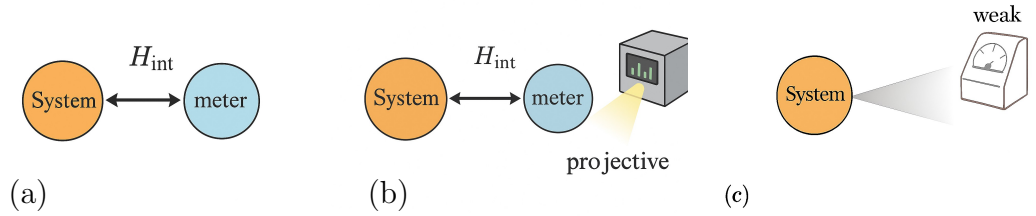

Figure 1.3.: Representation on the process yielding a weak measurement. (a) A system is coupled weakly to an inaccessible meter. (b) the meter is projectively measured. (c) The projective measure on the meter has an effect of the system, which can be recast in terms of a weak measurement operator.

For the sake of simplicity, we can avoid considering the bare Hamiltonians of the system and the meter, having the global Hamiltonian only containing the interaction term $\hat{H}_{\text{int}}$. The initial state for the global system is separable and reads

$$|\Phi\rangle = |\psi\rangle \otimes |\Psi\rangle = \int dx\, dX\, \psi(x)\, \Psi(X)\ |x\rangle \otimes |X\rangle\,, \tag{1.46}$$

where $\psi(x) = \langle x|\psi\rangle$ is the system's wavefunction and $\Psi(X) = \langle X|\Psi\rangle$ is the meter's wavefunction. The effect of acting with the interaction Hamiltonian over the system's state for a time interval dt is

$$\begin{aligned} |\Phi'\rangle &= e^{-i\, dt\, \hat{H}_{\text{int}}}\ |\Phi\rangle \\ &= \int dx\, dX\, e^{-ig\, x\hat{P}}\, \psi(x)\, \Psi(X)\ |x\rangle \otimes |X\rangle\,, \\ &= \int dx\, dX\, \psi(x)\, \Psi(X - gx)\ |x\rangle \otimes |X\rangle\,. \end{aligned} \tag{1.47}$$

With a rescaling of x, and projectively measuring the position $\hat{X}$ of the meter we get to understand what the effect of this procedure is on the system. Suppose the projective measurement gives as readout r. The state after the projection will be :

$$\langle X = r|\Phi'\rangle = \left|\tilde{\psi}'\right\rangle = \int dx\, \psi(x)\, \Psi(r - x)\ |x\rangle = \hat{M}_r\, |\psi\rangle\,. \tag{1.48}$$

Thus, we can interpret the coupling to the meter and the meter's position projective measurement as the action on the system of the non-unitary operator

$$\hat{M}_r = \Psi(r - \hat{x}). \tag{1.49}$$

The process is illustrated in Fig. 1.3.

Two facts should be noticed. The first one is the $\hat{M}_r^\dagger \hat{M}_r$ is a positive-valued operator measurement (POVM) [76, 77] as $\int dr \hat{M}_r^\dagger \hat{M}_r = \mathbb{1}$. Moreover, being a non-unitary operator, the system's state $\left|\tilde{\psi}\right\rangle$ is not normalized, and the post-measurement state

should be appropriately written as

$$|\psi'\rangle = \frac{\hat{M}_r |\psi\rangle}{\sqrt{\langle\psi|\hat{M}_r^\dagger \hat{M}_r|\psi\rangle}}. \tag{1.50}$$

This simple picture shows us how to get any kind of measurement operator shape simply by modeling the state of the meter. The weak measurement we will use many times in this thesis is obtained from a Gaussian wavefunction for the meter.

We thus define a general Gaussian measurements operator, for measurements of $\hat{R}$, as [32, 33, 78]

$$\hat{M}_r = \left(\frac{2\gamma\delta t}{\pi}\right)^{1/4} e^{-\gamma\delta t\,(r-\hat{R})^2}, \tag{1.51}$$

where γ is the measurement strength. We will always consider $\hat{R}$ such that it has a continuous spectrum and its eigenstates form a complete basis for the Hilbert space. In this case, from the spectral decomposition $\hat{M}_r \propto \int dR\, e^{-\gamma\delta t(r-R)^2} |R\rangle \langle R|$, we see that the operator is a superposition of projection operators on eigenstates of the operator $\hat{R}$, weighted by a Gaussian factor.

Consider now the following setting: we have a system with Hamiltonian $\hat{H}$. We evolve an initial state $|\psi_0\rangle$ by dividing the time evolution from $t_0 = 0$ to t in A small time steps δt, such that $A = t/\delta t$. At each time step we apply both the evolution operator $\hat{\mathcal{U}}(\tau + \delta t, \tau) = \hat{\mathcal{U}}_{\delta t} = \exp\left\{-i\delta t\hat{H}\right\}$ and the Gaussian measurement operator $\hat{M}_r$.

The un-normalized evolved state in the continuous limit is:

$$\left|\tilde{\psi}(t)\right\rangle = \lim_{\substack{\delta t\to 0 \\ A\to\infty}} \left[\prod_{a=1}^{A} \hat{M}_{r_a}\, \hat{\mathcal{U}}_{\delta t}\right] |\psi_0\rangle\,, \tag{1.52}$$

where the operators with smaller a act before the operators with a bigger, and the $\tilde{\bullet}$ (tilde) signals non-normalized states.

The collection of readouts throughout the whole evolution, $\{r_1, ..., r_a, ...r_A\} \xrightarrow{\delta t\to 0} r(t)$ is called a **quantum trajectory** [79, 80] and represents a realization of the continuous monitoring process. It constitutes the building unit for describing the dynamics of monitored systems.

Consider now just one of the bricks building this kind of monitored dynamics. We exploit the fact that δt is an infinitesimally small time-step and the Hausdorff-Campbell-Formula. For the sake of simplicity and without loss of generality, we fix for this moment only the measurement operator to be the position operator $\hat{R} = \hat{x}$, as it allows us to fix more easily a basis and choose a representation. For a general Hamiltonian

$\hat{H} = \frac{\hat{p}^2}{2m} + V(\hat{x})$, we get:

$$\hat{\mathcal{U}}_{\delta t}\,\hat{M}_r \propto e^{-i\delta t(\frac{\hat{p}^2}{2m}+V(\hat{x}))}\, e^{-\gamma\delta t(r-\hat{x})^2} \sim e^{-i\delta t\left(\frac{\hat{p}^2}{2m}+V^+_{\text{eff}}(\hat{x})\right)}, \tag{1.53}$$

$$\hat{M}_r\,\hat{\mathcal{U}}^\dagger_{\delta t} \propto, e^{-\gamma\delta t(r-\hat{x})^2}\, e^{+i\delta t(\frac{\hat{p}^2}{2m}+V(\hat{x}))} \sim e^{+i\delta t\left(\frac{\hat{p}^2}{2m}+V^-_{\text{eff}}(\hat{x})\right)}, \tag{1.54}$$

where we have introduced the complex effective potentials

$$V^\pm_{\text{eff}}(\hat{x}) = V(\hat{x}) \mp i\gamma(r-\hat{x})^2. \tag{1.55}$$

This is particularly useful, as it allows straightforwardly to express the dynamics of the un-normalized state via a Keldysh path integral formalism, where each branch is constructed *á la Feynman* using the effective potential $\hat{V}^+_{\text{eff}}$ for the backward branch and $\hat{V}^-_{\text{eff}}$ for the forward branch. This yields for an initial state $\hat{\rho}_0$ in position representation [75]:

$$\tilde{\rho}(x,x';t) = \int dx_0\, dx'_0\, \rho_0(x_0,x'_0) \int_{x_1(0)=x_0}^{x_1(t)=x} \mathcal{D}x_1 \int_{x_2(0)=x'_0}^{x_2(t)=x'} \mathcal{D}x_2 \cdot \\ \cdot\, e^{i(S[x_1,\dot{x}_1]-S[x_2,\dot{x}_2])-\gamma\int_0^t dt'\left[(r(t')-x_1)^2+(r(t')-x_2)^2\right]}. \tag{1.56}$$

This expression connects directly with the path integral formulation of the dynamics we have derived for open quantum systems in Eq. (1.9). In this case, the influence functional is not given by a direct tracing out of the bath's degrees of freedom but depends on the Gaussian measurement operator. It should be noted also that, in this case, the dissipative imaginary part depends specifically on measurement outcomes that one obtains along the whole dynamics, i.e. depends on the quantum trajectory. The quantum trajectory is shared between the two branches and makes them interact.

Beyond the suggestive vision given by the path integral formulation, it is also particularly interesting to focus on a single time step δt. Let us return to the more general setting in which we measure a general operator $\hat{R}$. First of all, notice that from Eq. (1.48) follows that for a single time step, the probability of getting the measurement outcome r is

$$P(r) = \text{Tr}\left\{\hat{M}^\dagger_r \hat{M}_r\,|\psi\rangle\langle\psi|\right\} = \int dR \left(\frac{2\gamma\delta t}{\pi}\right)^{1/2} e^{-2\gamma\delta t(r-R)^2}|\psi(R)|^2. \tag{1.57}$$

From this, it immediately follows that the average value and variance for the readout r will be

$$\overline{r} = \int dr\, r\, P(r) = \left\langle \hat{R}\right\rangle_\psi \qquad \sigma^2_r = \int dr\,(r-\overline{r})^2 P(r) = \frac{1}{4\gamma\delta t}, \tag{1.58}$$

while all the other cumulants are zero. This allows for the interpretation of r as a Wiener-like stochastic process [78]:

$$r = \left\langle \hat{R}\right\rangle_\psi + \frac{dW}{\sqrt{4\gamma\delta t}}, \qquad \text{with } \overline{dW} = 0,\ dW^2 = \delta t. \tag{1.59}$$

This interpretation leads to a peculiar rewriting of the measurement operator as $\hat{M}_r = \hat{M}_{dW} = \left(\frac{2\gamma\delta t}{\pi}\right)^2 \exp\left\{-\gamma\delta t(\hat{R} - \langle R\rangle_\psi - \frac{dW}{2\sqrt{\gamma}\delta t})^2\right\}$, and suggest how the quantum trajectory is given by a realization of the Wiener stochastic process dW.

We use this fact to derive the master equation along quantum trajectories. Along a tiny time-step δt the initial (mixed or pure) state $\hat{\rho}(t)$ evolves to a new normalized state according to:

$$\hat{\rho}(t+\delta t) = \frac{\hat{\mathcal{U}}_{\delta t}\,\hat{M}_{dW}\,\hat{\rho}(t)\,\hat{M}_{dW}^\dagger\,\hat{\mathcal{U}}_{\delta t}^\dagger}{\mathrm{Tr}\left\{\hat{M}_{dW}^\dagger\hat{M}_{dW}\hat{\rho}(t)\right\}}. \tag{1.60}$$

Expanding the above equation up to first order in δt and to second order in dW (since for Ito's rule $dW^2 = \delta t$), one gets the stochastic master equation for Gaussian Measurements:

$$d\hat{\rho}(t) = -idt\left[\hat{H},\hat{\rho}(t)\right] + \gamma dt\left(\hat{R}\hat{\rho}(t)\hat{R} - \frac{1}{2}\left\{\hat{R}^2,\hat{\rho}(t)\right\}\right) + \sqrt{\gamma}dW\left\{\hat{R} - \left\langle\hat{R}\right\rangle_\rho,\hat{\rho}(t)\right\} \tag{1.61}$$

The generalization to the many-body setting or to multiple independent measurements (M) is straightforward:

$$d\hat{\rho}(t) = -idt\left[\hat{H},\hat{\rho}(t)\right] + \sum_{j=1}^{M}\gamma_j dt\left(\hat{R}_j\hat{\rho}(t)\hat{R}_j - \frac{1}{2}\left\{\hat{R}_j^2,\hat{\rho}(t)\right\}\right) \tag{1.62}$$

$$+\sum_{j=1}^{M}\sqrt{\gamma_j}dW_j\left\{\hat{R}_j - \left\langle\hat{R}_j\right\rangle_\rho,\hat{\rho}(t)\right\} \tag{1.63}$$

with $dW_j dW_i = \delta t\,\delta_{i,j}$.

The master equation we have written is also named *quantum state diffusion* [81] when describing the evolution of pure states, and the measurement technique representing this equation is named *homodyne detection* [32]. The equation has the following important properties:

- It describes the evolution of a state along the trajectory characterized by the sequence of dW.
- It is a stochastic equation which is also **non-linear** in the system state. This is manifest in the last term of the equation where $\left\langle\hat{R}_j\right\rangle_\rho\hat{\rho}(t) = \mathrm{Tr}\left\{\hat{R}_j\rho(t)\right\}\hat{\rho}(t)$ appears. These are crucial differences from the Lindblad equation.
- Averaging both l.h.s. and r.h.s., one obtains a master equation for the state $\overline{\hat{\rho}}$ averaged over all the possible trajectories, i.e., over all the possible realizations of the measurement process. The master equation for the average state is

$$d\overline{\hat{\rho}}(t) = -i\left[\hat{H},\overline{\hat{\rho}}(t)\right] + \sum_{j=1}^{M}\gamma_j\left(\hat{R}_j\overline{\hat{\rho}}(t)\hat{R}_j - \frac{1}{2}\left\{\hat{R}_j^2,\overline{\hat{\rho}}(t)\right\}\right).$$

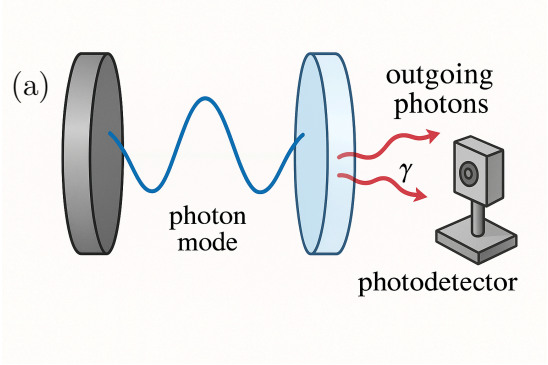

Figure 1.4.: Representation of photons escaping a cavity and being detected by a measurement device: the photodetector. This is a classical setting to introduce the concept of quantum jumps, associated in this case with photons escaping with a rate γ and being detected.

> This is a Lindblad equation! When we have a measurement process and we don't care about specific measurement outcomes (so we average over them), the only effect remaining is the dissipation associated with the measurement procedure.

The latter fact is particularly important as it states the connection between continuous measurements and open quantum systems and, most importantly, gives us another way to deal with Lindblad equations [81] with jump operators $\sqrt{\gamma_j}\hat{L}_j = \sqrt{\gamma_j}\hat{R}_j$. For pure states indeed, the quantum state diffusion equation becomes simply

$$d\left|\psi(t)\right\rangle = \left[-idt\hat{H} - \sum_{j=1}^{M}\frac{\gamma_j}{2}dt\left(\hat{R}_j - \left\langle\hat{R}\right\rangle_\psi\right)^2 + \sum_{j=1}^{M}\sqrt{\gamma_j}\left(\hat{R}_j - \left\langle\hat{R}_j\right\rangle_\psi\right)dW_j\right]\left|\psi(t)\right\rangle. \tag{1.64}$$

If the density matrix has linear size D, solving the Lindblad equations is computationally expensive as D^2, while solving the above master equation and averaging over trajectories has a cost which is only D, i.e. linear in the Hilbert space dimension.

This approach to solve dissipative dynamics, named as *homodyne unraveling* of the Lindblad equation, is a standard approach for open many-body quantum systems [1, 80, 81].

1.2.2. Counting events, or quantum jump measurements

The next kind of measurement we would like to describe is based on the concept of counting the occurrences of specific events. The situation we will have in mind throughout this part of the Thesis is photodetection. We can, for example picture a cavity containing photons, with photons leaking from the cavity at a rate γ. The leakage of photons is caught by a detector, which signals every time it has been hit by a photon. This is represented in Fig. 1.4.

In the rest of the Section, we will dub the detection event as a *quantum jump* occurrence, a name coming from the fact that the state of the system is suddenly modified. Non-detection, instead, will correspond to a non-occurrence of the jump.

In this picture, at each time step the measurement outcome is essentially binary: either a jump has occurred (a photon escaping has been detected), or nothing has occurred: nothing escaped the cavity. The **quantum trajectory** for this type of measurement is thus entirely specified by the precise time at which a jump has occurred, as this allows us to build the binary string of detection/non-detection events in time.

The way to represent this in quantum mechanics requires the use of two operators, one for each measurement outcome [32, 33, 82] (detection/non-detection), $\hat{u}_1, \hat{u}_0$. We will now try to identify $\hat{u}_0, \hat{u}_1$ such that $\hat{u}_1$ is the non-unitary measurement operator corresponding to detection, while $\hat{u}_0$ is the non-unitary measurement operator corresponding to non-detection.

Let us consider, for a moment again, the picture of a quantum single-mode cavity with leaking photons at a rate γ. Suppose that the system is in the state $\hat{\rho}$.
Over a short time-step δt, the probability of having a photon escaping, i.e. the occurrence of a quantum jump, is $p_1 \propto \gamma\delta t$. This should be obtained in terms of $\hat{u}_1$ as

$$\gamma\delta t \propto \mathrm{Tr}\Big\{\hat{u}_1\hat{\rho}\hat{u}_1^\dagger\Big\} = p_1. \tag{1.65}$$

This means that $\hat{u}_1 \propto \sqrt{\delta t}$. Since the loss of a photon is determined by the action of the bosonic operator $\hat{a}$ over the system's state, we can interpret

$$\hat{u}_1 = \sqrt{\delta t}\,(\sqrt{\gamma}\hat{a})\,, \tag{1.66}$$

with the **jump operator** $\sqrt{\gamma}\hat{a}$ being a constant operator over the small time window δt.

Having now identified the operator $\hat{u}_1$, we can easily identify $\hat{u}_0$ remembering that together they must define a POVM measurement: $\hat{u}_0^\dagger\hat{u}_0 + \hat{u}_1^\dagger\hat{u}_1 = \mathbb{I}$. Thus

$$\hat{u}_0^\dagger\hat{u}_0 = \mathbb{I} - dt\gamma\,\hat{a}^\dagger\hat{a} \sim e^{-\gamma\delta t\hat{a}^\dagger\hat{a}}. \tag{1.67}$$

This leads to the form of the non-detection operator:

$$\hat{u}_0 = e^{-\frac{\gamma\delta t}{2}\hat{a}^\dagger\hat{a}}. \tag{1.68}$$

Notice the non-occurrence probability is found correctly as $p_0 = 1-p_1 = 1-\gamma\delta t\,\mathrm{Tr}\big\{\hat{a}^\dagger\hat{a}\hat{\rho}\big\}$.

Thus, in the picture of a cavity with photon losses we have an evolution for the state as

$$|\psi(t+\delta t)\rangle = \begin{cases} \dfrac{\hat{u}_1|\psi(t)\rangle}{\sqrt{\langle\psi(t)|\hat{u}_1^\dagger\hat{u}_1|\psi(t)\rangle}} = \dfrac{\hat{a}|\psi(t)\rangle}{\sqrt{\langle\psi(t)|\hat{a}^\dagger\hat{a}|\psi(t)\rangle}} & \text{with } p_1 = \gamma\delta t\,\big\langle\hat{a}^\dagger\hat{a}\big\rangle_{\psi(t)} \\ \dfrac{\hat{u}_0|\psi(t)\rangle}{\sqrt{\langle\psi(t)|\hat{u}_0^\dagger\hat{u}_0|\psi(t)\rangle}} \sim \dfrac{e^{-\frac{\gamma\delta t}{2}\hat{a}^\dagger\hat{a}}|\psi(t)\rangle}{\sqrt{1-\gamma\delta t\langle\psi(t)|\hat{a}^\dagger\hat{a}|\psi(t)\rangle}} & \text{with } p_0 = 1-p_1 \end{cases} \tag{1.69}$$

This photons' picture helps us understand what information we gain from this type of measurement [83]. Suppose the state of the cavity to be a superposition of Fock states: $|\psi(t)\rangle = \sum_{n=0}^{N} c_n |n\rangle$.

- The probability of detecting a photon depends not only on the rate γ but also on the system state and on its photons availability: if the state has few photons $\mathcal{N} = \sum_n |c_n|^2 n$, it is less likely it will lose one. Taking the concept to its extreme: an empty cavity will not lose photons, as it should be.
- If a photon is lost (detection event), we gain information about the system's state as we know that it has one photon less and we know how it changes: $|\psi(t+\delta t)\rangle \propto \sum_{n=0}^{N-1} c_n \sqrt{n} |n-1\rangle$.
- If a photon is not lost (non-detection) we anyway gain information about the system's state. We learn that it is more likely that the cavity has few photons and, for this reason, is not losing them. The operator $\hat{u}_0$ indeed modifies the weight of the Fock superposition as $c_n \to e^{-\frac{\gamma \delta t}{2} n} c_n$, giving more relevance to Fock states with less photons in the superposition.

We can now come back to a more general scenario. Consider a many-body system with Hamiltonian $\hat{H}$, and consider that we have M jump operators representing events we want to count in this many-body system. Each has a rate γ_i with $j = 1, .., M$ such that the jump operators are $\sqrt{\gamma_j}\hat{R}_j$. In this case, the probability of a jump (any jump) happening is $p_1 = \delta t \sum_j^M \gamma_j \left\langle \hat{R}_j^\dagger \hat{R}_j \right\rangle = \sum_j^M p_1^{(j)}$. The state evolves at every time step δt as

$$|\psi(t+\delta t)\rangle = \begin{cases} \frac{\hat{R}_j|\psi(t)\rangle}{\sqrt{\langle\psi(t)|\hat{R}_j^\dagger \hat{R}_j|\psi(t)\rangle}} & \text{with } p_1^{(j)} = \gamma_j \delta t \left\langle \hat{R}_j^\dagger \hat{R}_j \right\rangle_\psi \\ \frac{e^{-i\delta t H_{\text{nh}}}|\psi(t)\rangle}{\sqrt{1-\sum_j \gamma_j \delta t \langle\psi(t)|\hat{R}_j^\dagger \hat{R}_j|\psi(t)\rangle}} & \text{with } p_0 = 1 - \sum_j p_1^{(j)} \end{cases} \tag{1.70}$$

where we have introduced the non-Hermitian Hamiltonian

$$\hat{H}_{\text{nh}} = \hat{H} - i \sum_j \frac{\gamma_j}{2} \hat{R}_j^\dagger \hat{R}_j. \tag{1.71}$$

Essentially, observing a system through event counting produces a smooth non-hermitian dynamics interrupted at random times by sudden jumps which instantaneously modify the system's state. Having a non-hermitian type of evolutor is again reminiscent of what we have seen in the previous Section about open quantum physics. In this case, a direct connection with the open quantum evolution is slightly more difficult, as the evolution of the last Section was always smooth, while quantum jumps produce discontinuous changes in the system's state.

We can also ask in this case what happens if we do not care about every single realization of the measurement process, and we want to know about the average dynamics produced by this type of measurement.

Over a short time step δt, we can write [83]:

$$\overline{\hat{\rho}(t+\delta t)} = (1-p_1)\frac{e^{-i\hat{H}_{\rm nh}\delta t}\,|\psi(t)\rangle}{\sqrt{1-p_1}}\frac{\langle\psi(t)|\,e^{i\delta t\hat{H}^*_{\rm nh}}}{\sqrt{1-p_1}} + p_1\sum_j \frac{p_1^{(j)}}{p_1}\frac{\sqrt{\gamma_j}\hat{R}_j\,|\psi(t)\rangle}{\sqrt{p_1^j/\delta t}}\frac{\langle\psi(t)|\,\hat{R}_j^\dagger\sqrt{\gamma}_j}{\sqrt{p_1^{(j)}/\delta t}} \tag{1.72}$$

$$= \left(1-i\delta t\,\hat{H}_{\rm nh}\right)\,\hat{\rho}(t)\left(1+i\delta t\,\hat{H}^*_{\rm nh}\right) + \delta t\,\sum_j \gamma_j\hat{R}_j\,\hat{\rho}(t)\,\hat{R}_j^\dagger, \tag{1.73}$$

where $\overline{\bullet}$ labels once again averages over quantum trajectories. Keeping all the terms up to first order in δt, we get the following master equation for the average state:

$$\partial_t\overline{\hat{\rho}(t)} = -i\left[\hat{H},\overline{\hat{\rho}(t)}\right] + \sum_j \gamma_j\left(\hat{R}_j\,\overline{\hat{\rho}(t)}\,\hat{R}_j^\dagger - \frac{1}{2}\left\{\hat{R}_j^\dagger\hat{R}_j,\overline{\hat{\rho}(t)}\right\}\right). \tag{1.74}$$

The master equation describing the evolution of the system when we discard the information about the specific realization of the measurement process is once again the Lindblad equation. The quantum jumps we are counting correspond to the quantum jumps of the Lindblad equation, and once again, the Lindblad picture captures the underlying dissipation mechanism behind measurement's non-unitarity.

Again, as in the case of Gaussian measurements, we can think of quantum jumps as a way to simulate in a computationally efficient way the evolution of a density matrix through a Lindblad master equation. This type of unraveling was proposed in Ref. [83] and has been presented as a Monte Carlo approach to solve dissipative dynamics.

Returning to the general setting of weak measurements, the monitored dynamics generated by the interplay of quantum measurements and unitary dynamics can produce intriguing phenomena in the steady state. Specifically, we will be interested in the study of critical phenomena induced by quantum measurements. This important concept will be the object of the next Chapter in Sec. 2.2 and will connect to and generalize the concept of dissipative phase transitions. Throughout the Thesis we will see many examples of this new kind of critical phenomena, emerging from very diverse quantum many-body systems, such as spin-boson models 4.2, spin chains 4.3 and interacting bosonic systems 5.

2. Critical Phenomena in Open Quantum Systems

So far, we have introduced several tools and concepts to describe the non-unitary dynamics of many-body systems, both in the case of pure dissipation and in the case of non-unitarity introduced by quantum measurements. The dynamical description we have carried out has relied on a path integral formalism, which also allows us to describe measurements and general non-Markovian dynamics, and on the Lindblad master equation, opening to the discussion of Markovian quantum dynamics.

Non-unitary dynamics is a central topic in this Thesis; however, the discussion of open quantum many-body systems cannot overlook a thorough description of the steady states and long-time properties generated by this kind of dynamics. In particular, the analysis of critical phenomena arising in this context deserves special mention in this Thesis.

This Chapter will deal with the analysis of critical phenomena generated by the competition of the unitary dynamics stemming from the Hamiltonian, and dissipation or quantum measurements.

The first part of the Chapter, Sec. 2.1, deals with the interplay of Hamiltonian dynamics and dissipation, and is thus centered on *dissipative phase transitions*. The general concept will be introduced starting from the concept of Liouvillian spectrum introduced in the previous Chapter, Sec. 1.1.2. Examples and phenomena related to dissipative phase transitions will be introduced as well, as they will appear in the presentation of the works in Chap. 4.1.

The second part of the Chapter, Sec. 2.2, is instead based on the analysis of the long-time properties induced by the presence of quantum measurements. Specifically we will introduce *measurement-induced phase transitions*, discussing their emergence and all the practical, theoretical, and experimental problems related to their detection.

2.1. Dissipative phase transitions

This Section reconnects directly with the concept introduced in Sec.1.1.1,1.1.2, about dissipative dynamics. The aim is very simple, and consists in an analysis of the long-

time behaviour of the dynamics generated by a system in contact with an environment.

The concepts introduced in this Section will be particularly useful to understand the effects that dissipation generates in the models studied in the next Chapters. For example, Chap. 3 deals with a dissipative phase transition emerging from the non-Markovian dynamics of open quantum rotors, which is described in a path integral formalism; and Chap. 4 describes peculiar dissipative transitions stemming from Lindblad dynamics.

While, as mentioned, the concept of dissipative phase transitions is very general and emerges from all the different formalisms we have presented, in this Section we will focus on the analysis of the steady-states emerging from Lindblad dynamics. This will allow for an easier interpretation and exposition through the features of the Liouvillian spectrum.

For this reason, we recall Eq.(1.42) describing the dynamics of a Markovian open quantum system in a vectorized form:

$$\mathscr{C}_\mu = \langle\langle\, l_\mu \,|\rho(0)\,\rangle\rangle, \qquad\qquad |\rho(t)\rangle\rangle = \sum_\mu \mathscr{C}_\mu\, e^{\lambda_\mu\, t}\ |r_\mu\rangle\rangle.$$

The discussion of steady-state properties and dissipative phase transitions must be conducted taking the infinite-time limit of this equation and thus relies only on the longest-lived eigenvectors and relative eigenvalues of the Liouvillian. Specifically, we will discuss properties emerging from the steady state, already introduced as,

$$\hat{\rho}_{\rm SS} \to |r_0\rangle\rangle, \ \text{ with } \lambda_0 = 0, \tag{2.1}$$

and the eigenvector forming the Liouvillian gap, supposing it to be real,

$$\hat{\tilde{\rho}} \to |\tilde{r}\rangle\rangle, \ \text{ with } \tilde{\lambda} = -\Gamma. \tag{2.2}$$

In the case of a conjugated pair of complex eigenvalues forming the Liouvillian gap, both their eigenvectors should be considered. Let us now introduce the concept of dissipative phase transitions through the analysis of these long-lived states.

Dissipative phase transitions arise in many-body open quantum systems as the competition between dissipation and Hamiltonian dynamics generates an abrupt change in the structure of the steady state. Usually, these non-analytic changes are probed through order parameters based on the average value in the steady state of a suitable operator $\hat{A}$. Suppose that the non-analyticity in the steady state appears by varying a parameter η which quantifies the competition between the dissipative and the unitary part of the Lindblad dynamics. The order parameter should then be studied as a function of η: $\mathcal{A}(\eta) = \mathrm{Tr}\Big\{\hat{A}\,\hat{\rho}_{\rm SS}(\eta)\Big\}$.

Then the phase transition can be identified by the singular behaviour of

$$\lim_{\eta\to\eta_c} \left(\frac{d}{d\eta}\right)^k \mathcal{A}(\eta), \tag{2.3}$$

where η_c is the critical value at which the non-analyticity occurs, and k is the order of the derivative showing the singular behaviour. The value of k determines the order of the phase transition.

Fig. 1.2 shows an example of how the dynamics and the steady state dramatically change across a phase transition: panel (a) and (b) show the (exponentiated) spectrum of the Liouvillian in two different phases of the Tavis-Cummings models, and present a totally different structure, differentiating the behaviour in the two phases.

In general, at the level of Liouvillian spectrum, dissipative phase transitions are related to the closure of the Liouvillian gap $\Gamma = -\mathrm{Re}\lambda^*$ in the thermodynamics limit and to the properties of non-decaying eigenvectors and eigenvalues. This gives rise to a wide pletora of possibilities, including continuous and discontinuous phase transitions, along with spontaneous breaking or not-breaking of the symmetries of the system [14, 15].

A comprehensive discussion of all of these critical phenomena is beyond the scope of this Thesis. However, the following Sections present some phases and phenomena associated to dissipative phase transitions that may stem from open quantum dynamics. These special examples serve as paradigma to show how dissipation can be leveraged to produce peculiar phases of matter, and to illustrate in more details some phenomena emerging in the next Chapters. Specifically we will see time-crystals phases of matter in Sec. 2.1.1, as they will appear in Secs. 4.2,4.3, and we will describe bistability in Sec. 2.1.2 as it will characterize Sec.4.2.

2.1.1. Persistent oscillations and Time Crystals

This Section describes a dissipative phase transition that we will see emerging in Chap. 4 in spins and bosonic systems. The phase we want to describe, dubbed a time crystal, emerges from the closure of the Liouvillian gap by complex eigenvalues, and the next paragraphs aim at introducing this phase and explaining how it emerges from the spectrum of $\mathcal{L}$.

Time crystals phases, recently introduced and theorized by Wilczek [21, 84], are based on a very peculiar type of symmetry breaking: the spontaneous breaking of time-translation symmetry. Time-translation symmetry can be both continuous and discrete [85, 86]: a simple example of breaking of continuous time-translational symmetry has a time-independent Hamiltonian showing oscillations in the steady state; an easy framework showing breaking of discrete time-translational symmetry is given instead by period doubling.

It is extremely important to highlight that open quantum many-body systems constitute an ally in the quest for time-crystal phases as they overcome the no-go theorems [22] stating that time crystallinity cannot emerge in ground states and equilibrium

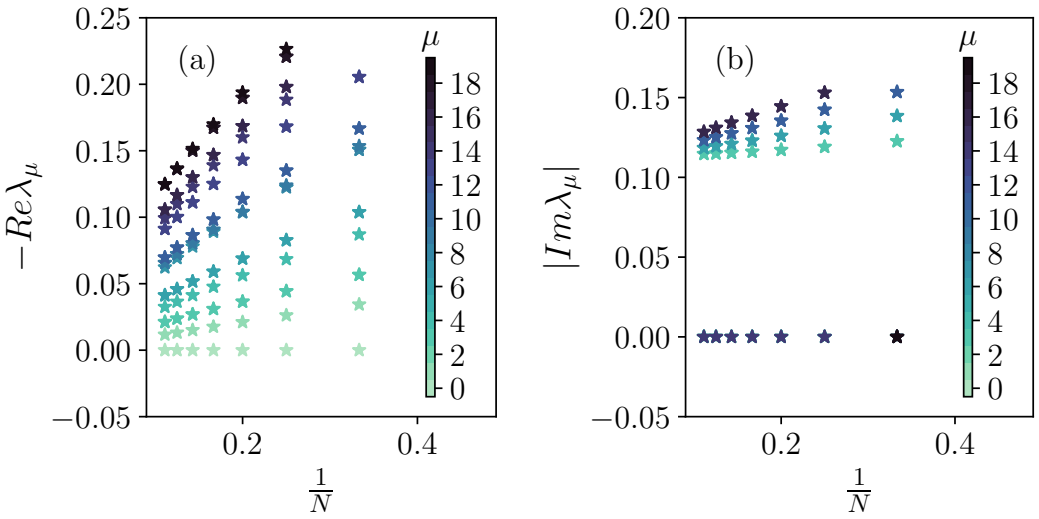

Figure 2.1.: Spectrum of the Liouvillian for a time-crystal phase. The two plots, containing respectively the real and the imaginary part of the eigenvalues λ_μ, versus the inverse of the system's size (for the accessible sizes $N = 2$-$N = 9$ spins). The legend represents the number of the eigenvalue, ordered with respect to their real part. Both plots are drawn for the Tavis-Cummings model and correspond to the Liouvillian spectrum contained in Fig. 1.2(b). (a) Real part of the Liovillian eigenvalues vs. $1/N$. Increasing the system size, the Liouvillian gap increasingly closes. (b) Imaginary part of the Liouvillian eigenvalues. Some of them, while having a real part which closes the gap, tend to form a band structure having a non-zero value.

states. Several studies have indeed focused on the emergence of this phenomenon out of equilibrium, and have considered both open Floquet types of settings [23], and driven-dissipative frameworks [24].

In this thesis, we will study driven-dissipative systems with N spins presenting a time crystal phase that spontaneously breaks continuous time translation symmetry in the thermodynamic limit. The mechanism responsible for the emergence of this phase lies in the structure of the spectrum of the Liouvillian, and in how it changes by increasing the size if the system.

Diagonalizing the Liouvillian at finite size $\hat{\hat{\mathcal{L}}}_N$, one gets a unique steady state $|r_0\rangle\!\rangle_N$ corresponding to $\lambda_0 = 0$, and a long-lived eigenvector $|\tilde{r}\rangle\!\rangle_N$ corresponding to the eigenvalue $\tilde{\lambda}_N = -\Gamma(N) + i\Omega(N)$ (along with its conjugate). In the presence of time-crystallinity, one can compare the spectrum for different sizes and realize that

$$\lim_{N\to\infty} \Gamma(N) = 0, \qquad \lim_{N\to\infty} \Omega(N) = \tilde{\Omega} \neq 0. \tag{2.4}$$

The real part $\Gamma(N)$ vanishes for increasing system sizes, closing the Liouvillian gap, and shows that the long-lived eigenvectors become non-decaying. These new non-decaying eigenvectors concur in determining the properties of the steady state. The non-zero imaginary part in the thermodynamic limit sets the frequency of the time-crystal's persistent oscillations.

An example of this time-crystal realization is shown in Fig. 2.1, showing how the gap closes in panel (a) for eigenvalues having a non-zero imaginary part, shown in panel (b). This example is drawn from the time-crystal phase of the Tavis-Cummings model, discussed in Sec. 4.2.

This behaviour is typical of boundary time-crystals, introduced in the context of open quantum many-body systems in Ref. [24] and found for the first time in a resonance fluorescence model.

It is worth mentioning that Lindblad theory is not the only formalism showing the emergence of time crystals. A phase transition to a time crystal phase can also be witnessed from a Keldysh field theory perspective. This framework allows for example to compute 2-times connected correlation functions such as $\left\langle \hat{A}(t)\hat{A}(t')\right\rangle - \left\langle \hat{A}(t)\right\rangle \left\langle \hat{A}(t')\right\rangle$ for some operator $\hat{A}$. This specific object should show long-range order and present oscillations in time crystal phases, serving as diagnostics for this type of phase transitions in a Keldysh setting [86].

2.1.2. Bistability

Another interesting phenomenon we will witness near a dissipative critical point is the presence of *bistability* (or *multistability*) emerging from the competition between

two (or several) long-lived states. As in the case of time crystals, we can identify some non-trivial properties of this phenomenon starting from the analysis of the Liouvillian spectrum and its eigenvectors. Let us introduce the concept of bistability and then link it to the properties of the spectrum we have introduced.

A prototypical bistability scenario displays, in the thermodynamic limit and for a region of parameters $\eta \in [\eta_A, \eta_B]$, the existence of two possible steady states, $\hat{\rho}_1$ and $\hat{\rho}_2$. The state reached at long times depends on the choice of the initial state, thus

$$\lim_{t\to\infty}\lim_{N\to\infty} e^{\mathcal{L}(\eta)t}\hat{\rho}_{a,b}(0) = \hat{\rho}_{1,2}, \tag{2.5}$$

where $\hat{\rho}_{a,b}$ are two possible initial states.

At the same time, a general Liouvillian at finite size has a unique steady state [87]:

$$\lim_{N\to\infty}\lim_{t\to\infty} e^{\mathcal{L}(\eta)t}\hat{\rho}_{a,b} = \hat{\rho}_{\mathrm{SS}}, \tag{2.6}$$

where the steady state is the eigenvector $|r_0\rangle\!\rangle$ with $\lambda_0 = 0$ at a specific η.

This highlights a typical feature of bistability: the non-commutativity of the thermodynamic and long-time limits, i.e., $\lim_{N\to\infty}\lim_{t\to\infty} \neq \lim_{t\to\infty}\lim_{N\to\infty}$. Taking the thermodynamic limit first yields a steady state that depends on the initial state. Taking the infinite-time limit first always yields a unique steady state.

One ingredient to explain the emergence of this non-commutativity is the closure, in the thermodynamic limit, of the Liouvillian gap across the entire bistability region. This translates, in the case of $\tilde{\lambda} \in \mathbb{R}$, to

$$\lim_{N\to\infty} \Gamma(\eta) = 0 \quad \text{for} \quad \eta \in [\eta_A, \eta_B]. \tag{2.7}$$

The two pictures stemming from the two possible orderings of the limits are, nevertheless, connected [88]. At finite sizes, the Liouvillian eigenvectors responsible for the long-time behavior are $\hat{\rho}_{\mathrm{SS}} \to |r_0\rangle\!\rangle$ (with $\lambda_0 = 0$) and $\hat{\tilde{\rho}} \to |\tilde{r}\rangle\!\rangle$ (with $\tilde{\lambda} = \Gamma \in \mathbb{R}$ and $\lim_{N\to\infty}\Gamma = 0$). These two states must then be related to the states we observe when taking the thermodynamic limit first: $\hat{\rho}_1$, $\hat{\rho}_2$.

One can argue that the states $\hat{\rho}_{1,2}$ must be different combinations of the long-lived states $\hat{\rho}_{\mathrm{SS}}$ and $\hat{\tilde{\rho}}$. The only possibility to guarantee trace unity for the steady state $\hat{\rho}_0$, and zero trace for $\hat{\tilde{\rho}}$, is the following decomposition at finite sizes:

$$\hat{\rho}_{\mathrm{SS}} = \frac{a_1\hat{\rho}_1 + a_2\hat{\rho}_2}{a_1 + a_2}, \tag{2.8}$$

$$\hat{\tilde{\rho}} = \hat{\rho}_1 - \hat{\rho}_2. \tag{2.9}$$

In this situation, the closure of the Liouvillian gap throughout the bistable region in the thermodynamic limit complicates the picture and leads to the non-commutativity

of the infinite-time and thermodynamic limits. This explicitly shows the connection between the Liouvillian spectrum, yielding $\hat{\rho}_0$, $\hat{\tilde{\rho}}$, and the $N \to \infty$ states $\hat{\rho}_{1,2}$.

This last fact, connecting the steady and longest-lived states to $\hat{\rho}_1$ and $\hat{\rho}_2$, highlights another special feature of bistable regions, particularly important in Sec. 4.2: a *bimodal probability distribution* of observables in the steady state. For example, the observable $\hat{o}$ will have a bimodal probability distribution $P_{\mathrm{SS}}(o)$ in the steady state, showing two peaks around precise values $o_{1,2}$.

Through the decomposition of the steady state in terms of $\hat{\rho}_{1,2}$ made above, one can easily realize that this steady-state probability distribution is a weighted superposition of the distributions of $\hat{o}$ over the two states $\hat{\rho}_{1,2}$, each with probability distributions $P_{1,2}(o)$ peaked at $o_{1,2}$. This leads to a bimodal

$$P(o) = \frac{a_1 P_1(o) + a_2 P_2(o)}{a_1 + a_2}, \tag{2.10}$$

explaining the phenomenon [88].

This feature is often present in regions around dissipative phase transitions and is usually related to a bistability between the steady states of the two phases meeting at the critical point [14], such that $\eta_c \in [\eta_A, \eta_B]$, with η_c being the critical point. We will see a similar phenomenon in Chap. 4.2.

Before concluding the discussion on bistable regions, we briefly mention that Chap. 4.2 also studies bistability through an unraveling of the Lindblad equation, analyzing single-trajectory evolutions. It is worth noting that single trajectories exhibit switching behavior between the two states $\hat{\rho}_1$ and $\hat{\rho}_2$ in the bistable region. While the lifetimes of the two switching modes are finite inside the bistable region, one of them always diverges outside this region, determining the properties of the phase.

2.2. Measurement-induced phase transitions

We now reconnect to the concepts of Secs.1.1, in which we have introduced quantum measurements and derived the master equations for evolving the quantum state according to the outcome of the measurement process of our choice. The idea of this Section is to analyze the properties of the steady states of such dynamics.

Weak measurements and their interplay with Hamiltonian dynamics are not, however, the only possibility for studying the monitored dynamics of quantum many-body systems. Another very common and widely studied setting, focuses on the dynamics and the long-time behaviour of quantum circuits interspersed by measurements. The most prototypical example of a circuit presenting measurements has its dynamics built in the following way: N qubits (or qudits) interact between themselves through the application of unitary gates, and the next layer of operations involves the application of

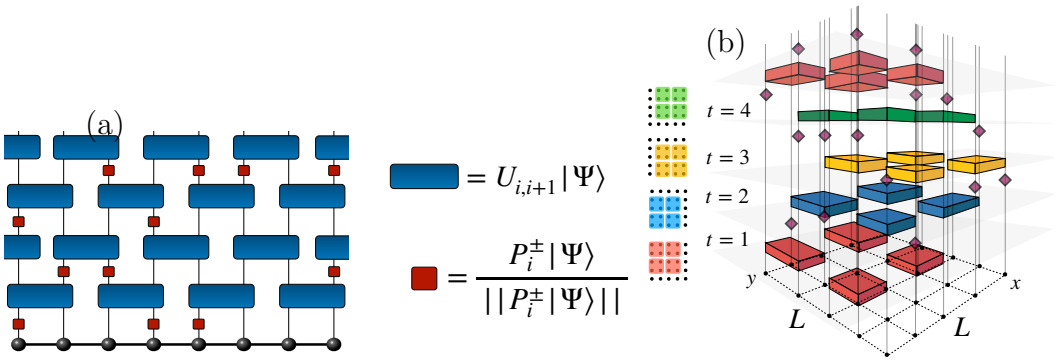

Figure 2.2.: Pictures from [89, 90]. Representations of quantum circuits with projective measurements in $1+1$d (a), and $2+1$d (b). In both cases, unitary gates are represented as boxes, while local projective measurements are diamonds or squares on single-qubit lines.

local projective measurements, which occur on each qubit with a probability p. These two layers are then repeated several times to generate the whole dynamics. An example of this structure in $1d$ and $2d$ can be found in Fig.2.2. Despite seeming a very specific setting, it allows for some freedom as the gates can be chosen in any way and can mimic several types of Hamiltonians. This setting is indeed intrinsically connected to the Hamiltonian settings, as gates can be chosen to implement $\hat{U} = \exp\left\{-i\hat{H}\right\}$ with a fictitious time-step (here set to one).

While studying the monitored dynamics of quantum circuits, it was recently realized that continuously monitoring a many-body system produces effects that go beyond the dissipation process [40]. Experiments and theory can collect vast statistics about measurement realizations. However, if the analysis is limited to the average state over quantum trajectories, one only observes dynamics governed by the Lindblad equation, which is blind to the measurement process, as discussed in Secs. 1.2.1 and 1.2.2. To retain information about the monitoring, one must go beyond the average and study higher moments of the state. This has unveiled the emergence of a new critical phenomenon: measurement-induced phase transitions.

The first studies on this phenomenon [40–42] focused on quantum circuits with N qubits, using random unitary gates or Floquet-like dynamics, interspersed with local projective measurements. These studies aimed to quantify quantum correlations using Rényi entropies or the entanglement entropy, and to characterize how they change in the thermodynamic limit as the measurement rate p varies. Note that Rényi entropies and the entanglement entropy, denoted here as S, are nonlinear functionals of the system's state. Therefore, computing their average over trajectories requires evaluating higher moments of the quantum states. The results are striking:

- For $p < p_C$, with p_C being a critical measurement's rate, the dynamics generated by unitary gates manages to spread quantum correlations through the systems and the thermodynamic limit is characterized by volume-law quantum correla-

tions. In $d-$dimensions:

$$S \propto N^d.$$

- For $p > p_C$, the unitary dynamics is limited by the action of projective measurements which disentangle single quibits from the rest of the system, and do not manage to spread entanglement as efficiently as before. The disentangling action of measurements results in an area-law phase for quantum correlations:

$$S \propto N^{d-1}.$$

This results have a deep meaning: the rate p at which measurements occur tunes the importance of measurements over unitary dynamics. From their interplay, a phase transition in quantum correlations arises: the two phases are either an area-law, signaling that the disentangling action of measurements is taking over unitary dynamics, or a volume-law phase in which Hamiltonian dynamics wins. The important bit in this picture, is that these phase transitions can only be seen through Rényi entropies or entanglement entropy calculations, as only looking at the average-state dynamics would have yield just dissipative dynamics.

These findings sparked a vast body of work aimed at understanding and characterizing this new type of critical phenomenon and its associated phases. Studies explored alternative settings, including long-range unitary gates and Clifford circuits [40–42, 91–96], and have spread as well to the setting we have introduced in Sec. 1.2, in which an Hamiltonian system is continuously measured through weak measurements [43–45, 97–105]. In the Hamiltonian case, the role of the measurement rate p is played by the measurement strength γ, which tunes the competition between unitary dynamics and weak measurements.

In this Thesis, we will focus on this second setting and study measurement-induced phase transitions emerging from monitoring with quantum jumps (Sec. 1.2.2) or Gaussian measurements (Sec. 1.2.1) a variety of quantum systems, including cavity models, spin chains and bosonic models.

Before dealing with the characterization of these phases, it is important to understand on a more quantitative level why the emergence of measurement-induced phase transition can be probed only considering complex functional of the system's state such as Renyi entropies or the entanglement entropy as shown before.

The reason is mathematically very simple, and is based on the fact that while performing calculations in the context of monitored dynamics, one needs to keep in mind that there are two averaging processes taking place: we are calculating the average over the quantum state $\langle \bullet \rangle$, and the average over quantum trajectories $\overline{\bullet}$.

While calculating averages of observables, the ordering of the averages doesn't affect the calculation because of the linearity of the trace operation. We show this with a

general operator $\hat{o}$, and labeling trajectories with γ:

$$\overline{\mathrm{Tr}\{\hat{\rho}_\gamma\,\hat{o}\}} \;=\; \mathrm{Tr}\big\{\overline{\hat{\rho}}\,\hat{o}\big\}. \tag{2.11}$$

If one has higher moments of the system's state, then the ordering matters. Suppose we want to calculate the variance of the same operator $\hat{o}$ as before:

$$\overline{\mathrm{Tr}\{\hat{\rho}_\gamma\hat{o}^2\} - \mathrm{Tr}\{\hat{\rho}_\gamma\,o\}^2} \neq \mathrm{Tr}\big\{\overline{\hat{\rho}}\hat{o}^2\big\} - \mathrm{Tr}\big\{\overline{\hat{\rho}}\,o\big\}^2, \tag{2.12}$$

where the commuting problem lies in the quadratic term as $\overline{\hat{\rho}_\gamma^2} \neq \overline{\hat{\rho}}^2$ in general.

Notice now that, while computing the average of observables, one only has to deal with the density matrix averaged over trajectories. Since this object follows the Lindblad master equation and only knows about the dissipative process induced by measurements, it doesn't retain information about the specific measurement process. Thus, observables can be considered good order parameters to probe dissipative phase transitions, but not to witness measurement-induced phase transitions.

Instead, dealing with non-linear objects in the system's state preserves some information about measurements: on an operational level, one needs to follow a single trajectory, calculate the non-linear object of interest along that specific trajectory, and repeating this procedure many times until the average over trajectories can be calculated accurately. This allows for preserving information about the measurements process. Indeed, a completely different result, related only to dissipation, would appear by inverting the two average processes.

This will be the general procedure that we will use to study measurement induced phase transitions in this Thesis: if interested in dissipative phase transitions, we will exploit observables as order parameters; otherwise, in order to probe MIPTs, we will follow the above prescription about averages of non-linear objects in the system's state.

2.2.1. The complexity of monitored systems

Throughout the thesis we will not only be interested in the theoretical prediction of measurement-induced phase transitions, but also in the theoretical and experimental complexity associated with the stochastic nature of the problem.

The issues we encounter in this field touch indeed all the points of view and methods we can use to study the problem.

Theoretical studies involving analytical analysis, generally require carrying out very complex calculations based on stochastic calculus. Several studies attempted to pursue these calculations, and generally have involved mappings to known stochastic models, such as percolation [40] and the use of tools drawn from random matrix theory [94, 106] and disordered systems [100, 104, 107, 108]. Such studies often involve the calculation of path integrals, both over the system's degrees of freedom such as ($\int \mathcal{D}x_{1,2}$ in Eq. 1.56),

and over the readouts of quantum measurements, such as (for a functional f of the system's state):

$$\overline{f[\hat{\rho}_r]} = \int \mathcal{D}r(t')\, P[r;t]\, f[\hat{\rho}_r(t)],$$

where $P[r;t]$ is the probability of the trajectory $r(t)$, required by Born's rule, and $\int \mathcal{D}r(t')$ takes the average over all possible measurement outcomes. Having generally to consider very complicated non-linear functionals of $\hat{\rho}_\gamma$ to be averaged over trajectories, many studies have relied on the Replica Trick [100, 104, 108–111], drawn from Spin-Glass Theory, and reduced the complexity of the calculation by working with many copies of the quantum state along a trajectory; Others have relied instead on stochastic path integrals [112, 113] requiring the use of auxiliary fields (as in the Martin-Siggia-Rose formalism [114, 115]). In this Thesis, we will deal with the same type of complexity in Chap.5 from a different point of view, while monitoring free and interacting bosons.

Numerical studies do not escape the complexity due to the presence of measurements. Simulating and numerically integrating Eqs. (1.62),(1.70), requires building the many-body state and evolving it in its entirety along many trajectories which must be generated randomly and which must sample in a complete way the probability distribution of quantum trajectories. In order to see the emergence of phase transitions in the steady-state one needs to run simulations for a very long time and characterize the many-body quantum state continuously along this evolution. This type of simulations are in general very hard in terms of storage and time resource, and can be carried out easily only in small systems, collective and infinite-range systems, or Gaussian systems. Moreover, simulations techniques like tensor-networks which are usually able to deal with many-body systems by truncating the size of the simulations, usually fail in capturing volume-law phases which are central in the field of measurement-induced phase transitions. Some approximations have been developed to deal with this type of simulations [116], and proposing others to understand the behaviour of long-range systems will be the aim of this Thesis in Sec. 4.3.

Beyond theory, the greatest challenge in studying measurement-induced phase transitions comes from experiments. The issue lies in the fact that measurement-induced phase transitions must be probed by selecting a trajectory and characterizing its steady state through non-linear functionals of the state itself, repeating for many different trajectories, and then averaging over the results. The extremely difficult bit is characterizing a quantum state conditioned to some specific measurement outcome. In the worst-case scenario, one needs to do full tomography of a many-body quantum state, and this requires reproducing many times the same state conditioned to the same measurement outcome. The probability of measuring a specific trajectory is usually exponentially small both in the system's size and in the time needed to evolve the system: $P(r) \propto e^{-N} e^{-t}$[47, 117]. This makes experiments very hard in practice, and has greatly limited the experimental witnessing of measurement-induced phase transitions, which are limited to References [118–120]. This experimental issue, known as the **post-selection problem** [46, 48], cannot be overcome in general, and many studies

are now centered on ways of mitigating it [46, 48, 121, 122]. This discussion will be central to Chap. 4.1, which will expand this discussion and propose some solutions in infinite- and long-range systems.

3. Quantum Synchronization

In this Chapter we explore the first dissipative phase transition of the Thesis, and the first example of how dissipation can help in realizing collective emergent phenomena.

The fundamental question we address in this Chapter is whether synchronization, a well-known dynamical phenomenon in classical fields, can occur in a quantum setting, and how it differs from classical findings [28]. We choose to answer this question in the context of open many-body quantum systems, to the correct counterpart for classical models based on noisy settings with friction.

Synchronization is an emergent collective phenomenon that can be observed in various physical systems, such as pendula [123], fireflies [124, 125], and neurons [126]. In classical mechanics, synchronization can occur when two or more oscillators interact with each other through a common coupling [127, 128].

However, in the quantum domain, synchronization becomes even more intriguing, as it has to deal with quantum fluctuations and entanglement. Specifically, the problem of quantum fluctuations has already attracted interest in theoretical studies, and has been addressed in models of coupled Van der Pol rotors with non-linear dissipation [26, 129] and non-dissipative Hamiltonian rotors [130]. Understanding synchronization in the quantum realm may be a useful resource for quantum technological applications [131, 132], for example in quantum thermal machines [133–135]. For this reason, an intense theoretical activity aimed at quantifying synchronization in quantum systems from continuous variables[136–144] to discrete degrees of freedom [134, 145–158]. Different measures of synchronization have been introduced, ranging from phase-space or correlation quantities [159–164] to information-theoretical approaches[160, 165–167].

This large body of work, however, did not address a seemingly natural question: how to extend a paradigmatic model of classical synchronization, the Kuramoto model [168], to study synchronization in the presence of quantum fluctuations. This is the starting point for our work. The classical model describes the behaviour of interacting rotors with a non-linear dynamics, and exhibits a phase transition from a dynamically disordered phase, to an ordered one characterized by phase locking. Generalizations of the model [169–175] have allowed to explore and enrich the phase diagram by studying also the effects of noise, inertia, disorder and long-range interactions on the emergence of synchronization, and extending the concept of rotors to nonabelian objects [176].

Despite efforts to study and understand the emergence of collective behavior of rotors in a semiclassical regime, where quantum fluctuations become relevant and modify the system's dynamics [177], a systematic analysis of spontaneous synchronization in the fully quantum regime is still lacking. Can quantum synchronization emerge in a low-temperature regime or do quantum fluctuations dominate the system's behavior, preventing spontaneous synchronization?

The chapter will thoroughly address this question. To provide a comprehensive discussion on quantum synchronization, we start from its classical counterpart, which allows for a more intuitive exemplification of how synchronization emerges when rotors are bound by interactions. Specifically, Sec. 3.1 introduces the concept of phase-locking, the primary mechanism inducing synchronization, and then shows the emergence of synchronization in the classical Kuramoto-Sakaguchi model. Sec. 3.2 generalizes these concepts to the quantum regime and analyzes the similarities and differences in the dynamics of the two settings.

3.1. Classical Synchronization

Before digging into the extension of the Kuramoto model to a quantum many-body systems, it is important to understand the features of classical synchronization. This Section will be dedicated to the exposition of some basic concepts, like the **phase locking mechanism** [127] responsible for the emergent synchronization in the Kuramoto model, and to address the onset of classical synchronization in a classical stochastic model - the Kuramoto-Sakaguchi model.

3.1.1. Basics of synchronization: phase locking

Let us consider, for this section only, a simplified model.

Suppose we have two rotors, which will be labeled as θ_1 and θ_2 as their position is entirely specified by the rotation angle $\theta_i \in [0, 2\pi)$.

The toy model we consider is deterministic and involves two rotors driven at different frequencies, ω_1 and ω_2. Interaction is key to achieving synchronization, and we suppose that the two rotors interact through a force that depends on their phase difference. The equations of motion for this setting are

$$\begin{cases} \dot{\theta}_1 &= \omega_1 - J\sin(\theta_1 - \theta_2), \\ \dot{\theta}_2 &= \omega_2 - J\sin(\theta_2 - \theta_1). \end{cases} \tag{3.1}$$

For $J = 0$ we see that the two rotors evolve independently, rotating at their own frequency. When $J \neq 0$, the interaction competes with the drive and tries to lock the

phase difference in the steady state. This procedure can be seen more easily by going to an average $\theta_+ = (\theta_1 + \theta_2)/2$ and relative $\theta_- = \theta_1 - \theta_2$ coordinate and determining the steady state of these equations.

$$\begin{cases} \dot{\theta}_+ &= \frac{\omega_1+\omega_2}{2} \\ \dot{\theta}_- &= (\omega_1 - \omega_2) - J\sin(\theta_-). \end{cases} \tag{3.2}$$

While the equation for the average coordinate does not have a steady state, representing the fact that the center of mass of the rotors will rotate indefinitely at an average frequency $(\omega_1 + \omega_2)/2$, the relative coordinate can admit a steady-state:

$$\theta_-^* = \arcsin \frac{\omega_1 - \omega_2}{J} \Leftrightarrow |\frac{\omega_1 - \omega_2}{J}| < 1. \tag{3.3}$$

This means that if the ratio $|(\omega_1 - \omega_2)/J| = \zeta$ is $\zeta > 1$, there is no steady state also for the relative coordinate, and the two rotors will continue rotating independently. If $\zeta < 1$ instead, a steady state is achieved for the relative coordinate, and the phase difference of the two rotors is fixed at the θ_-^* value forever.

This is synchronization reached through **phase locking**: the two rotors are stuck to have a phase difference θ_-^*, while their center of mass rotates at their average frequency. We will see this happening in a many-body context in the next part of the Section.

3.1.2. The Kuramoto-Sakaguchi model

We are now able to extend the simple concept of phase-locking to a more complex setting.

The Kuramoto model describes the behaviour of N interacting planar rotors, as in Fig. 3.1(a). It exhibits two phases: an incoherent phase characterized by the rotors moving independently, and a synchronized phase in which the system behaves collectively. The mechanism underlying the synchronization process is *phase locking*, which causes the emergence of a fixed relation between the phases of the rotors.

The state of each rotor is characterised by a phase θ_i, an angular velocity v_i, with $i = 1, ..., N$. The evolution of this state is determined by a frequency ω_i, and a damping γ. The characteristic frequencies ω_i are independent of each other and, throughout the paper, will be drawn from an even, unimodal frequency distribution $g(\omega)$, with average $\overline{\omega} = \langle\omega\rangle_{g(\omega)} = 0$ and variance σ^2.

We consider here the massive version of this model described by the following set of Langevin equations:

$$\begin{cases} \dot{\theta}_i = v_i \\ \\ m\dot{v}_i + m\gamma v_i = F[\boldsymbol{\theta}; \omega_i] + \xi_i \end{cases} \tag{3.4}$$

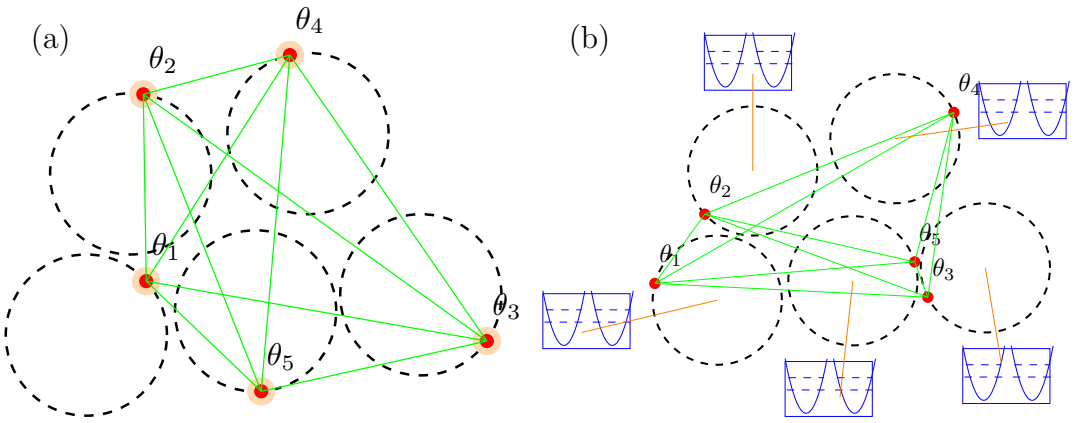

Figure 3.1.: (a) Representation of the classical Kuramoto model for $N = 5$. A set of rotors (dots on dashed circles) evolves with independent frequencies. Their mutual interactions (green solid lines) induce a phase transition to synchronised dynamics. (b) Representation of the quantum Kuramoto model. Same as panel (a), with the rotors as quantum systems. The coupling to independent identical quantum baths is explicitly shown as a solid line connecting to a set of harmonic oscillators (blue boxes)

Here, $\boldsymbol{\theta} = (\theta_1, ..., \theta_N)$ and

$$F[\boldsymbol{\theta}; \omega_i] = \omega_i - \frac{J}{N} \sum_{j=1}^{N} \sin(\theta_i - \theta_j) \ . \tag{3.5}$$

The noise in the Langevin equation is a Gaussian stochastic process with $\langle \xi_i(t) \rangle = 0$, $\langle \xi_i(t) \xi_j(t') \rangle = 2D\delta_{i,j}\delta(t - t')$. The initial conditions $\boldsymbol{\theta}(0) = \boldsymbol{\theta}_0$, $\mathbf{v}(0) = \mathbf{v}_0$ are drawn independently for every rotor from a distribution $\rho(\theta_0, v_0)$.

In the massless limit ($m\gamma = \text{const}$, $m \to 0$) the Langevin equation reduces to the Kuramoto-Sakaguchi model [178]

$$\dot{\theta}_i = F[\boldsymbol{\theta}, \omega_i] + \xi_i \qquad \forall i = 1, .., N \ . \tag{3.6}$$

The synchronized behaviour is signaled by a non-zero value, in the stationary state, of the modulus of the complex order parameter $\psi(t)$ defined as

$$\psi(t) = r(t)\, e^{i\varphi(t)} = \frac{1}{N} \sum_{j=1}^{N} e^{i\theta_j(t)} \ . \tag{3.7}$$

The modulus r of the order parameter ψ is bounded to the interval $r(t) \in [0, 1]$. It efficiently detects synchronization since it averages to zero if the rotors evolve incoherently. The phase φ corresponds to the phase of the collective motion of the rotors.

In the thermodynamic limit, the definition of the order parameter is regarded as an average over the frequency distribution, the noise distribution, and the distribution of the initial conditions, namely

$$\psi(t) = \int_{-\infty}^{\infty} d\omega \, g(\omega) \left\langle e^{i\theta(t;\omega,\xi)} \right\rangle_{\xi,\theta_0,v_0} \ , \tag{3.8}$$

where the phase $\theta(t;\omega,\xi)$ satisfies the Langevin equation (3.4) with $F[\boldsymbol{\theta};\omega] = F[\theta;\omega,\psi] = \omega - Jr\sin(\theta-\varphi)$. Notice that, to formally decouple the evolution of the rotors, we have used $\frac{J}{N}\sum_{j=1}^{N}\cos(\theta_i-\theta_j) = \frac{J}{2}e^{i\theta_i}\left(\frac{1}{N}\sum_{j=1}^{N}e^{-i\theta_j}\right) + \text{c.c.} = Jr\cos(\theta_i-\varphi)$. This results in (3.8) becoming a self-consistent equation for the order parameter.

For further convenience, it is useful to express the average that defines the order parameter in a path integral form [171]. Discretizing à la Ito, one can express (3.8) as (see Appendix B.1 for details):

$$\psi(t) = \int_0^{2\pi} d\theta\, e^{i\theta}\int_{-\infty}^{\infty} dv \int_{-\infty}^{\infty} d\omega\, g(\omega)\,\rho(\theta,v,t;\omega,\psi)\ . \tag{3.9}$$

.

Here $\rho(\theta,v,t;\omega,\psi)$ is a probability distribution that quantifies the probability for the ith rotor to have phase and angular velocity (θ,v) at time t, and can be expressed as [114, 179, 180], [115][Chap.4].

$$\begin{aligned}\rho(\theta,v,t;\omega,\psi) = \mathcal{N}\int_0^{2\pi} d\theta_0 \int_{-\infty}^{\infty} dv_0 \\ \int_{\theta(0)=\theta_0}^{\theta(t)=\theta}\mathcal{D}\theta \int_{v(0)=v_0}^{v(t)=v}\mathcal{D}v\,\delta(\dot\theta(\tau)-v(\tau))\,e^{iS_{cl}[\theta(\tau),v(\tau)]}\,\rho(\theta_0,v_0),\end{aligned} \tag{3.10}$$

where the classical action is given by:

$$S_{cl} = \frac{i}{4D}\int_0^t dt'\Big(m\dot v(t') + m\gamma v(t') - F[\theta(t');\omega,\psi(t')]\Big)^2\ . \tag{3.11}$$

Solving the self-consistent equation for the order parameter allows to gain knowledge about the phase transition. The behavior of the system is determined by the interplay between the coupling strength J, the width of the frequency distribution, σ, and of the noise distribution, D. In general, the phase transition for the model described by Eq. (3.4) is first-order, but it becomes a continuous phase transition in the overdamped limit [127, 171].

An interesting case is the massless model, for which the critical coupling is known analytically to be

$$J_C^{cl} = 2\Big(\int_{-\infty}^{\infty} d\omega\, g(\omega)\,\frac{D}{D^2+\omega^2}\Big)^{-1}\ . \tag{3.12}$$

From this formula, the effects of noise and the width of the frequency distribution are evident. Noise hinders the phase-locking mechanism, and so does increasing the variance of the frequency distribution. In the case of the noiseless model, the critical coupling becomes simply $J_C^{cl} = \frac{2}{\pi g(0)}$.

3.2. From Classical to Quantum synchronization

In the classical world, Eq. (3.12) shows how harder it gets to synchronize a many-body system of rotors in the presence of noise. What we would like to do in this Section is take this problem to the quantum realm at low temperatures, where the competition between quantum and thermal fluctuations enriches the dynamical behaviour of the system. In particular, we are interested in understanding if quantum fluctuations play a role similar to classical noise in hindering synchronization and what the differences are between the two mechanism.

We first need to introduce a quantum model that reproduces the results of the classical Kuramoto-Sakaguchi model in the classical regime, identified for us by having high temperatures.

Once described this model, we will study its properties and witness the onset of quantum sycnrhonization.

3.2.1. The Quantum Kuramoto model

Our goal is now to construct a model that reproduces the classical one in the high-temperature limit. Since the classical Kuramoto-Sakaguchi model is characterized by noise and dissipation, it cannot be obtained as a classical limit of a quantum Hamiltonian model.

The classical model has friction along with a noise stochastic term which is independent for each rotor. Thus, we introduce a local dissipation in the quantum regime via the Caldeira-Leggett [62] model we have introduced in Sec. 1.1.1, by coupling each rotor to its own Caldeira-Leggett bath. The baths are independent but identical, as represented in Fig. 3.1.

The Lagrangian describing this model is

$$\mathscr{L}_{\mathrm{TOT}} = \mathscr{L}_S + \mathscr{L}_B + \mathscr{L}_{SB} \, . \tag{3.13}$$

$\mathscr{L}_S$ is the Lagrangian of the system of rotors

$$\mathscr{L}_S = \sum_{i=1}^{N} \left[\frac{m\dot{\theta}_i^2}{2} + \omega_i \theta_i + \frac{J}{2N} \sum_{j \neq i} \cos\left(\theta_i - \theta_j\right) \right] \, . \tag{3.14}$$

The characteristic frequencies ω_i are once again drawn from a distribution $g(\omega)$ having the same characteristics as in the classical case. $\mathscr{L}_B$ is the baths' Lagrangian:

$$\mathscr{L}_B = \sum_{i=1}^{N} \mathscr{L}_{B_i} = \sum_{i=1}^{N} \sum_{j_i=1}^{M} \left[\frac{M\dot{x}_{j_i}^2}{2} - \frac{1}{2} M \Omega_{j_i}^2 x_{j_i}^2 \right] \, . \tag{3.15}$$

$\mathscr{L}_{SB}$ is the interaction Lagrangian

$$\mathscr{L}_{SB} = \sum_{i=1}^{N} \mathscr{L}_{SB_i} = C \sum_{i=1}^{N} \theta_i \sum_{j_i=1}^{M} x_{j_i} \ . \tag{3.16}$$

In order to decouple the equations, as in the classical case, it is convenient to work in the thermodynamic limit with a mean-field model. We assume $\frac{1}{N}\sum_{j=1}^{N} e^{i\theta_j} = \left\langle \frac{1}{N}\sum_{j=1}^{N} e^{i\theta_j} \right\rangle + \delta\psi$ with $\delta\psi$ infinitesimal and define $\psi = re^{i\varphi} = \left\langle \frac{1}{N}\sum_{j=1}^{N} e^{i\theta_j} \right\rangle$ where the quantum averages are taken over the rotors' reduced density matrix. The mean-field Lagrangian $\mathscr{L}$ becomes up to first order in $\delta\psi$

$$\mathscr{L} = \sum_{i=1}^{N} \left(\mathscr{L}_{S_i} + \mathscr{L}_{B_i} + \mathscr{L}_{SB_i} \right) , \tag{3.17}$$

with $\mathscr{L}_{S_i} = \frac{m\dot{\theta}_i^2}{2} + \omega_i\theta_i + Jr\cos(\theta_i - \varphi)$. Notice that the mean-field model is described by a Lagrangian decoupled in a sum of terms depending only on the ith rotor. From now on for brevity

$$V[\theta] = -\omega\theta - Jr\cos\left(\theta - \varphi\right) \ . \tag{3.18}$$

In order to reproduce the friction term in Eq. (3.4) in the classical limit, The Caldeira-Leggett's model requires an Ohmic bath [62], as can be understood from Sec. 1.1.1. We therefore demand that, for each and every bath, the distribution of frequencies for the collection of harmonic oscillators is

$$\sum_{i=1}^{M} \frac{C^2}{2M\Omega_i}\, \delta(\Omega_i - \nu) \xrightarrow[M\to\infty]{} \frac{m\gamma\nu}{\pi}\Theta(\omega_c - \nu) \ , \tag{3.19}$$

where $\Theta(\cdot)$ is the Heaviside function and ω_c is a cutoff for the frequencies of the baths' harmonic oscillators.

A few comments about the definition domain of the phases θ_i are in order. Two choices are possible: the phases of the rotors can be defined over the circle, i.e. $\theta_i \in [0, 2\pi)$, or they can be defined over the line $\theta_i \in \mathbb{R}$. The difference lies in identifying or not the position θ with $\theta + 2n\pi$, $n \in \mathbb{Z}$. The Langevin equation that describes the classical model in Eq. (3.4) is not dependent on the choice of the phases' domain since it is inherently 2π periodic. For the quantum model we define $\theta_i \in \mathbb{R}$. The tilted potential term $\omega\theta$ and the linear coupling with the bath are compatible with this choice [2][Chap.2]. We note that with this choice of phase domain, the Lagrangian in Eq. (3.14) can be regarded as the Lagrangian of a resistively shunted Josephson Junction [181].

In order to understand if the system described by the mean-field Lagrangian (3.17) can sustain synchronization, an order parameter should be defined. In analogy with the classical case, we define

$$\psi(t) = r(t)\, e^{i\varphi(t)} = \frac{1}{N}\sum_{j=1}^{N} \mathrm{Tr}\left\{ e^{i\theta_j}\, \rho_S(t) \right\} \tag{3.20}$$

where $\rho_S(t)$ is the reduced density matrix of the system of rotors evolved to time t after tracing out the baths' degrees of freedoms. Notice that, once again, in the mean-field approximation, this is a self-consistent equation for the order parameter, since the density matrix evolves with a Lagrangian dependent on ψ.

The initial state of the evolution is chosen to be separable in the rotors; the mean-field approximation and the choice of independent baths allow to maintain the density matrix separable in the rotors at any time. For this reason, from now on, the discussion will focus only on the evolution of the density matrix $\rho_{SB}^{(i)}$ of a single rotor and its own bath. The initial density matrix for the ith rotor and the bath is also assumed to be separable: $\rho_{SB}^{(i)} = \rho_i \otimes \rho_B$.

The evolution of the reduced density matrix of a single rotor can be obtained through the Feynman-Vernon's influence functional method [7, 55] introduced in Sec. 1.1, appropriate to treat quantum systems with a classical limit given by a stochastic equation of motion [60, 61, 63, 182] and already introduced in Sec. (1.1). Applying the Feynman-Vernon method along the lines of Ref. [62], the density matrix element $\rho_i(\theta_1, \theta_2) = \langle\theta_2|\hat{\rho}_i|\theta_1\rangle$ is given at time t by

$$\rho_i(\theta_1, \theta_2, t) = \int_{-\infty}^{\infty} d\theta_1' \int_{-\infty}^{\infty} d\theta_2' \int_{\theta_1(0)=\theta_1'}^{\theta_1(t)=\theta_1} \mathcal{D}\theta_1 \int_{\theta_2(0)=\theta_2'}^{\theta_2(t)=\theta_2} \mathcal{D}\theta_2 \; e^{\frac{i}{\hbar}(S_0[\theta_1]-S_0[\theta_2])}\, \Phi[\theta_1, \theta_2]\, \rho_i(\theta_1', \theta_2', 0) \tag{3.21}$$

where $S_0 = \int_0^t dt' \mathscr{L}_{S_i}(t')$ for the ith rotor, and $\Phi[\theta_1, \theta_2]$ is the Feynman-Vernon's influence functional that accounts for the effects of the interaction with the bath.

We can regard the previous equation as an evolution of the density matrix due to an effective action $S_{\text{eff}}[\theta_1, \theta_2] = S_0[\theta_1] - S_0[\theta_2] - i\hbar \ln \Phi[\theta_1, \theta_2]$. Switching to the more convenient Keldysh rotated variables $\theta_{\text{cl}} = (\theta_1 + \theta_2)/2$, $\theta_{\text{q}} = \theta_1 - \theta_2$ as introduced in App A:

$$\begin{aligned} S_{\text{eff}}[\theta_{\text{cl}}, \theta_{\text{q}}] = \int_0^t dt' \Big(& m\dot{\theta}_{\text{cl}}\dot{\theta}_{\text{q}} - \sum_{q=\pm 1} (-1)^q V[\theta_{\text{cl}} + q\tfrac{\theta_{\text{q}}}{2}] \\ & - m\gamma\theta_{\text{q}}\dot{\theta}_+ + \frac{iD}{\hbar} \int_0^t dt''\, \theta_{\text{q}}(t') K(t'-t'') \theta_{\text{q}}(t'') \Big) \,. \end{aligned} \tag{3.22}$$

In the previous equation $D = m\gamma k_B T$, and $K(t)$ is given by the Fourier transform $K(t) = \int_{-\omega_c}^{\omega_c} \frac{d\nu}{2\pi} \mathcal{K}(\nu) e^{-i\nu t}$, with

$$\mathcal{K}(\nu) = \frac{\hbar\nu}{2k_B T} \coth\left(\frac{\hbar\nu}{2k_B T}\right) . \tag{3.23}$$

The temperature T is set by the bath, and the signatures of its interaction with the rotor are the friction term $m\gamma\theta_{\text{q}}\dot{\theta}_{\text{cl}}$ and the imaginary term containing the memory kernel $K(t)$, as already explained in details in Sec. (1.1.1).

Before proceeding with the calculation of the order parameter, it is worth noticing how the classical dynamics is recovered in the high temperature limit of the quantum model. In the infinite temperature limit, the memory kernel becomes $K(t) \xrightarrow{T\to\infty} \delta(t)$ and the imaginary damping term prevents $\theta_{\rm q}$ to vary [61], [2][Chap.5]. This means that, starting from a "classical" diagonal state with $\theta_{\rm q}(0) = 0$, the density matrix will always remain diagonal (the off-diagonal term are exponentially suppressed). Moreover, expanding up to first order $\theta_{\rm q}(t)$, the evolution becomes

$$\rho_i(\theta_{\rm cl}, \theta_{\rm q}, t) = \int_{-\infty}^{\infty} d\theta'_{\rm cl} \int_{\theta_{\rm cl}(0)=\theta'_{\rm cl}}^{\theta_{\rm cl}(t)=\theta_{\rm cl}} \mathcal{D}\theta_{\rm cl} \int_{\theta_{\rm q}(0)=\theta'_{\rm q}=0}^{\theta_{\rm q}(t)=0} \mathcal{D}\theta_{\rm q}\, e^{\frac{i}{\hbar}S_{\rm eff}[\theta_{\rm cl},\theta_{\rm q}]}\, \rho_i(\theta'_{\rm cl}, \theta'_{\rm q}=0, 0)\ , \quad (3.24)$$

with the effective action being

$$S_{\rm eff}[\theta_{\rm cl}, \theta_{\rm q}] = \int_0^t dt' \left(\frac{iD}{\hbar}\theta_{\rm q}^2(t') - \theta_{\rm q}(t')\Big(m\ddot{\theta}_{\rm cl} + m\gamma\dot{\theta}_{\rm cl} - \omega + Jr\sin(\theta_{\rm cl} - \varphi)\Big)\right)\ , \quad (3.25)$$

where we have used the fact that, at first order in $\theta_{\rm q}$, $V[\theta] \approx \theta_{\rm q} F[\theta_{\rm cl}]$. With the change of variables $\frac{\theta_{\rm q}(\tau)}{\hbar} \to \eta(\tau)$, one recovers the classical effective action for the stochastic process (3.4) showed in Eq. (B.3) after the integration of the δ-function in the angular velocity. Thus, the quantum model reproduces correctly the massive Kuramoto-Sakaguchi model in the infinite temperature limit.

3.2.2. Self-consistent equation for the order parameter

In order to obtain a self-consistent equation for the order parameter, we start by noticing that the reduced density matrix of the rotors at time t is given by $\rho_S(t) = \bigotimes_{i=1}^N \rho_i(t)$. Eq.(3.20) then takes the form

$$\begin{aligned} \psi(t) &= \frac{1}{N}\sum_{j=1}^{N} \mathrm{Tr}\{e^{i\theta_j}\,\rho_j(t)\} \bigotimes_{k\neq j, k=1}^{N} \mathrm{Tr}\{\rho_k\} \\ &= \frac{1}{N}\sum_{j=1}^{N} \mathrm{Tr}\{e^{i\theta_j}\,\rho_j(t)\}\ . \end{aligned} \quad (3.26)$$

In the thermodynamic limit, the previous expression corresponds to an average over the frequency distribution $g(\omega)$. Denoting as $\rho(t)$ the density matrix of a single rotor we have:

$$\psi(t) = \int_{-\infty}^{\infty} d\omega\, g(\omega) \int_{-\infty}^{\infty} d\theta_{\rm cl}\, e^{i\theta_{\rm cl}}\, \rho(\theta_{\rm cl}, \theta_{\rm q} = 0, t)\ . \quad (3.27)$$

To get a more explicit expression of the self-consistent equation for the order parameter, the path integration in Eq. (3.21) should be performed. The specific form of the potential (3.18) appearing in the effective action does not allow for a general calculation of the path integral. However, the knowledge of the behaviour of the classical model helps: in the overdamped limit the classical phase transition to the synchronized phase

is of second-order. We expect that the quantum phase transition in the overdamped limit is second order too. If this is the case, assuming $J \sim J_C$, we can perform a perturbative expansion in r for $r \sim 0$ of (3.27) to gain insight onto the quantum dynamics. Thus, we will hereafter focus explicitly on the overdamped regime $\frac{m\gamma}{\hbar} \gg 1$ of the model.

The perturbative expansion of the evolution of the density matrix in Eqs. (3.21),(3.22) involves only the approximation

$$\exp\left\{\frac{-iJr}{\hbar}\int_0^t dt' \sum_{q=\pm} q\cos\left(\theta_{\rm cl}(t') - q\tfrac{\theta_{\rm q}(t')}{2} - \varphi(t')\right)\right\} \sim \tag{3.28}$$
$$1 - \frac{iJr}{\hbar}\int_0^t ds\cos\left(\theta_{\rm cl}(s) - \tfrac{\theta_{\rm q}(s)}{2} - \varphi(s)\right) + \frac{iJr}{\hbar}\int_0^t ds\cos\left(\theta_{\rm cl}(s) + \tfrac{\theta_{\rm q}(s)}{2} - \varphi(s)\right) .$$

The zeroth order of the expansion of the density matrix (3.21) gives an evolution according to a Lagrangian with potential $V[\theta] = -\omega\theta$. This Lagrangian does not contain terms that can synchronize the rotors, hence it does not contribute to the self-consistent equation for the order parameter. The first order expansion, together with the *Ansatz* $\varphi(t) = 0$ and $r \sim 0$ constant, yields, for $t \to \infty$

$$r = rJ_C \lim_{t\to\infty}\int_{-\infty}^{\infty} d\omega\, g(\omega)\int_{-\infty}^{\infty} d\theta_{\rm cl} e^{i\theta_{\rm cl}}\rho'(\theta_{\rm cl},\theta_{\rm q},t) \tag{3.29}$$

where

$$\rho'(\theta_{\rm cl},0,t) = \frac{-i}{2\hbar}\sum_{c,c'=\pm1} c'\int_0^t ds\int_{-\infty}^{\infty} d\theta'_{\rm cl}\int_{-\infty}^{\infty} d\theta'_{\rm q}\int_{\theta_{\rm cl}(0)=\theta'_{\rm cl}}^{\theta_{\rm cl}(t)=\theta_{\rm cl}}\mathcal{D}\theta_{\rm cl}\int_{\theta_{\rm q}(0)=\theta'_{\rm q}}^{\theta_{\rm q}(t)=0}\mathcal{D}\theta_{\rm q}$$
$$\exp\left\{\frac{i}{\hbar}S'_{\rm eff}[\theta_{\rm cl},\theta_{\rm q};s,t]_{c,c'}\right\}\rho(\theta'_{\rm cl},\theta'_{\rm q},0) , \tag{3.30}$$

and

$$S'_{\rm eff}[\theta_{\rm cl},\theta_{\rm q};s,t]_{c,c'} = S'_{Re}[\theta_{\rm cl},\theta_{\rm q};s,t]_{c,c'} + i\,S'_{Im}[\theta_{\rm q};s,t]_{c,c'}$$
$$= \int_0^t dt'\Big\{m\,\dot\theta_{\rm cl}\dot\theta_{\rm q} - m\gamma\,\theta_{\rm q}\dot\theta_{\rm cl} + \omega\,\theta_{\rm q}$$
$$+ i\hbar c\,\theta_{\rm cl}(t')\delta(t'-s) - \frac{i\hbar cc'}{2}\,\theta_{\rm q}(t')\delta(t'-s) + \frac{iD}{\hbar}\int_0^t dt''\theta_{\rm q}(t')K(t'-t'')\theta_{\rm q}(t'')\Big\} . \tag{3.31}$$

The details of the derivation of Eqs. (3.31) can be found in Appendix (B.2).

If Eq. (3.29) admits a solution for $r \neq 0$, then the model admits a phase transition to a synchronized state in the overdamped limit, and the resulting J_C gives the value

of the critical coupling for the phase transition. Notice that the first order expansion does not contain information about the order of the phase transition, that could only be understood through a third order expansion. The goal is now to find the critical coupling and to study its dependence on the parameters that characterize the system: $m, \gamma, k_B T$, and the variance σ of the even unimodal frequency distribution $g(\omega)$.

From now on, we will work taking the limit $t \to \infty$ since we are interested in the steady-state properties of the system.
The expansion to first order in the self-consistent equation has produced a Gaussian path integral that can now be performed [63, 182]. The calculation can be performed via a decomposition of the effective action (3.31) in its real and imaginary part $S'_{\text{eff}} = S'_{Re}[\theta_{\text{cl}}, \theta_{\text{q}}] + iS'_{Im}[\theta_{\text{q}}]$, as can be seen from the previous equation.

The calculation, reported in Appendix B.2, produces the following result for the first order expansion of the self-consistent equation:

$$r = rJ_C \lim_{t\to\infty} \int_{-\infty}^{\infty} d\omega\, g(\omega) \int_{-\infty}^{\infty} d\theta_{\text{cl}}\, e^{i\theta_{\text{cl}}} \left(\frac{-i}{2\hbar}\right) \frac{m\gamma}{2\pi\hbar} \sum_{c,c'=\pm 1} c' \int_0^t ds \tag{3.32}$$
$$\int_{-\infty}^{\infty} d\theta'_{\text{cl}} \int_{-\infty}^{\infty} d\theta'_{\text{q}}\, \rho(\theta'_{\text{cl}}, \theta'_{\text{q}}, 0) \exp\left\{ -\frac{1}{\hbar} S'_{Im}[\tilde{\theta}_{\text{q}}; s, t]_{c,c'} - \frac{i}{\hbar} m\, \theta'_{\text{q}} \dot{\tilde{\theta}}_{\text{cl}}(0) + ic\, \tilde{\theta}_{\text{cl}}(s) \right\}$$

where $\tilde{\theta}_{\text{cl,q}}$, are the solutions of the equations

$$\begin{cases} \ddot{\tilde{\theta}}_{\text{q}}(t') & - & \gamma \dot{\tilde{\theta}}_{\text{q}}(t') - \frac{\hbar c}{m} \delta(t'-s) = 0 \\ \ddot{\tilde{\theta}}_{\text{cl}}(t') & + & \gamma \dot{\tilde{\theta}}_{\text{cl}}(t') - \frac{\omega}{m} + \frac{\hbar c c'}{2m} \delta(t'-s) = 0 \end{cases} . \tag{3.33}$$

The explicit solution of these equations is reported in appendix B.3.

The term $c = 1$ in the sum does not contribute because it gets completely damped by the imaginary part of the action. From now on we will consider only the term $c = -1$. The expression for $\dot{\tilde{\theta}}_{\text{cl}}(0)$ and $\tilde{\theta}_{\text{cl}}(s)$ can be deduced from the result in appendix B.1. It is convenient to proceed by calculating the integration over θ_{cl} first. Isolating the integration and all the terms of (3.32) involving θ_{cl}, we find

$$\frac{m\gamma}{2\pi\hbar} \int_{-\infty}^{\infty} d\theta_{\text{cl}} e^{i\theta_{\text{cl}} \left(-\frac{m\gamma}{\hbar}\theta'_{\text{q}} - e^{-\gamma s}\right)} = \delta\left(\theta'_{\text{q}} - \tfrac{\hbar}{m\gamma} e^{-\gamma s}\right) . \tag{3.34}$$

This constraints the initial value of θ_{q} as determined by the delta function. In the massless limit ($\gamma \to \infty$) the value that the delta function selects is $\theta'_{\text{q}} = 0$, in the general overdamped limit $\frac{m\gamma}{\hbar} \gg 1$ (m and γ finite) we select $\theta'_{\text{q}} \sim 0$. Performing now the integration over θ'_{q} to eliminate the delta function and denoting $\tilde{\theta}_{\text{q}}(t')\big|_{\theta'_{\text{q}} = \frac{\hbar}{m\gamma} e^{-\gamma s}}$ as $\theta^*_{\text{q}}(t'; s, t)$, the self-consistent equation becomes

$$r = \tag{3.35}$$
$$\frac{-iJ_C r}{2\hbar} \lim_{t\to\infty} \int_{-\infty}^{\infty} d\omega\, g(\omega) \int_0^t ds \sum_{c'=\pm 1} c' \exp\left\{ ic' \frac{\hbar}{2m\gamma} - i\frac{\omega(t-s)}{m\gamma} - \frac{1}{\hbar} S'_{Im}[\theta^*_{\text{q}}; s, t] \right\}$$

where we have used the fact that in the overdamped limit

$$\int_{-\infty}^{\infty} d\theta'_{\rm cl}\, \rho(\theta'_{\rm cl}, \frac{\hbar}{m\gamma}\, e^{-\gamma s}) \sim \int_{-\infty}^{\infty} d\theta'_{\rm cl}\, \rho(\theta'_{\rm cl}, 0) = {\rm Tr}\{\rho(t=0)\} = 1\ .$$

This approximation becomes exact in the massless limit. Also notice that the sign of the sine, $\sin\left(\frac{\hbar}{2m\gamma}\right) \sim \frac{\hbar}{2m\gamma}$, is always defined (and positive) in the overdamped limit, and that the expression does not depend on the initial state of the system.

We conclude that a non-trivial solution to the self-consistent equation exists (if the time limit exists), thus a phase transition happens at J_C.

3.2.3. Properties of the steady state

From the analysis of the previous Section, and Eq. (3.35) in particular, it follows that the quantum Kuramoto model in the overdamped limit admits a transition to a synchronized phase with a critical coupling given by

$$J_C = 2m\gamma \frac{1}{\lim\limits_{t\to\infty} \int_{-\infty}^{\infty} d\omega\, g(\omega) \int_0^t ds\, e^{-i\frac{\omega(t-s)}{m\gamma} - \frac{1}{\hbar} S'_{Im}[\theta^*_{\rm q}; s, t]}} \tag{3.36}$$

In the limit of high temperature $\hbar\gamma\beta \ll 1$ and vanishing mass, the critical value (3.12) is recovered. In this limit $K(\tau) \to \delta(\tau)$, and $\theta^*_{\rm q}$ has non-zero value only on the time interval $[s, t]$, over which $\theta^*_{\rm q}(t') = \frac{\hbar}{m\gamma}$ (see Appendix B.3). This implies that $S'_{Im}[\theta^*_{\rm q}] = \hbar\, \frac{k_B T}{m\gamma}\, (t - s)$, thus

$$J_C\Big|_{\hbar\gamma\beta\ll 1} = 2\left(\int_{-\infty}^{\infty} d\omega\, g(\omega)\, \frac{k_B T}{(k_B T)^2 + \omega^2}\right)^{-1} = J_C^{cl}(k_B T)\ .$$

The last result corresponds to the classical result reported in the literature for $D = k_B T$ [127, 171]. It is important to keep in mind that it holds only in the classical regime $\hbar\gamma\beta \gg 1$, nonetheless we will extend this formula to low temperatures in order to provide a comparison with the behaviour of the quantum result in the following discussion.

The dependence of the critical coupling on temperature and the comparison with its classical counterpart are reported in Fig. 3.2, where a Gaussian frequency distribution for the characteristic frequencies has been chosen to obtain the plots. From the analysis of panel (a) and (b), the existence of three regimes emerges. In the *classical regime*, defined by $\frac{k_B T}{\hbar\gamma} \gtrsim 1$, the classical results are recovered (cf upper fading line corresponding to the classical critical coupling for the overdamped massless model). The critical coupling in this latter case is (3.12), and becomes $J_C^{cl} = 2k_B T$ for $k_B T \gg \sigma$. The plots shows that this limit is reached asymptotically also by the quantum results.

A *semiclassical region* is met when decreasing the temperature. Comparing the result in this region with the classical one extendend to lower temperature, we notice that the quantum results start to deviate quantitatively from the classical, although the behaviour of the quantum and classical critical coupling remains qualitatively similar. Notably, the quantum critical coupling is consistently higher than the classical one, as shown in panel (c). This is due to the emergence of quantum fluctuations, which, as an extra source of noise, make the synchronization harder to be established [177]. The behaviour of J_C in this region can be understood through the expansion in $\theta_{\mathrm{q}} \sim 0$ already performed in Eq. (3.24) to recover the classical limit. Going beyond the first order expansion, which we have used to reobtain the classical result, the third order yields a description for the semiclassical regime [61].

The third-order expansion modifies the Kuramoto potential term as:

$$-Jr \sum_{s=\pm 1} (-1)^s \cos\left(\theta_{\mathrm{cl}} + s\frac{\theta_{\mathrm{q}}}{2} - \varphi\right) \sim Jr\,(1+\Delta_J)\,\theta_{\mathrm{q}} \sin\left(\theta_{\mathrm{cl}} - \varphi\right) \ , \tag{3.37}$$

with $\Delta_J \propto \frac{\hbar}{m\gamma}\frac{\hbar\gamma}{k_B T}$.

The above expansion tells us that in the semiclassical regime the motions happens in a potential of the same form of the classical one in Eq. (3.25), but renormalized by Δ_J. This yields the first deviation from the classical behaviour.

The *quantum region*, characterised by $\frac{k_B T}{\hbar\gamma} \sim 0$ shows the most significant deviations from the classical result. In this region quantum fluctuations make the behaviour of the two critical couplings different, and the deviation appears stronger.

This is particularly evident from panel (c) showing the ratio between the quantum and the classical extended result $\frac{J_C}{J_C^{cl}}$. The ratio is greater than one, enforcing the fact the it is more difficult to reach the synchronized phase in the quantum regime, as it increases approaching zero temperature.

An important result emerging from this discussion is the existence of a finite critical coupling at any temperature ranging from $T = 0$ to infinite T. A phase transition to a synchronized state is possible at every temperature and thus quantum fluctuations do not menage to prevent the emergence of this collective phenomenon, even at $T = 0$.

Another analysis should be carried out. Figure 3.3(a) shows the critical coupling for a fixed value of the overdamped ratio and for different choices of σ, the variance of the frequency distribution $g(\omega)$. In the plot, the lines represent quantum results, while the dots represent the classical results for $D = k_B T = 0$. This plot suggests that in the quantum realm, the width of the frequency distribution affects the critical coupling more than in the classical case, as the quantum case shows larger deviations between different σ values than the classical result. In both cases (quantum and classical), we notice that the wider the frequency distribution, the higher the critical coupling. The quantum regime seems to be more affected by this effect. This can be understood by studying the behaviour of just two rotors. Suppose the rotors θ_1 and θ_2, have

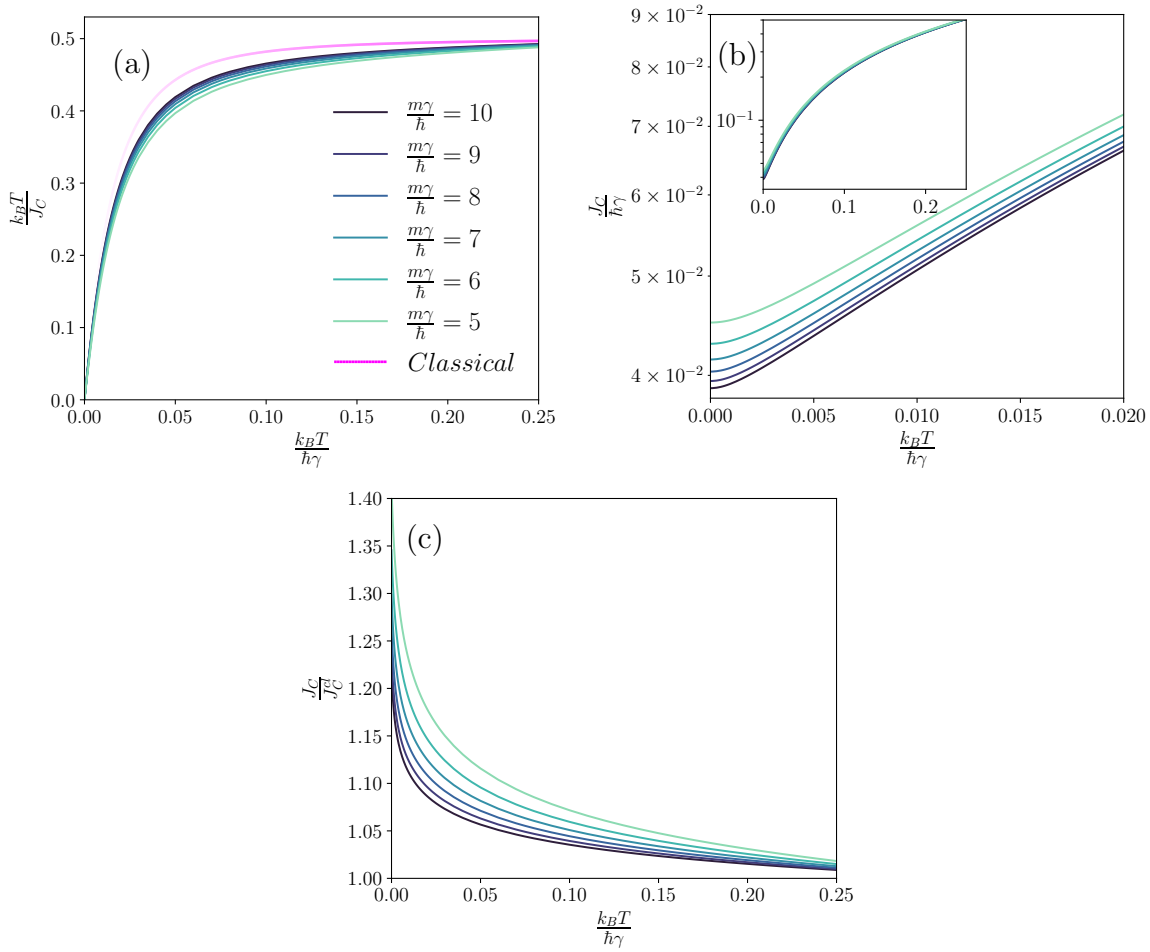

Figure 3.2.: Temperature-dependence of the inverse of critical coupling in units of temperature (a) and (b) in logarithmic scale for different values of $\frac{m\gamma}{\hbar}$. The legend in (a) holds for all the panels. In (a) the classical critical coupling (upper fading line) is plotted for reference for high temperatures. (c) Ratio between the quantum results and the classical one (extended to low temperatures) vs temperature. The difference in behaviour of the classical and quantum critical couplings is clearly evident close to zero temperature. All results are obtained for $g(\omega)$ Gaussian with zero mean and $\sigma = 2$

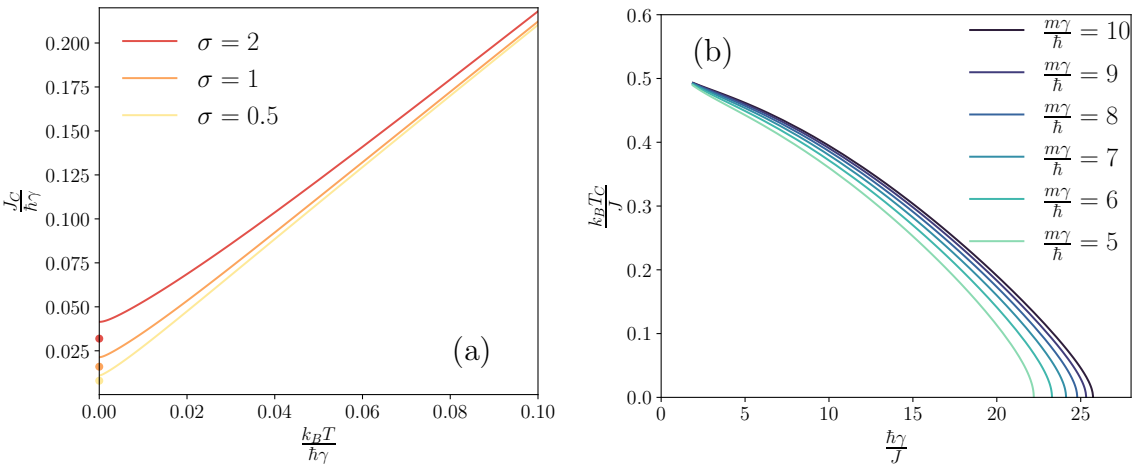

Figure 3.3.: (a) Critical coupling as a function of temperature for different choices of the variance σ of the Gaussian frequency distribution. The overdamped ratio is fixed $\frac{m\gamma}{\hbar} = 7$. The dots shown for $k_BT = 0$ represent $\frac{J_C^{cl}}{\hbar\gamma}$ for the classical noiseless model compatible with $D = k_BT = 0$. The colors of the dots are related to the choice of σ as shown in the legend. (b) Phase diagram of the quantum model in the coupling-temperature space, the region below the curves corresponds to the synchronized phase. A quantum phase transition appears at zero temperature. The result is obtained for a Gaussian distribution of frequencies with zero mean and variance $\sigma = 2$.

characteristic frequencies $\omega_1 = \sigma$, $\omega_2 = -\sigma$. Their phase difference $\Theta_- = \theta_1 - \theta_2$ has a behaviour that is determined by the washboard potential $V[\Theta_-] = -\sigma\Theta_- - J\cos(\Theta_-)$ and the coupling with the bath. If Θ_- is locked in a minimum of the potential, phase locking happens. For $\sigma < J$, the shape of the potential $V[\Theta_-]$ suggests that by decreasing σ, the height of the energy barrier that separates two minima, ΔV, increases, as $\Delta V = 2J\sqrt{1 - \frac{\sigma^2}{J^2}} + 2\sigma\sin^{-1}\left(\frac{\sigma}{J}\right) - \pi\sigma$. This makes it easier to lock Θ_- in a minimum. Notice that, in the semiclassical region, Eq. (3.37) suggests that the amplitude of the oscillations is given by $J(1 + \Delta_J) > J$, explaining the enhancement of the disorder effect outside the classical regime.

It should also be noticed that for any finite variance σ of the frequency distribution, the critical coupling at zero temperature is finite, yielding a quantum phase transition to a synchronized state. The interplay of different element emerges from this plot: decreasing the temperature increases the effects of quantum fluctuations and yields higher critical couplings with respect to the classical case, decreasing the width of the distribution helps the emergence of synchronization.

These considerations are summarized in Figure 3.3(b), which shows the phase diagram of the quantum model. The perspective for studying the model in this plot is reversed: the coupling is fixed to a value J, and the plot shows the behavior of the critical temperature T_C, below which the system is synchronized. The synchronized phase corresponds to the region below the lines in the plot, the part above the curves corresponds to the incoherent motion phase. Two important features are captured in

this picture. The quantum phase transition is evident: a finite coupling is required to synchronize the system at zero temperature. Moreover, the classical result for the massless overdamped model, given by $k_B T_C = J/2$ is reached by our results in the high temperature limit.

3.3. Conclusions to the Chapter

This Chapter has shown an intriguing dissipative phase transition with an emergent dynamical ordering. The procedure we have adopted here relies on the path integral description of open quantum many-body systems already introduced in Sec. 1.1, and has shown the emergence of a critical phenomenon from this formalism, extending the steady-state properties example we have introduced previously at the level of Liouvillian spectrum.

The Chapter also offers a new perspective on quantum synchronization: after introducing the classical Kuramoto model and its synchronization behaviour arising from the phase locking mechanism, we have extended it to a quantum low-temperature regime. This is a crucial step as the classical Kuramoto model has always be seen as a paradigm to study classical synchronization, and yet a quantum counterpart was missing.

The quantum Kuramoto model we have introduced in this Chapter admits a phase transition from a incoherent motion phase, to a synchronized one in the overdamped limit. The phase transition occurs at any temperature, yielding also a quantum phase transition at zero temperature. The critical coupling for the phase transition has been calculated analytically. It correctly reproduces the classical one in the high-temperature and shows deviation from this result extended to lower temperatures. In particular two regions can be observed beyond the classical regime. A semiclassical region is first met when decreasing the temperature below the inverse damping rate $\frac{1}{\hbar\gamma}$, here quantum fluctuations make the critical coupling slowly deviate from the classical result, yet behaving qualitatively similarly to the classical one. The quantum region, met around zero temperature $\frac{k_B T}{\hbar\gamma} \ll 1$, shows significant deviations from the classical result: around zero temperature a sudden increase of the ratio $\frac{J_C}{J_C^{cl}}$ happens, and at $T = 0$ the critical coupling for the quantum model is higher than the classical one but finite (for finite variances of the distribution of the characteristic frequencies). The ratio between the quantum and the classical extended result is always greater than one, signaling the fact that quantum fluctuations play against the emergence of synchronization without destroying it. The question of whether the behavior we found undergoes changes beyond the mean-field limit remains open. Gaining insight into the role that entanglement plays in quantum synchronization would be interesting. More specifically, it would be pertinent to determine whether entanglement monogamy and dissipation processes suffice to constrain the effects of entanglement on the findings of

our work.

4. Monitored infinite- and long-range systems

This Chapter will be devoted to the study of the dynamical and steady-state properties of many-body systems subject to continuous monitoring [29, 30]. The Chapter will be the chance to witness and discuss several phenomena. We will find the presence of dissipative phase transitions, associated to interesting steady-state behaviors such as time-crystallinity and bistability, discussed in Sec. 2.1. We will see the emergence of measurement-induced phase transitions from quantum correlations, drawing concepts from 2.2. But mostly, we will have the chance to discuss the complexity related to this kind of dynamics.

This Chapter, aims to identify which platforms are the most promising to experimentally observe a measurement-induced phase transition. Section 4.2 first analyzes the Tavis-Cummings model and its dissipative phase transitions, which have already been observed in laboratories. We find in this model a concurrent measurement-induced phase transition that mitigates the post-selection problem, can be observed through experimentally accessible observables, and is resistant to the typical time coarse-graining due to the resolution of real measurement devices. The second part of the Chapter, Sec. 4.3, then aims at generalizing these concepts, in particular the post-selection mitigation, to other relevant experimental platforms which implement long-range physics. This generalization will involve devising a new numerical method to simulate stochastic dynamics in an exponentially large Hilbert space. The method is based on spin-wave theory and efficiently reduces the computational cost of these simulations.

4.1. Infinite- and Long-Range models, and the post-selection problem

The post-selection problem represents a fundamental limitation to the experimental realization of measurement-induced phase transitions. While it seems not possible to find a general recipe to overcome the need to reproduce the same trajectory many times experimentally, many proposals to reduce or eliminate the post-selection problem have been carried out in the past years, mainly based on the detection of MIPTs from very specific quantum circuit setting. They mostly involve peculiar symmetries

and structures of the gates and measurement architecture [46, 119, 183], feedback mechanisms [184–193], or rely on hybrid classical-quantum approaches [122, 194].

In this Section, we follow another path, focusing on the setting of Hamiltonian systems rather than circuits. Specifically, we aim at identifying platforms relevant for experimental physics that have good dynamical properties, helping in the mitigation of post-selection. Our work builds on Ref. [47], in which mitigation of post-selection was found. The authors study a spin model with a collective Hamiltonian and collective jumps:

$$\hat{H} = \Omega \sum_{i=1}^{N} \frac{\hat{\sigma}_i^x}{2} = \Omega\, \hat{S}_x \qquad\qquad \hat{L} = \sqrt{\gamma} \sum_{i=1}^{N} \frac{\hat{\sigma}_i^-}{2} = \sqrt{\gamma} \hat{S}^-, \tag{4.1}$$

where $\hat{S}_\mu = \frac{1}{2}\sum_{i=1}^{N} \sigma_i^\mu$ with $\mu = x, y, z, \pm$ are collective spin operators.

The measurement process in this case is related to counting events associated to the collective $\hat{S}^-$ operators. This setting is usually obtained as an effective theory from a light-matter cavity model in which photodetection is performed, after having eliminated adiabatically the cavity from the description in the so-called bad-cavity regime [30].

Several nice ideas about post-selection arise from this picture.

- There is only one jump operator for the whole many-body system. This means that trajectories are entirely determined by a binary evolution at each time step: either we have detection or non-detection of events associated to $\hat{S}^-$. This yield that the number of trajectories increases as 2^t, where t is the time we are experimentally measuring for.

- The probability of measuring a trajectory γ than can be roughly estimated as $P_\gamma \propto e^{-t}$. MIPTs are seen in the steady-state, which is attained at times τ_S (dubbed as saturation time), thus the probability of measuring a trajectory giving information about a MIPT is

$$P_\gamma \propto e^{-\tau_S} \tag{4.2}$$

- For this collective system the dynamics of the entanglement entropy is very fast and it reaches a steady behaviour at $\tau_S \propto \log N$. MIPTs in the entanglement entropy are seen, for this collective model by post-selecting trajectories with a probability which is only polynomially small in systems size

$$P_\gamma \propto e^{-\log N} = \frac{1}{N} \tag{4.3}$$

Being, in general, $P_\gamma \propto e^{-N}$ [46], this collective model greatly reduces an exponential problem to a polynomial form.

In the next sections, we will try to generalize this result. In Sec. 4.2 we will consider a collective system which has already been realized experimentally, which generalizes

the spin model we have just presented. We will take the chance to both understand if having a polynomial post-selection problem is a general feature of collective systems, and to ask about other properties of the experimental realization of an MIPT.

In Sec. 4.3 we will extend this picture to long-range systems, suitable for a description in terms of trapped ions and Rydberg atoms.

4.2. The Tavis-Cummings model

The driven-dissipative Tavis-Cummings model, also known as collective resonance fluorescence model [195–202] serves as a natural playground to study the infinite-range interaction between a single-mode cavity and resonant spins. In particular, we are interested in analyzing the steady state of this model, whose richness stems from the dynamic interplay between an external drive, light and matter interaction, and dissipation processes.

The model, sketched in Fig. 4.1(a), is described by N spins in a single-mode cavity. The spins and the cavity mode are resonant with characteristic frequency ω_c. The spins collectively interact with the single bosonic mode with a strength λ proportional to the single photon Rabi frequency and experience a coherent driving field of strength Ω and frequency ω_d. The Hamiltonian can be written as $\hat{H} = \frac{\omega_c}{2}\hat{S}^z + \omega_c \hat{a}^\dagger \hat{a} + \frac{\lambda}{\sqrt{N}}(\,\hat{a}^\dagger \hat{S}^- + \hat{a}\hat{S}^+\,) + \Omega(\,\hat{S}^+ e^{-i\omega_d t} + \hat{S}^- e^{i\omega_d t}\,)$, where $\hat{a}^\dagger$, $\hat{a}$ are photons creation and annihilation operators, and $\hat{S}^\mu = 1/2 \sum_{i=1}^{N} \hat{\sigma}_i^\mu$ with $\mu = x, y, z, \pm$, are collective spin operators.

In the frame rotating at the driving frequency, and assuming the drive to be resonant with the cavity, $\omega_c = \omega_d$, the Hamiltonian reduces to the simpler form

$$\hat{H} = \Omega(\hat{S}^+ + \hat{S}^-) + \frac{\lambda}{\sqrt{N}}\left(\hat{a}^\dagger \hat{S}^- + \hat{a}\hat{S}^+\right). \tag{4.4}$$

Infinite range interactions allow us to express the Hamiltonian through collective $\hat{S}^\mu$ spin operators, highlighting the collective nature of the model. Due to S^2 conservation, starting from initial states with maximal $\hat{S}^2$ eigenvalues, we can effectively describe this model as a single $N/2$ spin interacting with photons in the cavity.

We monitor the photons leaking out of the cavity with a rate κ. The jump operator in this case is only one: $\hat{R} = \hat{a}$. This type of detection falls in the category of counting events, described in Sec. 1.2.2.

Given the Hamiltonian and the kind of monitoring we decided to apply, we can now study dynamical and steady-state properties. We will start by studying the dissipative phase transitions, obtained by discarding the information about the measurement process and averaging the quantum state. This type of analysis is contained in Sec. 4.2.1. We will then focus on the monitoring properties and find the presence of measurement

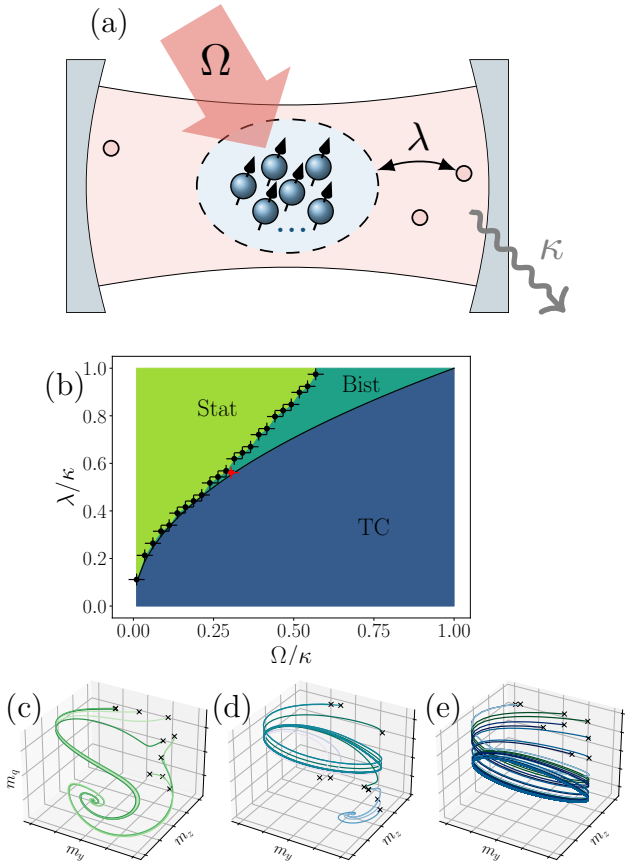

Figure 4.1.: (a) Sketch of the infinite-range driven-dissipative Tavis-Cummings Model. Spins are depicted as blue dots with arrows inside a cavity. They interact with photons (red dots) with strength λ and are driven by an external field with strength Ω. The photons can leak from the cavity with fixed rate κ. (b) Mean-field phase diagram of the driven-dissipative Tavis-Cummings Model for the dissipative phase transition, also known as the collective resonance fluorescence model. The border of the time-crystal phase (TC) is known analytically, and the border between the stationary (Stat) and bistability phase (Bist) is determined numerically. The red dot signals the tricritical point. (c), (d), and (e) show semiclassical trajectories in the (m_y, m_z, m_q) space from several initial conditions (signaled by $\times$) respectively in the stationary (c), bistable (d), and time crystal(e) phases.

phase transitions in Sec. 4.2.2

4.2.1. Dissipative phase transition

In this first part, we are interested in the dynamics and steady-state properties of the average state. For this reason, we start by analyzing the Lindblad equation associated to the average of the measurement process:

$$\frac{d\hat{\rho}}{dt} = -i\left[\hat{H},\hat{\rho}\right] + \kappa\left(\hat{a}\hat{\rho}\hat{a}^{\dagger} - \frac{1}{2}\left\{\hat{a}^{\dagger}\hat{a},\hat{\rho}\right\}\right). \tag{4.5}$$

The dissipative behavior of this model has been studied in the thermodynamic limit through mean-field equations for the spins' magnetizations and the field's quadratures [203]. To this stand, it is important to introduce the normalized operators $\hat{m}_j = 2\hat{S}^j/N$ with $j = x, y, z, \pm$, $\hat{m}_q = (\hat{a}^{\dagger}+\hat{a})/\sqrt{2N}$ and $\hat{m}_p = i(\hat{a}^{\dagger}-\hat{a})/\sqrt{2N}$. These operators are well-defined in the thermodynamic limit and admit vanishing commutators for $N \to \infty$, which justifies the mean-field decoupling $\langle \hat{m}_i \hat{m}_j \rangle = \langle \hat{m}_i \rangle \langle \hat{m}_j \rangle \equiv m_i m_j$ [204] in the semiclassical picture.

The average values of the magnetizations and quadratures evolve according to Heisenberg equations given by the adjoint master equation [1]. Setting $\langle \hat{m}_p(0) \rangle = 0$ and $\langle \hat{m}_x(0) \rangle = 0$, one simply can study:

$$\begin{aligned}
\frac{\partial m_y}{\partial t} &= -2\Omega m_z - \sqrt{2}\lambda m_q m_z, \\
\frac{\partial m_z}{\partial t} &= 2\Omega m_y + \sqrt{2}\lambda m_q m_y, \\
\frac{\partial m_q}{\partial t} &= -\frac{\lambda}{\sqrt{2}} m_y - \frac{\kappa}{2} m_q,
\end{aligned} \tag{4.6}$$

where $m_\mu = \langle \hat{m}_\mu \rangle$.

The semiclassical dynamics of the model can be studied through phase-space deterministic trajectories characterized by the evolution of the expectation values $(m_y(t), m_z(t), m_q(t))$. Due to conservation laws, the dynamics we are studying occurs on the surface of the cylinder given by $m_y^2 + m_z^2 = 1$ and $m_q \in \mathbb{R}$.

Based on the type of phase-space trajectories, three phases can be identified as in Fig. (4.1)(b):

- A stationary phase (Stat), characterized by a unique steady-state corresponding to the $\lambda = 0$ eigenvalue of the Liouvillian as explained in 1.1.2. In this case the phase-space trajectories end up in a fixed point as in Fig. 4.1(c).
- A Time-crystal phase (TC), characterized by spontaneous symmetry breaking of continuous time translations [203]. The mechanism is the same as explained in

Sec. 2.1, in which, in the thermodynamic limit, an imaginary eigenvalue closes the Liouvillian Gap. The phase-space trajectories are characterized by limit cycles as in Fig. 4.1(e).

- A bistable phase (Bist), corresponding exactly to the mechanism described in Sec. 2.1. Different initial state, in the thermodynamic limit, show two possible classes of steady states: fixed points or limit cycles. This is shown in Fig. 4.1(d).

The boundary of the time-crystal phase can be derived analytically: $\Omega_C/\kappa = \lambda^2/\kappa$. The boundary between the stationary phase and the bistability phase can only be determined numerically by checking the uniqueness of the steady state from several random initial conditions. It corresponds to the line with error bars in Fig. 4.1(b). Notice that the phase diagram presents a tricritical point (red dot), above which the bistability region appears.

The difference between stationary behavior and time crystal behavior can be characterized by the magnetization order parameter:

$$\tilde{m}_z = \lim_{t_f \to \infty} \frac{1}{t_f} \int_0^{t_f} dt\, m_z(t), \tag{4.7}$$

that corresponds to the average value over time of the magnetization $m_z(t)$. Solving the differential equations (4.6) one can easily realize that the stationary behavior yields $\tilde{m}_z \leq 0$, while the time-crystal limit cycle behavior attains positive values for the order parameter [203, 205]. Notice that the order parameter is blind to the bistability region. In this phase, $\tilde{m}_z$ can only detect the type of behavior given by the chosen initial state.

Through this order parameter, a continuous phase transition between stationary and time-crystal phases can be witnessed below the tricritical point. Above the tricritical point, $\tilde{m}_z$ detects a first-order phase transition between stationary and time crystal behavior that happens in the bistable phase with a critical point determined by the initial condition.

Two comments are in order. The dissipative phase transition in the good cavity regime: $\lambda^2/\kappa \gg \Omega$, has been recently realized in an experiment at JILA, Boulder [202]. The transition in this case has been observed in a slightly general setting in which spins are subject to decoherence, and the loss of photons is not the only dissipation effect. Moreover, this model is reduced to the one already presented from Ref. [47] in the bad-cavity limit when the cavity can be eliminated adiabatically. The Tavis-Cummings model then generalizes the picture by introducing intriguing dynamical effects such as optical bistabilities.

4.2.2. Measurement-induced phase transitions in the entanglement entropy

In this section, we characterize the quantum correlations in the monitored driven-dissipative Tavis-Cummings Model, focusing on the correlations between spins and intra-cavity photons. The trajectory-averaged entanglement entropy is defined as

$$\overline{S}_E(t) = -\frac{1}{N_{\text{traj}}} \sum_{\gamma=1}^{N_{\text{traj}}} \text{tr}\left[\hat{\rho}^{(\gamma)}_{\text{spins}} \log \hat{\rho}^{(\gamma)}_{\text{spins}}\right] , \tag{4.8}$$

with $\hat{\rho}^{(\gamma)}_{\text{spins}} = \text{Tr}_{\text{cav}}\left[|\psi_\gamma\rangle \langle\psi_\gamma|\right]$ the reduced density matrix of the spins. The average of this quantity over the time window $\kappa t \in [0, +\infty)$, labeled as $\tilde{S}_E$, will also be useful in our work since it can capture the steady state properties of quantum correlations.

To have a full understanding of the entanglement entropy behavior across the parameters space $(\Omega/\kappa, \lambda/\kappa)$, we will need to refer to some properties of the magnetization, specifically we will study in some cases the trajectory-averaged magnetization $\overline{m}_z$, and its time-average $\tilde{m}_z$ computed over the time window $\kappa t \in [0, +\infty)$.

Before analyzing the result, some details on the simulations are needed. The unraveling of the Lindblad equation has been carried out using the QuTiP package [206, 207]. The quantum jump unraveling has already been applied to several spin semiclassical systems with $\hat{S}^2$ conservation [47, 205], whose Hilbert space $\mathcal{H}$ has dimension scaling linearly with N, the number of spins. In our case, we need also to keep track of the bosonic Hilbert space, which is, in general, infinite-dimensional, and which we truncate. The truncation reads [30]:

$$\dim\{\mathcal{H}\} = (M_{\text{max}} + 1)(N + 1) = \chi N(N + 1)\,. \tag{4.9}$$

This means we are truncating the Hilbert space of the photons to have size χN, with χ depending on λ/κ and Ω/κ. In general $\chi \lesssim 1$ below the tricritical point, while $\chi > 1$ above the tricritical point.

With this Hilbert-space approximation, will first focus on the dynamically simpler regime $\lambda/\kappa = 0.2$; Later we will analyze the model for $\lambda/\kappa = 0.8$.

Quantum correlations at $\lambda/\kappa = 0.2$

We start the study of the entanglement entropy by reminding some features of the magnetization transition that will be useful as a reference for the following discussion. The mean-field phase diagram of the magnetization indicates that the region $\lambda/\kappa = 0.2$ hosts a continuous phase transition from stationary phase to time-crystal phase at $\Omega_C/\kappa = 0.04$. Moreover, the steady state is unique and this region shows no dependence on the choice of initial state.

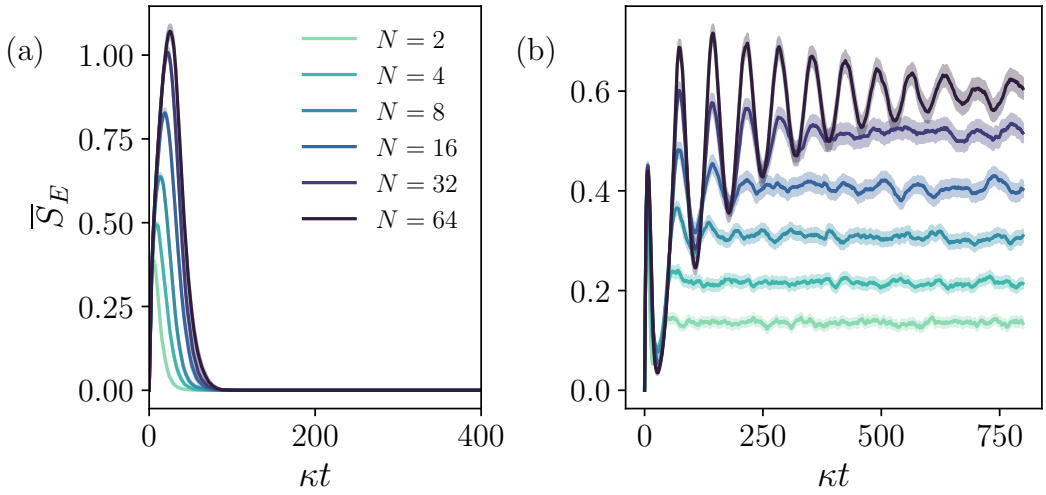

Figure 4.2.: Dynamics of the trajectory-averaged entanglement entropy in the (a) stationary phase $\Omega/\kappa = 0.01$ and (b) in the time-crystal phase $\Omega/\kappa = 0.06$. All the pictures are obtained for $\lambda/\kappa = 0.2$ and from $N_{\text{traj}} = 5000$ trajectories. The legend is shared.

We carry out the simulations of the entanglement setting as initial state $|\psi_0\rangle = |\psi_{\text{cav}}\rangle \otimes |\psi_{\text{spin}}\rangle = |0\rangle \otimes |\uparrow, \uparrow, ..., \uparrow\rangle$ (any other state belonging to the same symmetry sector would lead to the same conclusions).

Fig. 4.2 shows the time-evolution of entanglement entropy between photons and spins averaged over trajectories, $\overline{S_E}$. From these plots, we notice that the qualitative features of the temporal behavior of the magnetization is present also in the entanglement dynamics. The first plot corresponds to $\Omega/\kappa = 0.01$ which would yield a stationary behavior for the magnetization. Similarly, the entanglement entropy has a stationary behavior. The same holds for the second plot ($\Omega/\kappa = 0.06$): for this choice of Ω/κ the magnetization has oscillations and so does the entanglement entropy.

The time-average of $\tilde{S}_E$ carries important information about the steady state properties of the entanglement entropy. In Fig. 4.3(a) this quantity exhibits a phase transition between a non-entangled region in which $\tilde{S}_E \propto N^0$ and a highly-entangled one with $\tilde{S}_E \propto \log^p N$ with p dependent on Ω, $p < 1$. The red dot-dashed line at $\Omega_C/\kappa = 0.04$ signals the maximum of the of $\partial_\Omega \tilde{S}_E$ as shown in the inset. We identify this value of Ω/κ as critical point. The entanglement phase transition occurs along with the magnetization one, signaling the entangled nature of the time-crystal phase in the Tavis-Cummings model [203]. The scaling with the size of the entanglement entropy in the two phases is shown in [panel (b)].

The saturation time obtained from the dynamics (more details in Appendix C.1), grows as powers of $\log(N)$, yielding a fast-saturating process, see Fig. 4.3(c). This makes calculating entanglement entropy with trajectories a partially post-selection-free problem as the probability of measuring a specific trajectory is suppressed only

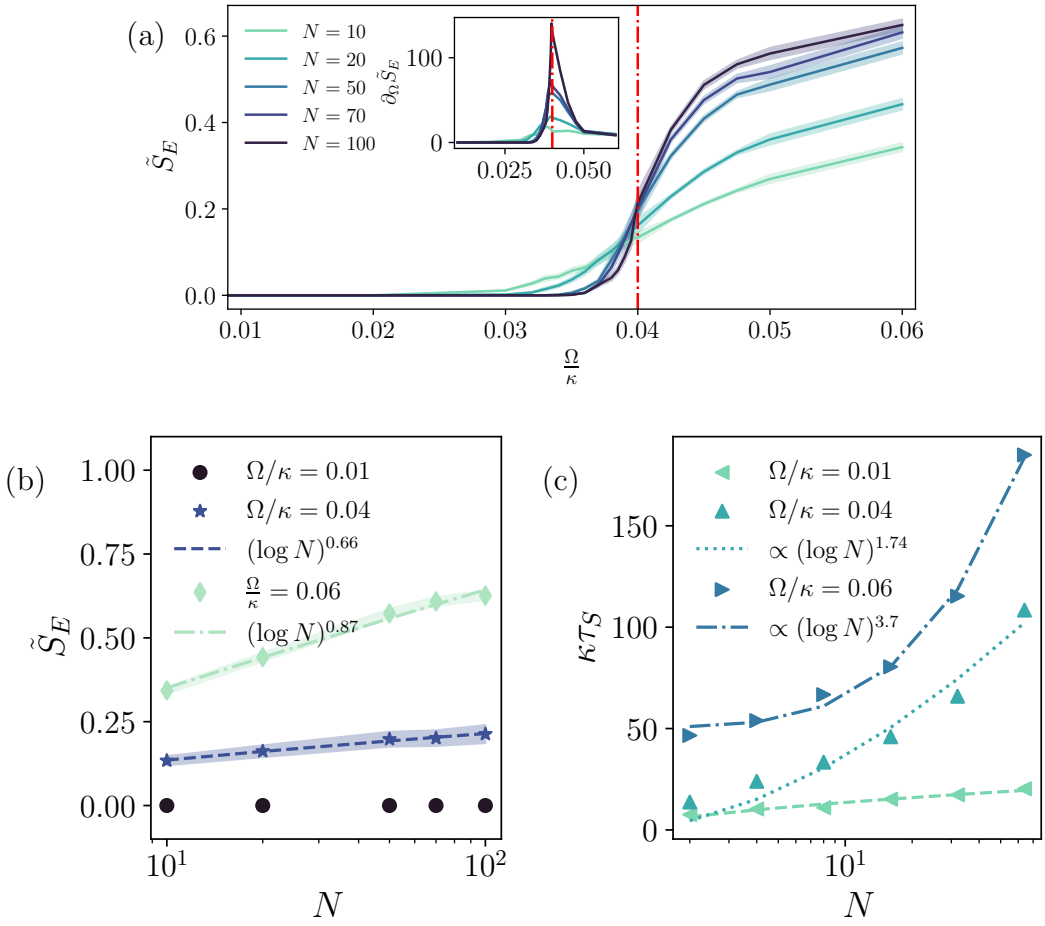

Figure 4.3.: (a) $\tilde{S}_E$ for different sizes and its derivative in the inset. The vertical dash-dot line signals the maximum of the derivative and corresponds to the critical point for the mean-field magnetization. (b) Scaling of $\tilde{S}_E$ with the size of the system. (c) Saturation time τ_S with respect to N for different values of Ω/κ

.

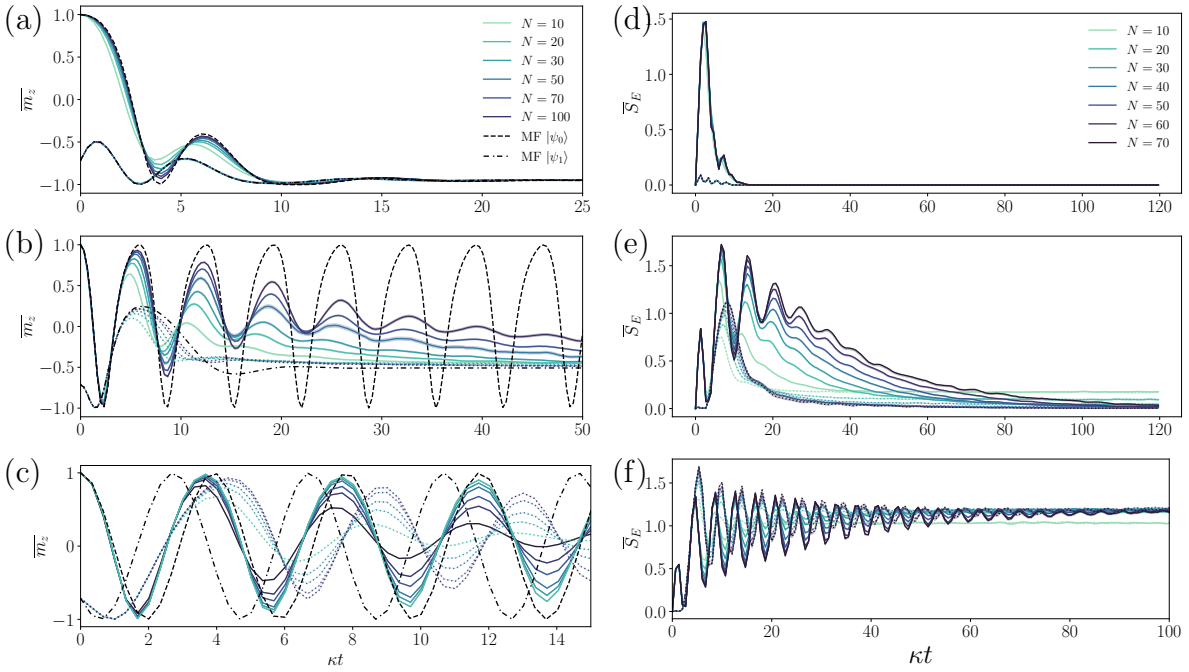

Figure 4.4.: $\overline{m_z}$ (left panels) and $\overline{S_E}$ (right panels) from initial states $|\psi_0\rangle$ (solid lines) and $|\psi_1\rangle$ (dotted lines) for different N (corresponding to gradient colors) compared to the mean-field for $|\psi_0\rangle$ (black dashed line) and $|\psi_1\rangle$ (black dotdashed line). (a)/(d), (b)/(e) and (c)/(f) are respectively $\Omega/\kappa = 0.2, 0.55, 0.8$. All the plots are obtained from $N_{\text{traj}} = 5000$ trajectories and the legend is shared among each column.

.

subexponentially in the system size N.

Quantum correlations at $\lambda/\kappa = 0.8$

The analysis of quantum correlations in this region is strongly affected by the bistable nature of the model. Therefore, it is convenient to start by carefully analyzing the finite-size dynamics of the magnetization. In the following plots, the bistable region will be signaled by a light yellow shadowed region.

Fig. 4.4[panels (a),(b),(c)] shows the time-evolution of the magnetization starting from two initial states: $|\psi_0\rangle = |m_y = 0, m_z = 1, m_q = 0\rangle = |0\rangle \otimes |\uparrow, \uparrow, ..., \uparrow\rangle$ and $|\psi_1\rangle = |m_y = 0.7, m_z = -0.71, m_q = -1\rangle$, for which the mean-field phase diagram predicts a phase transition respectively at $\Omega_C^{(0)}/\kappa = 0.46$ and $\Omega_C^{(1)}/\kappa = 0.57$. The plot presents their dynamics at finite sizes compared to the mean-field one. The finite-N magnetization's evolution in the stationary and time-crystal phases shows the same behavior starting from the two initial states and matches the predictions of the mean field. See [panels (a) and (c)]. [Panel (b)] shows instead the dynamics in the bistable region for $\Omega/\kappa = 0.55$, a value between the critical points of the two states. The finite size magnetization has an interesting behavior in this case: $|\psi_0\rangle$ yields a magnetization with oscillations in a transient time, and then a decay to a steady-state value; $|\psi_1\rangle$ shows

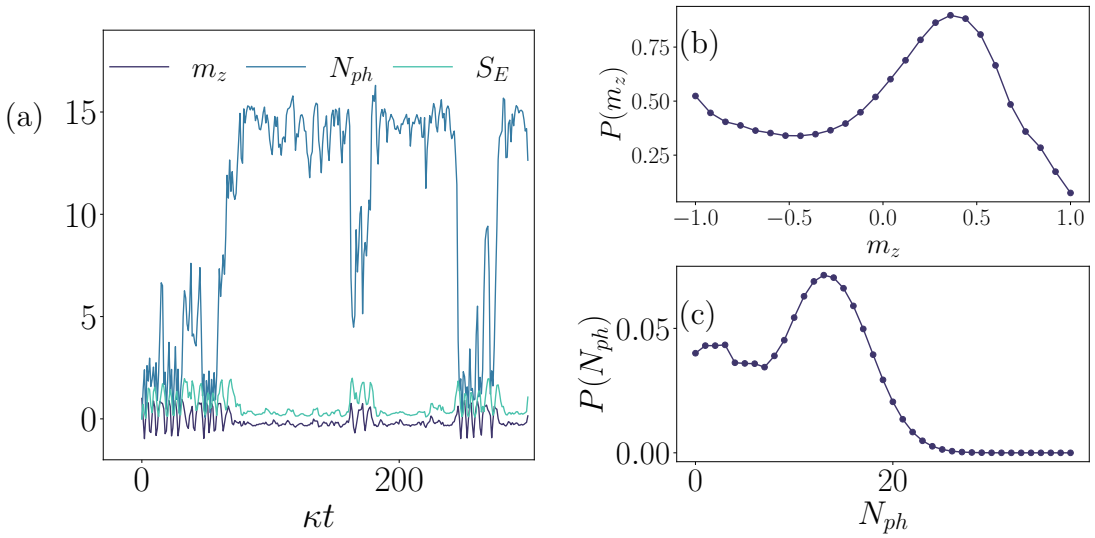

Figure 4.5.: Plots for $N = 25$, and $\Omega/\kappa = 0.62$. (a) Single-trajectory values for the average magnetization, number of photons, and entanglement entropy in the bistable phase. (b) and (c) show the bimodality in the probability distribution of the magnetization and the number of photons in the steady-state.

.

a transient stationary behavior which then leads to the same steady-state value as $|\psi_0\rangle$. Furthermore, the duration of the transient increases as the size is increased, and in this time interval the finite-size magnetizations match their respective mean-field predictions: oscillatory for $|\psi_0\rangle$ and stationary for $|\psi_1\rangle$.

This indicates the non-commutativity of the thermodynamic limit and the infinite-time limit

$$\lim_{t\to\infty}\lim_{N\to\infty}\overline{m_z(t)} \neq \lim_{N\to\infty}\lim_{t\to\infty}\overline{m_z(t)}. \tag{4.10}$$

As already seen in Sec. (2.1), this is a typical feature of bistable systems. The dynamics here is even more peculiar, as we have bistability between two long-lived states: one with a stationary behaviour, the other one presenting oscillations.

Bistability is not only witnessed in averaged observables but also at a single-trajectory level, and this fact complements what we have already said about bistability in Sec. 2.1. Along one trajectory we notice the switching between two different behaviors: an oscillating highly-entangled one with a low average number of photons $N_{\text{ph}} = \langle \hat{a}^\dagger \hat{a} \rangle$, and a stationary one with a high number of photons which is separable between spins and photons, see Fig. 4.5. In the bistable phase, for N finite, the lifetime of the states between which we observe a switching is finite and comparable. In the stationary and time-crystal phases, one of the two behaviors dominates while the other gets suppressed, this yields a commutativity of the thermodynamic and infinite-time limit outside the bistable region. Bistability can also be noticed as bimodality in the steady-state probability distribution of the observables m_z and N_{ph} [208], see panels (b) and (c) of Fig. 4.5.

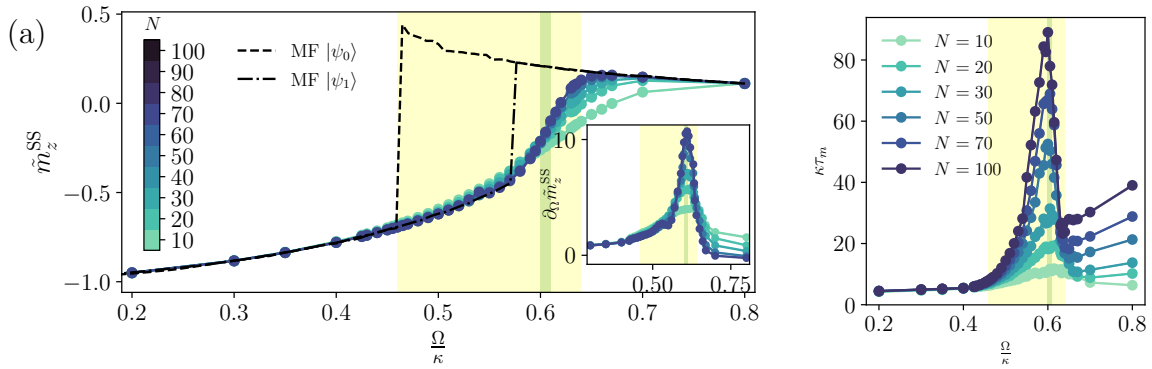

Figure 4.6.: (a) Steady-state phase diagram for finite size compared with mean-field phase diagram for $|\psi_0\rangle$ (dashed line) and $|\psi_1\rangle$ (dash-dot line). Derivative of $\tilde{m}_z^{\mathrm{SS}}$ in the inset. The green narrow region signals the critical point. The yellow shadowed region corresponds to the bistable phase. (b) Saturation time of the magnetization for different sizes. The plot is obtained for $|\psi_0\rangle$, but the same holds from $|\psi_1\rangle$. The yellow part corresponds to the bistable phase.

An important consequence of the non-commutativity of the two limits is that the phase diagram of the model is twofold: it can be obtained with the limit ordering $\lim_{t\to\infty}\lim_{N\to\infty}$, corresponding to a 'dynamical' phase diagram that only studies the transient time and leads to the magnetization mean-field phase diagram in Fig. 4.1(b); it can be obtained with the opposite ordering $\lim_{N\to\infty}\lim_{t\to\infty}$, corresponding to the phase diagram of the steady-state, independent on the choice of the initial state since the steady state is unique for finite sizes.

To obtain the *dynamical* and *steady-state* phase diagram, the following procedures are adopted. The decay time to the steady state τ_m is obtained from the time evolution of the magnetization, see Appendix C.1. Choosing $\mathcal{T} = 3\tau_m$ as the boundary between transient and steady state, one can simply define the order parameter for the *steady-state* phase diagram as:

$$\tilde{m}_z^{\mathrm{SS}} = \lim_{t_f\to\infty} \frac{1}{(t_f - \mathcal{T})} \int_{\mathcal{T}}^{t_f} dt\, \overline{m}_z(t). \tag{4.11}$$

The order parameter for the *dynamical* phase diagram, can be instead defined as

$$\tilde{m}_z^{\mathrm{Dyn}} = \frac{1}{\mathcal{T}} \int_0^{\mathcal{T}} dt\, \overline{m}_z(t). \tag{4.12}$$

The latter definition of order parameter leads to the already presented mean-field phase diagram and therefore will not be presented in this section.

The *steady-state* phase diagram and its comparison with the mean-field (or *dynamical* for $N \to \infty$) phase transitions for $|\psi_0\rangle$ and $|\psi_1\rangle$ are presented in Fig. 4.6(a). The steady-state magnetization has a behavior that does not match any of the mean-field first-order transitions. The dark-shadowed green line signals the value of $\Omega_C^{\mathrm{SS}}/\kappa \sim 0.61$ in which

the Ω-derivative of $\tilde{m}_z^{\mathrm{SS}}$ has a maximum and separates two regions with positive and negative magnetizations. We identify this value as critical point for the magnetization phase transition. In all plots (Figs. 9,11-13) the bistable region is indicated with a yellow shadowed region.

The saturation time of the magnetization is able to capture the full picture of the magnetization phase diagram, as in Fig. 4.6(b). The critical point of the *steady-state phase diagram* is signaled by the divergence of the saturation time with system size, a feature related to the critical slowing down around this transition. The *dynamical phase diagram* is captured by the following properties: the stationary behaviour has a size-independent magnetization time, while the time crystal behavior appears after a cusp at the border with the bistability region, corresponding to the one with an exploding saturation time.

The same procedure is applied again to properly analyze the entanglement entropy. The time-evolution of the entanglement entropy in Fig. 4.4 [panels (d),(e),(f)], obtained from $|\psi_0\rangle$ and $|\psi_1\rangle$, shows once again the non-commutativity of the thermodynamic limit and infinite time limit in the bistable region.

Also in this case, a *steady-state* and a *dynamical* order parameter can be defined. Following closely the procedure already used for the magnetization, we can identify a τ_S saturation time from the time-evolution of the entanglement entropy, set $\mathcal{T} = 3\tau_S$ and define $\tilde{S}_E^{\mathrm{SS}}$ with a time-average over $[\mathcal{T}, \infty]$ and $\tilde{S}_E^{\mathrm{Dyn}}$ through a time-average over the window $[0, \mathcal{T}]$.

The unique *steady-state* phase diagram in Fig. 4.7(a) shows an entanglement transition between a non-entangled region in which $\tilde{S}_E^{\mathrm{SS}} \propto N^0$ and an entangled region with $\tilde{S}_E^{\mathrm{SS}} \propto N^0$ (scalings shown in [panel (b)]). The green shadowed line, which separates the two phases, indicates the value $\Omega_C^{\mathrm{SS}} \sim 0.61$ at which the derivative has a maximum. This value precisely coincides with what we found in the magnetization *steady-state* phase diagram. Once again, we have found in the driven-dissipative Tavis-Cummings model an entanglement transitions occurring together with a magnetization transition. However, an important difference arises from the previous entanglement phase transition found at $\lambda/\kappa = 0.2$. The saturation time at criticality scales in this case superlinearly, without mitigating the post-selection barrier. Fig. 4.7(c) shows the saturation time at criticality for $\lambda/\kappa = 0.8$ and deeper in the bistable region at $\lambda/\kappa = 1$: in both cases, the entanglement presents a slow saturation worsened by the increase of λ/κ. We argue that bistability, which causes a slowdown of the dynamics with a non-commutativity of the $N \to \infty$ and $t \to \infty$ limits, does not allow for a reduction of the post-selection problem.

The *dynamical* computation of $\tilde{S}_E^{\mathrm{Dyn}}$ shows for both initial states a jump in the entanglement entropy around a critical point that matches exactly the critical point for the magnetization transition in the mean-field (*dynamical*) phase diagrams, as shown in Fig. 4.8. We conclude that also in this different type of phase diagram, we have an

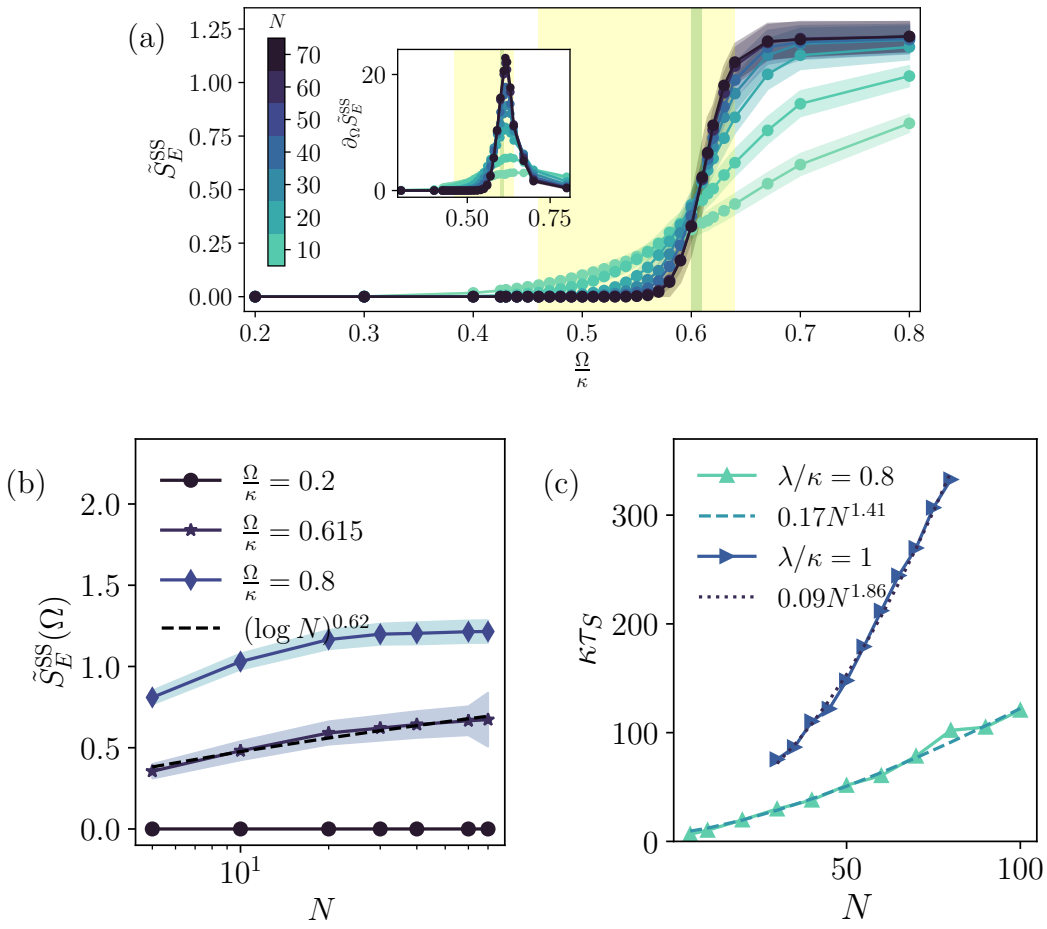

Figure 4.7.: (a) $\tilde{S}_E^{SS}$ for different size and its derivative in the inset. The green narrow region signals the critical point. (b) Scaling of $\tilde{S}_E$ with N in the steady-state phase diagram. (c) Scaling of the entanglement entropy saturation time with system size N at criticality. The lines correspond to two different values of λ/κ both affected by the bistability. The yellow region corresponds to the bistable phase.

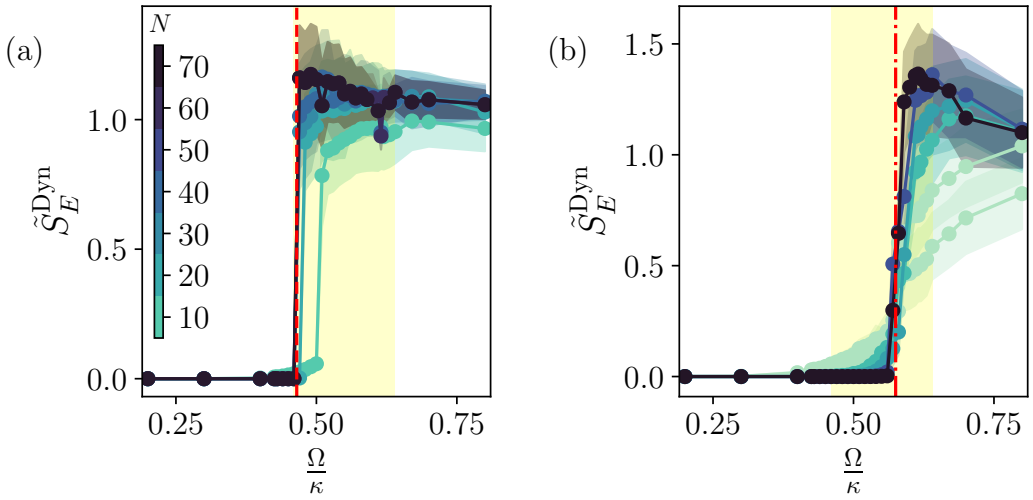

Figure 4.8.: (a) $\tilde{S}_E^{\mathrm{Dyn}}$ calculated from $|\psi_0\rangle$ and critical value as red dashed line. (b) $\tilde{S}_E^{\mathrm{Dyn}}$ calculated from $|\psi_1\rangle$ and critical value as red dot-dash line. The yellow shadowed region corresponds to the bistable phase and the legend is shared.

entanglement transition occurring along with the magnetization one.

4.2.3. Experimentally-relevant details

The study carried out so far has obtained the following important results:

- Having a collective system is not enough to mitigate post-selection. In the presence of bistabilities and critical slowing-downs, the post-selection problem is again exponential in system size, and thus platforms in regimes presenting these features are not good candidates for the experimental realization of an MIPT.
- A regime with good post-selection property has been found anyway. Labeling as λ^T the value of interaction corresponding to the tricritical point, we can safely analyze $\lambda < \lambda^T$ and have a fast saturating entanglement, and a good candidate platform.

Having found a region of the Tavis-Cummings model in which postselection is efficiently mitigated, we can adopt a more experimentally-oriented perspective on the study of the model.

We propose an experimental realization for the bad-cavity limit of the Tavis-Cummings model, which slightly modifies the already implemented one in Ref. [202]. In this case, the implementation uses instead ^{87}Sr. This implementation has typical values $\kappa = 2\pi \times 153$ kHz, a single photon Rabi frequency of $2g = 2\pi \times 8$ Hz [209], and $N = 10^4 - 10^5$ leads to $\lambda/\kappa = 0.001 - 0.01$. This is very close to the horizontal axis in Fig. 4.1(b), but still displays a transition between a stationary phase and a time crys-

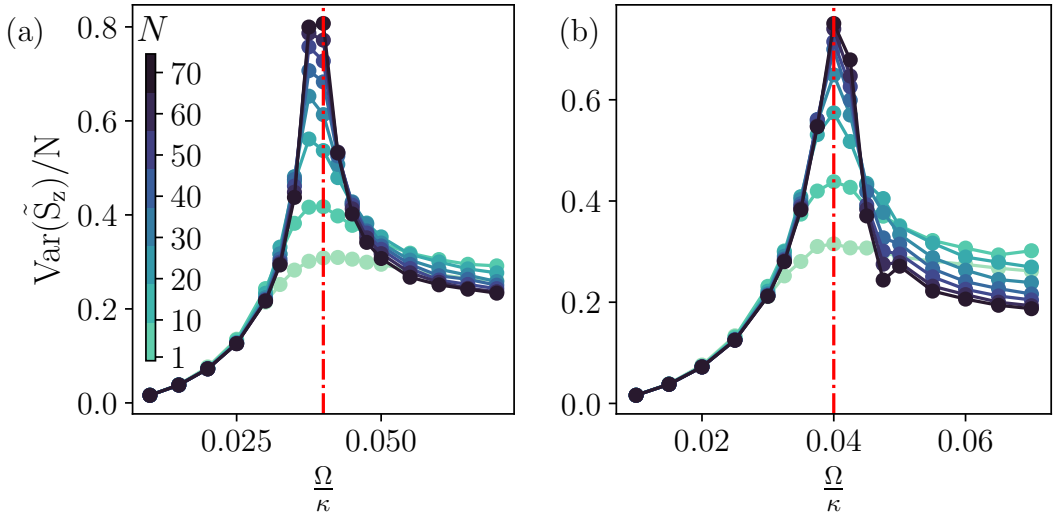

Figure 4.9.: Phase diagrams obtained from the size-rescaled variance $\hat{S}_z$. All the plots are obtained with $N_{\mathrm{traj}} = 4000$ trajectories at $\lambda/\kappa = 0.2$. The plots correctly signal the monitored critical point $\Omega_C/\kappa = 0.04$ and share the legend. (a) Phase diagram obtained in the steady state. (b) Phase diagram obtained respectively at $\kappa t = 110$ smoothing the oscillations in the entangled phase with a Gaussian filter with variance equal to the oscillations' period.

tal phase. In this limit the ensuing dissipative/measurement dynamics occurs with the timescale λ^2/κ $(15 - 150$ ms) [24, 79] and the average time between photon detections increases. Furthermore, spontaneous emission into free space now has a $1/e$ decay time ~ 100 s, and is thus not relevant when compared to λ^2/κ.

This implementation raises some more questions about post-selection.

Question one: can we use other non-linear objects?

The entanglement entropy is notoriously a difficult quantity to get directly from experiments. Although techniques like randomized measurements [210, 211] and classical shadows [212] have been proposed to measure it more efficiently, measuring objects like variances is something generally easier and well-established in laboratories [47, 213].

An example is using spin squeezing, related to the variance of $\hat{S}_z$, as it can be proved to be an entanglement witness [214–216]. In Fig. 4.9(a), we prove that spin squeezing exactly finds the same critical point as the entanglement entropy measurement-induced phase transition.

Question two: can we improve the scaling's coefficient?

Fig. 4.3(c) indicates that the dependence of $\kappa\tau_S$ with particle number is weak, with $\kappa\tau_S \approx A(\log N)^\alpha$. The large number of trajectories is instead a consequence of the prefactor A being large. The favorable scaling with N means that measurement strategies aimed at reducing the postselection overhead would be effective even for reasonably large numbers of particles.

In order to reduce A we notice that the spin squeezing phase diagram shown in Fig. 4.9(b) is obtained at times $\kappa t = 110 < \kappa\tau_S$, and still displays the same critical point and qualitative behavior.

Question three: can we take into account the time resolution of real devices?

The experimental realization of the physics we are presenting, has an additional intrinsic challenge compared to numerical simulations: the fact that experimental devices have a finite resolution $\Delta\mathscr{T}$, which does not allow to distinguish trajectories that differ within time intervals $\delta t < \Delta\mathscr{T}$. For example, two trajectories having a jump at different jump times inside the interval $[t, t + \Delta\mathscr{T}]$, may not be distinguishable in experimental implementations. Not knowing the precise occurrence of quantum jumps implies partial information about the quantum state, hence, the quantum state is no longer pure. In practice, this means that the building block of our simulations, the pure-state-trajectory, is replaced in experiments by a mixed-state-trajectory corresponding to the average of pure-state-trajectories that differ only inside bins. Suppose $\{|\psi_{\gamma_1}\rangle, ..., |\psi_{\gamma_n}\rangle\}$ is a family of pure-state-trajectories which are indistinguishable from an experimental point of view. The associated mixed-state-trajectory is defined as

$$\hat{\rho}_\gamma = \frac{1}{n}\sum_{i=1}^{n} |\psi_{\gamma_i}\rangle \langle\psi_{\gamma_i}| \tag{4.13}$$

This inaccuracy in the trajectories' resolution does not affect average observables but does modify those quantities that are non-linear in the state. For this reason, the question we would like to answer concerns how the experimental resolution $\Delta\mathscr{T}$ affects the transition we are witnessing from the exact simulations. In the case of entanglement entropy, the question translates to understanding how the binned time evolution decreases the purity of $\hat{\rho}_\gamma$ and whether the change in the behavior of the (entanglement) entropy reflects the behavior of quantum correlations or classical correlations.

We tackle this problem by writing a conditional master equation for an approximate time evolution of $\hat{\rho}_\gamma$. This allows us to estimate the (entanglement) entropy in the steady state and verify how the scaling with the system size changes. The procedure corresponds to a rewriting of the quantum jump master equation considering the evolution at fixed time steps $t_i \in (0, \Delta\mathscr{T}, 2\Delta\mathscr{T}, ..., t_f)$ of the mixed state $\hat{\rho}_\gamma$.

Consider now a system described by a Hamiltonian $\hat{H}_0$. We monitor events associated with the quantum jump $\hat{L}$ occurring with rate κ. Our discussion is trivially generalized to the case of multiple dissipative channels. Restricting to the case in which the waiting time is comparable with the experimental resolution $\Delta\mathscr{T}$, we can assume to have only zero jumps or one jump inside a bin.

We label as $\hat{\rho}_\gamma(t_i)$ the state of the system at time t_i, and as $\hat{\mathcal{U}}_{\Delta\mathscr{T}} = \exp\{-i\Delta\mathscr{T}(\hat{H}_0 - \frac{i\kappa}{2}\hat{L}^\dagger\hat{L})\}$ the non-unitary evolution operator corresponding to non-detection.

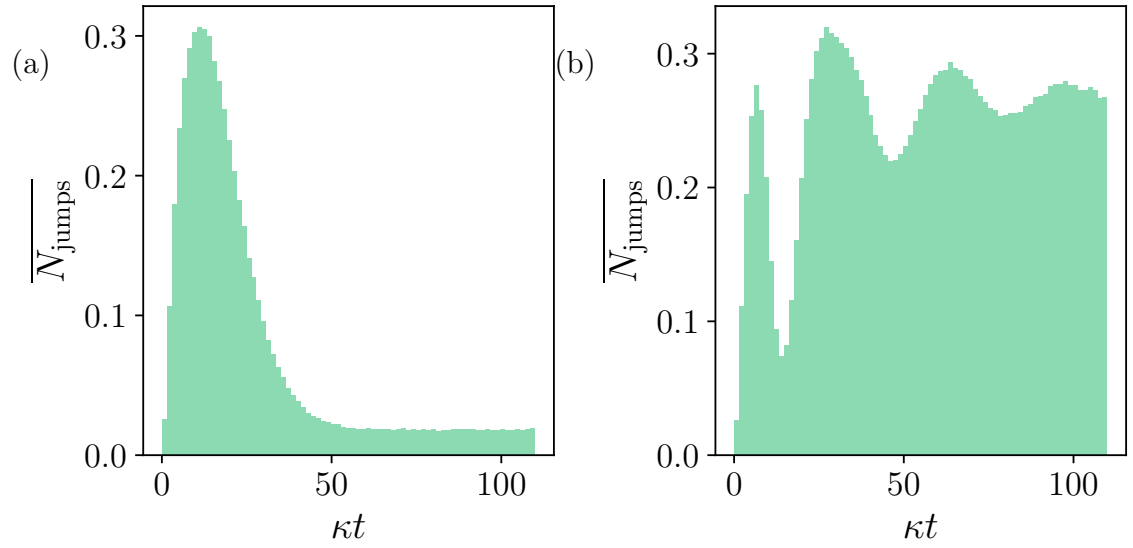

Figure 4.10.: (a) and (b): average number of jumps for the binned evolution, respectively in the stationary and time crystal phase. The bin width is $\Delta\mathscr{T} = 1.4/\kappa$ and the statistics has been obtained from 120 000 pure-state-trajectories for $N = 5$.

The evolved state at time t_{i+1} is given with probability $p_0 = 1 - \kappa\Delta\mathscr{T}\left\langle \hat{L}^\dagger\hat{L}\right\rangle_{t_i}$ by

$$\hat{\rho}_\gamma(t_{i+1})^{0\text{J}} = \frac{\hat{\mathcal{U}}_{\Delta\mathscr{T}}\ \hat{\rho}_\gamma(t_i)\ \hat{\mathcal{U}}^\dagger_{\Delta\mathscr{T}}}{\text{Tr}\left\{\hat{\mathcal{U}}^\dagger_{\Delta\mathscr{T}}\hat{\mathcal{U}}_{\Delta\mathscr{T}}\,\hat{\rho}_\gamma(t_i)\right\}}, \tag{4.14}$$

in the non-detection case, or with probability $p_1 = \kappa\Delta\mathscr{T}\left\langle \hat{L}^\dagger\hat{L}\right\rangle_{t_i}$ by

$$\hat{\rho}_\gamma(t_{i+1})^{1\text{J}} = \int_0^1 \frac{\hat{\mathcal{U}}_{x\Delta\mathscr{T}}\,\hat{a}\,\hat{\mathcal{U}}_{(1-x)\Delta\mathscr{T}}\,\hat{\rho}_\gamma(t_i)\,\hat{\mathcal{U}}^\dagger_{(1-x)\Delta\mathscr{T}}\,\hat{a}^\dagger\,\hat{\mathcal{U}}^\dagger_{x\Delta\mathscr{T}}}{\text{Tr}\left\{\hat{\mathcal{U}}_{x\Delta\mathscr{T}}\,\hat{a}\,\hat{\mathcal{U}}_{(1-x)\Delta\mathscr{T}}\,\hat{\rho}_\gamma(t_i)\,\hat{\mathcal{U}}^\dagger_{(1-x)\Delta\mathscr{T}}\,\hat{a}^\dagger\,\hat{\mathcal{U}}^\dagger_{x\Delta\mathscr{T}}\right\}}\,dx.$$

in the detection case. The last expression takes into account the fact that the jump may happen at any time inside the bin and calculates the average over all the possibilities.

A further approximation has been introduced: we are defining the probability of the jump event based on the density $\left\langle \hat{L}^\dagger\hat{L}\right\rangle$ calculated at the beginning of the bin, while it may change due to the intra-bin evolution. We assume the approximation to hold since the resolution should be smaller than the timescale of the dynamics in all reasonably accurate experimental setups.

We apply this method to the Tavis-Cummings model, focusing on the region with $\lambda/\kappa = 0.2$ where the mitigation of the post-selection problem applies.

We repeat the simulation for several choices of bin widths, each corresponding to a different time resolution of a putative experimental setup. The bin widths we choose cover the range $\Delta\mathscr{T} \in [0.1/\kappa, 1.1/\kappa]$. The statistics of jumps has been studied for each

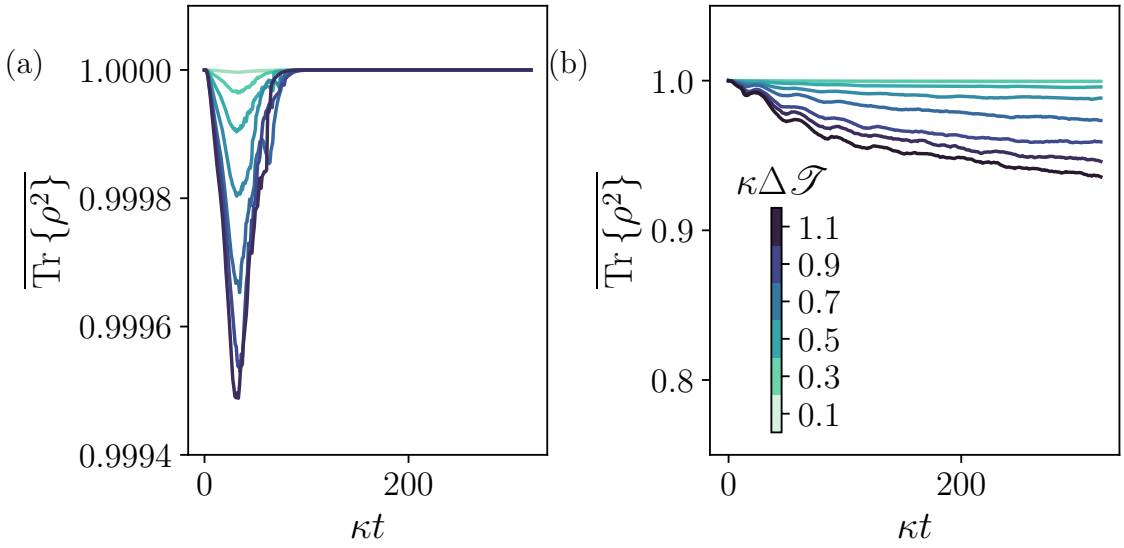

Figure 4.11.: (a) and (b): Purity evolution respectively in the stationary and time crystal phase for several binning choices. The average is obtained from 1000 mixed-state trajectories for $N = 9$. The legend is shared.

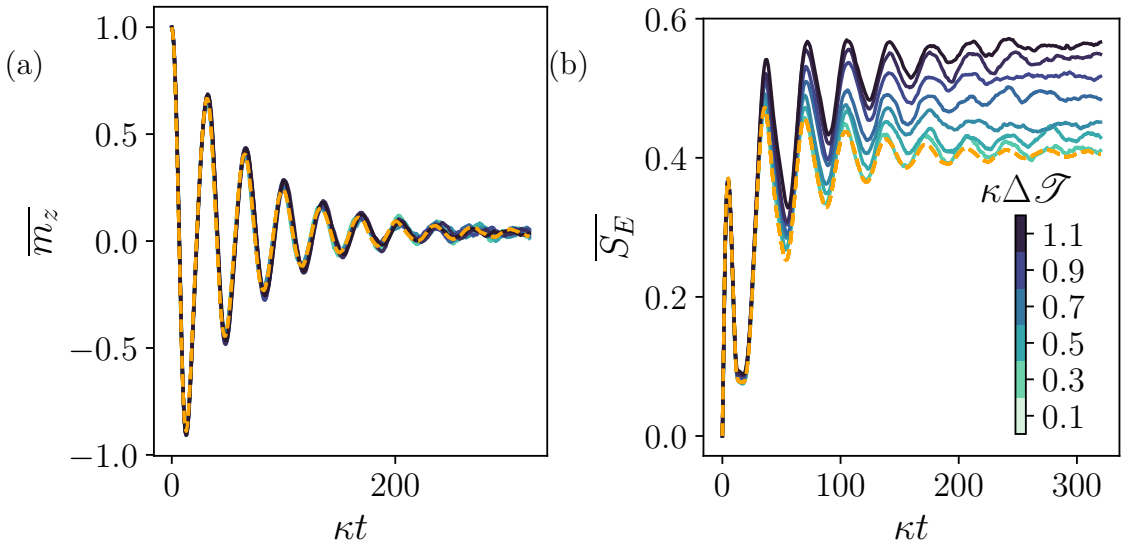

Figure 4.12.: (a) Magnetization dynamics for several bin sizes compared to the exact result (orange dashed line). (b) Entanglement dynamics for several bin sizes compared to the exact result (orange dashed line). For both plots the average is obtained from 1000 mixed-state trajectories for $N = 9$. The legend is shared and both plot represent the dynamics in the time-crystal phase.

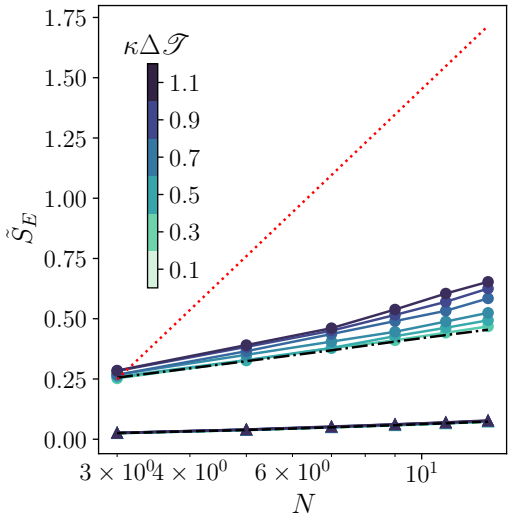

Figure 4.13.: Steady state value of the entanglement entropy with respect to system size for several bin widths. ▲ markers correspond to the stationary phase, the • markers correspond to the time-crystal phase. The exact results for the stationary and time crystal steady-state S_E are reported respectively with a dashed and dash-dot line. The red dot line shows $\log N$ for reference. The average is obtained from 1000 mixed-state trajectories.

binning (an example for $N = 5$ is shown in Fig. 4.10) and for each bin and size the condition $\kappa\Delta\mathscr{T}\langle\hat{a}^\dagger\hat{a}\rangle < 1$ is verified, meaning that on average the number of jumps is less than one inside each bin and the proposed master equation represents a good approximation. Furthermore, to confirm the quality of the approximation, we show that the purity does not decrease dramatically in Fig. 4.11, justifying the calculation of the entanglement entropy as if the state were pure. Interestingly, notice how the purity of the stationary phase in [panel (a)] can be safely considered to be always 1, indicating this phase to be stable with respect to the choice of binning. In cases in which the state cannot be regarded as pure, other measures of entanglement such as the logarithmic negativity [217] or the quantum Fisher information [47] should be used.

As anticipated, observable averages do not depend on the binning procedure as the trajectory and quantum average commute. [Panel (a)] of Fig. 4.12 shows an example of the dynamics of the magnetization for $N = 9$ in the time crystal phase, compared to the exact simulations (orange dashed line). They match perfectly. [Panel (b)] compares the entanglement entropy obtained with finite time resolutions and the exact simulation. In this case, we observe a strong dependence on the bin size of the steady-state value.

In Fig. 4.13 we show the steady-state value of the entanglement entropy in the stationary phase (with markers ▲) and in the time-crystal phase (with • markers). The stationary phase has the property of having a low number of photons in the steady state, resulting in having few jumps along trajectories. This causes the steady-state value of $\tilde{S}_E$ to be robust to variations of the binning size. We always obtain results that are consistent with the exact simulations (black dashed line). The time-

crystal phase, exhibiting a higher number of photons and jumps, is strongly affected by the change in the bins' size and deviates from the exact result (black dash-dot line). Also in this case, the scaling is given by $(\log N)^{\alpha}$ with $\alpha < 1$. The power α increases for increasing bin sizes, as the entanglement entropy in these cases also accounts for classical correlations. Notice however that a resolution $\Delta\mathscr{T} \sim 1/\kappa$ yields a scaling qualitatively different from $\log N$, which corresponds to the scaling of the (entanglement) entropy given by the Lindblad equation (red dotted line). Thus, we can say that for $\Delta\mathscr{T} \sim 1/\kappa$ the entropy is mostly governed by quantum correlations, and the entanglement transition can be witnessed by the experimental device.

As a closing remark, we notice that our approximation of the master equation is reliable as long as the typical waiting time $\propto (\kappa \langle \hat{a}^\dagger \hat{a} \rangle)^{-1}$, which scales at most as N^{-1}, is smaller than the bin size $\Delta\mathscr{T}$. To take into account larger sizes with a smaller waiting time one should allow for the occurrence of more than one jumps in the master equation. For example, allowing for the presence of two jumps one would have the following modified master equation: the non-detection state (4.14) occurs with probability $p_0 = 1 - \kappa\Delta\mathscr{T} \langle (\hat{a}^\dagger \hat{a})^2 \rangle$; the detection state, happening with probability $p_{1,2} = p_1 + p_2 = \kappa\Delta\mathscr{T} \langle (\hat{a}^\dagger \hat{a})^2 \rangle$ is instead modified to

$$\hat{\rho}_\gamma^{1,2\mathrm{J}} = \frac{p_1}{p_{1,2}} \hat{\rho}_\gamma^{1\mathrm{J}} + \frac{p_2}{p_{1,2}} \hat{\rho}_\gamma^{2\mathrm{J}} \tag{4.15}$$

with $\hat{\rho}_\gamma^{1\mathrm{J}}$ as in eq. (4.15) and $\hat{\rho}_\gamma^{2\mathrm{J}}$ being the average over all the trajectories having two jumps inside the bin. The probabilities in the above expression are defined as $p_1 = \kappa\Delta\mathscr{T} \langle \hat{a}^\dagger \hat{a} \rangle$ (probability of having one jump) and as $p_2 = \kappa\Delta\mathscr{T}(\langle (\hat{a}^\dagger \hat{a})^2 \rangle - \langle (\hat{a}^\dagger \hat{a}) \rangle)$ (probability of having two jumps).

4.3. Long-Range models

We now aim to extend the concept of fast entanglement dynamics and post-selection mitigation to a wider class of systems: long-range interacting systems. Exploring this type of physics hold a fundamental importance, both from a theoretical point of view [218, 219], and from an experimental point of view, as platforms such as trapped ions [220], Bose-Einstein condensates in cavities [221], dipolar [222], polar [223], and Rydberg atoms [224], or driven ultra-cold atomic gases [225] showcase frameworks where the system interactions scale as a power law of the distance.

The goal of this Section is to show the presence of new measurement-induced phase transitions and understand under which circumstances the post-selection problem can be mitigated in long-range systems.

We focus on spin models, in which the long-range is set by the power α:

$$\hat{H} = \omega \hat{S}^x + \frac{2sJ}{\mathcal{N}} \sum_{i,j} \frac{\sigma_z^i \sigma_z^j}{||\mathbf{r}_i - \mathbf{r_j}||^\alpha}\,, \tag{4.16}$$

where ω is the amplitude of a collective drive and J is the interaction strength. The factor $2s$ ensures that the mean-field theory is $s-$independent, which can be ignored for spin-half ($s = 1/2$) systems. $\mathcal{N}$ is the Kac-normalization ensuring an extensive energy for the system. The symbol $||\bullet||$ corresponds to the distance in $D-$dimension, using periodic boundary conditions.

The type of detection we decide to implement in this Section is a generalization of the homodyne detection, exposed in Sec. 1.2.1. We will use *heterodyne detection*, which corresponds to the complex generalization of the homodyne procedure, in which the noise dw, dw^* has stochastic real and imaginary parts. The general equations describing the state evolution through heterodyne detection due to measurements of the $\hat{L}_i$ operators are:

$$d\hat{\rho} = dt\mathcal{L}(\hat{\rho}) + \sum_i [dw_i^* \left(\hat{L}_i - \langle \hat{L}_i \rangle\right) \hat{\rho} + dw_i \hat{\rho} \left(\hat{L}_i^\dagger - \langle \hat{L}_i^\dagger \rangle\right)] , \tag{4.17}$$

$$\mathcal{L}(\hat{\rho}) \equiv -\left[\hat{H}, \hat{\rho}\right] + \mathscr{D}(\hat{\rho}) , \tag{4.18}$$

$$\mathscr{D}(\hat{\rho}) \equiv \sum_{i,j} f_{ij} \left(\hat{L}_i \hat{\rho} \hat{L}_j^\dagger - \frac{1}{2}\left\{\hat{L}_j^\dagger \hat{L}_i, \hat{\rho}\right\}\right) . \tag{4.19}$$

where $\hat{\rho}$ is the density matrix, $\mathcal{L}$ is the Liouvillian superoperator, and the noise is governed by the equations

$$\overline{dw_i} = 0 , \quad dw_i^* dw_j = f_{ij} dt , \; dw_i dw_j = 0 , \tag{4.20}$$

In our case, we will simply measure the collective spin operator $\hat{S}^-$ yielding:

$$d\hat{\rho} = dt\mathcal{L}(\hat{\rho}) + dw^* \left(\hat{S}^- - \langle \hat{S}^- \rangle\right) \hat{\rho} + dw \hat{\rho} \left(\hat{S}^+ - \langle \hat{S}^+ \rangle\right) , \tag{4.21}$$

$$\mathcal{L}(\hat{\rho}) \equiv -\left[\omega \hat{S}^x + \frac{2sJ}{\mathcal{N}} \sum_{i,j} \frac{\sigma_z^i \sigma_z^j}{||\mathbf{r}_i - \mathbf{r_j}||^\alpha}, \hat{\rho}\right] + \frac{\kappa}{S}\left(\hat{S}^- \hat{\rho} \hat{S}^+ - \frac{1}{2}\left\{\hat{S}^+ \hat{S}^-, \hat{\rho}\right\}\right) . \tag{4.22}$$

Notice that in the $\alpha \to 0$ model we re-obtain a model very similar to our starting point: Reference [47].

Beside the stochastic complexity naturally raised by the measurement process, we immediately realize that numerical simulations require much more storage and time capacity than the simulations carried out in Sec. (4.2). In the previous section and in Ref. [47], we were essentially simulating a $N/2$ spin, while in this case, long-range interactions between single spins as in Eq. (4.16), require simulating the full Hilbert space having an exponentially big size $\propto s^N$.

To deal with this problem, we propose a method which exploits the simplifications granted by long-range interactions: they typically lead to underlying semi-classical dynamics, allowing quantum excitations and fluctuations to be treated perturbatively on top of a classical model. These observations lead to a class of approximation methods

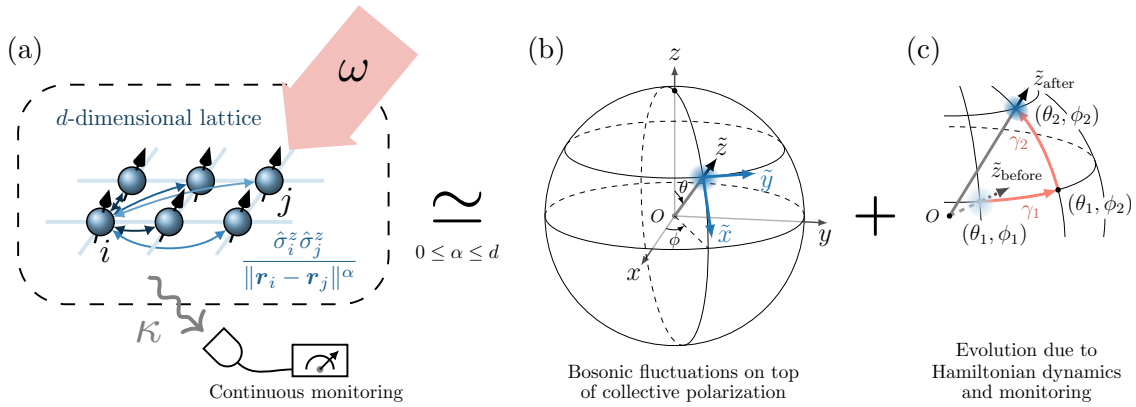

Figure 4.14.: Sketch of a long-range spin model and the representation of its monitored dynamics in the spin-wave approximations. (a) The spins on a d-dimensional lattice are collectively driven (at amplitude ω) and interact via $z-z$ coupling, whose strength decays as a power law of the distance (with exponent α). The system is subjected to a collective dissipation (at rate κ) and continuously monitored. (b) In the infinite-range or long-range regime ($0\le\alpha\le d$), the state of the system can be represented in the spin-wave approximations, where spin fluctuations around the collective polarization are bosonized. Here, $Oxyz$ depicts the lab frame and $O\tilde{x}\tilde{y}\tilde{z}$ is the instantaneous frame where $\tilde{z}$ aligns with the collective spin polarization. (c) The evolution of the state under both the Hamiltonian dynamics and the continuous monitoring. In the proposed method, the angles (θ,ϕ) of the instantaneous frame $O\tilde{x}\tilde{y}\tilde{z}$ are updated to match the collective spin direction after its evolution in each infinitesimal time step. The dashed (solid) straight arrow represents the $\tilde{z}$ axis before (after) the re-alignment step and the curved arrows represent the paths γ_1 and γ_2 as defined in Eq. (4.39) for evaluating the integral of Eq. (4.38).

known as the spin-wave theory. Historically, the spin-wave theory was first introduced by Bloch [226] in 1932 for ferromagnetic spin systems in equilibrium. An equivalent formulation of the theory was later given by Holstein and Primakoff [227]. The spin-wave theory has been highly successful in describing equilibrium ground states in a wide range of magnetic materials, showing good accordance with experimental data [228]. More recently, it has been generalized to the time-dependent regime [229, 230], capturing non-equilibrium dynamics in closed quantum systems undergoing unitary time evolution governed by a Hamiltonian and in driven-dissipative systems [231] described by a Lindblad master equation.

In this Section, we will thus first introduce the spin-wave method for quantum trajectories, and then use it to show MIPTS and post-selection mitigation in long-range systems.

4.3.1. The spin-wave theory for quantum trajectories

The central assumption is that the system admits a strong collective spin polarization, on top of which spin-wave excitations are bosonized via a Holstein-Primakoff expansion truncated to the lowest order:

$$\hat{s}_i^{\tilde{z}}(\theta,\phi) = s - \hat{b}_i^\dagger \hat{b}_i \,, \tag{4.23}$$

$$\hat{s}_i^{\tilde{x}}(\theta,\phi) \simeq \sqrt{\frac{s}{2}}(\hat{b}_i^\dagger + \hat{b}_i) \,, \tag{4.24}$$

$$\hat{s}_i^{\tilde{y}}(\theta,\phi) \simeq i\sqrt{\frac{s}{2}}(\hat{b}_i^\dagger - \hat{b}_i) \,. \tag{4.25}$$

Here, the $\hat{s}^{\tilde{\alpha}}$'s are spin operators in the rotated frame $O\tilde{x}\tilde{y}\tilde{z}$ as illustrated in Fig. 4.14 (b). They are related to the lab-frame spin operators via $\hat{s}_i^{\tilde{\alpha}}(\theta,\phi) = \hat{U}(\theta,\phi)\hat{s}_i^{\alpha}\hat{U}^\dagger(\theta,\phi)$ with $\hat{U}(\theta,\phi) = e^{-i\phi\hat{s}^z}e^{-i\theta\hat{s}^y}$. The $\tilde{z}$ axis of the rotated frame is aligned with the collective (average) polarization of all the spins, which can be met by imposing $\langle\hat{S}^{\tilde{x}}\rangle = \langle\hat{S}^{\tilde{y}}\rangle = 0$. The $\hat{b}_i$'s are bosonic operators, representing spin fluctuations around the collective magnetization, with standard bosonic commutation relations $[\hat{b}_i, \hat{b}_j^\dagger] = \delta_{ij}$. This transformation becomes exact only when $\langle\hat{b}_i^\dagger\hat{b}_i\rangle = 0$, i.e., when the system is in a spin coherent state. Thus, the density of bosonic excitations

$$\epsilon \equiv \frac{1}{Ns}\sum_i \langle\hat{b}_i^\dagger\hat{b}_i\rangle \,, \tag{4.26}$$

also referred to as spin-wave density, serves as a natural control parameter for the approximation [231].

The bosonic modes are then approximated with a Gaussian ansatz [116, 232] parametrized by first and second moments. This allows us to uniquely specify the state of the entire system with the following variational parameters:

$$\theta \,, \phi \,, \beta_i \equiv \langle\hat{b}_i\rangle \,, u_{ij} \equiv \langle\hat{\delta}_i\hat{\delta}_j\rangle \,, v_{ij} \equiv \langle\hat{\delta}_i^\dagger\hat{\delta}_j\rangle \,, \tag{4.27}$$

where $\hat{\delta}_i \equiv \hat{b}_i - \beta_i$. Therefore, this method requires only $o(N^2)$ parameters to represent the state in the most general case, which is exponentially efficient as compared to the dimension of the full Hilbert space 2^N, and the complexity can be further reduced in the presence of additional symmetries.

Initializing the parameters at $t = 0$ such that the rotated frame parametrized by (θ,ϕ) has its $\tilde{z}$ axis aligned with the collective spin (which implies $\sum_i \beta_i = 0$), we proceed stroboscopically by repeating the two following steps until the desired time t is reached:

1. Calculate the infinitesimal increments for the Gaussian parameters $\delta\beta_i$, δu_{ij} and δv_{ij} using Eq. (4.17), and update these quantities with the increments. Note that the frame angles (θ,ϕ) are kept constant within this step, which implies that the $\tilde{z}$ axis no longer aligns with the collective spin after the update as $\sum_i \delta\beta_i \neq 0$ in general.

2. Update frame angles (θ, ϕ) such that $\sum_i \beta_i = 0$ in the new rotated frame [see Fig. 4.14 (c) for a schematic representation of this step]. This can be achieved self-consistently by considering the evolution of the bosonic mode $\hat{b}_i$ generated by the (passive) rotation of the frame alone. Then update the Gaussian parameters β_i, u_{ij} and v_{ij} accordingly (due to the rotation of the frame). Finally, increase the time by δt and start a new iteration.

Before entering into the details of the method, let us remark that it maintains a N^2 computational cost in any dimensionality and lattice geometry. Moreover since our approximations are formulated at the level of single trajectories and not the average dynamics, our variational ansatz allows us to reach a larger class of density matrices [116] compared to previous methods working on the level of the density matrix [231]. Indeed, the mixture of Gaussian states, such as those describing single trajectories, is a non-Gaussian state in general, hence encodes non-trivial correlations between the spin-waves.

1. Infinitesimal increments

Let us analyze the first step of the evolution. We will work in the more general setting of Eq. (4.17), without considering from the beginning collective spin operators in the dissipator.

The stochastic master equation (4.17) determines the time evolution of the expectation value of operators. For a time-independent operator $\hat{o}$, the expectation $\langle \hat{o} \rangle = \mathrm{tr}[\hat{\rho}\hat{o}]$ evolves as follows;

$$d\langle \hat{o} \rangle = dt \left\langle \mathcal{L}^\dagger(\hat{o}) \right\rangle + \sum_i \left[dw_i^* \left(\langle \hat{o}\hat{L}_i \rangle - \langle \hat{o} \rangle \langle \hat{L}_i \rangle \right) + dw_i \left(\langle \hat{L}_i^\dagger \hat{o} \rangle - \langle \hat{L}_i^\dagger \rangle \langle \hat{o} \rangle \right) \right] , \tag{4.28}$$

where $\mathcal{L}^\dagger$ is the adjoint Liouvillian.

The infinitesimal increments for the expectation of the time-independent operator $\hat{b}_i$ can be therefore obtained by setting $\hat{o} = \hat{b}_i$ in Eq. (4.28) and labeling $\beta = \left\langle \hat{b} \right\rangle$:

$$\begin{aligned} d\beta_i = i dt \left\langle [\hat{H}, \hat{b}_i] \right\rangle + dt \sum_{j,l} f_{jl} \left\langle \hat{L}_l^\dagger \hat{b}_i \hat{L}_j - \frac{1}{2} \left\{ \hat{L}_l^\dagger \hat{L}_j, \hat{b}_i \right\} \right\rangle \\ + \sum_l \left(dw_l^* \langle \hat{\delta}_i \hat{L}_l \rangle + dw_l \langle \hat{L}_l^\dagger \hat{\delta}_i \rangle \right) . \end{aligned} \tag{4.29}$$

For the two-point covariance u_{ij}, which is the expectation of the time-dependent observable $\hat{\delta}_i \hat{\delta}_j$, their increments can be obtained using the Ito differentiation rule. Specifically

for $u_{ij} = \langle \hat{\delta}_i \hat{\delta}_j \rangle$ we have:

$$\begin{aligned} du_{ij} =& idt\langle [\hat{H}, \hat{\delta}_i \hat{\delta}_j] \rangle + dt \sum_{l,m} f_{lm} \langle \hat{L}_m^\dagger \hat{\delta}_i \hat{\delta}_j \hat{L}_l - \frac{1}{2} \left\{ \hat{L}_m^\dagger \hat{L}_l, \hat{\delta}_i \hat{\delta}_j \right\} \rangle \\ &+ \sum_l \left[dw_l^* \langle \left(\hat{\delta}_i \hat{\delta}_j - u_{ij} \right) \hat{L}_l \rangle \right] + dw_l \langle \hat{L}_l^\dagger \left(\hat{\delta}_i \hat{\delta}_j - u_{ij} \right) \rangle \\ &- dt \sum_{l,m} \left(f_{lm} \langle \hat{\delta}_i \hat{L}_l \rangle \langle \hat{L}_m^\dagger \hat{\delta}_j \rangle + f_{ml} \langle \hat{\delta}_j \hat{L}_m \rangle \langle \hat{L}_l^\dagger \hat{\delta}_i \rangle \right) . \end{aligned} \tag{4.30}$$

where the last term proportional to dt comes from the time-dependence of $\hat{\delta}_i \hat{\delta}_j$. Similarly, we have for $v_{ij} = \langle \hat{\delta}_i^\dagger \hat{\delta}_j \rangle$,

$$\begin{aligned} dv_{ij} =& idt\langle [\hat{H}, \hat{\delta}_i^\dagger \hat{\delta}_j] \rangle + dt \sum_{l,m} f_{lm} \langle \hat{L}_m^\dagger \hat{\delta}_i^\dagger \hat{\delta}_j \hat{L}_l - \frac{1}{2} \left\{ \hat{L}_m^\dagger \hat{L}_l, \hat{\delta}_i^\dagger \hat{\delta}_j \right\} \rangle \\ &+ \sum_l \left[dw_l^* \langle \left(\hat{\delta}_i^\dagger \hat{\delta}_j - v_{ij} \right) \hat{L}_l \rangle + dw_l \langle \hat{L}_l^\dagger \left(\hat{\delta}_i^\dagger \hat{\delta}_j - v_{ij} \right) \rangle \right] \\ &- dt \sum_{l,m} \left(f_{lm} \langle \hat{\delta}_i^\dagger \hat{L}_l \rangle \langle \hat{L}_m^\dagger \hat{\delta}_j \rangle + f_{ml} \langle \hat{\delta}_j \hat{L}_m \rangle \langle \hat{L}_l^\dagger \hat{\delta}_i^\dagger \rangle \right) . \end{aligned} \tag{4.31}$$

In the equations above, the Hamiltonian $\hat{H}$ and the dissipation operators $\hat{L}_i$ should be expressed in terms of the bosonic operators $\hat{b}_i$ using the substitution rules defined in Eq. (4.23). The Gaussian approximation then allows evaluating the expectation value of every term beyond quadratic order thanks to the Wick theorem. The increments $\delta\beta_i$, δu_{ij}, and δv_{ij} are then discretized considering a small time step δt. The noise is approximated with $dw_i \to \delta w_i = \sqrt{\delta t}(X_i + iY_i)$, where the pair of random vectors $(\mathbf{X}, \mathbf{Y})$ at every time step is drawn from a multivariate real Gaussian distribution with zero mean and the following covariance matrix,

$$\mathbf{K} = \begin{pmatrix} \mathbf{K^{XX}} & \mathbf{K^{XY}} \\ \mathbf{K^{YX}} & \mathbf{K^{YY}} \end{pmatrix} \tag{4.32}$$

with matrix elements

$$(\mathbf{K^{XX}})_{ij} = (\mathbf{K^{YY}})_{ij} = \frac{1}{2}\mathrm{Re} f_{ij} , \quad (\mathbf{K^{XY}})_{ij} = -(\mathbf{K^{YX}})_{ij} = \frac{1}{2}\mathrm{Im} f_{ij} . \tag{4.33}$$

The Gaussian parameter can now be updated as:

$$\beta_i \leftarrow \beta_i + \delta\beta_i , \quad u_{ij} \leftarrow u_{ij} + \delta u_{ij} , \quad v_{ij} \leftarrow v_{ij} + \delta v_{ij} . \tag{4.34}$$

Notice now that the increments include terms up to first order in $1/S$, which account for finite-size effects in the dynamics as a correction to the mean-field (zeroth order) theory.

2. Realignment of the frame

The second step now requires the rotation of the frame such that the $\tilde{z}$ axis aligns with the updated direction of the collective spin. This condition is equivalent to requiring the following quantity to be zero,

$$\underline{\beta} \equiv \frac{1}{N}\sum_{i=1}^{N}\beta_i\,, \tag{4.35}$$

as a direct implication of Eq. (4.23). This can be achieved by moving the frame smoothly along a path $\theta(\tau), \phi(\tau)$ parametrized by some parameter τ. The unitary transformation $\hat{U}(\theta,\phi)$ therefore becomes τ-dependent,

$$\hat{U}(\tau) = \hat{U}(\theta(\tau),\phi(\tau))\,. \tag{4.36}$$

The rotation of the frame induces some apparent (fictitious) dynamics on the state, whose generator takes the form of an "inertial Hamiltonian":

$$\hat{H}_{\mathrm{RF}} = -i\frac{d\hat{U}}{d\tau}\hat{U}^{\dagger} = \sin\theta\frac{d\phi}{d\tau}\hat{S}^{\tilde{x}} - \frac{d\theta}{d\tau}\hat{S}^{\tilde{y}} - \cos\theta\frac{d\phi}{d\tau}\hat{S}^{\tilde{z}}\,. \tag{4.37}$$

We then use the bosonized $\hat{H}_{\mathrm{RF}}$ in terms of $\hat{b}_i$. To find the amount of rotation of the frame to achieve $\underline{\beta}=0$, let us consider the apparent evolution of the operator $\hat{b}_i$ along the moving frame:

$$\frac{\mathbf{d}\hat{b}_i}{d\tau} = i\left[\hat{H}_{\mathrm{RF}},\hat{b}_i\right] = -i\sqrt{\frac{s}{2}}\sin\theta\frac{d\phi}{d\tau} - \sqrt{\frac{s}{2}}\frac{d\theta}{d\tau} - i\cos\theta\frac{d\phi}{d\tau}\hat{b}_i\,. \tag{4.38}$$

This equation can be integrated analytically by considering the path on the Bloch sphere from (θ_1,ϕ_1) to (θ_2,ϕ_2) following the two segments [as illustrated in Fig. 4.14 (c)]:

$$\gamma_1 : \theta(\tau) = \theta_1, \phi(\tau=0) = \phi_1, \phi(\tau=1) = \phi_2\,; \tag{4.39}$$

$$\gamma_2 : \phi(\tau) = \phi_2, \theta(\tau=1) = \theta_1, \theta(\tau=2) = \theta_2\,. \tag{4.40}$$

The solution is then

$$\hat{b}_i(\theta_2,\phi_2) = \left[\sqrt{\frac{s}{2}}\tan\theta_1 + \hat{b}_i(\theta_1,\phi_1)\right]e^{-i\Delta\phi\cos\theta_1} - \sqrt{\frac{s}{2}}\tan\theta_1 - \sqrt{\frac{s}{2}}\Delta\theta\,, \tag{4.41}$$

where $\Delta\theta \equiv \theta_2-\theta_1$ and $\Delta\phi\equiv\phi_2-\phi_1$. As our goal is to find the amount of rotations $\Delta\theta$ and $\Delta\phi$ starting from $\theta_1=\theta$ and $\phi_1=\phi$ such that $\underline{\beta}(\theta+\Delta\theta,\phi+\Delta\phi)=0$, we simply set the right-hand side of the equation above to zero, giving our final expressions for the angle increments:

$$\Delta\phi = \frac{1}{\cos\theta}\arctan\left\{\frac{\mathrm{Im}\underline{\beta}}{\sqrt{\frac{s}{2}}\tan\theta + \mathrm{Re}\underline{\beta}}\right\} \tag{4.42}$$

$$\Delta\theta = \left(\tan\theta + \sqrt{\frac{2}{s}}\mathrm{Re}\underline{\beta}\right)\cos(\Delta\phi\cos\theta) + \sqrt{\frac{2}{s}}\mathrm{Im}\underline{\beta}\sin(\Delta\phi\cos\theta) - \tan\theta\,. \tag{4.43}$$

With the angular increments in hand, the first moments β_i of the Gaussian ansatz can be updated directly using Eq. (4.41) with the operator $\hat{b}_i$ replaced by its expectation value β_i. This equation also implies the evolution of the fluctuation operators $\hat{\delta}_i = \hat{b}_i - \beta_i$, which is simply

$$\hat{\delta}_i(\theta_2, \phi_2) = \hat{\delta}_i(\theta_1, \phi_1) e^{-i\Delta\phi\cos\theta_1} . \tag{4.44}$$

We obtain, therefore,

$$u_{ij}(\theta_2, \phi_2) = u_{ij}(\theta_1, \phi_1) e^{-2i\Delta\phi\cos\theta_1} , \quad v_{ij}(\theta_2, \phi_2) = v_{ij}(\theta_1, \phi_1) . \tag{4.45}$$

With this, we complete the full update step, summarized as follows:

$$\begin{cases} \theta \leftarrow & \theta + \Delta\theta , \\ \phi \leftarrow & \phi + \Delta\phi , \\ \beta_i \leftarrow & \left[\sqrt{\frac{s}{2}}\tan\theta + \beta_i\right] e^{-i\Delta\phi\cos\theta} - \sqrt{\frac{s}{2}}\tan\theta - \sqrt{\frac{s}{2}}\Delta\theta , \\ u_{ij} \leftarrow & u_{ij} e^{-2i\Delta\phi\cos\theta} , \\ v_{ij} \leftarrow & v_{ij} . \end{cases} \tag{4.46}$$

Finally, we increase the (physical) time t to the next step $t \leftarrow t + \delta t$ and we are ready for a new iteration.

4.3.2. A benchmark: the infinite range case

We consider the spin chain from Eq. (4.16) and focus on the infinite range case $\alpha = 0$ with $s = 1/2$ spins. We fix the interaction strength at $J = 0.1\kappa$ for the rest of the section.

For this model, mean-field theory predicts a dissipative phase transition from a stationary phase to a time-crystal phase, as in the lower part of the phase diagram of Sec. 4.2, and Ref. [47]. Mean-field can be obtained as before by defining the $N-$independent average magnetizations:

$$m_\mu \equiv \frac{\langle \hat{S}^\mu \rangle}{S} = \frac{1}{N}\sum_{i=1}^{N} \langle \hat{\sigma}_i^\mu \rangle , \quad \mu \in \{x, y, z\} , \tag{4.47}$$

whose evolution under the Lindblad dynamics can be obtained with the adjoint master equation from Eq- (4.21) [1]. Within the mean-field approximation, where we assume the factorization $\langle \hat{\sigma}_i^\mu \hat{\sigma}_j^\lambda \rangle = \langle \hat{\sigma}_i^\mu \rangle \langle \hat{\sigma}_j^\lambda \rangle$ at $N \to \infty$, and that $\langle \hat{\sigma}_i^\mu \rangle$ has no $i-$dependence, we obtain the following equations of motion for the average magnetization:

$$\frac{dm_x}{dt} = -4Jm_y m_z + \kappa m_x m_z , \tag{4.48}$$

$$\frac{dm_y}{dt} = -\omega m_z + 4Jm_x m_z + \kappa m_y m_z , \tag{4.49}$$

$$\frac{dm_z}{dt} = \omega m_y - \kappa(m_x^2 + m_y^2) . \tag{4.50}$$

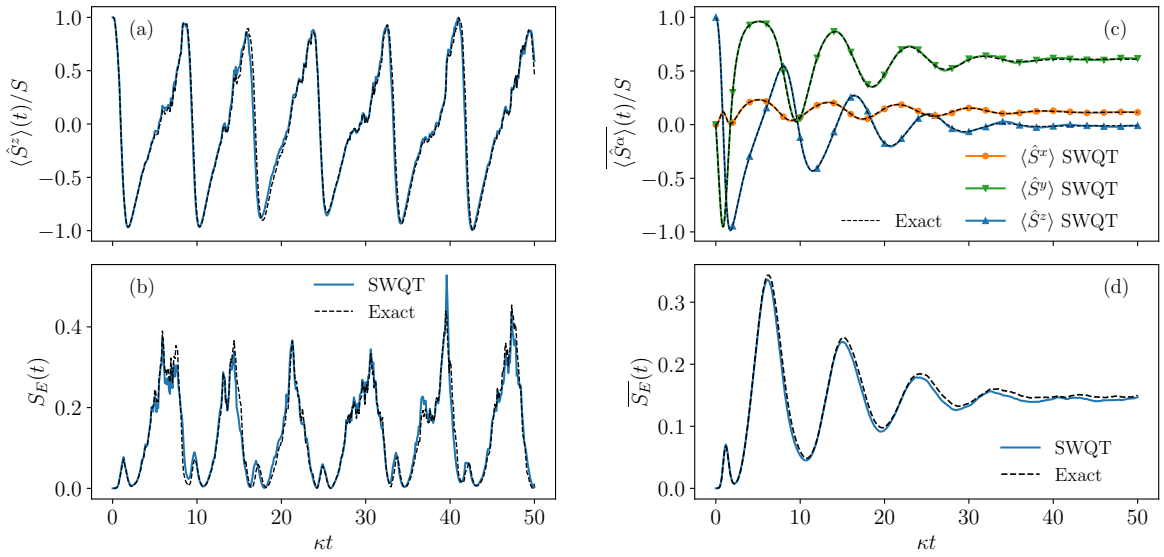

Figure 4.15.: Benchmark of the spin-wave quantum trajectory (SWQT) method against the exact solution for the time-evolution of the following quantities: (a) the magnetization $\langle \hat{S}^z \rangle$ along a single trajectory; (b) the half-system entanglement entropy S_E along the same trajectory as in (a); (c) trajectory-average of the collective spin vector $\overline{\langle \hat{S}^\alpha \rangle}$; (d) trajectory-average of the half-system entanglement entropy $\overline{S_E}$. In single-trajectory benchmarks [(a) and (b)], the same noise realization is adopted by both the spin-wave quantum trajectory and the exact integration of the stochastic master equation. The trajectory-average benchmarks [(c) and (d)] are performed over 4000 trajectories. Parameters: $\omega = 1.25\kappa$, $J = 0.1\kappa$, $S = 64$, $\kappa\delta t = 10^{-4}$.

The steady-state magnetization can be found by imposing the time derivatives to zero, which yields

$$m_z = -\sqrt{1 - \frac{\omega^2}{16J^2 + \kappa^2}}\,. \tag{4.51}$$

Beyond the critical point $\omega_{\mathrm{MF}}^{(c)} = \sqrt{16J^2 + \kappa^2}$, this stationary solution no longer exists, and the magnetization admits only permanently oscillating solutions with zero mean when averaged over long times. The mean-field theory therefore, predicts a continuous phase transition from a stationary phase to a time-crystal phase on the level of the Lindblad dynamics of the average state.

This setting is a great playground to test the validity of the approximations, not only because we have mean-field exact results in the thermodynamic limit, but also because we can compare the spin-wave method's results with the exact simulations. Indeed, in the collective $\alpha = 0$ case, simulations can be carried out easily as the theory is effectively describing a big spin $S = N/2$.

We benchmark our results by evaluating both linear (e.g., observables) and non-linear (e.g., entanglement entropy) functions of the state, to test the ability to predict both dissipative and measurement-induced phase transitions.

To put the spin-wave quantum trajectories in fair comparison with the exact ones, we integrate the exact stochastic master equation (4.17) using the Euler-Maruyama method, adopting the same time step and the same noise realization as used in the spin-wave calculation. An example of a single-trajectory benchmark for the spin-wave method is shown in Fig. 4.15 (a) and (b), where we compare trajectories for both the magnetization $\langle \hat{S}^z \rangle$ and the half-system entanglement entropy [233, 234]) S_E against exact ones. The considered system has $S = 64$ and $\omega = 1.25\kappa$, which, as predicted by the mean-field theory, corresponds to the time-crystal phase in the thermodynamical limit. The initial state is the fully polarized Dicke state (all spins pointing up) for both simulations. Surprisingly, the trajectories obtained with the spin-wave method faithfully reproduce the dynamics of both quantities throughout most of the evolution. This suggests that the proposed method can be used as an approximation to resolve dynamics on the level of single trajectories.

We also evaluate the performance of the spin-wave method on trajectory-averaged quantities. Fig. 4.15 (c) shows the time-evolution of the spin expectations $\overline{\langle \hat{S}^{x,y,z} \rangle}$ obtained by averaging spin-wave quantum trajectories. These are then benchmarked against the exact solution of the Lindblad master equation (4.21). As expected from the single-trajectory performance, the average dynamics is accurately reproduced. Notably, the decaying oscillations of the magnetization are due to the finite size effect and therefore require corrections beyond the mean-field level to capture. It is interesting to note that the length of the averaged collective spin vector $\overline{\langle \hat{S}^{\alpha} \rangle}$ is only a fraction of the maximal value S, which implies the that the average density matrix, of highly mixed nature, is far from a state that can be well approximated by the spin-wave

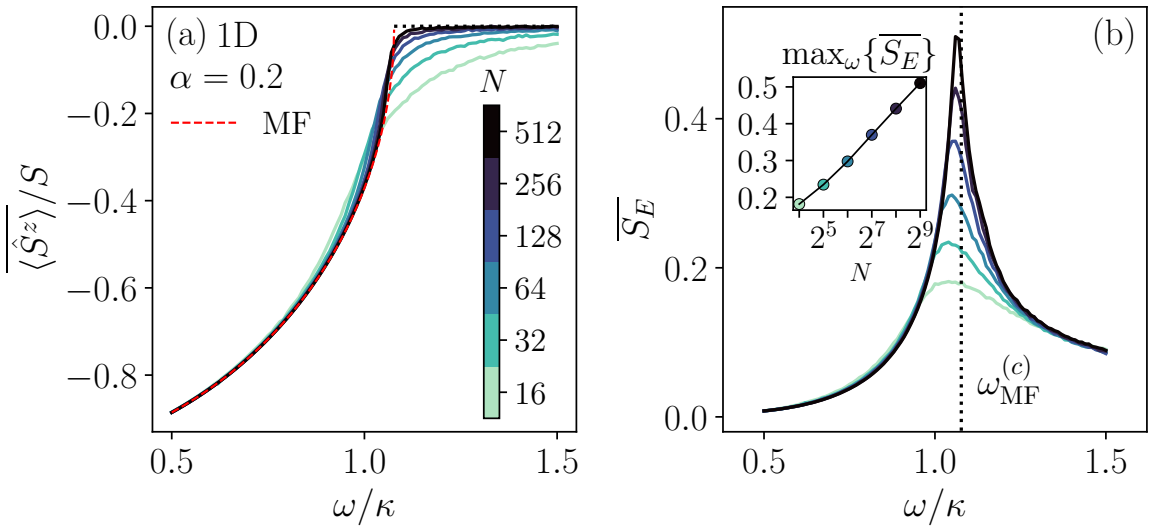

Figure 4.16.: Results for the power-law interacting model in the long-range regime ($\alpha = 0.2$, $J = 0.1\kappa$) of different system sizes (colorbar shared across panels). The dashed line marks the mean-field (MF) solution. (a) Steady-state average z magnetization as a function of the drive ω. (b) Steady-state of the trajectory-averaged half-chain entanglement entropy as a function of ω. The vertical dotted line marks the critical point predicted by the mean-field theory $\omega^{(c)}_{\mathrm{MF}} \simeq 1.077\kappa$. Inset: scaling of the maximum entropy versus N in linear-log scale.

approximations. As a consequence, a deterministic version of the spin-wave theory with the same approximations applied to the averaged state, e.g., the one proposed in Ref. [231], will completely fail to capture the dynamics in this regime. In Fig. 4.15 (d), we compare the trajectory-averaged entanglement entropy with that calculated from exact trajectories, which shows a good agreement again. We also report the average spin-wave density to be $\bar{\epsilon} \lesssim 10^{-2}$ throughout the time evolution.

4.3.3. MIPTs and Post-Selection in long-range systems

Let us now go back to the spin model introduced in Eq. (4.16), with collective $\hat{S}^-$ dissipation.

With the new method we developed, we are not only able to solve the dissipative dynamics of equation (4.21) in a much more efficient way, but we can also easily follow the dynamics along trajectories and predict the behaviour of non-linear quantities in the system state to probe measurement-induced phase transitions.

To investigate the effect of a finite long-range interaction and the entanglement dynamics in this regime, we first apply the spin-wave method to the model in one dimension (1D) with $\alpha = 0.2$. Fig. 4.16 (a) shows the steady-state expectation of the collective magnetization $\overline{\langle \hat{S}^z \rangle}$ as a function of the drive amplitude ω and the system size N. As we approach the thermodynamic limit by increasing N, the spin-wave solu-

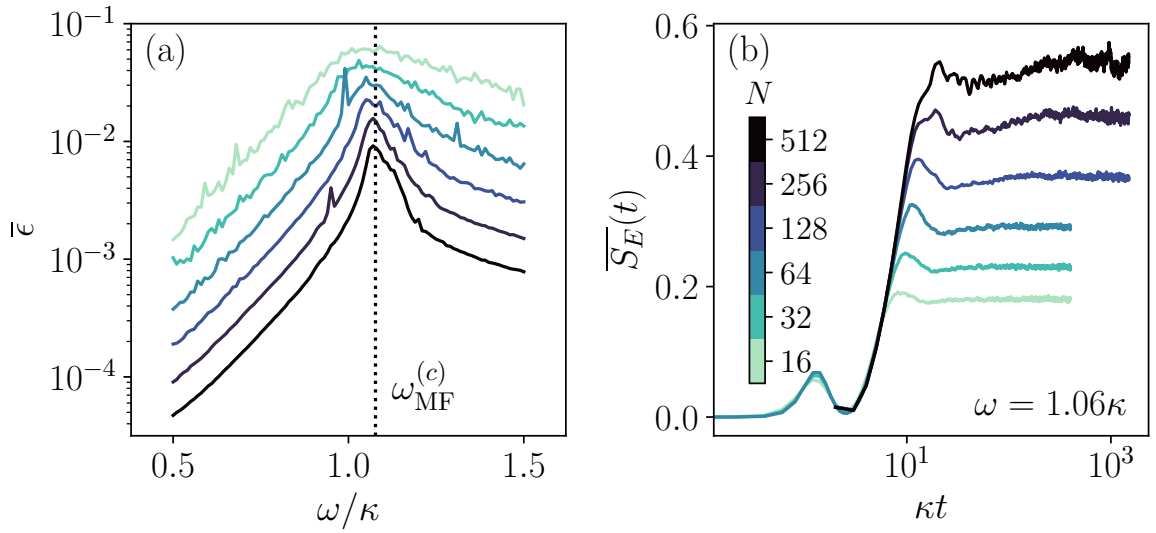

Figure 4.17.: Results for the power-law interacting model in the case of $\alpha = 0.2$, $J = 0.1\kappa$ of different system sizes in 1D (colorbar shared across panels). (a) The scaling of the steady-state average spin-wave density $\bar{\epsilon}$ as a function of the drive ω, in log-linear scale. The vertical dotted lines mark the critical point predicted by the mean-field theory $\omega_{\mathrm{MF}}^{(c)} \simeq 1.077\kappa$. (b) Time evolution of the trajectory-average entanglement entropy at a driving value close to criticality $\omega = 1.06\kappa$, in linear-log scale.

tion converges towards the mean-field prediction and a continuous transition emerges separating the normal phase with $\langle \hat{S}^z \rangle \neq 0$ and the time-crystal phase with $\langle \hat{S}^z \rangle = 0$. Fig. 4.16 (b) shows the behavior of the long-time-averaged half-chain entanglement entropy across this dissipative phase transition. The entanglement develops a logarithmic divergence as a function of N at the critical point (as implied by the finite-size scaling analysis of the maximum value of the entanglement entropy), while it appears to be N-independent for drive values deep inside both phases. This suggests the emergence of an entanglement phase transition separating two area-law phases. To prove the goodness of the spin-wave method also in this conetext, we additionally study the scaling of the steady-state spin-wave density of the power-law spin model on a 1D chain with $\alpha = 0.2$ as considered in the main text, as shown in Fig. 4.17 (a).

When the system size N increases, the spin-wave density is suppressed (including its peak value), which is a signature of the long-range nature of the model: in the $N \to \infty$ limit, a vanishing spin-wave density suggests that the system becomes equivalent to a mean-field (infinite-range) one.

In Fig. 4.17 (b), we study the time evolution of the trajectory-averaged entanglement entropy at a driving value $\omega = 1.06\kappa$, which is close to where the maximum steady-state entanglement is achieved for the finite system sizes we studied. Note that we are increasing N exponentially between the different considered values, while the entanglement quickly reaches the steady-state value in all cases, suggesting the **mitigation of the exponential overhead for observing the entanglement transition via**

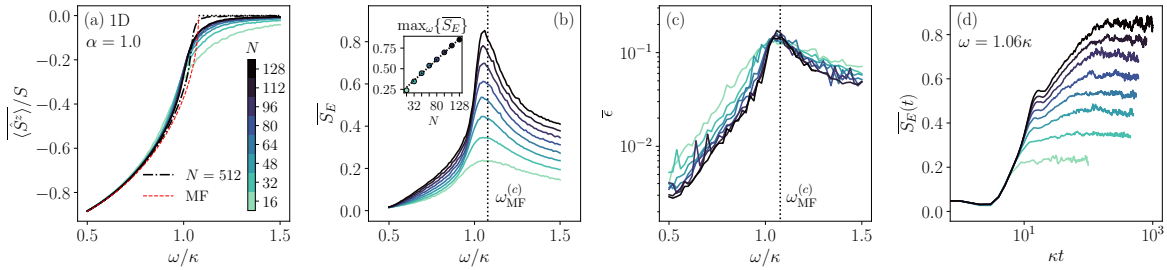

Figure 4.18.: Results for the power-law interacting model in the case of $\alpha = 1.0$, $J = 0.1\kappa$ for different system sizes in 1D (colorbar shared across all panels). (a) Steady-state average z magnetization as a function of the drive ω. The dashed line marks the mean-field solution. (b) Steady-state of the trajectory-averaged half-chain entanglement entropy as a function of ω. The vertical dotted lines mark the critical point predicted by the mean-field theory $\omega^{(c)}_{\mathrm{MF}} \simeq 1.077\kappa$. Inset: scaling of the maximum entropy versus N in linear scale. The dotted line is a linear fit for N ranging from 32 to 128 and we report the coefficient of determination to be $R^2 = 0.9980$. (c) Steady-state spin-wave density in log-linear scale. (d) Dynamics of the trajectory-averaged half-chain entanglement entropy for a driving value $\omega = 1.06\kappa$, in linear-log scale.

brute-force post selection.

The situation changes quite dramatically by decreasing the range of interactions. We consider the shorter-range case with $\alpha = 1$ on a 1D chain for comparison. The steady-state magnetization $\overline{\langle \hat{S}^z \rangle}$, as shown in Fig. 4.18 (a), exhibits qualitatively similar behavior to the long-range case, while it shows more deviation from the mean-field prediction. This could result from more significant finite-size effects due to short-range interactions. (Note that the mean-field theory does not account for the interaction range parameter α and therefore gives identical predictions regardless of α.) In sharp contrast, Fig. 4.18 (b) shows that the entanglement entropy of the short-range systems grows much faster with the system size N. Finite-size scaling suggests a volume law for the maximum entanglement entropy as well as around the critical point. The spin-wave density, as shown in Fig. 4.18 (c), also presents a qualitatively different behavior from the long-range case. Close to the maximal entanglement, the spin-wave density does not appear to decrease with the system size N, and remains around $\bar{\epsilon} \lesssim 0.2$. This suggests that the short-range model does not reduce to a mean-field (infinite-range) one even in the thermodynamic limit of $N \to \infty$, and that higher-order corrections to the theory are expected to have a more significant contribution. Finally, we show in Fig. 4.18 (d) the time dynamics of the trajectory-averaged entanglement entropy at $\omega = 1.06\kappa$. Contrary to the fast saturation of entanglement in the long-range (or infinite-range) regime, the time it takes to reach the steady-state value scales rapidly with N. Despite the relatively high spin-wave density at the considered driving, we expect our result to hold qualitatively.

In Fig. 4.19 (a) we show how the properties of the measurement-induced phase transitions change dramatically depending on the range in 1D: the maximum entanglement

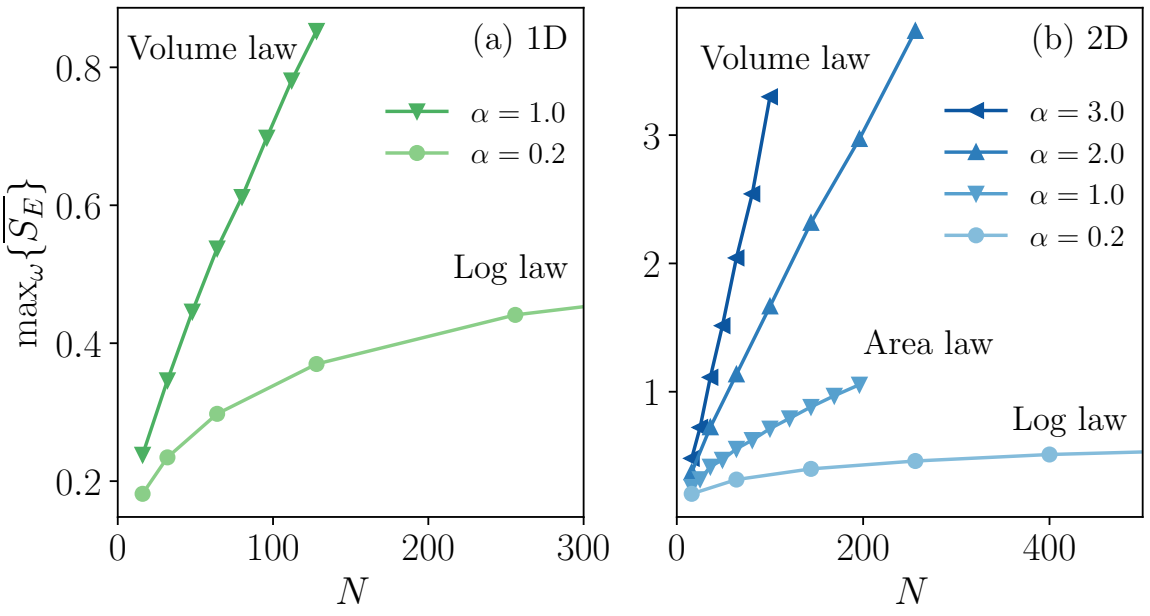

Figure 4.19.: Maximum steady-state entanglement as a function of system size N (total number of spins) for different interaction range α in (a) 1D and (b) 2D. Different scaling behaviors can be observed (see annotation). Note that the horizontal axes are truncated for better visualization, and the maximum number of spins we report is $N = 1024$ in 2D. We report that the value of the drive ω maximizing the entanglement is asymptotically independent of N.

for $\alpha = 1.0$ in 1D exhibits a volume-law scaling in contrast to the log scaling for $\alpha = 0.2$ discussed above.

We also perform simulations in 2D (for up to $32 \times 32 = 1024$ long-range interacting spins) to study the entanglement scaling as a function of α, as shown in Fig. 4.19 (b) for a square lattice of size $N = L^2$. As we shorten the interaction range by increasing α, the entanglement scaling changes from the log law to area law ($\propto L$) and volume law ($\propto L^2$), which suggests the presence of a phase transition driven by α between the different entanglement scaling behavior. We report that even in the volume-law phase under moderately short-range settings ($\alpha = 2.0$ and $\alpha = 3.0$), the spin-wave density remains small at $\bar{\epsilon} \lesssim 0.1$. On the other hand, the increase of the spin-wave density with higher values of α suggests the eventual breakdown of the spin-wave approximations in the presence of sufficiently short-range interactions.

4.4. Comments on the results

Analyzing non-trivial infinite-range and long-range spin models, we have found several interesting phenomena in the dynamics and steady-states of these systems.

All the systems we have analyzed share some features:

- They present dissipative phase transitions visible at the level of Lindblad dynamics. The phase transition always divides a stationary phase from a time-crystal one, characterized by persistent oscillations in the magnetization.
- When subject to continuous monitoring of collective operators (quantum jumps in Sec. 4.2, and heterodyne detection for Sec. (4.3)), they undergo measurement-induced phase transitions in the entanglement entropy. The MIPTs always occur at the same critical point of the dissipative phase transition.

I would like to stress and comment on this last point. The coincidence of the critical point of the dissipative phase transition has been shown to be a typical feature of semiclassical systems. The occurrence of the MIPT along with the dissipative phase transition has been witnessed in the previous section in the collective case, and the strong-long range regime, in which the spin-wave theory works exactly as the spin-wave density decreases with the system size.

In Ref. [31], we have shown that in these cases the thermodynamic limit $N \to \infty$ kills quantum fluctuation and the stochasticity of the equation along trajectories, yielding deterministic equations for the spin-wave's parameter β_i, u_{ij}, v_{ij} introduced in the equations before.

The deterministic equations for β_i, u_{ij}, v_{ij} of motion have some important features: they have a term simply coming from the dissipative Lindblad dynamics, they have a term coming from the continuous monitoring which is deterministic thanks to Ito's rule (e.g. $dwdw^* \propto dt$ for heterodyne detection). This implies that any non-analyticity in the dissipative part of the equations will lead to a non-analyticity also in the equations of motion of the spin-waves' parameters. This will yield, in turn, a non-analytic behaviour in the entanglement properties of the system.

Despite being related in the thermodynamic limit, one should not think that the entanglement MIPT is the same transition as the dissipative one: the Lindblad equation is blind to the measurement process, while the equations of motion for β_i, u_{ij}, v_{ij} are not (through Ito's deterministic terms).

It has indeed been proved that decreasing the range of interactions and, consequently, abandoning the possibility of having the semiclassical description, yields two distinct critical points for the dissipative and the measurement-induced phase transition [92]. This should be captured as well in the spin-wave picture for a range of interaction α greater than the dimensionality.

4.5. Conclusions to the Chapter

This chapter has discussed several issues related to the underlying complexity of measurement-induced phase transitions, both from theoretical and experimental per-

spectives.

We began by studying spin models with infinite and long-range interactions, which exhibit dissipative phase transitions in magnetization from a stationary phase to a time-crystal phase. The phase transitions we examined are both continuous and discontinuous and can show signatures of bistability. Beyond these phenomena - contained within the Lindblad framework - we revealed the presence of measurement-induced phase transitions which, despite being fundamentally different in nature, share the same critical point. The reason this occurs in infinite and strongly long-range systems has been discussed and is intimately related to the system becoming semiclassical and losing stochasticity in the thermodynamic limit.

Additionally, we demonstrated that in certain cases, these monitored transitions can enable effective post-selection properties, thereby addressing the experimental challenge of identifying such phases. Specifically, we showed that bistabilities and short-range interactions tend to inhibit efficient post-selection dynamics, requiring longer times for entanglement to spread across the system.

This study allowed us to identify the Tavis-Cummings model in the bad-cavity limit as a promising candidate platform for experimentally realizing measurement-induced phase transitions (MIPTs). Moreover, the work enabled discussion of several other experimental challenges, such as defining a quantum trajectory in practice, and led to new questions such as how to identify more experimentally accessible non-linear observables and study their saturation properties, or how to explore the concept of typicality in quantum trajectories, which could help reduce the post-selection overhead beyond simple system-size scaling.

Other promising candidates include strongly long-range interacting systems, as they exhibit fast-saturating entanglement. Studying these systems required the development of a new theory based on stochastic spin-waves to address the numerical complexity of simulating the full Hilbert space of a spin ensemble. This method not only provided insight into the monitored dynamics of such systems but also opens the way for simulating more complex systems and exploring how the distinction between MIPTs and dissipative phase transitions emerges.

5. Monitored interacting bosonic models

The previous Sections have discussed in detail some of the consequences that the stochastic nature of quantum measurements have on the experimental and numerical possibilities of studying the monitored dynamics of many-body systems. We have studied on a theoretical ground how to improve numerical simulations, and we have identified some good candidate platforms for experimental realizations of MIPTs.

The study we have carried out so far were mainly based on the numerical simulation of the dynamics along quantum trajectories, and have relied on statistical analysis of the results of such simulations. It is however, possible to use an analytical approach to study the monitored phases of many-body systems, based on the path integration technique we have already developed in both Sec.s 1.1.1 and 1.2.1.

This Chapter, deals with this type of calculation [235]. Analytical calculations in the context of many-body monitored dynamics often involve complex path integrals, which are usually evaluated through intricate approximations and methods drawn from the theory of disordered systems [94, 100, 104, 106–111, 236]. In the next pages, we aim to offer a new perspective on these matters, with a focus on the simplification both of the many-body problem and the stochastic problem raised by measurements.

More specifically, the ultimate goal of this Chapter is to offer a way to treat analytically monitored bosonic systems, starting from a simpler quadratic setting, and arriving to a more complicated one presenting interactions. In the latter case, the stochastic nature of monitored quantum dynamics adds to the well-known challenges of treating interactions in many-body systems.

For monitored Gaussian bosonic systems, as in Ref. [217], the dynamics can be described by a closed set of stochastic equations of motion. Although generally difficult to solve, the set of equations can be greatly simplified using Wick's theorem.

In contrast, interacting theories typically lead to an infinite, unclosed set of coupled stochastic equations of motion, making analytical or numerical treatment significantly harder. This computational barrier has so far prevented the development of studies of interacting bosonic models via analytical techniques, which have instead be limited to free settings or to the use of numerical tools [217, 237–239].

This motivates the work described in this Chapter, in which we focus on the well-known Sine-Gordon model[240]. To tackle the aim of analytically treating monitored interacting bosonic models, we follow the dynamics of the most likely trajectory alone, extracted from the analysis of the probability distribution of quantum trajectories. This provides a significant reduction of the complexity of the full stochastic problem by obtaining a deterministic non-Hermitian type of dynamics. Moreover, we manage the complexity arising from interactions by using a well-established approximation: the Self-Consistent Time-Dependent Harmonic Approximation (SCTDHA) [241, 242]. The SCTDHA helps incredibly by mapping the model into a quadratic self-consistent time-dependent theory.

The Chapter deals initially with the analytical description of the probability distribution of quantum trajectories, using both a stochastic formalism and a path integral one, as contained in Sec. 5.1. The key point of the Section lies in the definition and identification of the most likely trajectory, which dominates the ensemble of quantum trajectories and will be used alone to characterize the monitored dynamics of bosons. The method we introduce is then benchmarked in Sec. 5.2 for a well-known case, the free bosons CFT already studied in Ref. [217], whose results will be reproduced faithfully by our theory. Section 5.3 is finally devoted to the application of our method to the study of a very important many-body interacting model: the Sine-Gordon model. In this section, the most likely trajectory approach used in synergy with the self-consistent time-dependent harmonic approximation will allow to unveil the presence of a MIPT in the steady-state and to characterize and discuss its properties.

5.1. The most likely trajectory

The measurement setting we are going to use throughout this Section of the thesis, has already been introduced in the Introductory part of the thesis in Sec. 1.2.1: Gaussian weak measurements. For this initial part, we will focus on measurements of a general operator $\hat{R}$, supposing that it has a continuous spectrum and that its eigenvectors form a complete (or overcomplete) basis for the Hilbert space.

Let us now analyze how the dynamics builds up step-by-step and how probabilities of different measurement outcomes naturally come out of this description.

Specifically, we will now study the evolution due to a Hamiltonian evolution operator $\hat{\mathcal{U}}_{\delta t} = e^{-i\delta t\hat{H}}$, and the Gaussian weak-measurements operator $\hat{M}_r \propto e^{-\gamma\delta t(r-\hat{R})^2}$:

$$\left|\tilde{\psi}_{r_1}\right\rangle = \hat{\mathcal{U}}_{\delta t}\,\hat{M}_{r_1}\,|\psi_0\rangle\,. \tag{5.1}$$

The monitored evolution described in Eq. (5.1) is non-unitary, leading to an unnormalized state. Unnormalized states will be labeled as $\left|\tilde{\psi}\right\rangle$ or $\hat{\tilde{\rho}}$. Their trace corresponds to the probability of obtaining the measurement outcome r_1 conditioned by starting

from the initial state $|\psi_0\rangle$:

$$P(r_1|\psi_0) = \mathrm{Tr}\Big\{\Big|\tilde{\psi}_{r_1}\Big\rangle\Big\langle\tilde{\psi}_{r_1}\Big|\Big\}. \tag{5.2}$$

This allows to write the evolved physical state as $|\psi_{r_1}\rangle = \Big|\tilde{\psi}_{r_1}\Big\rangle / \sqrt{P(r_1|\psi_0)}$, and can be easily generalized to the case of a mixed state.

The continuous dynamics up to time t, is instead given by

$$\Big|\tilde{\psi}_r\Big\rangle = \lim_{\substack{\delta t\to 0\\ K=\frac{t}{\delta t}\to\infty}} \prod_{k=1}^{K} \left[\hat{\mathcal{U}}_{\delta t}\, \hat{M}_{r_k}\right] |\psi_0\rangle\,. \tag{5.3}$$

As already anticipated in Sec. 1.2.1, $\{r_k\}_{k=1}^{K} \xrightarrow{\delta t\to 0} r(t')$ $(t' \in [0,t])$ constitutes a quantum trajectory. The probability of measuring the trajectory $r(t')$ - i.e. the joint probability of the collection r given the initial state - is obtained by tracing the unnormalized fully evolved state.

$$P(\,r\,|\psi_0) = \mathrm{Tr}\Big\{\Big|\tilde{\psi}_r\Big\rangle\Big\langle\tilde{\psi}_r\Big|\Big\}. \tag{5.4}$$

This can be understood in terms of single steps' conditional probabilities, Eq. (5.2). For two time steps, we have

$$\begin{aligned} P(\{r_1,r_2\}\,|\psi_0) =& P(r_2|r_1,\psi_0)\, P(r_1|\psi_0)\\ =& \mathrm{Tr}\Big\{\hat{M}_{r_2}\,|\psi_{r_1}\rangle\,\langle\psi_{r_1}|\,\hat{M}_{r_2}\Big\}\ \mathrm{Tr}\Big\{\Big|\tilde{\psi}_{r_1}\Big\rangle\Big\langle\tilde{\psi}_{r_1}\Big|\Big\}\\ =& \mathrm{Tr}\Big\{\hat{M}_{r_2}\hat{\mathcal{U}}_{\delta t}\hat{M}_{r_1}\,|\psi_0\rangle\,\langle\psi_0|\,\hat{M}_{r_1}\hat{\mathcal{U}}_{\delta t}^{\dagger}\hat{M}_{r_2}\Big\}. \end{aligned} \tag{5.5}$$

Repeating this for $K = t/\delta t$ steps reproduces Eq. (5.4) and shows how the two objects in Eq. (5.4) and Eq. (5.2) are intimately related.

The conceptual steps made above allow one to define the conditional and joint probability distributions for quantum trajectories.

The **conditional probability distribution** for obtaining the outcome r given that the system is in the state $|\psi\rangle$, can be written as

$$P(r|\psi) = \left(\frac{2\gamma\delta t}{\pi}\right)^{1/2} \int dR\, e^{-2\gamma\delta t\,(r-R)^2} |\psi(R)|^2, \tag{5.6}$$

where $\psi(R) = \langle R|\psi\rangle$.

Having continuous monitoring allows for the expression of the **Joint probability distribution** of a string of readouts in terms of the path integral formalism [75] already introduced in Sec. 1.2.1 through Eq. (1.56). To derive it in a fully general setting, we consider both the operator $\hat{R}$ and its canonically conjugated operator. Simple examples are position measurements $\hat{R} = \hat{x}$, with the canonically conjugated $\hat{p}$ momentum as in Ref. [75], or momentum measurements $\hat{R} = \hat{p}$ with the position $\hat{x}$ being the conjugate as

we will consider throughout this paper. Then, in the $R-$representation, starting from the initial state $\hat{\rho}_0$ and taking the continuous limit $\delta t \to 0$ in equations (5.3), (5.4), we get:

$$\begin{aligned} &P[r;t] = \\ &= \int dR_0\, dR_0'\, dR\ \rho(R_0, R_0') \int_{R_1(0)=R_0}^{R_1(t)=R} \mathcal{D}R_1(t') \int_{R_2(0)=R_0'}^{R_2(t)=R} \mathcal{D}R_2(t')\, e^{iS[R_1;t]-iS[R_2;t]+S_{\text{meas}}[R_1,R_2;t]} \\ &S_{\text{meas}}[R_1,R_2;t] = -\gamma \int_0^t dt' \left[(r(t')-R_1(t'))^2 + (r(t')-R_2(t'))^2\right] \end{aligned} \tag{5.7}$$

Where $S[R_1;t]$ and $S[R_2;t]$ are the actions (in $R-$representation) given by unitary dynamics along the forward and backward Keldysh branches. The above expression simply represents the evolution of the trace of the un-normalized state along the trajectory $r(t')$, and connects directly to the path integral setting introduced in Sec. 1.2.1 through Eq. (1.56). The effect of the measurement in this framework corresponds to a coupling of the forward and backward branches through the imposition of the same trajectory $r(t')$ along the two branches. Despite the joint probability distribution explicitly depending on the initial state $\hat{\rho}_0$, we omit the explicit dependence in the label $P[r;t]$ to simplify the notation.

Now, according to Born's rule, we can compute averages of any trajectory functional $F[r]$ over this probability distribution as

$$\overline{F[r]} = \int \mathcal{D}r(t')\, P[r;t]\, F[r], \tag{5.8}$$

where the measure of the path integration over trajectories is defined as

$$\int \mathcal{D}r(t') = \lim_{\substack{\delta t\to 0 \\ K\to\infty}} \prod_{k=1}^{K} \left(\frac{2\gamma\delta t}{\pi}\right)^{1/2} \int_{-\infty}^{+\infty} dr_k. \tag{5.9}$$

In order to probe measurement-induced phase transitions from this formalism, we need to calculate non-linear objects in the system state, like variances or entanglement. These objects generally have a very complex structure in $r(t')$, consider for example the non-linear part of the variance of an operator $\hat{o}$ ($\sigma_o = \langle \hat{o}^2 \rangle_{\rho_r} - \langle \hat{o} \rangle_{\rho_r}^2$):

$$\overline{\text{Tr}\{\hat{\rho}_r\, \hat{o}\}^2} = \int \mathcal{D}r(t')\, P[r;t]\ \text{Tr}\{\hat{\rho}_r\, \hat{o}\}^2 = \int \mathcal{D}r(t')\, \frac{\text{Tr}\left\{\hat{\tilde{\rho}}_r\, \hat{o}\right\}}{P[r;t]}, \tag{5.10}$$

where we have canceled the probability coming from Born's Rule with one the the normalizations of the quadratic form in the density matrix. Notice that $\hat{\tilde{\rho}}_r$ is the unnormalized density matrix.

The complicated part of the calculation here lies in the presence of the denominator, which is generally already by itself, a complex functional of the trajectory. The tools,

which are typically introduced in this context to deal with the complications generated by the path integral over trajectories are the Replica Trick [100, 104, 108–111] and supersymmetry [107]. For instance, the Replica trick allows simplifications of Eq. (5.8) at the price of considering the dynamics of many copies of the state $\hat{\rho}_r$ sharing the same sequence of measurement outcomes.

In the following part of the Section, we will introduce a different method to reduce the complexity generated by dealing with the full ensemble of trajectories.

5.1.1. How to build the most-likely trajectory

Our idea relies on the study of the structure of the probability distribution we have introduced in the previous Section. Specifically, we aim to simplify the complexity of computing averages over the whole probability distribution by determining which trajectory dominates the distribution and characterizing the monitored dynamics in terms of that trajectory only.

We first build the most likely trajectory starting from a single time step perspective and restoring again the more general setting which measures $\hat{R}$. Suppose the system is in the state $|\psi\rangle$, the conditional probability (5.6) can be approximated as

$$P(r) \sim \left(\frac{2\gamma\delta t}{\pi}\right)^{1/2} e^{-2\gamma\delta t(r-\langle\hat{R}\rangle_\psi)^2}. \tag{5.11}$$

The conceptual step in this approximation lies in noticing that in eq. (5.6) the Gaussian $e^{-2\gamma\delta t(r-R)^2}$ will be much broader than the wavefunction's probability distribution for $\delta t \to 0$, such that [78]

$$|\psi(R)|^2 \sim \delta(R - \left\langle \hat{R} \right\rangle_\psi). \tag{5.12}$$

This means that (unimodal) wavefunctions can be approximated as delta-functions with respect to the broad Gaussian measurements operator.

From the previous approximation, we notice that the most likely measurement read-out for the time step corresponds to $r^* = \left\langle \hat{R} \right\rangle_\psi$. For Gaussian measurements this also corresponds to the average value $\overline{r} = \int dr\, r\, P(r)$.

It is now possible to build the full trajectory out of single time steps:

$$r^*(t) = \overline{r(t)} = \left\langle \hat{R} \right\rangle_{\psi^*(t)} \tag{5.13}$$

$$\text{with } |\psi^*(t)\rangle \propto \lim_{\substack{\delta t\to 0 \\ K=t/\delta t\to\infty}} \prod_{k=1}^{K-1} \left[\hat{\mathcal{U}}_{\delta t}\, \hat{M}_{r_k^*}\right] |\psi_0\rangle\,. \tag{5.14}$$

This means that the most likely trajectory is built using the step-by-step procedure:

- Select r_k^* as the most likely value of the conditional probability distribution for $|\psi^*(t'-\delta t)\rangle$;
- Impose the evolution of the state to be conditioned on the r_k^* value and update the state: $|\psi^*(t')\rangle \propto \hat{\mathcal{U}}_{\delta t}\hat{M}_{r_k^*}|\psi^*(t'-\delta t)\rangle$
- Obtain the next step by repeating the whole procedure, starting with the evolved state $|\psi^*(t')\rangle$ as new initial state;

Notice that the conditional probability distribution for r in Eq. (5.6) can be recast in the classic form of Wiener stochastic processes, as the measurement outcome can be expressed as [33, 78]

$$r = \left\langle \hat{R} \right\rangle_\psi + \frac{dW}{2\sqrt{\gamma}\delta t}, \qquad \overline{dW} = 0, \qquad dW^2 = \delta t, \tag{5.15}$$

In this framework, following the most likely trajectory means imposing

$$dW = 0 \ \ \forall t. \tag{5.16}$$

Notice that this implies $dW^2 = 0$. This differs from the standard Ito rule $dW^2 = \delta t$, which produces additional deterministic terms in the master equation.

Once the most likely trajectory is identified, we are able to study the evolution of the system conditioned to that trajectory only. The master equation to evolve the quantum state can be obtained from a linear expansion in δt of a one-step evolution equation

$$\hat{\rho}^*_{\mathbf{r}}(t+\delta t) = \frac{\hat{\mathcal{U}}_{\delta t}\,\hat{\mathcal{M}}_{\mathbf{r}^*}\,\hat{\rho}_{\mathbf{r}^*}(t)\,\hat{\mathcal{M}}_{\mathbf{r}^*}\hat{\mathcal{U}}^\dagger_{\delta t}}{\mathrm{Tr}\left\{\hat{\mathcal{M}}_{\mathbf{r}^*}\,\hat{\rho}_{\mathbf{r}^*}(t)\,\hat{\mathcal{M}}_{\mathbf{r}^*}\right\}}, \tag{5.17}$$

which yields for the measurement setting we have introduced:

$$\begin{aligned}\dot{\hat{\rho}}^*(t) \;\; = \;\; & -i\left[\hat{H},\hat{\rho}^*(t)\right] - \gamma\sum_{j=1}^{M}\left\{\hat{R}_j^2 - \left\langle\hat{R}_j^2\right\rangle_{\rho^*(t)},\hat{\rho}^*(t)\right\} \\ & +2\gamma\sum_{j=1}^{M}\left\langle\hat{R}_j\right\rangle_{\rho^*(t)}\left\{\hat{R}_j - \left\langle\hat{R}_j\right\rangle_{\rho^*(t)},\hat{\rho}^*(t)\right\}.\end{aligned} \tag{5.18}$$

where we have relabeled $\hat{\rho}_{\mathbf{r}^*}$ as $\hat{\rho}^*$ for simplicity.

Notice that the master equation we have obtained is trace preserving by construction, and is non-linear in the system's state. This last fact is what fundamentally makes the most likely trajectory (average trajectory $dW = 0$) approach different from the Lindblad (average state $\overline{\hat{\rho}}$) master equation and the state-diffusion master equation ($\overline{dW} = 0$, $dW^2 = \delta t$), which instead considers the full statistics of trajectories and loses information about the specific measurement procedure.

This equation fully captures the power of this approximation: the master equation is now deterministic and preserves information about the measurement process.

Considering the whole evolution, the procedure we have presented is also understood in terms of a Saddle Point of the joint probability distribution setting. We consider a more general setting, and suppose now to monitor *independently* a collection of operators $\hat{R}_i$ $i = 1, .., M$, i.e. our measurement operator becomes

$$\hat{\mathcal{M}}_{\mathbf{r}} = \prod_{i=1}^{M} \hat{M}_{r_i}, \tag{5.19}$$

where $\mathbf{r} = (r_1, ..., r_M)$ contains the measurement outcomes associated to the independent measurements of the set of $\{\hat{r}_i\}$. Notice that in this context i labels the ith operator and does not label time anymore.

The generalization of the joint probability distribution in Eq. (5.7) for M independent measurements is trivial and can be found in App. D.1.

From the conditional probability setting, we have noticed how the most-likely measurement outcome also corresponds to the average one, in this case $\overline{\mathbf{r}(t)} = \mathbf{r}^*(t) = \left\langle \hat{\mathbf{R}} \right\rangle_{\psi_r^*}$. Thus we start from a simple case and calculate the average trajectory according to the joint probability distribution

$$\overline{\mathbf{r}(t)} = \int \mathcal{D}\mathbf{r}(t')\, \mathbf{r}(t)\, P[\mathbf{r}; t], \tag{5.20}$$

where t is the final time of the path integral.

We introduce the fictitious action

$$\mathcal{S}[\mathbf{r}; t] = \log P[\mathbf{r}; t], \tag{5.21}$$

and we proceed via Saddle Point approximation for the integration over $r(t)$, which is Gaussian. The Saddle point equation reads:

$$\overline{r_j(t)} \sim r_j^*(t), \quad \text{with} \quad r_j^*(\tau): \left. \frac{\partial \mathcal{S}[\mathbf{r}; t]}{\partial r(\tau)} \right|_{r_j^*(\tau)} = 0. \tag{5.22}$$

As calculated explicitly in App. D.1, one finds the implicit equation for the most-probable trajectory:

$$\mathbf{r}^*(t) = \left\langle \hat{\mathbf{R}} \right\rangle_{\hat{\rho}_{\mathbf{r}^*(t)}}. \tag{5.23}$$

Notice that this result corresponds exactly to what we have found from the conditional probability distribution in Eq. (5.13). When the fictitious action $\mathcal{S}[r]$ is quadratic, usually for free theories subject to Gaussian measurements, the Saddle Point method is exact. In these cases, the most likely trajectory (coinciding with the average in this case) is a good representative trajectory of the full ensemble as it dominates it [112, 243]. Additionally, notice how the saddle point approximation we have performed highly depends on the function we are averaging over. For a general non-linear functional of

the quantum trajectory $F[r]$, the average $\overline{F[r]} = \int \mathcal{D}r(t')\, F[r]\, P[r]$ might produce a different Saddle Point trajectory. However, as long as the structure of $F[r]P[r]$ remains the same of $P[r]$ alone, which is usually the case for Gaussian theories, as we will see in the next Section, the Saddle point will remain the one we found.

This formalism allows however to go beyond the Saddle Point and consider Gaussian fluctuations around the Saddle Point solution. We report the expression for completeness:

$$\overline{\mathbf{r}(t)} \sim \int \mathcal{D}\mathbf{r}(t')\, \mathbf{r}(t)\; e^{\mathcal{S}[\mathbf{r}^*]}\; e^{\frac{1}{2}\int dt'dt''(\mathbf{r}(t')-\mathbf{r}^*(t'))\,\mathbb{S}^{(2)}\,[\mathbf{r}^*;t,t'](\mathbf{r}(t'')-\mathbf{r}^*(t''))},$$

where we have introduced

$$\mathbb{S}^{(2)}_{i,j}[\mathbf{r}^*;t',t''] = \frac{\partial^2 \mathcal{S}[r(t)]}{\partial r_j(t')\partial r_i(t'')}\bigg|_{\mathbf{r}^*} = -4\gamma\delta_{i,j}\delta(t-t') + 16\gamma^2\sigma^{++}_{R_i,R_j}(t',t''). \tag{5.24}$$

Above we have defined $\sigma^{++}_{R_iR_j}(t,t') = \left\langle R^+_j(t)R^+_i(t')\right\rangle_{\rho_{r^*}} - \left\langle R^+_j(t)\right\rangle_{\rho_{r^*}}\left\langle R^+_i(t')\right\rangle_{\rho_{r^*}}$ with $\hat{R}^+$ being the classical Keldysh component of the field, and the averages being computed for the theory along the most likely trajectory, as explained in App. D.1. Despite having a clear expression, this object remains very complicated to compute (depends on the underlying many-body theory and on the explicit time-dependent expression of the most likely trajectory), and its calculation will not be performed in this work. However its meaning is clear: the dominance of the most-likely trajectory is determined by the second derivative of the action $\mathcal{S}[\mathbf{r};t]$, which depends both on the measurement strength γ, and on two-point correlations of the operators we are measuring. As we discuss later, the general procedure for interacting non-Gaussian theories within the most-likely trajectory approach consists, thus, in approximating the joint probability distribution to be Gaussian, and then picking the trajectory that maximizes this Gaussian approximation.

5.2. A benchmark: the Free Bosons CFT

We start by benchmarking our method with a free theory, which can be exactly solved analytically. We consider a Free Bosons model, already studied in Ref. [217]. In his lattice version, the Hamiltonian reads for N sites:

$$\hat{H}_{\text{FB}} = \frac{\omega}{2}\sum_{j=1}^{N}\left(\hat{p}_j^2 + (\hat{x}_{j+1}-\hat{x}_j)^2 + r_N^2\,\hat{x}_j^2\right), \tag{5.25}$$

with $r_N^2 = \Omega/N/\omega$ being a cutoff to normalize the spectrum at zero momentum and $[\hat{x}_j, \hat{p}_{j'}] = i\delta_{j,j'}$. We consider periodic boundary conditions. The Hamiltonian essentially describes a massless model for free bosons and is represented in Fig. 5.1(a).

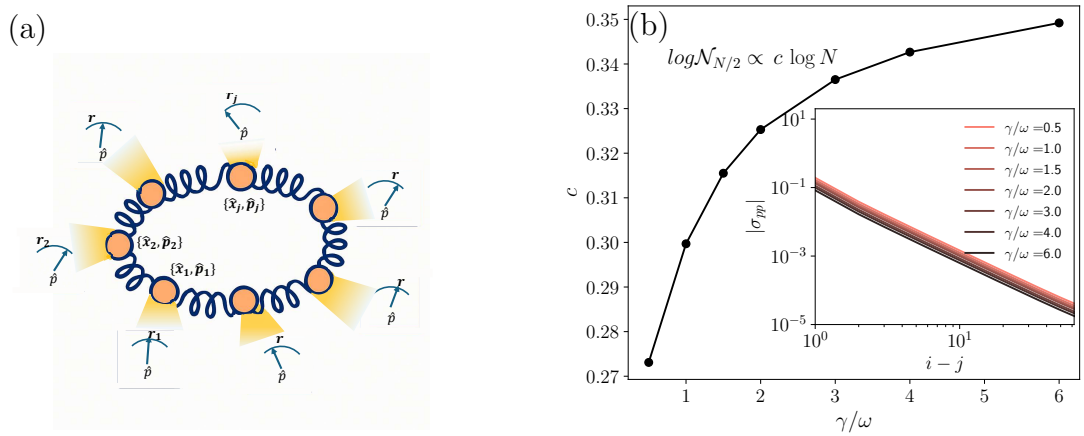

Figure 5.1.: (a) Representation for the Free Bosons CFT for $N = 7$. The picture shows a chain of harmonic oscillators in periodic boundary conditions. Each oscillator, represented with a red sphere, has its momentum $\hat{p}_i$ measured independently at each time step from distinct measurement devices. (b) Logarithmic Negativity for the Free Bosons CFT lattice model, the plot shows the coefficient for the fit $\log \mathcal{N}_{N/2} \sim c \log N$, which is always non-zero in this case. Inset: power-law decaying correlations in log-log scale.

We consider weak momentum measurements occurring independently at each site, implemented through the operator

$$\hat{\mathcal{M}}_{\mathbf{r}} = \prod_{i=1}^{N} \hat{M}_{r_i} = \prod_{i=1}^{N} \left(\frac{2\gamma\delta t}{\pi}\right)^{1/4} e^{-\gamma\,\delta t(r_i - \hat{p}_i)^2}. \tag{5.26}$$

Ref. [217] predicts for this specific setting a trajectory-averaged power-law decaying σ_{pp} correlations along with a bipartite logarithmic negativity scaling as $\log \mathcal{N} \sim \log N$ for all measurement strengths γ, and hence the absence of a measurement-induced phase transition. The exact stochastic and trajectory-averaged equations to evolve averages and connected correlations can be found in Appendix D.2. An important feature to keep in mind is that this exact approach yields, at the level of trajectories, stochastic equations for the averages $\langle \hat{x}_j \rangle, \langle \hat{p}_j \rangle$ and deterministic equations for the correlations. This characteristic is peculiar to free bosonic systems. We can now try to reproduce the trajectory-averaged results with our method. The master equation to evolve the many-body state along the most-likely trajectory is obtained by in inserting the Free Bosons Hamiltonian (5.25) into the master equation derived in Eq. (5.18).

$$\begin{aligned}\dot{\hat{\rho}}^*(t) &= -i\left[\hat{H}_{\mathrm{FB}}, \hat{\rho}^*(t)\right] - \gamma \sum_{j=1}^{N} \left\{\hat{p}_j^2 - \langle \hat{p}_j^2 \rangle_{\rho^*(t)}, \hat{\rho}^*(t)\right\} \\ &\quad + 2\gamma \sum_{j=1}^{N} \langle \hat{p}_j \rangle_{\rho^*(t)} \left\{\hat{p}_j - \langle \hat{p}_j \rangle_{\rho^*(t)}, \hat{\rho}^*(t)\right\}. \end{aligned} \tag{5.27}$$

Exploiting the Gaussianity through Wick theorem, we can derive the deterministic

Heisenberg equations to determine the evolution of averages and correlations:

$$\partial_t \langle \hat{x}_i \rangle = \omega \langle \hat{p}_i \rangle \tag{5.28a}$$
$$\partial_t \langle p_i \rangle = -2\omega \langle \hat{x}_i \rangle + \omega \left(\langle \hat{x}_{i+1} \rangle + \langle \hat{x}_{i-1} \rangle \right) \tag{5.28b}$$
$$\partial_t \sigma_{xx}^{i,j} = \omega \left(\sigma_{xp} + \sigma_{px} \right)^{ij} - 4\gamma (\sigma_{xp} \sigma_{xp}^T)^{ij} + \gamma \delta_{ij} \tag{5.28c}$$
$$\partial_t \sigma_{pp}^{i,j} = \omega \left[-(1 + \frac{r_N^2}{2}) \sigma_{xp}^{i,j} + (\sigma_{xp}^{i-1,j} + \sigma_{xp}^{i+1,j}) + (i \leftrightarrow j) \right] - 4\gamma (\sigma_{pp}^2)^{ij} \tag{5.28d}$$
$$\partial_t \sigma_{xp}^{i,j} = \omega (\sigma_{pp}^{i,j} - (2 + r_N^2) \sigma_{xx}^{i,j} + \sigma_{xx}^{i,j-1} + \sigma_{xx}^{i,j+1}) - 2\gamma ((\sigma_{xp} + \sigma_{px}) \sigma_{pp})^{ij} \tag{5.28e}$$

As can be checked by comparing these equations with Appendix D.2 reporting the exact results, the evolution along the most-likely trajectory for a free bosonic system is the same as the exact trajectory-averaged equations. In particular, Eq.s (5.28a), (5.28b) reproduce exactly the trajectory average of the stochastic equations found by [217], and Eq.s (5.28c)- (5.28e) reproduce exactly the deterministic equations found in the same Reference. This fact is strikingly important: the most likely trajectory fully encodes the properties of the trajectory-averaged monitored dynamics of free bosonic systems for what concerns variances. Eq.s (5.28c)- (5.28e) contain information about the full stochastic process (characterized by the average $\overline{dW} = 0$ and fluctuations dW^2), while our equations contain information about the average/most-likely value only. Yet the equations for the variances are the same and produce exactly the same steady-state values.

Trivially, our equations also reproduce the exact steady-state predictions of Ref. [217], proving again the absence of a measurement-induced phase transition. To show this, we study the scaling of σ_{pp} correlations and the logarithmic negativity of the steady state of the system in Fig. 5.1(b). The latter object quantifies the quantum correlations between bipartitions of the system and is defined as

$$\log \mathcal{N}_{N/2} = \log \left\{ \mathrm{Tr} \left\{ \rho_{\mathrm{SS}}^{T_{N/2}} \right\} \right\}, \tag{5.29}$$

where $\rho_{\mathrm{SS}}^{T_{N/2}}$ is the partial transpose of a bipartition of the many-body density matrix in the steady-state. The peculiarity of a Gaussian system is that the logarithmic negativity can be expressed directly in terms of $\hat{x}_j$ and $\hat{p}_j$ correlations [244–246], as reported in Appendix D.2.

These calculations show that our method is exact for free bosonic theories. Having a quadratic theory, makes the joint probability distribution $P[\mathbf{r}; t]$ quadratic in $\mathbf{r}$ in turn. This means that the Saddle Point over the fictitious trajectory action $\mathcal{S}[\mathbf{r}; t]$ is exact, allowing the correct identification of the dominant trajectory in the ensemble.

It should also be noticed that bosonic Gaussian theories can rely on another useful property. The calculation we have performed in this section essentially can be summed up in

$$\overline{F_k[\mathbf{r}(t)]} = \int \mathcal{D}\, \mathbf{r}(t')\, F_k[\mathbf{r}(t)]\, P[\mathbf{r}; t] \sim F_k[\mathbf{r}^*(t)],$$

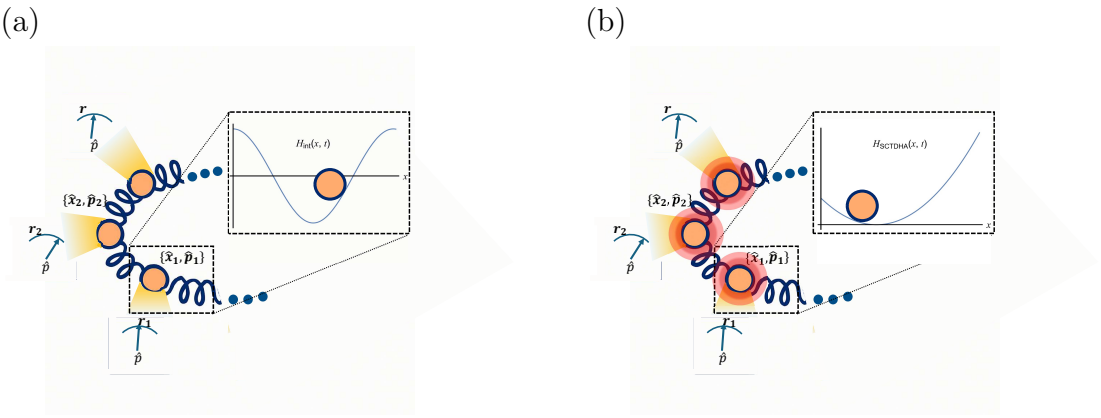

Figure 5.2.: (a) Truncated representation for the Sine-Gordon model. The picture shows a chain of harmonic oscillators in periodic boundary conditions. Each oscillator, represented with a red sphere, is subject independently to a cosine potential, displayed in the zoomed window, and has its momentum $\hat{p}_i$ measured at each time step from distinct measurement devices. (b) Truncated representation for the Sine-Gordon model in the SCTDHA. The picture shows a chain of 'dressed' harmonic oscillators in periodic boundary conditions. Each oscillator, represented with a red sphere, has its own time-dependent effective mass (the shade in the picture) and has its momentum $\hat{p}_i$ measured at each time step from distinct measurement devices. The theory is quadratic again, as showed in the zoomed window.

with $k = 1, 2$ and $F_1[\mathbf{r}] = \left\langle \hat{R} \right\rangle_{\hat{\rho}^*}$, $F_2[\mathbf{r}] = \left\langle \hat{R} \right\rangle^2_{\hat{\rho}^*}$. For free theories the structures in $\mathbf{r}$ generated by the products $F_1[r(t)]P[\mathbf{r};t]$ and $F_2[r(t)]P[\mathbf{r};t]$ is always the same as in Eq. 5.22. Thus, the (exact) saddle Point which determines the most probable trajectory is also a saddle point for $F_1[r(t)]P[\mathbf{r};t]$ and $F_2[r(t)]P[\mathbf{r};t]$, demonstrating the exactness for free theories.

5.3. The monitored Sine-Gordon Model

To explore the applicability of the most likely trajectory approach, we study the monitored dynamics of an interacting model content by adding a Sine-Gordon potential [240, 247] to the free Gaussian model in the previous Section. Specifically

$$\begin{aligned} \hat{H} &= \hat{H}_{\mathrm{FB}} + \hat{H}_{\mathrm{int}}, \\ \hat{H}_{\mathrm{int}} &= -\frac{J}{\alpha^2} \sum_{j=1}^{N} \cos\left(\alpha \hat{x}_j\right), \end{aligned} \tag{5.30}$$

with $\hat{H}_{\mathrm{FB}}$ given in Eq. (5.25). We monitor the model through weak measurements of the momentum operator at each site, described again by the operator from Eq. (5.26). A representation of the model is presented in Fig. 5.2(a).

A few comments are in order before analyzing the properties of the model.

- In the $\alpha \to \infty$ we obtain again the Free Bosons CFT model of Ref. [217]. In this limit, we know the most-likely trajectory approach to be exact as the model is free.
- For finite α, the interaction Hamiltonian tends to localize the jth oscillator in one of the wells of the cosine potential. Momentum $\hat{p}_j$ measurements tend to delocalize in contrast, as shown in the Free Bosons model. We expect these two effects to compete and eventually lead to a measurement-induced phase transition.

The master equation generating the system's evolution can be directly obtained from Eq. (5.27) adding the interaction Hamiltonian from Eq. (5.30). As trivial for an interacting theory, the Heisenberg equations for $\hat{x}_i$ and $\hat{p}_i$ include all the moments of each operators due to the commutator with $\hat{H}_{\text{int}}$. The equations cannot be closed anymore at the level of second-order cumulants as in the case of a free theory.

This issue is unrelated to the monitoring and, among the various approximations developed to address it, we use the Self-Consistent-Time-Dependent Harmonic Approximation (SCTDHA). The SCTDHA is particularly suited to our case since it self-consistently reduces the theory to a Gaussian one, where monitoring can be accounted for exactly as in the previous Section. Specifically, the SCTDHA approximates self-consistently the evolution generated by the interaction term with a quadratic time-dependent one, i.e.

$$\hat{\mathcal{U}}_t = e^{-i(\hat{H}_{\text{FB}}+\hat{H}_{\text{int}})t} \sim e^{-i\hat{H}_{\text{FB}}\,t - i\int_0^t dt'\,\hat{\tilde{H}}_{\text{int}}(t')}. \tag{5.31}$$

The method is commonly used in the framework of the Sine-Gordon model and has been tested both at equilibrium [241] and out-of-equilibrium in the setting of quantum quenches [242].

The time-dependent approximation of the interaction Hamiltonian is

$$\begin{aligned}
\hat{\tilde{H}}_{\text{int}}(t) &= \sum_{j=1}^{N} \left(f_j(t) \;+\; g_j(t)\,\hat{x}_j + h_j(t)\,\hat{x}_j^2 \right) \\
g_j(t) &= \frac{J}{\alpha} e^{-\frac{\alpha^2}{2}\sigma_{xx}^{j,j}(t)} \left(\sin\!\left(\alpha \left\langle \hat{x}_j \right\rangle_t\right) - \alpha \left\langle \hat{x}_j \right\rangle_t \cos\!\left(\alpha \left\langle \hat{x}_j \right\rangle_t\right) \right) \\
h_j(t) &= \frac{J}{2} e^{-\frac{\alpha^2}{2}\sigma_{xx}^{j,j}(t)} \cos\!\left(\alpha \left\langle \hat{x}_j \right\rangle_t\right)
\end{aligned} \tag{5.32}$$

where $\langle \bullet \rangle_t$ and $\sigma_{xx}^{jj}(t)$ are the average and variance of the $\hat{x}_j$ operator calculated over the state at time t. The term $\sum_j f_j(t)$ doesn't affect the dynamics of the system, and for this reason, it does not need to be specified.

A detailed calculation about the derivation of the approximated interaction Hamiltonian for our specific model can be found in Appendix D.3. We report in this section the conceptual steps used at each time step to derive the SCTDHA:

1. A shift of the operators:

$$\hat{\xi}_j = \hat{x}_j - \left\langle \hat{x}_j \right\rangle_t, \;\text{ with }\; \left\langle \xi_j \right\rangle_t = 0.$$

2. A second-order expansion of the interaction Hamiltonian:

$$\tilde{\hat{H}}'_{\text{int}} \sim \sum_{j=1}^{N} \left(\mathcal{C}_j(t) + \hat{\mathcal{V}}_j(t)\hat{\xi}_j + \hat{\mathcal{M}}_j(t)\hat{\xi}_j^2 \right)$$

3. A Hartree factorization $\hat{\mathcal{V}}_j \to \left\langle \hat{\mathcal{V}}_j \right\rangle_t$, $\hat{\mathcal{M}}_j \to \left\langle \hat{\mathcal{M}}_j \right\rangle_t$.

The expression of the coefficients $\left\langle \hat{\mathcal{V}}_j \right\rangle$ and $\left\langle \hat{\mathcal{M}}_j \right\rangle$, along with the procedure to recast them into Eq. (5.32) can be found in App. (D.3).

An important consequence of this approximation is that it incorporates the interaction effects in the time dependence of the parameters f_j, g_j, h_j while making, at each time step, the Hamiltonian fully quadratic. We are now describing a quadratic model of bosons having an effective time-dependent mass $h_j(t)$ and a time-dependent drive $g_j(t)$. We can visualize it as in Fig. 5.2(b). This quadratic effective description of the Sine Gordon model enables the closure of the Heisenberg equations at the level of variances of $\hat{x}_j$ and $\hat{p}_j$ operators, as we can use Wick theorem to decouple higher moments. We stress that this approximation goes beyond a simple quadratic expansion of the interaction Hamiltonian $\hat{H}_{\text{int}} \sim J/\alpha^2 - J\hat{x}_j^2/2$ as, at each time step, the SCTDHA finds the best quadratic approximation of the exact Hamiltonian, taking into account the correlation structure of the state at each time.

Before starting the analysis of the dynamical and steady-state properties of the Sine-Gordon model through the lens of the most-likely trajectory approach, we analyze the equation of motions coming from quantum state diffusion to describe the model in the SCTDHA. This will immediately highlight the power of the most-likely trajectory approach in solving interacting systems.

From quantum state diffusion, we obtain:

$$d\langle x_i \rangle (dW) = dt\, \omega \langle p_i \rangle + 2\sqrt{\gamma} \sum_{j=1}^{N} dW_j\, \sigma_{xp}^{ji} \tag{5.33a}$$

$$\begin{aligned} d\langle p_i \rangle (dW) = dt \Big[-g_i(t;dW) - 2\Big(\omega + h_i(t;dW)\Big) \langle x_i \rangle + \omega \Big(\langle x_{i+1} \rangle + \langle x_{i-1} \rangle \Big) \Big] + \\ + 2\sqrt{\gamma} \sum_{j=1}^{N} dW_j\, \sigma_{pp}^{ji} \end{aligned} \tag{5.33b}$$

$$\partial_t \sigma_{xx}^{i,j}(dW) = \omega \left(\sigma_{xp} + \sigma_{px}\right)^{ij} - 4\gamma (\sigma_{xp}\sigma_{xp}^T)^{ij} + \gamma \delta_{ij} \tag{5.33c}$$

$$\begin{aligned} \partial_t \sigma_{pp}^{i,j}(dW) = -\omega(2 + r_N^2)\sigma_{xp}^{i,j} + \Big[\omega(\sigma_{xp}^{i-1,j} + \sigma_{xp}^{i+1,j}) - 2\sigma_{xp}^{i,j}\, h_j(t;dW) + (i \leftrightarrow j) \Big] + \\ - 4\gamma(\sigma_{pp}^2)^{ij} \end{aligned} \tag{5.33d}$$

$$\begin{aligned} \partial_t \sigma_{xp}^{i,j}(dW) = \omega(\sigma_{pp}^{i,j} - (2 + r_N^2)\sigma_{xx}^{i,j} + \sigma_{xx}^{i,j-1} + \sigma_{xx}^{i,j+1}) - 2\, h_j(t;dW)\sigma_{xx}^{i,j} + \\ - 2\gamma((\sigma_{xp} + \sigma_{px})\sigma_{pp})^{ij} \end{aligned} \tag{5.33e}$$

The key point lies in the stochasticity of $\langle \hat{x}_i \rangle$. The parameters h_i and g_i of the SCTDHA depend crucially on $\langle \hat{x}_i \rangle$ itself, which makes the effective mass and the external drive stochastic in turn. Since the correlations $\boldsymbol{\sigma}_{xx}$, $\boldsymbol{\sigma}_{xp}$, $\boldsymbol{\sigma}_{pp}$ depend again on the parameters of the SCTDHA, we are obtaining stochastic correlations.

This is a highly relevant aspect of the model we are presenting. We are working with an interacting model through the SCTDHA lenses: while the Hamiltonian $\tilde{H}_{\text{int}}$ is formally Gaussian, the self-consistent equations determining the parameters of the quadratic version of the interaction keep information about the interaction. This manifests in the monitored dynamics by yielding stochastic equations along trajectories for the correlations, as characteristic of interacting systems, and in sharp contrast to the free bosons CFT model.

Having stochastic correlations is thus a result of both the complexities of the monitored problem and the interacting many-body problem. The most important consequence of this fact is that now the set of equations (5.33), despite being close, is now impossible to solve analytically and requires a full numerical study of the model considering the whole body of trajectories.

The complexity of the problem is significantly reduced by the most-likely trajectory approach, as we will see in the next paragraphs.

5.3.1. Dynamics

We will now use the master equation of the SCTDHA in the most-likely trajectory setting, adding the transformed interaction Hamiltonian $\hat{H}_{\text{int}} \to \tilde{\hat{H}}_{\text{int}}$ to Eq. (5.27).

Before proceeding, note the differences between the Free Bosons CFT case and the Sine-Gordon model in the SCTDHA. Despite being both quadratic theories, the Sine Gordon model presents additional time-dependent terms in the Hamiltonian: the j^{tth} oscillator experiences a drive $g_j(t)$ and an effective mass given by $h_j(t)$. Both terms break the scale invariance, which characterizes the free boson CFT model, and this hints at a possible breaking of the logarithmic Negativity scaling as $\log N$ discussed in [217]. Notice that, coherently with what observed for the exact sine Gordon model (5.30), the limit $\alpha \to \infty$ in Eq. (D.3) suppresses the effective mass and drive, resulting again in the Free Boson CFT model.

From the master equation, we can derive the equations of motion for along the most-likely trajectory for $\langle \hat{x}_i \rangle_t$, $\langle \hat{p}_i \rangle_t$, $\sigma^{i,j}_{xp}(t)$, $\sigma^{i,j}_{xx}(t)$, $\sigma^{i,j}_{pp}(t)$, which in the context of the SCTDHA again fully characterize the system's many-body state. From now on, we

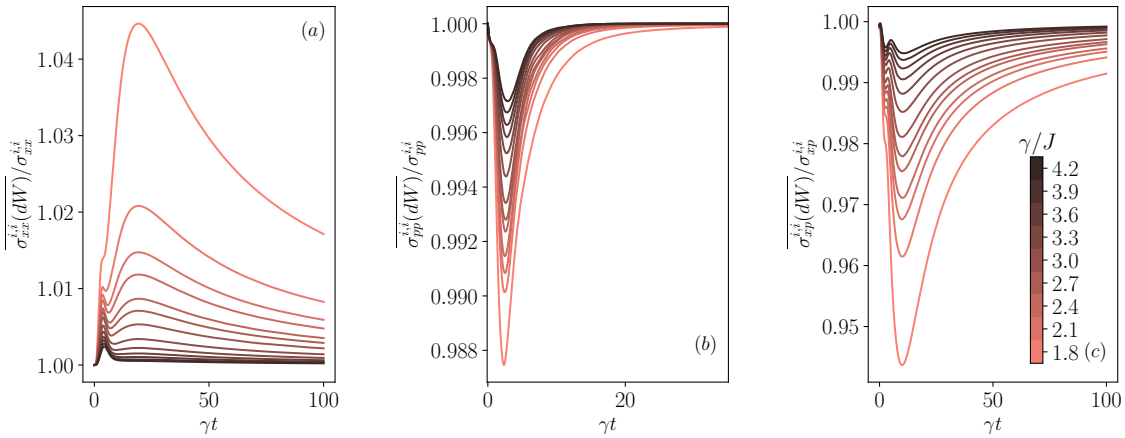

Figure 5.3.: Ratio between trajectory averaged results obtained from quantum state diffusion and 1000 trajectories, and the results along the most-likely trajectory for (a) $\sigma^{i,i}_{xx}$, (b) $\sigma^{i,i}_{pp}$, (c) $\sigma^{i,i}_{xp}$. The parameters for the plot are $N = 7$, $\omega/J = 1/2$, $\alpha = 2.1$. The legend is shared between the panels.

will omit the time-dependence of these objects for simplicity.

$$\partial_t \langle \hat{x}_i \rangle = \omega \langle \hat{p}_i \rangle \tag{5.34a}$$

$$\partial_t \langle \hat{p}_i \rangle = -g_i(t) - 2(\omega + h_i(t)) \langle \hat{x}_i \rangle + \omega \left(\langle \hat{x}_{i+1} \rangle + \langle \hat{x}_{i-1} \rangle \right) \tag{5.34b}$$

$$\partial_t \sigma^{i,j}_{xx} = \omega \left(\sigma_{xp} + \sigma_{px} \right)^{ij} - 4\gamma (\sigma_{xp} \sigma^T_{xp})^{ij} + \gamma \delta_{ij} \tag{5.34c}$$

$$\partial_t \sigma^{i,j}_{pp} = \left[-\omega(2 + r_N^2)\sigma^{i,j}_{xp} + \omega(\sigma^{i-1,j}_{xp} + \sigma^{i+1,j}_{xp}) - 2\sigma^{i,j}_{xp} h_j(t) + (i \leftrightarrow j) \right] - 4\gamma(\sigma^2_{pp})^{ij} \tag{5.34d}$$

$$\partial_t \sigma^{i,j}_{xp} = \omega(\sigma^{i,j}_{pp} - (2 + r_N^2)\sigma^{i,j}_{xx} + \sigma^{i,j-1}_{xx} + \sigma^{i,j+1}_{xx}) - 2h_j(t)\, \sigma^{i,j}_{xx} - 2\gamma((\sigma_{xp} + \sigma_{px})\sigma_{pp})^{ij} \tag{5.34e}$$

Despite the deterministic equations being *formally* the same as (5.33), there is a fundamental difference as $\langle \hat{x}_i \rangle$ is now deterministic. This makes the effective mass $h_i(t)$ and drive $g_i(t)$ along with all the correlations $\boldsymbol{\sigma}_{xx}$, $\boldsymbol{\sigma}_{xp}$, $\boldsymbol{\sigma}_{pp}$ deterministic in turn.

This makes the closed set of equations exactly solvable analytically, and here lies the power of our approach.

However, it should be noticed that in contrast with the free case, equations (5.34) do not correspond to the averaged stochastic equations (5.33), since we now have a more complex structure in the stochastic equations as

$$\overline{\sigma^{i,j}_{ab} h_i(t; dW)} \neq \sigma^{ij}_{a,b} h_i(t; 0), \text{ with } a, b = x \text{ or } p. \tag{5.35}$$

Nonetheless, the most likely trajectory approximation remains reliable, as can be checked in Fig. 5.3, which represents the comparison between trajectory-averaged correlations and correlations along the most-likely trajectory during time evolution. From

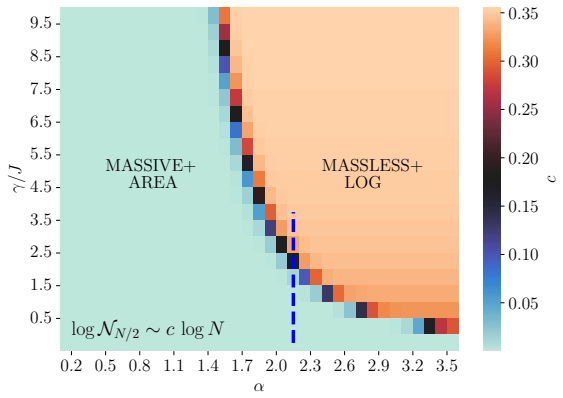

Figure 5.4.: Phase diagram of the model: the color code is given by the fitting parameter c such that $\log \mathcal{N} \sim c \log N$ for $\omega/J = 1/2$. The plot shows the phase transition between the area-law massive region and the log-law massless region, which reproduces the Free Bosons CFT results. The dashed line corresponds to the values of γ/J and α/J used in Figs. 5.3 and 5.5. The plot is obtained for $\omega/J = 1/2$.

these plots, it is clear that the most likely trajectory approach describes with great accuracy the steady-state of our system within the SCTDHA.

5.3.2. Steady state properties

We will now use most likely trajectory approach within the SCTDHA to discuss the properties of the steady state of the Sine Gordon model. We highlight once more the power of the most-likely trajectory approach by noticing that it allows to determine the steady state analytically from Eq.s (5.34c)- (5.34e) for any system size, in sharp contrast with the stochastic state diffusion approach which would require (i) the generation of a full ensemble of trajectories, (ii) the evolution of the correlation matrix from $t = 0$ to the steady-state for each trajectory, (iii) averaging over all the trajectory evolutions and studying the steady state properties.

The steady-state equations for determining the correlations can be obtained through a Fourier transform exploiting translation invariance. To simplify the equations we set, without loss of generality, the initial state to have $\langle \hat{x}_j \rangle = \langle \hat{p}_j \rangle = 0 \forall j$.

$$\sigma^q_{xp} = \sigma_{xp} = \frac{\omega - \sqrt{\omega^2 + 4\gamma^2}}{4\gamma} \tag{5.36}$$

$$\sigma^q_{pp} = \sqrt{-\frac{\omega}{2\gamma}\sigma_{xp}}\sqrt{4\sin\left(\frac{q}{2}\right)^2 + r_N^2 + \frac{J}{\omega}e^{-\frac{\alpha^2}{2}S_x}} \tag{5.37}$$

$$\sigma^q_{xx} = \sqrt{-\frac{\omega}{2\gamma}\sigma_{xp}}(1 - \frac{4\gamma}{\omega}\sigma_{xp})\frac{1}{\sqrt{4\sin\left(\frac{q}{2}\right)^2 + r_N^2 + \frac{J}{\omega}e^{-\frac{\alpha^2}{2}S_x}}} \tag{5.38}$$

$$S_x = \frac{1}{N}\sum_q \sigma^q_{xx} \sim \sqrt{-\frac{\omega}{2\gamma}\sigma_{xp}}(1 - \frac{4\gamma}{\omega}\sigma_{xp})\frac{4}{\pi}\frac{1}{\sqrt{r_N^2 + \frac{J}{\omega}e^{-\frac{\alpha^2}{2}S_x} + 4}}\cdot \tag{5.39}$$
$$\cdot \mathrm{K}(\frac{4}{4 + r_N^2 + \frac{J}{\omega}e^{-\frac{\alpha^2}{2}S_x}}),$$

where the last equation is needed for self-consistency, and $\mathrm{K}(\bullet)$ is the complete elliptic integral of the first kind. In particular, S_x defines the steady-state value of the effective mass:

$$h_j = h = \frac{J}{2}e^{-\frac{\alpha^2}{2}S_x}. \tag{5.40}$$

The study of the results of the steady-state equations gives rise to the phase diagram in Fig. 5.4.

The phase diagram shows the presence of two regions: a massive, area-law phase found for α/J and γ/J small, and a massless, log-law phase found in the opposite regime.

The mass properties are obtained from the analysis of the effective mass from the SCTDHA, h_j, while the entanglement properties are obtained from the analysis of the half-chain logarithmic negativity.

Analyzing the phase diagram at fixed α, for instance by setting the value indicated by the blue dashed line in Fig. 5.4, one can notice interesting properties of the model. Consistent with the localization-delocalization picture proposed at the beginning, we notice that at fixed α, the massive region is found for low γ/J. This indicates that the Sine-Gordon potential wins the competition with the weak measurements and confines the jth oscillator in one of the wells of the cosine. This is expressed by the finite mass of the SCTDHA as the h coefficient is related to the second-order expansion at the bottom of the wells of the cosine. In contrast, for higher values of γ/J, the stronger measurements do not allow the oscillator to localize in a well of the Sine-Gordon potential, resulting in $h = 0$ as localization is not possible anymore.

The massive-massless transition, which is how the SCTDHA interprets the delocalization process arising from momentum measurements, is signaled not only by changes in the value of the effective mass h, but also by the transition between exponentially decaying to power-law decaying momentum-momentum correlations, and also by the

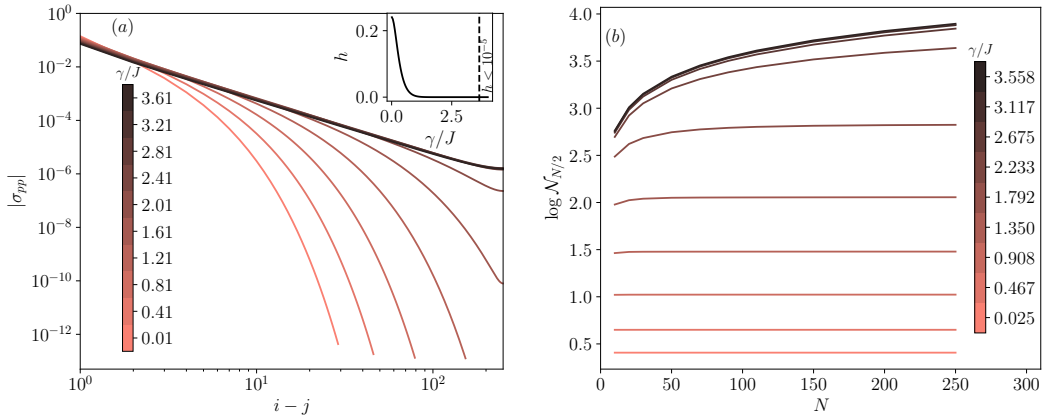

Figure 5.5.: Some steady-state properties for the Sine-Gordon model with $\omega/J = 1/2$. (a) Momentum-momentum correlations in the main plot and effective mass in the inset for $N = 500$ and fixed $\alpha = 2.1$. The plot is in log-log scale, showing that when the model is massless ($\gamma/J \gtrsim 2.64$), correlations decrease polynomially, in contrast with lines corresponding to a massive model, which decrease exponentially. Inset: behaviour of the effective mass vs γ/J for $\alpha = 2.1$. The vertical dashed line signals $\gamma/J \gtrsim 2.64$, beyond this line $h < 10^{-5}$. (b) Logarithmic Negativity for fixed $\alpha = 2.1$ and $\omega/J = 1/2$ for several measurement strengths, showing the change from area law to log law by increasing the measurement strength.

transition between area law and log-law scalings in the logarithmic negativity. This is shown in Fig. 5.5, representing for $\alpha = 2.1$ (corresponding to the dashed line in Fig. 5.4) both the momentum-momentum correlation properties, panel (a), and entanglement properties, panel (b).

Some comments are in order. The results we obtain for $\alpha \gg 1$ are consistent with the Free Bosons CFT's results predicted in Ref. [217]. We obtain, as expected, a massless theory with power-law decaying correlations and a logarithmic entanglement.

Moreover, the phase diagram in Fig. 5.4 shows only a finite set of γ/J values. Increasing them one does not find a saturation value for the critical value of α (α_C) which signals the transitions, as the steady state equations indicate an increasing shrinking of the massive phase with $\alpha_C \to 0$. Thus, projective measurement would inevitably lead to a total delocalization of the bosons, yielding a massless phase only.

The most-likely trajectory approach within the SCTDHA is thus predicting some striking results for the Sine-Gordon Model: for fixed α, measurements are tuning a transition from a massive, localized, area-law region to a massless, delocalized, logarithmic region comprising the Free Bosons CFT behaviour. The competition between the Sine-Gordon potential and the momentum measurements is, as anticipated, driving a non-trivial change in the behaviour of the system.

5.4. Conclusions to the Chapter

In this Chapter, we have developed a new method to address the monitored dynamics of many-body bosonic systems. The method is based on the concept of the most likely trajectory, demonstrating how the trajectory that dominates the joint probability distribution of quantum trajectories can effectively describe the full monitored dynamics alone. We have benchmarked our method with free boson CFT, exactly reproducing the results obtained in Ref. [217]. The strong performance of our method in free theories has motivated us to explore its application in interacting systems, which were previously inaccessible analytically because of the complications emerging from interactions and the stochastic nature of the measurement process. Specifically, combining our most likely trajectory method with the Self-Consistent Time-Dependent Harmonic Approximation of the Sine-Gordon model has allowed us to close the equations of motion at the level of second moments, and to study the simple dynamics along a single trajectory. This has enabled us to identify deterministically the steady state of the monitored dynamics and to reliably identify a measurement-induced phase transition in the logarithmic negativity, signaling a change from an area-law to a logarithmic scaling of entanglement.

Our approach has thus proven capable not only of exactly recovering known results in free theories but also of revealing new phenomena emerging in interacting systems that were previously inaccessible.

The strength of the method lies in its ability to produce deterministic equations of motion that are possible to solve analytically, significantly simplifying the study of monitored quantum systems. While we have applied this approach to bosonic systems, it would be important to test its applicability in models of a different nature, such as fermionic or spin systems. In particular, we expect promising results for semiclassical spin systems, which can often be effectively bosonized.

It would be interesting as well to connect our method to other well-known types of non-Hermitian deterministic master equations, such as the no-click limit.

To conclude, we observe that the deterministic theory along the most likely trajectory of the monitored Sine-Gordon model has been benchmarked against the exact stochastic one within the SCTDHA approximation, showing very good agreement. However, a further check is still necessary: the SCTDHA alone should be tested and compared with the exact theory at the level of Lindblad dynamics of the Sine-Gordon model. This aspect goes beyond the results currently available in the literature, where the SCTDHA for the Sine-Gordon model has always been considered for closed systems (or quenches). Since the current work is still in preparation, this complementary check remains preliminary and will be incorporated into the final work at a later time.

6. Conclusions

Open quantum many-body systems exhibit a wide variety of behaviors shaped by the interplay of interactions, dissipation, and continuous measurements. We have seen many examples of this throughout the Thesis, where the same language, the theory of many-body open quantum systems, has been able to describe very different and intricate phenomena such as quantum synchronization, time-crystal phases, and measurement-induced phase transitions.

Through the lens of dissipative systems, we have studied the dynamics and steady-state properties of various systems. A path-integral formalism has allowed us to characterize the onset of synchronization in a quantum many-body setting governed by complex non-Markovian dynamics. A more master-equation-based study, centered on the Markovian Lindblad equation, has instead revealed the emergence of time-crystal phases in spin chains and cavity-QED setups. Despite their diverse nature, all these models share the important feature of exhibiting time-ordering phenomena arising from dissipation. These systems inherit peculiar characteristics from their interaction with the environment, leading to unique dynamical structures and to dissipative phase transitions with an ordering that is difficult to achieve in isolated, closed systems. These concepts and results are central to the Thesis, as they demonstrate the power of many-body open quantum systems: the frameworks we have presented not only capture real-life phenomena and experimental conditions, but also enable to witness the emergence of new phases of matter. These phases, while fundamentally interesting from a theoretical perspective, also present potential for practical application: specifically, in our case, both time crystallinity and synchronization can represent building blocks for quantum metrology and sensing [248–253].

Time-ordered phenomena such as quantum synchronization and time-crystals emerging from dissipative phase transitions, although deeply insightful, do not fully capture the potential of open quantum systems. They can all be studied through Lindblad equations (in the Markovian case) or Feynman-Vernon techniques (in the general non-Markovian case). Thus, in terms of quantum trajectories, they rely only on ensemble-averaged properties.

In this Thesis, we have taken a step further by studying how continuously measuring a system and keeping track of properties beyond the ensemble average can unveil new and fascinating features. By investigating the same systems as before, i.e. cavity models, spin chains, and bosonic models, we have demonstrated how measurements

can reveal the aforementioned dissipative phase transitions at the level of average system states, and also uncover measurement-induced phase transitions in entanglement entropy, made visible by considering higher-order moments of the system's state.

This brings us to another key concept of the Thesis: continuously monitoring a many-body system can produce dissipative dynamics and phase transitions when we are concerned with averaged observables and do no care bout specific measurement outcomes, but can also give rise to an entirely different class of transitions, measurement-induced phase transitions, which emerge from the measurement process itself and appear in nonlinear quantities of the system's state.

This has enabled us to reveal the presence of several MIPTs across different systems studied in the Thesis. The characterization of these phases was conducted with particular attention to the complexity introduced by the stochastic nature of quantum measurements, which impacts all perspectives from which one can study MIPTs: analytical, numerical, and experimental. This led to several significant results, including the identification of experimentally accessible platforms for observing MIPTs, the development of a new spin-wave-based technique for analyzing stochastic quantum trajectories, and the proposal of a deterministic method, based on the concept of the most-likely trajectory, to solve relevant equations analytically, thereby exposing the emergence of MIPTs.

Taken together, these results provide a coherent and multifaceted perspective on open quantum many-body systems. The methods and concepts applied across both the dissipative and monitored points of view are deeply intertwined, reinforcing each other and giving rise to broader questions.

While specific outlooks have been discussed in each section of the Thesis, we observe that some concepts touched upon in this work remain open and leave space for further exploration. On one hand, we have addressed the concept of non-Markovianity in the context of the Kuramoto model, but the concept has not been expanded or studied in detail. Non-Markovianity should be explored more thoroughly in the context of open many-body quantum systems, as it can arise in many interesting scenarios, such as multimode or strong couplings in cavity settings [254–257], and in systems subject to feedback [258, 259]. Feedback mechanisms could be particularly relevant, especially in the framework of monitoring quantum circuits, as they can be implemented to modify the evolution according to specific measurement outcomes [184, 186, 193]. Another topic that has recurrently appeared throughout the Thesis, starting from the Kuramoto picture and ranging to the tools used to study the monitored dynamics through path integrals, is disorder. Its interplay with both measurements [97, 104] and dissipative dynamics in general deserves further investigation, particularly in the context of frustration settings.

To conclude, we highlight that the synthesis of these two perspectives, dissipative and measurement-driven, points toward a deeper understanding of dissipation and

monitoring in many-body quantum systems, advancing our ability to control, exploit, and fundamentally comprehend the quantum world.

A. Appendix to Chapter 1

A.1. Keldysh field theory for Caldeira-Leggett's bath

This appendix explore in a more detailed way some important tools of Keldysh field theory thorugh the derivation of the influence functional for the Caldeira and Leggett's bath model.

We will use the same Hamiltonians and initial thermal initial states as already introduced in Sec. (1.1.1).

The start point is the expression for the jth influence functional, related to the jth bath of the collection of harmonic oscillators defining the bath.

$$\Phi_j[x_1, x_2] = \int dX_0^j \, dX_0'^j \, dX^j \; \mathcal{F}(X^j, X^j, t; X_0^j, X_0'^j, 0) \tag{A.1}$$

with the already defined functional

$$\mathcal{F}(X^j, X^j, t; X_0^j, X_0'^j, 0) = \int_{X^j{}_1(0)=X^j{}_0}^{X^j{}_1(t)=X^j} \mathcal{D}X_1^j \int_{X^j{}_2(0)=X^j{}_0'}^{X^j{}_2(t)=X^j} \mathcal{D}X_2^j \, \rho_B^{(j)}(X_0^j, X_0'^j) \tag{A.2}$$
$$\exp\left\{ i \int_0^t dt \left(\frac{M(\dot{X}_1^j - \dot{X}_2^j)}{2} - \frac{1}{2} M\Omega_j^2 (X_1^{j^2} - X_2^{j^2}) - C\left(x_1 X_1^j - x_2 X_2^j\right) \right) \right\}$$

Let us now sketch the path integral calculation. It is useful to perform a Keldysh rotation and introduce the classical and quantum fields [58]

$$X_{cl}^j = \frac{X_1^j + X_2^j}{2}, \qquad X_q^j = X_1^j - X_2^j. \tag{A.3}$$

.

The meaning of this rotation can be understood by focusing for one moment on the bath's action, discarding just for now the interaction with the system.

$$S_B[X_{\text{cl}}^j, X_{\text{q}}^j] = \int_0^t dt' \left[M\dot{X}_{cl}^j \dot{X}_q^j - M\Omega_j^2 X_{cl}^j X_q^j \right] \sim - \int_0^t dt' X_{\text{q}}^j \left[M\ddot{X}_{cl}^j + M\Omega_j^2 X_{cl}^j \right].$$

The functional integration of this action over the quantum field would lead to a delta function of the argument of the square brackets. This yields the classical equations of motion for the classical field, explaining the meaning of its name: $\ddot{X}_{\text{cl}}^j + \Omega_j^2 \, X_{\text{cl}} = 0$.

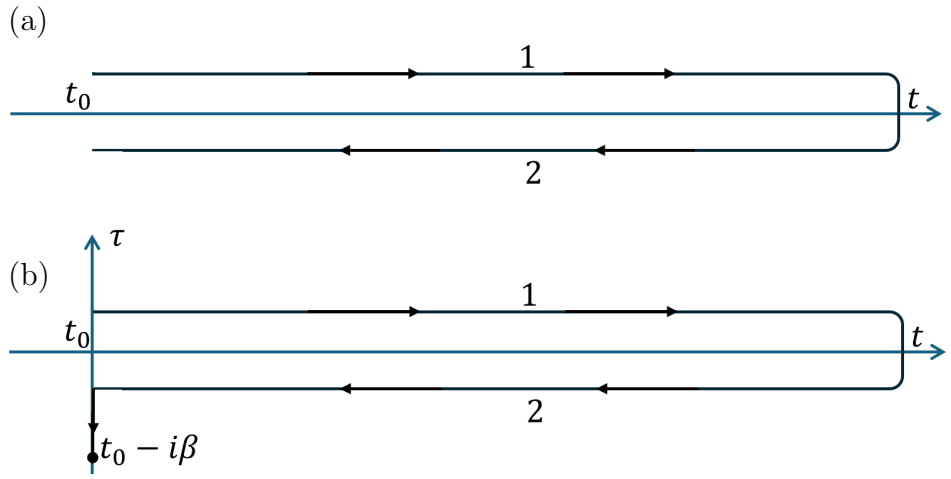

Figure A.1.: (a) Representation of the standard Keldysh contour with the forward (1) and backward (2) branches from t_0 to t. (b) Modification of the Keldysh contour to imaginary time to insert the thermal state along the imaginary axis. The added path goes from t_0 to $t_0 - i\beta$

Keeping in mind the meaning of these fields, we can proceed with the full calculation, involving also the interaction term. In terms of these new fields, the path integral for the Caldeira-Leggett influence functional reads

$$\mathcal{F}(X^j, X^j, t; X_0^j, X_0'^j, 0) = \int_{X^j{}_{cl}(0)=(X^j{}_0+X_0^{j\prime})/2}^{X^j{}_{cl}(t)=X^j} \mathcal{D}X_{cl}^j \int_{X^j{}_q(0)=X^j{}_0'-X_0^{j\prime}}^{X^j{}_q(t)=X^j} \mathcal{D}X_q^j \, \rho_B^{(j)}(X_0^j, X_0'^j) \quad \text{(A.4)}$$
$$\exp\left\{ i \int_0^t dt \left(M\dot{X}_{cl}^j \dot{X}_q^j - M\Omega_j^2 X_{cl}^j X_q^j - C(x_1 - x_2) X_{cl}^j - \frac{C}{2}(x_1 + x_2) X_q^j \right) \right\}$$

Some steps are now required to easily perform the calculation. First of all, let us extend the time integration from $t_0 = -\infty$ to $t = \infty$. Then we use the following procedures

1. The action is time-local, and can be simplified by rewriting through a Fourier transform $X_{\mathrm{q,cl}}(t) = \frac{1}{2\pi} \int d\omega \, e^{-i\omega t} \, X_{\mathrm{q,cl}}(\omega)$. For example the kinetic term becomes $\int dt' \, dt'' X_{\mathrm{q}} \, \delta''(t' - t'') \, X_{\mathrm{cl}} \to \int d\omega \, \omega^2 \, X_{\mathrm{q}}(\omega) X_{\mathrm{cl}}(-\omega))$

2. The thermal initial state (1.15) can be rewritten using a path integral formalism and incorporated into an Euclidean action
$\rho_{\mathrm{B},0}(X_0^j, X_0'^j) = \int_{\tilde{X}^j(0)=X_0^j}^{\tilde{X}^j(\tau)=X_0'^j} \mathcal{D}\tilde{X} \, \exp\left\{ - \int_0^\beta d\tau \left(M\dot{\tilde{X}}_j^2 + M\Omega_j^2 \, \tilde{X}_j^2 \right) \right\}$,
where τ is an imaginary time. Labeling the Euclidean action as $S_E[\tilde{X}]$, this corresponds to adding an imaginary leg to the Keldysh contour, as can be seen in Fig. A.1. What we are doing is thus defining a cumulative action $S_{\mathrm{B}}[X_1, X_2] + iS_{\mathrm{E}}[\tilde{X}]$ over this modified complex contour.

We now have a fully Gaussian path integral on the modified Keldysh contour. The

integration simply gives, in a matrix form

$$\Phi[x_1,x_2]=\prod_{j=1}^{N_{\rm B}} e^{\frac{iC^2}{2}\int\frac{d\omega}{2\pi}\begin{pmatrix}x_1(\omega)-x_2(\omega) & \frac{x_1(\omega)+x_2(\omega)}{2}\end{pmatrix}\mathbb{G}^j(\omega)\begin{pmatrix}x_1(-\omega)-x_2(-\omega)\\ \frac{x_1(-\omega)+x_2(-\omega)}{2}\end{pmatrix}}, \quad \text{(A.5)}$$

where we have introduced the matrix $\mathbb{G}(\omega)$ which contains the Green's function for j^{th} harmonic oscillators at temperature $T=1/\beta$. The general structure of this matrix for a scalar field is

$$\mathbb{G}(\omega)=\begin{pmatrix}G_K(\omega) & G_R(\omega)\\ G_A(\omega) & 0\end{pmatrix}=-i\begin{pmatrix}\left\langle X^j_{cl}(\omega)X^j_{cl}(-\omega)\right\rangle & \left\langle X^j_{cl}(\omega)X^j_{q}(-\omega)\right\rangle\\ \left\langle X^j_{q}(\omega)X^j_{cl}(-\omega)\right\rangle & 0\end{pmatrix}, \quad \text{(A.6)}$$

with the averages being defined as

$$\langle X_a(t_1)X_b(t_2)\rangle\sim\int\mathcal{D}X^j_{\rm cl}\int\mathcal{D}X^j_{\rm q}\int\mathcal{D}\tilde{X}^j\,e^{S_B[X^j_{\rm cl},X^j_{\rm q}]+iS_E[\tilde{X}^j]}\,X_a(t_1)\,X_b(t_2)$$

and $a,b=\mathrm{cl/q}$.

Notice that the matrix contains the three types of Green's functions of Keldysh field theory: the **retarded** $G_R(\omega)$ and **advanced** $G_A(\omega)$ Green's function, related to the quantum-classical correlations; the Keldysh Green's function related to the classical-classical correlations [56–59].

With the initial state being the equilibrium state at temperature T, the Green's functions have the specific forms:

$$G^j_{R/A}(\omega)=\frac{1}{M\left((\omega\pm i\epsilon)^2-\Omega_j^2\right)} \quad \text{(A.7)}$$

$$G^j_K(\omega)=\coth\frac{\omega}{2T}\left[G^j_R(\omega)-G^j_A(\omega)\right]. \quad \text{(A.8)}$$

The expression linking the Keldysh Green's function to the retarded and advanced ones holds only for equilibrium cases (having the same Euclidean action as these cases) and does not hold in general for non-equilibrium settings. The ϵ regularization is needed in order to ensure causality for the retarded green's function or anti-causality for the advanced one ($G_{R/A}(t)\propto\theta(\pm t)$).

With this calculation, we have derived the specific form of the influence functional for Caldeira and Leggett's bath, shedding some light on the results shown in Chaps. 1.1.1, as well as on the Keldysh calculations performed both in Chaps. 3 and 5.

B. Appendix to Chapter 3

B.1. Path integral formulation for the classical stochastic process

The average value over disorder of the observable $e^{i\theta(t;\omega,\xi)}$ must encode the fact that the phase θ satisfies the Langevin equation (3.4). With a path integral formalism and discretizing a la Ito, it gives:

$$\left\langle e^{i\theta(t;\omega;\xi)}\right\rangle_\xi = \mathcal{N}\int_0^{2\pi} d\theta \int_{-\infty}^{\infty} dv \int \mathcal{D}\xi \int_{\theta(0)=\theta_0}^{\theta(t)=\theta} \mathcal{D}\theta \int_{v(0)=v_0}^{v(t)=v} \mathcal{D}v \tag{B.1}$$
$$\exp\left\{-\frac{1}{4D}\int_0^t dt'\xi^2(t') + i\theta(t)\right\}\delta(\dot\theta_\tau - v_\tau)\,\delta\big(m\dot v_\tau + m\gamma v_\tau - F[\theta_\tau;\omega,\psi] + \xi_\tau\big)\,.$$

The second delta function, enforcing the Langevin dynamics, can be represented in exponential form through the use of an auxiliary field $\eta(\tau)$:

$$\delta\big(m\dot v_\tau + m\gamma v_\tau - F[\theta_\tau;\omega,\psi] + \xi_\tau)\big) \propto \int \mathcal{D}\eta\, \exp\left\{i\int_0^t dt'\eta(t')\xi(t')\right\} \tag{B.2}$$
$$\exp\left\{i\int_0^t dt'\eta(t')\left[m\dot v(t') + m\gamma v(t') - F[\theta(t');\omega,\psi(t')]\right]\right\}\,.$$

Notice that choosing this representation of the delta function, we now have a Gaussian path integral over the noise variable $\xi(t)$ with both quadratic and linear term. This integration generates another Gaussian form in the auxiliary variable η:

$$\left\langle e^{i\theta(t;\omega;\xi)}\right\rangle_\xi = \mathcal{N}\int_0^{2\pi} d\theta e^{i\theta}\int_{-\infty}^{\infty} dv \int \mathcal{D}\eta \int_{\theta(0)=\theta_0}^{\theta(t)=\theta} \mathcal{D}\theta \int_{v(0)=v_0}^{v(t)=v} \mathcal{D}v\,\delta(\dot\theta(\tau) - v(\tau)) \tag{B.3}$$
$$\exp\left\{-D\int_0^t dt'\eta^2(t')\right\}\exp\left\{i\int_0^t dt'\eta(t')\Big(m\dot v(t') + m\gamma v(t') - F[\theta(t');\omega,\psi(t')]\Big)\right\}\,.$$

It is straightforward to see that the Gaussian integration over the auxiliary field η yields:

$$\left\langle e^{i\theta(t;\omega;\xi)}\right\rangle_\xi = \mathcal{N}\int_0^{2\pi} d\theta\, e^{i\theta}\int_{-\infty}^{\infty} dv \int_{\theta(0)=\theta_0}^{\theta(t)=\theta} \mathcal{D}\theta \int_{v(0)=v_0}^{v(t)=v} \mathcal{D}v\,\delta(\dot\theta(\tau) - v(\tau)) \tag{B.4}$$
$$\exp\left\{-\frac{1}{4D}\int_0^t dt'\Big(m\dot v(t') + m\gamma v(t') - F[\theta(t');\omega,\psi(t')]\Big)^2\right\}\,.$$

The previous expression describes the average value of the observable $e^{i\theta(t;\omega,\xi)}$ for a stochastic process in the form of Eq. (3.4). It is also convenient to write down the same average value for the same stochastic process in the massless limit. Keeping in mind that the only constraint is now satisfying the Langevin equation $\dot{\theta} = F[\theta;\omega,\psi] + \xi(t)$, one can follow the previous steps and write:

$$\left\langle e^{i\theta(t;\omega;\xi)} \right\rangle_{\xi} = \mathcal{N} \int_0^{2\pi} d\theta\, e^{i\theta} \int_{\theta(0)=\theta_0}^{\theta(t)=\theta} \mathcal{D}\theta \exp\left\{ -\frac{1}{4D} \int_0^t dt' \Big(\dot{\theta}(t') - F[\theta(t');\omega,\psi(t')] \Big)^2 \right\} \tag{B.5}$$

B.2. First order expansion of the self-consistent equation

The expansion to first order of the self-consistent equations along with the *Ansatz* $\varphi(t) = 0$ and $r \sim 0$ constant, yields

$$\begin{aligned} r = -\frac{iJ_C r}{\hbar} \lim_{t\to\infty} \int_{-\infty}^{\infty} d\omega\, g(\omega) \int_{-\infty}^{\infty} d\theta_{\rm cl}\, e^{i\theta_{\rm cl}} \int_{-\infty}^{\infty} d\theta'_{\rm cl,q} \int_{\theta_{\rm cl}(0)=\theta'_{\rm cl}}^{\theta_{\rm cl}(t)=\theta_{\rm cl}} \mathcal{D}\theta_{\rm cl} \int_{\theta_{\rm q}(0)=\theta'_{\rm q}}^{\theta_{\rm q}(t)=0} \mathcal{D}\theta_{\rm q} \\ \int_0^t ds \left(\cos\left(\theta_{\rm cl}(s) - \frac{\theta_{\rm q}(s)}{2} \right) - \cos\left(\theta_{\rm cl}(s) + \frac{\theta_{\rm q}(s)}{2} \right) \right) \\ \exp\left\{ \frac{i}{\hbar} \int_0^t dt' \left(m\dot{\theta}_{\rm q}\dot{\theta}_{\rm cl} - m\gamma\theta_{\rm q}\dot{\theta}_{\rm cl} + \omega\theta_{\rm q} \right) \right\} \\ \exp\left\{ -\frac{D}{\hbar^2} \int_0^t dt' dt'' \theta_{\rm q}(t') K(t'-t'') \theta_{\rm q}(t'') \right\} \rho(\theta'_{\rm cl}, \theta'_{\rm q}) \,. \end{aligned} \tag{B.6}$$

Rewriting the trigonometric term in exponential form, one gets straightforwardly

$$\begin{aligned} r = -\frac{iJ_C r}{2\hbar} \lim_{t\to\infty} \int_{-\infty}^{\infty} d\omega\, g(\omega) \int_{-\infty}^{\infty} d\theta_{\rm cl}\, e^{i\theta_{\rm cl}} \int_{-\infty}^{\infty} d\theta'_{\rm cl,q} \int_{\theta_{\rm cl}(0)=\theta'_{\rm cl}}^{\theta_{\rm cl}(t)=\theta_{\rm cl}} \mathcal{D}\theta_{\rm cl} \int_{\theta_{\rm q}(0)=\theta'_{\rm q}}^{\theta_{\rm q}(t)=0} \mathcal{D}\theta_{\rm q} \\ \int_0^t ds \sum_{c,c'=\pm} c' \exp\left\{ ic\theta_{\rm cl}(s) - \frac{icc'}{2}\theta_{\rm q}(s) \right\} \\ \exp\left\{ \frac{i}{\hbar} \int_0^t dt' \left(m\,\dot{\theta}_{\rm q}\dot{\theta}_{\rm cl} - m\gamma\,\theta_{\rm q}\dot{\theta}_{\rm cl} + \omega\theta_{\rm q} \right) \right\} \\ \exp\left\{ -\frac{D}{\hbar^2} \int_0^t dt' dt'' \theta_{\rm q}(t') K(t'-t'') \theta_{\rm q}(t'') \right\} \rho(\theta'_{\rm cl}, \theta'_{\rm q}) \,. \end{aligned} \tag{B.7}$$

Denoting the argument of the exponential as $S'_{\rm eff}[\theta_{\rm cl}, \theta_{\rm q}]$ and regarding it as a new effective action, one finally gets Eq. (3.31).

The path integration that now should be calculated is simply Gaussian. Decomposing the new effective action (3.31) in its real and imaginary part $S'_{\rm eff} = S'_{Re}[\theta_{\rm cl}, \theta_{\rm q}] + iS'_{Im}[\theta_{\rm q}]$, one can easily get the result of the path integration. The real part of the effective action contains quadratic and linear terms in both fields $\theta_{\rm cl}$ and $\theta_{\rm q}$. The imaginary

part contains only a quadratic term in $\theta_{\rm q}$. Notice that there are not quadratic terms just in the field $\theta_{\rm cl}$.

The strategy is now to find the saddle point of S'_{Re}, i.e. to find $\tilde{\theta}_{\rm cl}(t')$ and $\tilde{\theta}_{\rm q}(t')$ such that the first derivative in both fields is zero, respecting the boundary conditions $\tilde{\theta}_{\rm cl,q}(t) = \theta_{\rm cl,q}(t)$ and $\tilde{\theta}_{\rm cl,q}(0) = \theta_{\rm cl,q}(0)$.

Then, the following change of variables should be performed: $\theta_{\rm cl,q}(t') = \tilde{\theta}_{\rm cl,q}(t') + \delta\theta_{\rm cl,q}(t')$, with $\delta\theta_{\rm cl,q}(0) = \delta\theta_{\rm cl,q}(t) = 0$. The path integration will be now performed over the fields $\delta\theta_{\rm cl}(\tau)$ and $\delta\theta_{\rm q}(\tau)$. After having performed the change of variables, it is convenient to rewrite the action in matrix form:

$$\begin{aligned} & S'_{\rm eff}[\delta\theta_{\rm cl}, \delta\theta_{\rm q}; s, t]_{c,c'} = S'_{\rm eff}[\tilde{\theta}_{\rm cl}, \tilde{\theta}_{\rm q}; s, t]_{c,c'} + \qquad \text{(B.8)} \\ = \; & \frac{1}{2}\int_0^t dt'dt'' \begin{pmatrix} \delta\theta_{\rm cl}(t') & \delta\theta_{\rm q}(t') \end{pmatrix} \mathbf{A}(t'-t'') \begin{pmatrix} \delta\theta_{\rm cl}(t'') \\ \delta\theta_{\rm q}(t'') \end{pmatrix} + \int_0^t dt' \mathbf{B}(t')^T \begin{pmatrix} \delta\theta_{\rm cl}(t') \\ \delta\theta_{\rm q}(t') \end{pmatrix} \end{aligned}$$

with

$$\begin{aligned} \mathbf{A}(t'-t'') &= \begin{pmatrix} 0 & -m\delta''(t'-t'') + m\gamma\delta'(t'-t'') \\ -m\delta''(t''-t') - m\delta'(t''-t') & \frac{2iD}{\hbar}K(t'-t'') \end{pmatrix}, \\ \mathbf{B}(t') &= \frac{iD}{\hbar}\begin{pmatrix} 0 \\ \int_0^t dt'' \left(K(t'-t'') + K(t''-t')\tilde{\theta}_{\rm q}(t'') \right). \end{pmatrix} \end{aligned}$$

A is the matrix that contains the coefficients of the quadratic terms in the fields $\tilde{\theta}_{\rm q}$, and B contains the coefficients of the linear terms. Notice that the first entry of both A and B is zero, since there aren't quadratic and linear terms in the fields $\delta\theta_{\rm cl}$ only.

The Gaussian path integration over the variables $\delta\theta_{\rm cl,q}$ yields just the factor $\mathcal{N}(t) = \frac{m\gamma}{2\pi\hbar(1-e^{-\gamma t})}$.Thus:

$$\begin{aligned} \rho'(\theta_{\rm cl}, 0, t) &= \frac{-i}{2\hbar}\sum_{c,c'=\pm 1} c' \int_0^t ds \int_{-\infty}^{\infty} d\theta'_{\rm cl} \int_{-\infty}^{\infty} d\theta'_{\rm q}\, \mathcal{N}(t)\, \exp\left\{ \frac{i}{\hbar} S'_{\rm eff}[\tilde{\theta}_{\rm cl}, \tilde{\theta}_{\rm q}; s, t]_{c,c'} \right\} \\ & \exp\left\{ -\frac{1}{4}\int_0^t dt'dt'' B(t')^T A^{-1}(t'-t'')B(t'') \right\}. \qquad \text{(B.9)} \end{aligned}$$

Since the inverse of the matrix A has the form $A^{-1} = \begin{pmatrix} a & b \\ c & 0 \end{pmatrix}$, the matrix product appearing above gives $B^T A^{-1} B = 0$ and does not contribute to the result of the path integration.

Thus, the last issue we are left with is finding the solutions to the saddle point equations:

$$\begin{aligned} \left.\frac{\partial S'_{Re}}{\partial \theta_{\rm cl}}\right|_{\tilde{\theta}_{\rm cl,q}} &= \ddot{\tilde{\theta}}_-(t') - \gamma\dot{\tilde{\theta}}_-(t') - \frac{\hbar c}{m}\delta(t'-s) = 0 \qquad \text{(B.10)} \\ \left.\frac{\partial S'_{Re}}{\partial \theta_{\rm q}}\right|_{\tilde{\theta}_{\rm cl,q}} &= \ddot{\tilde{\theta}}_+(t') + \gamma\dot{\tilde{\theta}}_+(t') - \frac{\omega}{m} + \frac{\hbar cc'}{2m}\delta(t'-s) = 0 \end{aligned}$$

The solutions to these equations have jump discontinuities in the derivatives; the jump is proportional to $\frac{\hbar}{m\gamma}$, thus it gets smaller in the overdamped limit. In the massless limit, the discontinuities appear directly in the solutions (not just in the derivatives). The solutions to the saddle point equations can be found in appendix B.3.

Substituting the solutions (B.11),(B.12), in the first order approximation of the self-consistent equation, one gets in the infinite time limit

B.3. Solutions to the saddle point equations

The solutions to the saddle point equations (B.10) that respects the boundary conditions $\tilde{\theta}_{\pm}(0) = \theta'_{\pm}$, $\tilde{\theta}_{\mathrm{q}}(t) = 0$, $\tilde{\theta}_{\mathrm{cl}}(t) = \theta_{\mathrm{cl}}$ are:

$$\tilde{\theta}_{\mathrm{q}}(t') = \begin{cases} \theta'_{\mathrm{q}} + \frac{\left(e^{\gamma t'}-1\right)\left(-\theta'_{\mathrm{q}}+\frac{\hbar c e^{\gamma s}-\hbar c-\gamma m\theta'_{\mathrm{q}}e^{\gamma s}}{\gamma m\left(e^{\gamma t}-1\right)}-\frac{e^{\gamma t-\gamma s}\left(\hbar c e^{\gamma s}-\hbar c-\gamma m\theta'_{\mathrm{q}}e^{\gamma s}+\right)}{\gamma m\left(e^{\gamma t}-1\right)}\right)}{e^{\gamma s}-1} & \text{if } 0 \le t' \le s \\ \frac{e^{-\gamma s}\left(e^{\gamma t'}-e^{\gamma t}\right)\left(c\hbar e^{\gamma s}-c\hbar-\gamma m\theta'_{\mathrm{q}}e^{\gamma s}+\right)}{\gamma m\left(e^{\gamma t}-1\right)} & \text{if } s < t' \le t \end{cases} \tag{B.11}$$

$$\tilde{\theta}_{\mathrm{cl}}(t') = \begin{cases} -\frac{\left(e^{-\gamma t'}-1\right)\left(\frac{e^{\gamma t}\left(e^{-\gamma s}-e^{-\gamma t}\right)\left(-c\hbar c' e^{\gamma s}+c\hbar c'-2\gamma m\theta'_{+}+2\gamma\theta_{+}m-2t\omega\right)}{2\gamma m\left(e^{\gamma t}-1\right)}+\theta'_{+}-\theta_{+}+\frac{t\omega}{\gamma m}\right)}{e^{-\gamma s}-1}+\theta'_{+}+\frac{\omega t'}{\gamma m} & \text{if } 0 \le t' < s \\ -\frac{e^{\gamma t}\left(e^{-\gamma t'}-e^{-\gamma t}\right)\left(-c\hbar c' e^{\gamma s}+c\hbar c'-2\gamma m\theta'_{+}+2\gamma\theta_{+}m-2t\omega\right)}{2\gamma m\left(e^{\gamma t}-1\right)}+\theta_{+}+\frac{\omega t'}{\gamma m}-\frac{t\omega}{\gamma m} & \text{if } s \le t' \le t \end{cases} \tag{B.12}$$

It is interesting to notice that in the massless limit ($\frac{m\gamma}{\hbar}$ =cost, $\gamma \to \infty$), the expressions of the saddle point equations get easier but discontinuities appear:

$$\lim_{\substack{\gamma\to\infty \\ m\gamma/\hbar=\mathrm{cost}}} \tilde{\theta}_{\mathrm{q}}(t') = \begin{cases} \theta'_{\mathrm{q}} & 0 \le t' < s \\ \theta'_{\mathrm{q}} - c\frac{\hbar}{m\gamma} & s < t' < t \\ 0 & t' = t \end{cases} \tag{B.13}$$

$$\lim_{\substack{\gamma\to\infty \\ m\gamma/\hbar=\mathrm{cost}}} \tilde{\theta}_{\mathrm{cl}}(t') = \begin{cases} \theta'_{\mathrm{cl}} & t' = 0 \\ \theta_{\mathrm{cl}} + cc'\frac{\hbar}{2m\gamma} + \frac{\omega(t'-t)}{m\gamma} & 0 < t' < s \\ \theta_{\mathrm{cl}} + \frac{\omega(t'-t)}{m\gamma} & s \le t' \le t \end{cases} \tag{B.14}$$

C. Appendix to chapter 4

C.1. Saturation time

The saturation time τ corresponds to the time needed to reach the steady state value for the operator $\hat{o}(t)$. We are interested in particular in the saturation time of the magnetization and the entanglement entropy. In general, since the average value of the magnetization is linear in the density matrix ($\langle \hat{m}(t) \rangle = \mathrm{Tr}\{\hat{m}\hat{\rho}(t)\}$), the saturation time of the magnetization τ_m corresponds to the real part of the longest-lived eigenvalue of the Liouvillian. This procedure can be performed only for very small system sizes, thus we obtained τ_m numerically. Also the saturation time of the entanglement entropy τ_S has been obtained numerically due to its less trivial dependence on the density matrix.

We obtained the saturation time for the magnetization τ_m and the entanglement entropy τ_S from the data shown in Figs. 4.2, and 4.4. The procedure requires smoothing out the oscillations of the time traces of $\langle \hat{o}(t) \rangle$ with a Gaussian filter and fitting the smoothed curves with an exponential decay $F_{\mathrm{fit}}(t) = ae^{-t/b} + c$ [47]. In many cases, to obtain a better fit, it has been necessary to fit the function $|\langle \hat{o}(t) \rangle - o_{\mathrm{SS}}|$ with o_{SS} being the steady state value of the observable. The choice of fitting with a decaying exponential is due to the knowledge of the evolution of the density matrix:

$$|\rho(t)\rangle\!\rangle = e^{\mathcal{L}t} |\rho(0)\rangle\!\rangle = \sum_{\mu=0}^{\dim \mathcal{H}^2 - 1} \langle\!\langle l_\mu | \rho(0) \rangle\!\rangle \, e^{\lambda_\mu t} \, |r_\mu\rangle\!\rangle \, . \tag{C.1}$$

An estimate of the saturation time can be obtained from the b parameter of the fit.

An example of the procedure is shown in Fig. C.1 for the magnetization $\tilde{m}_z$ in the upper part of the phase diagram. The plot is obtained for $\Omega/\kappa = \lambda/\kappa = 0.8$ and shows the original curves (opaque solid lines), the smoothed-out curves (solid lines), and the exponential fit (dashed lines).

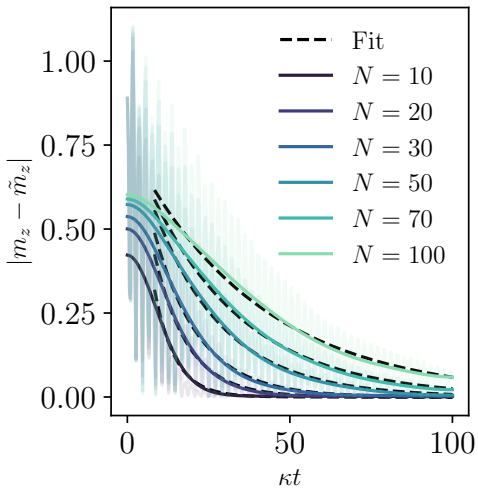

Figure C.1.: Smoothing of the magnetization curves for $\lambda/\kappa = 0.8$ and $\Omega/\kappa = 0.8$ for different sizes, and their exponential fit (dashed lines). The opaque solid lines correspond to the original oscillating function.

D. Appendix to chapter 5

D.1. Saddle-Point procedure for Measurements Path Integrals

In this Appendix, we present how to perform a Saddle-Point approximation over the joint probability distribution for quantum Gaussian measurements, highlighting the power of the path integrals approach to quantum measurements.

Consider the following setting (without loss of generality): we study the monitored evolution of a many-body system on an N sites lattice, with Hamiltonian $\hat{H}$ (leading to the action S), subject to momentum measurements on each site. We will thus use the measurement operator in Eq. (5.26).

Introducing the N-component fields classical and quantum Keldysh fields $\mathbf{p}_+(t') = (p_{+,1}(t'), ..., p_{+,N}(t'))$, $\mathbf{p}_+(t') = (p_{+,1}(t'), ..., p_{+,N}(t'))$ with $p_{+,i} = \frac{p_{1,i}+p_{2,i}}{2}, p_{-,i} = p_{1,i} - p_{2,i}$, the average trajectory can be calculated in momentum representation as

$$\overline{r_j(t)} = \int \mathcal{D}\mathbf{r}(t')\, r_j(t)\, e^{\mathcal{S}[\mathbf{r};t]} \tag{D.1}$$

$$\begin{aligned}\mathcal{S}[\mathbf{r};t] &= \log(P[\mathbf{r};t]) \\ &= \log\Bigg(\int d\mathbf{p}_0\, d\mathbf{p}'_0\, \mathbf{d}p\, \rho(\mathbf{p}_0 + \frac{\mathbf{p}'_0}{2}, \mathbf{p}_0 - \frac{\mathbf{p}'_0}{2}) \int_{\mathbf{p}_0}^{\mathbf{p}} \mathcal{D}\mathbf{p}_+(t') \int_{\mathbf{p}'_0}^{0} \mathcal{D}\mathbf{p}_-(t') \cdot \\ &\quad \cdot e^{iS[p_+,p_-] - \gamma \sum_{j=1}^{N} \int_0^t dt' \left[2(r_j(t') - p_{+,j}(t'))^2 + \frac{1}{4} p_{-,j}(t')^2\right]}\Bigg)\end{aligned} \tag{D.2}$$

The jth Saddle Point trajectory can be found by solving the equation

$$\left.\frac{\partial \mathcal{S}[\mathbf{r};t]}{\partial r_j(\tau)}\right|_{r_j^*(\tau)} = 0 \Rightarrow \quad \frac{-4\gamma}{P[\mathbf{r}^*;t]} \left(r_j^*(\tau)\, P[\mathbf{r}^*;t] - \langle p_{+,j}(\tau)\rangle_{\tilde{\hat{\rho}}_{r^*}}\right) = 0 \tag{D.3}$$

where $\tilde{\hat{\rho}}_{\mathbf{r}^*(\tau)}$ is the un-normalized density matrix evolved along $\mathbf{r}^*$ up to time τ- In particular, we find

$$r_j^*(\tau) = \langle \hat{p}_j \rangle_{\hat{\rho}_{r^*(\tau)}} \tag{D.4}$$

For Gaussian systems, for which the Saddle point is exact, we find $\overline{\mathbf{r}(t)} = \mathbf{r}^*(t)$, indicating that the trajectory defined from the conditional probability distribution maximizes both the joint and the conditional probability distribution.

We can now evaluate the second-order expansion around the $\mathbf{r}^*$ trajectory:

$$\mathcal{S}[\mathbf{r};t] \sim \mathcal{S}[\mathbf{r}^*;t] + \frac{1}{2}\int_0^t dt'dt''\,(r^*(t') - r(t'))\,\mathcal{S}^{(2)}[r^*;t',t'']\,(r^*(t'') - r(t'')). \tag{D.5}$$

The second-order Kernel can be obtained by deriving (D.3) once again:

$$\begin{aligned}
&\frac{\partial^2 \mathcal{S}[\mathbf{r};t]}{\partial r_j(t')\partial r_i(t'')}\bigg|_{\mathbf{r}^*} \qquad\qquad (D.6)\\
&= \frac{4\gamma}{P[\mathbf{r};t]^2}(r_j(t')P[\mathbf{r},t] - \langle p_{+,j}(t')\rangle_{\tilde{\hat{\rho}}_{\mathbf{r}^*}})(r_i(t'')P[\mathbf{r},t] - \langle p_{+,i}(t'')\rangle_{\tilde{\hat{\rho}}_{\mathbf{r}^*}}) - 4\gamma\delta_{i,j}\delta(t'-t'') + \\
&+ \frac{16\gamma^2}{P[\mathbf{r};t]}\Big(r_j(t')r_i(t'')P[\mathbf{r};t] - r_j(t)\,\langle p_{+,i}(t'')\rangle_{\hat{\hat{\rho}}_{\mathbf{r}^*}} - r_i(t'')\,\langle p_{+,j}(t')\rangle_{\hat{\hat{\rho}}_{\mathbf{r}^*}} + \langle p_{+,i}(t'')p_{+,j}(t')\rangle_{\hat{\hat{\rho}}_{\mathbf{r}^*}}\Big)\Big|_{\mathbf{r}^*}\\
&= -4\gamma\delta_{i,j}\delta(t'-t'') + 16\gamma^2\left[\langle p_{+,j}(t')p_{+,i}(t'')\rangle_{\hat{\rho}_{\mathbf{r}^*}} - \langle p_{+,j}(t')\rangle_{\hat{\rho}_{\mathbf{r}^*}}\langle p_{+,i}(t'')\rangle_{\hat{\rho}_{\mathbf{r}^*}}\right]. \qquad (D.7)
\end{aligned}$$

Using the brief label

$$\begin{aligned}
\sigma^{++}_{p_ip_j}(t',t'') &= \langle p_{+,j}(t')p_{+,i}(t'')\rangle_{\hat{\rho}_{\mathbf{r}^*}} \qquad (D.8)\\
&\quad - \langle p_{+,j}(t')\rangle_{\hat{\rho}_{\mathbf{r}^*}}\langle p_{+,i}(t'')\rangle_{\hat{\rho}_{\mathbf{r}^*}},
\end{aligned}$$

we get

$$\begin{aligned}
&\mathbb{S}^{(2)}_{ij}[\mathbf{r}^*;t',t''] = \qquad\qquad (D.9)\\
&\quad - 4\gamma\delta_{i,j}\delta(t'-t'') + 16\gamma^2\sigma^{++}_{p_ip_j}(t',t'').
\end{aligned}$$

While being exact for quadratic theories like free bosons, this result highlights how the most-likely trajectory approach is reliable for interacting theories, depending on the measurement strength and the classical-field correlations of the operator we are measuring. In the case of the Sine-Gordon model, this could be, for example determined in perturbation theory for $J/\alpha^2 \ll 1$.

D.2. Exact results for the Free Bosons CFT

In this appendix, we report results obtained from the Free Bosons CFT model using a quantum state diffusion perspective. This approach gives exact results when averaging over trajectories.

The Hamiltonian and the measurements we consider are contained in Eqs. (5.25), (5.26). The master equation describing the evolution along a dW stochastic trajectory is:

$$\frac{\partial\rho(t)}{\partial t} = -i\left[\hat{H}_{\rm FB},\hat{\rho}(t)\right] + \gamma\sum_{j=1}^{N}\left(\hat{p}_j\hat{\rho}(t)\hat{p}_j - \frac{1}{2}\left\{\hat{p}_j^2,\hat{\rho}(t)\right\}\right) \tag{D.10}$$
$$+\sqrt{\gamma}\sum_{j=1}^{N} dW_j\ \left\{\hat{p}_j - \langle\hat{p}_j\rangle_t\,,\hat{\rho}(t)\right\}$$

.

Exploiting the Gaussianity for the model, we can write the Heisenberg equations to evolve averages and correlations of $\hat{x}_i,\hat{p}_j$, which close at the level of second-order moments.

$$\partial_t\langle\hat{x}_i\rangle = \omega\langle\hat{p}_i\rangle + 2\sqrt{\gamma}\sum_{j=1}^{N} dW_j\,\sigma_{xp}^{ji} \tag{D.11a}$$

$$\partial_t\langle p_i\rangle = -2\omega\langle\hat{x}_i\rangle + \omega\left(\langle\hat{x}_{i+1}\rangle + \langle\hat{x}_{i-1}\rangle\right) + 2\sqrt{\gamma}\sum_{j=2}^{N} dW_j\,\sigma_{pp}^{ij} \tag{D.11b}$$

$$\partial_t\sigma_{xx}^{i,j} = \omega\left(\sigma_{xp}+\sigma_{px}\right)^{ij} - 4\gamma(\sigma_{xp}\sigma_{xp}^T)^{ij} + \gamma\delta_{ij} \tag{D.11c}$$

$$\partial_t\sigma_{pp}^{i,j} = \omega\left[-(1+\frac{r_N^2}{2})\sigma_{xp}^{i,j} + (\sigma_{xp}^{i-1,j}+\sigma_{xp}^{i+1,j}) + (i\leftrightarrow j)\right] - 4\gamma(\sigma_{pp}^2)^{ij} \tag{D.11d}$$

$$\partial_t\sigma_{xp}^{i,j} = \omega(\sigma_{pp}^{i,j} - (2+r_N^2)\sigma_{xx}^{i,j} + \sigma_{xx}^{i,j-1} + \sigma_{xx}^{i,j+1}) - 2\gamma((\sigma_{xp}+\sigma_{px})\sigma_{pp})^{ij} \tag{D.11e}$$

The Heisenberg equations show that the monitored dynamics along specific trajectories obey stochastic trajectories for averages and deterministic equations for correlations. This is a peculiarity of free systems, yielding a simple calculation for trajectory-averaged quantities. For instance, the logarithmic negativity is determined only in terms of connected correlations and, being deterministic in turn, is straightforward to average over trajectories. Indeed, exploiting the properties of a Gaussian states [244–246]

$$\log\mathcal{N}_{N/2} = \log{\rm Tr}\,\rho^{T_{N/2}} = \sum_n \log\max\left\{1,\frac{1}{2\nu_n}\right\}, \tag{D.12}$$

where $\rho^{T_{N/2}}$ is the partial transpose of a bipartition of the many-body density matrix, and ν_n are the symplectic eigenvalues of the partial transposed covariance matrix.

The covariance matrix can be written as

$$\boldsymbol{\sigma} = \begin{pmatrix}\boldsymbol{\sigma_{xx}} & \boldsymbol{\sigma_{xp}}\\ \boldsymbol{\sigma_{px}} & \boldsymbol{\sigma_{pp}}\end{pmatrix} \tag{D.13}$$

This is essentially a covariance matrix written on the $2N-$dimensional basis $\mathbf{r} = (x_1,...,x_N,p_1,...,p_N)$. Its half-chain partial transpose can be obtained through an operator $\boldsymbol{\mathcal{T}}_{N/2}$ as $\boldsymbol{\sigma}^{\boldsymbol{T_{N/2}}} = \boldsymbol{\mathcal{T}}_{N/2}\boldsymbol{\sigma}\boldsymbol{\mathcal{T}}_{N/2}$, where essentially $\boldsymbol{\mathcal{T}}$ flips $\mathbf{r} = (x_1,...,x_N,p_1,...,p_{N/2},...,p_N) \rightarrow$

$(x_1, ..., x_N, p_1, ..., -p_{N/2}, ..., -p_N)$. The symplectic diagonalization is instead obtained by taking the non-negative eigen values of $\boldsymbol{\sigma'} = i\boldsymbol{\Omega}\boldsymbol{\sigma}^{\boldsymbol{T_{N/2}}}$, where

$$\boldsymbol{\Omega} = \begin{pmatrix} \mathbb{O}_N & \mathbb{I}_N \\ -\mathbb{I}_N & \mathbb{O}_N \end{pmatrix}, \tag{D.14}$$

and $\mathbb{O}_N$ is a $N \times N$ null matrix.

The half-chain logarithmic negativity for the monitored free bosons CFT has a logarithmic behaviour

$$\log \mathcal{N}_{N/2} \sim c \log N \tag{D.15}$$

for any value of the measurement strength. Notice that for $\gamma \to 0$ we reproduce the known results for free bosons having central charge $c = 1$ [260, 261].

D.3. The Self-Consistent-Time-Dependent Harmonic Approximation For the Sine-Gordon model

In this Section, we report a detailed calculation to obtain the SCTDHA approximation [241, 242] of the Hamiltonian of the Sine-Gordon model studied in the main text, expanding the steps presented in the main text.

The SCTDHA consists, first of all, of a shift in the operators, defined at every time step:

$$\hat{\xi}_j = \hat{x}_j - \langle \hat{x}_j \rangle_t, \text{ with } \left\langle \hat{\xi}_j \right\rangle_t = 0 \tag{D.16}$$

We can now expand up to the second order the interaction Hamiltonian as

$$\tilde{\hat{H}}'_{\text{int}} \sim \sum_{j=1}^{N} \left(\mathcal{C}_j(t) + \hat{\mathcal{V}}_j(t)\hat{\xi}_j + \hat{\mathcal{M}}_j(t)\hat{\xi}_j^2 \right) \tag{D.17}$$

$$\mathcal{V}_j(t) = \frac{\partial H_{\text{int}}\left(\hat{x}_j(t)\right)}{\partial \hat{x}_j(t)}\bigg|_{\langle \hat{x}_j \rangle_t + \hat{\xi}_j(t)} \tag{D.18}$$

$$\mathcal{M}_j(t) = \frac{1}{2}\frac{\partial^2 H_{\text{int}}\left(\hat{x}_j(t)\right)}{\partial \hat{x}_j(t)^2}\bigg|_{\langle \hat{x}_j \rangle_t + \hat{\xi}_j(t)}, \tag{D.19}$$

and we perform the Hartree factorization: $\hat{\mathcal{V}}_j(t) \to \left\langle \hat{\mathcal{V}}_j(t) \right\rangle$, and $\hat{\mathcal{M}}_j(t) \to \left\langle \hat{\mathcal{M}}_j(t) \right\rangle$. Specifically, we get for the first order parameter of the expansion:

$$\begin{aligned}\langle \mathcal{V}_j(t)\rangle &= \frac{J}{\alpha}\left\langle \sin\left(\alpha\,\langle\hat{x}_j\rangle_t + \alpha\hat{\xi}_j\right)\right\rangle_t \\ &= \frac{J}{\alpha}\cos\big(\alpha\,\langle\hat{x}_j\rangle_t\big)\left\langle\sin\Big(\alpha\hat{\xi}_j\Big)\right\rangle_t + \frac{J}{\alpha}\sin\big(\alpha\,\langle\hat{x}_j\rangle_t\big)\left\langle\cos\Big(\alpha\hat{\xi}_j\Big)\right\rangle_t \\ &= \frac{J}{\alpha}\,e^{-\frac{\alpha^2}{2}\langle\hat{\xi}_j^2\rangle_t}\,\sin\big(\alpha\,\langle\hat{x}_j\rangle_t\big).\end{aligned} \tag{D.20}$$

The second order is instead

$$\begin{aligned}\langle \mathcal{M}_j(t)\rangle &= \frac{J}{2}\left\langle \cos\left(\alpha\,\langle\hat{x}_j\rangle_t + \alpha\hat{\xi}_j\right)\right\rangle_t \\ &= \frac{J}{2}\cos\big(\alpha\,\langle\hat{x}_j\rangle_t\big)\left\langle\cos\Big(\alpha\hat{\xi}_j\Big)\right\rangle_t - \frac{J}{2}\sin\big(\alpha\,\langle\hat{x}_j\rangle_t\big)\left\langle\sin\Big(\alpha\hat{\xi}_j\Big)\right\rangle_t \\ &= \frac{J}{2}\,e^{-\frac{\alpha^2}{2}\langle\hat{\xi}_j^2\rangle_t}\,\cos\big(\alpha\,\langle\hat{x}_j\rangle_t\big)\end{aligned} \tag{D.21}$$

where the facts that the Hamiltonian is quadratic in $\hat{\xi}_j$ and $\langle\xi_j\rangle_t = 0 \forall t$ have been used to carry out the Gaussian averaged in the equations above. Inserting the relation $\hat{\xi}_j = \hat{x}_j - \langle\hat{x}_j\rangle_t$ and defining

$$f_j = \mathcal{C}_j(t) + \langle\hat{x}_j\rangle_t\left(\left\langle\hat{\mathcal{M}}_j\right\rangle_t\langle\hat{x}_j\rangle_t - \left\langle\hat{\mathcal{V}}_j\right\rangle_t\right), \tag{D.22}$$

$$g_j = \left\langle\hat{\mathcal{V}}_j\right\rangle_t - 2\left\langle\hat{\mathcal{M}}_j\right\rangle_t\langle\hat{x}_j\rangle_t, \tag{D.23}$$

$$h_j = \left\langle\hat{\mathcal{M}}_j\right\rangle_t, \tag{D.24}$$

one finds the approximated Hamiltonian in Eq. (5.32).

Bibliography

[1] H.-P. Breuer and F. Petruccione, *The theory of open quantum systems* (OUP Oxford, 2002).

[2] U. Weiss, *Quantum dissipative systems* (World Scientific, 2012).

[3] C. Gardiner and P. Zoller, *Quantum noise: a handbook of Markovian and non-Markovian quantum stochastic methods with applications to quantum optics* (Springer Science & Business Media, 2004).

[4] I. R. Senitzky, *Dissipation in quantum mechanics. the harmonic oscillator,* Phys. Rev. **119**, 670 (1960).

[5] R. Zwanzig, *Ensemble method in the theory of irreversibility,* J. Chem. Phys. **33**, 1338 (1960).

[6] I. Prigonine and P. Resibois, *On the kinetics of the approach to equilibrium,* Physica **27**, 629 (1961).

[7] R. P. Feynman and F. L. Vernon Jr, *The theory of a general quantum system interacting with a linear dissipative system,* Ann. Phys. **24**, 118 (1963).

[8] G. Ford, M. Kac, and P. Mazur, *Statistical mechanics of assemblies of coupled oscillators,* (1965).

[9] C. Noh and D. G. Angelakis, *Quantum simulations and many-body physics with light,* Rep. Prog. Phys. **80**, 016401 (2016).

[10] W. P. Schleich, K. S. Ranade, C. Anton, M. Arndt, M. Aspelmeyer, M. Bayer, G. Berg, T. Calarco, H. Fuchs, E. Giacobino, *et al.*, *Quantum technology: from research to application,* App. Phys. B **122**, 1 (2016).

[11] M. J. Hartmann, *Quantum simulation with interacting photons,* J. Opt. **18**, 104005 (2016).

[12] J. I. Cirac and P. Zoller, *Goals and opportunities in quantum simulation,* Nat. Phys. **8**, 264 (2012).

[13] J. Marino, M. Eckstein, M. S. Foster, and A. M. Rey, *Dynamical phase transitions in the collisionless pre-thermal states of isolated quantum systems: theory and experiments,* Rep. Prog. Phys. **85**, 116001 (2022).

[14] R. Fazio, J. Keeling, L. Mazza, and M. Schiro, *Many-body open quantum systems,* arXiv preprint arXiv:2409.10300 (2024).

[15] L. M. Sieberer, M. Buchhold, J. Marino, and S. Diehl, *Universality in driven open quantum matter,* Rev. Mod. Phys. **97**, 025004 (2025).

[16] P. M. Harrington, E. J. Mueller, and K. W. Murch, *Engineered dissipation for quantum information science,* Nat. Rev. Phys. **4**, 660 (2022).

[17] B. Kraus, H. P. Büchler, S. Diehl, A. Kantian, A. Micheli, and P. Zoller, *Preparation of entangled states by quantum markov processes,* Phys. Rev. A: At. Mol. Opt. Phys. **78**, 042307 (2008).

[18] F. Iemini, D. Rossini, R. Fazio, S. Diehl, and L. Mazza, *Dissipative topological superconductors in number-conserving systems,* Phys. Rev. B **93**, 115113 (2016).

[19] S. Diehl, E. Rico, M. A. Baranov, and P. Zoller, *Topology by dissipation in atomic quantum wires,* Nat. Phys. **7**, 971 (2011).

[20] C.-E. Bardyn, M. A. Baranov, C. V. Kraus, E. Rico, A. İmamo**u**glu, P. Zoller, and S. Diehl, *Topology by dissipation,* New J. Phys. **15**, 085001 (2013).

[21] F. Wilczek, *Quantum time crystals,* Phys. Rev. Lett. **109**, 160401 (2012).

[22] P. Bruno, *Impossibility of spontaneously rotating time crystals: a no-go theorem,* Phys. Rev. Lett. **111**, 070402 (2013).

[23] A. Riera-Campeny, M. Moreno-Cardoner, and A. Sanpera, *Time crystallinity in open quantum systems,* Quantum **4**, 270 (2020).

[24] F. Iemini, A. Russomanno, J. Keeling, M. Schirò, M. Dalmonte, and R. Fazio, *Boundary time crystals,* Phys. Rev. Lett. **121**, 035301 (2018).

[25] I. Goychuk, J. Casado-Pascual, M. Morillo, J. Lehmann, and P. Hänggi, *Quantum stochastic synchronization,* Phys. Rev. Lett. **97**, 210601 (2006).

[26] T. E. Lee and H. R. Sadeghpour, *Quantum synchronization of quantum van der pol oscillators with trapped ions,* Phys. Rev. Lett. **111**, 234101 (2013).

[27] R. Xia, H. Zhang, and C. Fan, *Enhancement of quantum synchronization in triple-cavity system,* Sci. Rep. **15**, 744 (2025).

[28] A. Delmonte, A. Romito, G. E. Santoro, and R. Fazio, *Quantum effects on the synchronization dynamics of the kuramoto model,* Phys. Rev. A **108**, 032219 (2023).

[29] Z. Li, A. Delmonte, X. Turkeshi, and R. Fazio, *Monitored long-range interacting systems: spin-wave theory for quantum trajectories,* Nat. Commun. **16**, 1 (2025).

[30] A. Delmonte, Z. Li, G. Passarelli, E. Y. Song, D. Barberena, A. M. Rey, and R. Fazio, *Measurement-induced phase transitions in monitored infinite-range interacting systems,* Phys. Rev. Res. **7**, 023082 (2025).

[31] Z. Li, A. Delmonte, and R. Fazio, Emergent deterministic entanglement dynamics in monitored infinite-range bosonic systems, (2025), arXiv:2506.18624 [quant-ph] .

[32] H. M. Wiseman and G. J. Milburn, *Quantum measurement and control* (Cambridge university press, 2009).

[33] K. Jacobs, *Quantum measurement theory and its applications* (Cambridge University Press, 2014).

[34] T. F. Jordan, E. C. G. Sudarshan, and P. Valanju, *Measurement-damped oscillations,* Phys. Rev. A **44**, 3340 (1991).

[35] A. N. Korotkov, *Continuous quantum measurement of a double dot,* Phys. Rev. B **60**, 5737 (1999).

[36] A. N. Korotkov, *Selective quantum evolution of a qubit state due to continuous measurement,* Phys. Rev. B **63**, 115403 (2001).

[37] A. N. Korotkov, *Continuous measurement of entangled qubits,* Phys. Rev. A **65**, 052304 (2002).

[38] P. Zoller, M. Marte, and D. F. Walls, *Quantum jumps in atomic systems,* Phys. Rev. A **35**, 198 (1987).

[39] S. Gleyzes, S. Kuhr, C. Guerlin, J. Bernu, S. Deléglise, U. Busk Hoff, M. Brune, J.-M. Raimond, and S. Haroche, *Quantum jumps of light recording the birth and death of a photon in a cavity,* Nature **446**, 297â300 (2007).

[40] B. Skinner, J. Ruhman, and A. Nahum, *Measurement-induced phase transitions in the dynamics of entanglement,* Phys. Rev. X **9**, 031009 (2019).

[41] Y. Li, X. Chen, and M. P. A. Fisher, *Quantum zeno effect and the many-body entanglement transition,* Phys. Rev. B **98**, 205136 (2018).

[42] Y. Li, X. Chen, and M. P. A. Fisher, *Measurement-driven entanglement transition in hybrid quantum circuits,* Phys. Rev. B **100**, 134306 (2019).

[43] X. Cao, A. Tilloy, and A. D. Luca, *Entanglement in a fermion chain under continuous monitoring,* SciPost Phys. **7**, 024 (2019).

[44] O. Alberton, M. Buchhold, and S. Diehl, *Entanglement transition in a monitored free-fermion chain: From extended criticality to area law,* Phys. Rev. Lett. **126**, 170602 (2021).

[45] X. Turkeshi, A. Biella, R. Fazio, M. Dalmonte, and M. Schiró, *Measurement-induced entanglement transitions in the quantum ising chain: From infinite to zero clicks,* Phys. Rev. B **103**, 224210 (2021).

[46] M. Ippoliti and V. Khemani, *Postselection-free entanglement dynamics via space-time duality,* Phys. Rev. Lett. **126**, 060501 (2021).

[47] G. Passarelli, X. Turkeshi, A. Russomanno, P. Lucignano, M. Schirò, and R. Fazio, *Many-body dynamics in monitored atomic gases without postselection barrier,* Phys. Rev. Lett. **132**, 163401 (2024).

[48] S. J. Garratt and E. Altman, *Probing postmeasurement entanglement without postselection,* PRX Quantum **5**, 030311 (2024).

[49] Y. Makhlin, G. Schön, and A. Shnirman, *Quantum-state engineering with josephson-junction devices,* Rev. Mod. Phys. **73**, 357 (2001).

[50] M. Devoret, S. Girvin, and R. Schoelkopf, *Circuit-qed: How strong can the coupling between a josephson junction atom and a transmission line resonator be?* Ann. Phys. **519**, 767 (2007).

[51] A. Blais, R.-S. Huang, A. Wallraff, S. M. Girvin, and R. J. Schoelkopf, *Cavity quantum electrodynamics for superconducting electrical circuits: An architecture for quantum computation,* Phys. Rev. A **69**, 062320 (2004).

[52] J. Preskill, *Quantum Computing in the NISQ era and beyond,* Quantum **2**, 79 (2018).

[53] C. Cade, L. Mineh, A. Montanaro, and S. Stanisic, *Strategies for solving the fermi-hubbard model on near-term quantum computers,* Phys. Rev. B **102**, 235122 (2020).

[54] T. Olsacher, T. Kraft, C. Kokail, B. Kraus, and P. Zoller, *Hamiltonian and liouvillian learning in weakly-dissipative quantum many-body systems,* Quantum Sci. Technol. **10**, 015065 (2025).

[55] R. Feynman and A. Hibbs, *The path integral formulation of quantum mechanics,* McGraw-Hiill, New York (1965).

[56] L. V. Keldysh, *Diagram technique for nonequilibrium processes,* Zh. Eksp. Teor. Fiz **47**, 151 (1964).

[57] J. Schwinger, *Brownian motion of a quantum oscillator,* J. Math. Phys. **2**, 407 (1961).

[58] A. Kamenev, Field theory of non-equilibrium systems cambridge university, (2011).

[59] J. Rammer, *Quantum field theory of non-equilibrium states,* Quantum Field Theory of Non-equilibrium States (2011).

[60] H. Grabert, P. Schramm, and G.-L. Ingold, *Quantum brownian motion: The functional integral approach,* Phys. Rep. **168**, 115 (1988).

[61] A. Schmid, *On a quasiclassical langevin equation,* J. Low Temp. Phys. **49**, 609 (1982).

[62] A. O. Caldeira and A. J. Leggett, *Path integral approach to quantum brownian motion,* Physica A **121**, 587 (1983).

[63] V. Hakim and V. Ambegaokar, *Quantum theory of a free particle interacting with a linearly dissipative environment,* Phys. Rev. A **32**, 423 (1985).

[64] G. Lindblad, *On the generators of quantum dynamical semigroups,* Commun. Math. Phys. **48**, 119 (1976).

[65] A. Kossakowski, *On quantum statistical mechanics of non-hamiltonian systems,* Rep. Math. Phys. **3**, 247 (1972).

[66] V. Gorini, A. Kossakowski, and E. C. G. Sudarshan, *Completely positive dynamical semigroups of n-level systems,* J. Math. Phys. **17**, 821 (1976).

[67] D. Manzano, *A short introduction to the lindblad master equation,* Aip adv. **10** (2020).

[68] M. Zwolak and G. Vidal, *Mixed-state dynamics in one-dimensional quantum lattice systems: A time-dependent superoperator renormalization algorithm,* Phys. Rev. Lett. **93**, 207205 (2004).

[69] H. Weimer, A. Kshetrimayum, and R. Orús, *Simulation methods for open quantum many-body systems,* Rev. Mod. Phys. **93**, 015008 (2021).

[70] N. Bohr *et al.*, *The quantum postulate and the recent development of atomic theory*, Vol. 3 (Printed in Great Britain by R. & R. Clarke, Limited, 1928).

[71] P. A. M. Dirac, *The principles of quantum mechanics*, 27 (Oxford university press, 1981).

[72] J. v. Neumann, *Mathematische grundlagen der quantenmechanik*, Vol. 38 (Springer-Verlag, 2013).

[73] E. Schrödinger, *Die gegenwärtige situation in der quantenmechanik,* Naturwissenschaften **23**, 844 (1935).

[74] A. Barchielli, L. Lanz, G. Prosperi, *et al.*, *Model for the macroscopic description and continual observations in quantum mechanics,* Nuovo Cimento B;(Italy) **72** (1982).

[75] C. M. Caves, *Quantum mechanics of measurements distributed in time. a path-integral formulation,* Phys. Rev. D **33**, 1643 (1986).

[76] K. Kraus, A. Böhm, J. D. Dollard, and W. Wootters, *States, Effects, and Operations Fundamental Notions of Quantum Theory: Lectures in Mathematical Physics at the University of Texas at Austin* (Springer, 1983).

[77] A. Holevo and L. E. Ballentine, Probabilistic and statistical aspects of quantum theory, (1984).

[78] K. Jacobs and D. A. Steck, *A straightforward introduction to continuous quantum measurement,* Contemp. Phys. **47**, 279 (2006).

[79] H. J. Carmichael, *Statistical methods in quantum optics 2: Non-classical fields* (Springer Science & Business Media, 2007).

[80] H. J. Carmichael, *Statistical methods in quantum optics 1: master equations and Fokker-Planck equations* (Springer Science & Business Media, 2013).

[81] N. Gisin and I. C. Percival, *The quantum-state diffusion model applied to open systems,* J. Phys. A: Math. Gen. **25**, 5677 (1992).

[82] H. M. Wiseman and G. J. Milburn, *Quantum theory of field-quadrature measurements,* Phys. Rev. A **47**, 642 (1993).

[83] K. Mølmer, Y. Castin, and J. Dalibard, *Monte carlo wave-function method in quantum optics,* J. Opt. Soc. Am. B: Opt. Phys. **10**, 524 (1993).

[84] A. Shapere and F. Wilczek, *Classical time crystals,* Phys. Rev. Lett. **109**, 160402 (2012).

[85] K. Sacha, *Time crystals*, Vol. 114 (Springer, 2020).

[86] V. Khemani, R. Moessner, and S. L. Sondhi, A brief history of time crystals, (2019), arXiv:1910.10745 [cond-mat.str-el] .

[87] D. Nigro, *On the uniqueness of the steady-state solution of the lindblad–gorini–kossakowski–sudarshan equation,* J. Stat. Mech: Theory Exp. **2019**, 043202 (2019).

[88] H. Landa, M. Schiró, and G. Misguich, *Multistability of driven-dissipative quantum spins,* Phys. Rev. Lett. **124**, 043601 (2020).

[89] X. Turkeshi, *Measurement-induced criticality as a data-structure transition,* Phys. Rev. B **106** (2022).

[90] X. Turkeshi, R. Fazio, and M. Dalmonte, *Measurement-induced criticality in* $(2+1)$*-dimensional hybrid quantum circuits,* Phys. Rev. B **102**, 014315 (2020).

[91] A. Zabalo, M. J. Gullans, J. H. Wilson, S. Gopalakrishnan, D. A. Huse, and J. H. Pixley, *Critical properties of the measurement-induced transition in random quantum circuits,* Phys. Rev. B **101**, 060301 (2020).

[92] P. Sierant, G. Chiriacò, F. M. Surace, S. Sharma, X. Turkeshi, M. Dalmonte, R. Fazio, and G. Pagano, *Dissipative floquet dynamics: From steady state to measurement induced criticality in trapped-ion chains,* Quantum **6**, 638 (2022).

[93] P. Sierant and X. Turkeshi, *Universal behavior beyond multifractality of wave functions at measurement-induced phase transitions,* Phys. Rev. Lett. **128**, 130605 (2022).

[94] A. Zabalo, M. J. Gullans, J. H. Wilson, R. Vasseur, A. W. W. Ludwig, S. Gopalakrishnan, D. A. Huse, and J. H. Pixley, *Operator scaling dimensions and multifractality at measurement-induced transitions,* Phys. Rev. Lett. **128**, 050602 (2022).

[95] A. Lavasani, Y. Alavirad, and M. Barkeshli, *Measurement-induced topological entanglement transitions in symmetric random quantum circuits,* Nat. Phys. **17**, 342 (2021).

[96] D. Vu, A. Lavasani, J. Y. Lee, and M. P. A. Fisher, *Stable measurement-induced floquet enriched topological order,* Phys. Rev. Lett. **132**, 070401 (2024).

[97] S.-K. Jian, C. Liu, X. Chen, B. Swingle, and P. Zhang, *Measurement-induced phase transition in the monitored sachdev-ye-kitaev model,* Phys. Rev. Lett. **127**, 140601 (2021).

[98] M. Buchhold, Y. Minoguchi, A. Altland, and S. Diehl, *Effective theory for the measurement-induced phase transition of dirac fermions,* Phys. Rev. X **11**, 041004 (2021).

[99] E. Tirrito, A. Santini, R. Fazio, and M. Collura, *Full counting statistics as probe of measurement-induced transitions in the quantum Ising chain,* SciPost Phys. **15**, 096 (2023).

[100] M. Fava, L. Piroli, T. Swann, D. Bernard, and A. Nahum, *Nonlinear sigma models for monitored dynamics of free fermions,* Phys. Rev. X **13**, 041045 (2023).

[101] I. Poboiko, P. Pöpperl, I. V. Gornyi, and A. D. Mirlin, *Theory of free fermions under random projective measurements,* Phys. Rev. X **13**, 041046 (2023).

[102] G. Kells, D. Meidan, and A. Romito, *Topological transitions in weakly monitored free fermions,* SciPost Phys. **14**, 031 (2023).

[103] A. Paviglianiti and A. Silva, *Multipartite entanglement in the measurement-induced phase transition of the quantum ising chain,* Phys. Rev. B **108**, 184302 (2023).

[104] G. Giachetti and A. D. Luca, Elusive phase transition in the replica limit of monitored systems, (2023), arXiv:2306.12166 [cond-mat.stat-mech] .

[105] L. Lumia, E. Tirrito, R. Fazio, and M. Collura, *Measurement-induced transitions beyond gaussianity: A single particle description,* Phys. Rev. Res. **6**, 023176 (2024).

[106] V. B. Bulchandani, S. Sondhi, and J. Chalker, *Random-matrix models of monitored quantum circuits,* J. Stat. Phys. **191**, 55 (2024).

[107] K. Efetov, *Supersymmetry in Disorder and Chaos* (Cambridge University Press, 1996).

[108] C. Y. Leung, D. Meidan, and A. Romito, *Theory of free fermions dynamics under partial postselected monitoring,* Phys. Rev. X **15**, 021020 (2025).

[109] T. M. Müller, M. Buchhold, and S. Diehl, Monitored interacting dirac fermions, (2025), arXiv:2502.02645 [cond-mat.stat-mech] .

[110] Y. Bao, S. Choi, and E. Altman, *Theory of the phase transition in random unitary circuits with measurements,* Phys. Rev. B **101**, 104301 (2020).

[111] C.-M. Jian, Y.-Z. You, R. Vasseur, and A. W. W. Ludwig, *Measurement-induced criticality in random quantum circuits,* Phys. Rev. B **101**, 104302 (2020).

[112] A. Chantasri and A. N. Jordan, *Stochastic path-integral formalism for continuous quantum measurement,* Phys. Rev. A **92**, 032125 (2015).

[113] A. Chantasri, J. Dressel, and A. N. Jordan, *Action principle for continuous quantum measurement,* Phys. Rev. A **88**, 042110 (2013).

[114] U. C. Tauber, *Encyclopedia of Complexity and Systems Science* (Springer New York, 2009) pp. 3360–3374.

[115] J. Zinn-Justin, *Quantum Field Theory and Critical Phenomena; 4th ed.*, International series of monographs on physics (Clarendon Press, Oxford, 2002).

[116] W. Verstraelen, R. Rota, V. Savona, and M. Wouters, *Gaussian trajectory approach to dissipative phase transitions: The case of quadratically driven photonic lattices,* Phys. Rev. Res. **2**, 022037 (2020).

[117] M. Ippoliti, M. J. Gullans, S. Gopalakrishnan, D. A. Huse, and V. Khemani, *Entanglement phase transitions in measurement-only dynamics,* Phys. Rev. X **11**, 011030 (2021).

[118] J. M. Koh, S.-N. Sun, M. Motta, and A. J. Minnich, *Measurement-induced entanglement phase transition on a superconducting quantum processor with mid-circuit readout,* Nat. Phys. **19**, 1314 (2023).

[119] *Measurement-induced entanglement and teleportation on a noisy quantum processor,* Nature **622**, 481 (2023).

[120] C. Noel, P. Niroula, D. Zhu, A. Risinger, L. Egan, D. Biswas, M. Cetina, A. V. Gorshkov, M. J. Gullans, D. A. Huse, *et al.*, *Measurement-induced quantum phases realized in a trapped-ion quantum computer,* Nat. Phys. **18**, 760 (2022).

[121] G. Passarelli, P. Lucignano, R. Fazio, and A. Russomanno, *Dissipative time crystals with long-range lindbladians,* Phys. Rev. B **106**, 224308 (2022).

[122] Y. Li, Y. Zou, P. Glorioso, E. Altman, and M. P. A. Fisher, *Cross entropy benchmark for measurement-induced phase transitions,* Phys. Rev. Lett. **130**, 220404 (2023).

[123] C. Huygens and E. E. Project, Christiaan huygens correspondences, (2008).

[124] E. S. Morse, *Fireflies flashing in unison,* Science **43**, 169 (1916).

[125] J. Buck and E. Buck, *Mechanism of rhythmic synchronous flashing of fireflies,* Science **159**, 1319 (1968).

[126] C. Gray, P. König, A. Engel, and W. Singer, *Oscillatory responses in cat visual cortex exhibit inter-columnar synchronization which reflects global stimulus properties,* Nature **338**, 334â337 (1989).

[127] S. Gupta, A. Campa, and S. Ruffo, *Statistical Physics of Synchronization* (SpringerBriefs in Complexity, 2018).

[128] A. Pikovsky, M. Rosenblum, and J. Kurths, *Synchronization: A Universal Concept in Nonlinear Sciences*, Cambridge Nonlinear Science Series (Cambridge University Press, 2001).

[129] T. E. Lee, C.-K. Chan, and S. Wang, *Entanglement tongue and quantum synchronization of disordered oscillators,* Phys. Rev. E **89**, 022913 (2014).

[130] H. Wang, A. L. Chudnovskiy, A. Gorsky, and A. Kamenev, *Sachdev-ye-kitaev superconductivity: Quantum kuramoto and generalized richardson models,* Phys. Rev. Res. **2** (2020).

[131] C. Agnesi, M. Avesani, L. Calderaro, A. Stanco, G. Foletto, M. Zahidy, A. Scriminich, F. Vedovato, G. Vallone, and P. Villoresi, *Simple quantum key distribution with qubit-based synchronization and a self-compensating polarization encoder,* Optica **7**, 284 (2020).

[132] L. Calderaro, A. Stanco, C. Agnesi, M. Avesani, D. Dequal, P. Villoresi, and G. Vallone, *Fast and simple qubit-based synchronization for quantum key distribution,* Phys. Rev. Appl. **13**, 054041 (2020).

[133] N. Jaseem, M. Hajduvsek, V. Vedral, R. Fazio, L.-C. Kwek, and S. Vinjanampathy, *Quantum synchronization in nanoscale heat engines,* Phys. Rev. E **101**, 020201 (2020).

[134] P. Solanki, N. Jaseem, M. Hajduvsek, and S. Vinjanampathy, *Role of coherence and degeneracies in quantum synchronization,* Phys. Rev. A **105**, L020401 (2022).

[135] T. Murtadho, J. Thingna, and S. Vinjanampathy, Synchronization lower bounds the efficiency of near-degenerate thermal machines, (2023), arXiv:2301.04323 [quant-ph] .

[136] L. Ben Arosh, M. C. Cross, and R. Lifshitz, *Quantum limit cycles and the rayleigh and van der pol oscillators,* Phys. Rev. Res. **3**, 013130 (2021).

[137] S. Sonar, M. Hajduvsek, M. Mukherjee, R. Fazio, V. Vedral, S. Vinjanampathy, and L.-C. Kwek, *Squeezing enhances quantum synchronization,* Phys. Rev. Lett. **120**, 163601 (2018).

[138] C. Davis-Tilley, C. K. Teoh, and A. D. Armour, *Dynamics of many-body quantum synchronisation,* New J. Phys. **20**, 113002 (2018).

[139] A. Chia, L. C. Kwek, and C. Noh, *Relaxation oscillations and frequency entrainment in quantum mechanics,* Phys. Rev. E **102**, 042213 (2020).

[140] S. Walter, A. Nunnenkamp, and C. Bruder, *Quantum synchronization of a driven self-sustained oscillator,* Phys. Rev. Lett. **112**, 094102 (2014).

[141] S. Walter, A. Nunnenkamp, and C. Bruder, *Quantum synchronization of two van der pol oscillators,* Ann. Phys. **527**, 131 (2015).

[142] N. Lörch, S. E. Nigg, A. Nunnenkamp, R. P. Tiwari, and C. Bruder, *Quantum synchronization blockade: Energy quantization hinders synchronization of identical oscillators,* Phys. Rev. Lett. **118**, 243602 (2017).

[143] O. Zhirov and D. Shepelyansky, *Quantum synchronization,* Eur. Phys. J. D **38**, 375 (2006).

[144] A. Cabot, G. L. Giorgi, and R. Zambrini, *Metastable quantum entrainment,* New J. Phys. **23**, 103017 (2021).

[145] A. Roulet and C. Bruder, *Quantum synchronization and entanglement generation,* Phys. Rev. Lett. **121**, 063601 (2018).

[146] A. Roulet and C. Bruder, *Synchronizing the smallest possible system,* Phys. Rev. Lett. **121**, 053601 (2018).

[147] M. Koppenhöfer and A. Roulet, *Optimal synchronization deep in the quantum regime: Resource and fundamental limit,* Phys. Rev. A **99**, 043804 (2019).

[148] V. R. Krithika, P. Solanki, S. Vinjanampathy, and T. S. Mahesh, *Observation of quantum phase synchronization in a nuclear-spin system,* Phys. Rev. A **105**, 062206 (2022).

[149] O. V. Zhirov and D. L. Shepelyansky, *Synchronization and bistability of a qubit coupled to a driven dissipative oscillator,* Phys. Rev. Lett. **100**, 014101 (2008).

[150] O. V. Zhirov and D. L. Shepelyansky, *Quantum synchronization and entanglement of two qubits coupled to a driven dissipative resonator,* Phys. Rev. B **80**, 014519 (2009).

[151] G. L. Giorgi, F. Plastina, G. Francica, and R. Zambrini, *Spontaneous synchronization and quantum correlation dynamics of open spin systems,* Phys. Rev. A **88**, 042115 (2013).

[152] B. Bu**v**ca, C. Booker, and D. Jaksch, *Algebraic theory of quantum synchronization and limit cycles under dissipation,* SciPost Physics **12** (2022).

[153] B. Bellomo, G. L. Giorgi, G. M. Palma, and R. Zambrini, *Quantum synchronization as a local signature of super- and subradiance,* Phys. Rev. A **95**, 043807 (2017).

[154] M. V. Fistul, *Quantum synchronization in disordered superconducting metamaterials,* Sci. Rep. **7** (2016).

[155] M. Cattaneo, G. L. Giorgi, S. Maniscalco, G. S. Paraoanu, and R. Zambrini, *Bath-induced collective phenomena on superconducting qubits: Synchronization, subradiance, and entanglement generation,* Ann. Phys. **533**, 2100038.

[156] P. Vorndamme, H.-J. Schmidt, C. Schröder, and J. Schnack, *Observation of phase synchronization and alignment during free induction decay of quantum spins with heisenberg interactions,* New J. Phys. **23**, 083038 (2021).

[157] P. Reimann, P. Vorndamme, and J. Schnack, Non-equilibration, synchronization, and time crystals in isotropic heisenberg models, (2023), arXiv:2303.11148 [cond-mat.stat-mech] .

[158] J. Tindall, C. S. Munoz, B. Buca, and D. Jaksch, *Quantum synchronisation enabled by dynamical symmetries and dissipation,* New J. Phys. **22**, 013026 (2020).

[159] A. Mari, A. Farace, N. Didier, V. Giovannetti, and R. Fazio, *Measures of quantum synchronization in continuous variable systems,* Phys. Rev. Lett. **111**, 103605 (2013).

[160] N. Jaseem, M. Hajdu**v**sek, P. Solanki, L.-C. Kwek, R. Fazio, and S. Vinjanampathy, *Generalized measure of quantum synchronization,* Phys. Rev. Res. **2**, 043287 (2020).

[161] Y. Kato and H. Nakao, *Quantum asymptotic phases reveal signatures of quantum synchronization,* New J. Phys. **25**, 023012 (2023).

[162] Y. Kato and H. Nakao, *A definition of the asymptotic phase for quantum nonlinear oscillators from the Koopman operator viewpoint,* Chaos **32** (2022), 063133, https://pubs.aip.org/aip/cha/article-pdf/doi/10.1063/5.0088559/16499302/063133_1_online.pdf .

[163] M. R. Hush, W. Li, S. Genway, I. Lesanovsky, and A. D. Armour, *Spin correlations as a probe of quantum synchronization in trapped-ion phonon lasers,* Phys. Rev. A **91**, 061401 (2015).

[164] A. Cabot, G. L. Giorgi, F. Galve, and R. Zambrini, *Quantum synchronization in dimer atomic lattices,* Phys. Rev. Lett. **123**, 023604 (2019).

[165] H. Eneriz, D. Z. Rossatto, F. A. Cárdenas-López, E. Solano, and M. Sanz, *Degree of quantumness in quantum synchronization,* Sci. Rep. **9** (2019).

[166] F. Galve, G. L. Giorgi, and R. Zambrini, *Quantum correlations and synchronization measures,* in *Quantum Sci. Technol.* (Springer International Publishing, 2017) pp. 393–420.

[167] G. L. Giorgi, F. Galve, G. Manzano, P. Colet, and R. Zambrini, *Quantum correlations and mutual synchronization,* Phys. Rev. A **85**, 052101 (2012).

[168] Y. Kuramoto, *Self-entrainment of a population of coupled non-linear oscillators,* in *International Symposium on Mathematical Problems in Theoretical Physics: January 23–29, 1975, Kyoto University, Kyoto/Japan* (Springer, 1975) pp. 420–422.

[169] H. Sakaguchi and Y. Kuramoto, *A Soluble Active Rotater Model Showing Phase Transitions via Mutual Entertainment,* Prog. Theor. Phys. **76**, 576 (1986).

[170] H. Sakaguchi, S. Shinomoto, and Y. Kuramoto, *Mutual Entrainment in Oscillator Lattices with Nonvariational Type Interaction,* Prog. Theor. Phys. **79**, 1069 (1988).

[171] J. A. Acebrón, L. L. Bonilla, C. J. Pérez Vicente, F. Ritort, and R. Spigler, *The kuramoto model: A simple paradigm for synchronization phenomena,* Rev. Mod. Phys. **77**, 137 (2005).

[172] S. Gherardini, S. Gupta, and S. Ruffo, *Spontaneous synchronisation and nonequilibrium statistical mechanics of coupled phase oscillators,* Contemp. Phys. **59**, 1 (2018).

[173] S. Strogatz, *From kuramoto to crawford: Exploring the onset of synchronization in populations of coupled oscillators,* Physica D **143**, 1 (2000).

[174] S. Olmi, A. Navas, S. Boccaletti, and A. Torcini, *Hysteretic transitions in the kuramoto model with inertia,* Phys. Rev. E **90**, 042905 (2014).

[175] H. Daido, *Quasientrainment and slow relaxation in a population of oscillators with random and frustrated interactions,* Phys. Rev. Lett. **68**, 1073 (1992).

[176] L. DeVille, *Synchronization and stability for quantum kuramoto,* J. Stat. Phys. **174**, 160 (2018).

[177] I. Hermoso de Mendoza, L. A. Pachón, J. Gómez-Gardeñes, and D. Zueco, *Synchronization in a semiclassical kuramoto model,* Phys. Rev. E **90**, 052904 (2014).

[178] H. Sakaguchi, *Cooperative Phenomena in Coupled Oscillator Systems under External Fields,* Prog. Theor. Phys. **79**, 39 (1988).

[179] T. Pirey, L. Cugliandolo, V. Lecomte, and F. Wijland, *Path integrals and stochastic calculus,* Adv. Phys. , 1 (2023).

[180] A. K. Das, S. Panda, and J. R. L. Santos, *A path integral approach to the langevin equation,* Int. J. Mod. Phys. A **30**, 1550028 (2015).

[181] W. Zwerger, A. T. Dorsey, and M. P. A. Fisher, *Effects of the phase periodicity on the quantum dynamics of a resistively shunted josephson junction,* Phys. Rev. B **34**, 6518 (1986).

[182] M. P. A. Fisher and W. Zwerger, *Quantum brownian motion in a periodic potential,* Phys. Rev. B **32**, 6190 (1985).

[183] T.-C. Lu and T. Grover, *Spacetime duality between localization transitions and measurement-induced transitions,* PRX Quantum **2**, 040319 (2021).

[184] V. Ravindranath, Y. Han, Z.-C. Yang, and X. Chen, *Entanglement steering in adaptive circuits with feedback,* Phys. Rev. B **108**, L041103 (2023).

[185] T. Iadecola, S. Ganeshan, J. H. Pixley, and J. H. Wilson, *Measurement and feedback driven entanglement transition in the probabilistic control of chaos,* Phys. Rev. Lett. **131**, 060403 (2023).

[186] A. J. Friedman, O. Hart, and R. Nandkishore, *Measurement-induced phases of matter require feedback,* PRX Quantum **4**, 040309 (2023).

[187] M. Buchhold, T. Müller, and S. Diehl, Revealing measurement-induced phase transitions by pre-selection, (2022), arXiv:2208.10506 [cond-mat.dis-nn] .

[188] N. O'Dea, A. Morningstar, S. Gopalakrishnan, and V. Khemani, *Entanglement and absorbing-state transitions in interactive quantum dynamics,* Phys. Rev. B **109**, L020304 (2024).

[189] P. Sierant and X. Turkeshi, *Entanglement and absorbing state transitions in $(d+1)$-dimensional stabilizer circuits,* Acta Phys. Pol. A **144**, 474â485 (2023), arXiv:2308.13384 [cond-mat, physics:quant-ph].

[190] P. Sierant and X. Turkeshi, *Controlling entanglement at absorbing state phase transitions in random circuits,* Phys. Rev. Lett. **130**, 120402 (2023).

[191] V. Ravindranath, Z.-C. Yang, and X. Chen, *Free fermions under adaptive quantum dynamics,* Quantum **9**, 1685 (2025).

[192] A. A. Allocca, C. LeMaire, T. Iadecola, and J. H. Wilson, *Statistical mechanics of stochastic quantum control:d-adic rényi circuits,* Phys. Rev. E **110** (2024).

[193] C. LeMaire, A. A. Allocca, J. H. Pixley, T. Iadecola, and J. H. Wilson, Separate measurement- and feedback-driven entanglement transitions in the stochastic control of chaos, (2023), arXiv:2309.04520 [cond-mat.dis-nn] .

[194] H. Dehghani, A. Lavasani, M. Hafezi, and M. J. Gullans, *Neural-network decoders for measurement induced phase transitions,* Nat. Commun. **14**, 2918 (2023).

[195] R. H. Dicke, *Coherence in spontaneous radiation processes,* Phys. Rev. **93**, 99 (1954).

[196] K. Baumann, C. Guerlin, F. Brennecke, and T. Esslinger, *Dicke quantum phase transition with a superfluid gas in an optical cavity,* Nature **464**, 1301â1306 (2010).

[197] F. Brennecke, R. Mottl, K. Baumann, R. Landig, T. Donner, and T. Esslinger, *Real-time observation of fluctuations at the driven-dissipative dicke phase transition,* PNAS **110**, 11763â11767 (2013).

[198] A. Safavi-Naini, R. J. Lewis-Swan, J. G. Bohnet, M. Gärttner, K. A. Gilmore, J. E. Jordan, J. Cohn, J. K. Freericks, A. M. Rey, and J. J. Bollinger, *Verification of a many-ion simulator of the dicke model through slow quenches across a phase transition,* Phys. Rev. Lett. **121**, 040503 (2018).

[199] M. Tavis and F. W. Cummings, *Exact solution for an n-molecule—radiation-field hamiltonian,* Phys. Rev. **170**, 379 (1968).

[200] M. Tavis and F. Cummings, *The exact solution of n two level systems interacting with a single mode, quantized radiation field,* Physics Letters A **25**, 714 (1967).

[201] M. Tavis and F. W. Cummings, *Approximate solutions for an n-molecule-radiation-field hamiltonian,* Phys. Rev. **188**, 692 (1969).

[202] E. Y. Song, D. Barberena, D. J. Young, E. Chaparro, A. Chu, S. Agarwal, Z. Niu, J. T. Young, A. M. Rey, and J. K. Thompson, A dissipation-induced superradiant transition in a strontium cavity-qed system, (2024), arXiv:2408.11086 [quant-ph] .

[203] R. Mattes, I. Lesanovsky, and F. Carollo, *Entangled time-crystal phase in an open quantum light-matter system,* Phys. Rev. A **108**, 062216 (2023).

[204] F. Carollo and I. Lesanovsky, *Exactness of mean-field equations for open dicke models with an application to pattern retrieval dynamics,* Phys. Rev. Lett. **126**, 230601 (2021).

[205] A. Cabot, L. S. Muhle, F. Carollo, and I. Lesanovsky, *Quantum trajectories of dissipative time crystals,* Phys. Rev. A **108**, L041303 (2023).

[206] J. Johansson, P. Nation, and F. Nori, *Qutip 2: A python framework for the dynamics of open quantum systems,* Comput. Phys. Commun. **184**, 1234 (2013).

[207] J. Johansson, P. Nation, and F. Nori, *Qutip: An open-source python framework for the dynamics of open quantum systems,* Comput. Phys. Commun. **183**, 1760 (2012).

[208] H. Landa, M. Schiró, and G. Misguich, *Multistability of driven-dissipative quantum spins,* Phys. Rev. Lett. **124**, 043601 (2020).

[209] M. A. Norcia, R. J. Lewis-Swan, J. R. K. Cline, B. Zhu, A. M. Rey, and J. K. Thompson, *Cavity-mediated collective spin-exchange interactions in a strontium superradiant laser,* Science **361**, 259 (2018).

[210] T. Brydges, A. Elben, P. Jurcevic, B. Vermersch, C. Maier, B. P. Lanyon, P. Zoller, R. Blatt, and C. F. Roos, *Probing rÃ©nyi entanglement entropy via randomized measurements,* Science **364**, 260 (2019), https://www.science.org/doi/pdf/10.1126/science.aau4963 .

[211] A. Elben, B. Vermersch, C. F. Roos, and P. Zoller, *Statistical correlations between locally randomized measurements: A toolbox for probing entanglement in many-body quantum states,* Phys. Rev. A **99**, 052323 (2019).

[212] H.-Y. Huang, R. Kueng, and J. Preskill, *Predicting many properties of a quantum system from very few measurements,* Nat. Phys. **16**, 1050 (2020).

[213] A. G. Moghaddam, K. Pöyhönen, and T. Ojanen, *Exponential shortcut to measurement-induced entanglement phase transitions,* Phys. Rev. Lett. **131**, 020401 (2023).

[214] M. Kitagawa and M. Ueda, *Squeezed spin states,* Phys. Rev. A **47**, 5138 (1993).

[215] A. Sørensen, L.-M. Duan, J. I. Cirac, and P. Zoller, *Many-particle entanglement with bose–einstein condensates,* Nature **409**, 63 (2001).

[216] O. Gühne and G. Tóth, *Entanglement detection,* Phys. Rep. **474**, 1 (2009).

[217] Y. Minoguchi, P. Rabl, and M. Buchhold, *Continuous gaussian measurements of the free boson cft: A model for exactly solvable and detectable measurement-induced dynamics,* SciPost Phys. **12**, 009 (2022).

[218] N. Defenu, T. Donner, T. Macrì, G. Pagano, S. Ruffo, and A. Trombettoni, *Long-range interacting quantum systems,* Rev. Mod. Phys. **95**, 035002 (2023).

[219] N. Defenu, A. Lerose, and S. Pappalardi, *Out-of-equilibrium dynamics of quantum many-body systems with long-range interactions,* Phys. Rep. **1074**, 1 (2024).

[220] C. Monroe, W. C. Campbell, L.-M. Duan, Z.-X. Gong, A. V. Gorshkov, P. W. Hess, R. Islam, K. Kim, N. M. Linke, G. Pagano, P. Richerme, C. Senko, and N. Y. Yao, *Programmable quantum simulations of spin systems with trapped ions,* Rev. Mod. Phys. **93**, 025001 (2021).

[221] H. Ritsch, P. Domokos, F. Brennecke, and T. Esslinger, *Cold atoms in cavity-generated dynamical optical potentials,* Rev. Mod. Phys. **85**, 553 (2013).

[222] T. Lahaye, C. Menotti, L. Santos, M. Lewenstein, and T. Pfau, *The physics of dipolar bosonic quantum gases,* Rep. Prog. Phys. **72**, 126401 (2009).

[223] J. L. Bohn, A. M. Rey, and J. Ye, *Cold molecules: Progress in quantum engineering of chemistry and quantum matter,* Science **357**, 1002 (2017).

[224] H. Weimer, M. MÃ¼ller, I. Lesanovsky, P. Zoller, and H. P. BÃ¼chler, *A rydberg quantum simulator,* Nat. Phys. **6**, 382 (2010).

[225] G. Ferioli, A. Glicenstein, I. Ferrier-Barbut, and A. Browaeys, *A non-equilibrium superradiant phase transition in free space,* Nat. Phys. **19**, 1345 (2023).

[226] F. Bloch, *Zur Theorie des Austauschproblems und der Remanenzerscheinung der Ferromagnetika,* in *Zur Theorie des Austauschproblems und der Remanenzerscheinung der Ferromagnetika: Probleme des Atomkernbaues*, edited by F. Bloch (Springer, Berlin, Heidelberg, 1932) pp. 295–335.

[227] T. Holstein and H. Primakoff, *Field Dependence of the Intrinsic Domain Magnetization of a Ferromagnet,* Phys. Rev. **58**, 1098 (1940).

[228] J. Van Kranendonk and J. H. Van Vleck, *Spin Waves,* Rev. Mod. Phys. **30**, 1 (1958).

[229] A. Rückriegel, A. Kreisel, and P. Kopietz, *Time-dependent spin-wave theory,* Phys. Rev. B **85**, 054422 (2012).

[230] A. Lerose, B. **v**Zunkovi**v**c, J. Marino, A. Gambassi, and A. Silva, *Impact of nonequilibrium fluctuations on prethermal dynamical phase transitions in long-range interacting spin chains,* Phys. Rev. B **99**, 045128 (2019).

[231] K. Seetharam, A. Lerose, R. Fazio, and J. Marino, *Dynamical scaling of correlations generated by short- and long-range dissipation,* Phys. Rev. B **105**, 184305 (2022).

[232] W. Verstraelen and M. Wouters, *Gaussian quantum trajectories for the variational simulation of open quantum-optical systems,* App. Sci. **8**, 1427 (2018).

[233] A. Lerose and S. Pappalardi, *Origin of the slow growth of entanglement entropy in long-range interacting spin systems,* Phys. Rev. Res. **2**, 012041 (2020).

[234] A. Serafini, F. Illuminati, and S. D. Siena, *Symplectic invariants, entropic measures and correlations of Gaussian states,* J. Phys. B **37**, L21 (2003).

[235] A. Delmonte, Z. Li, R. Fazio, and A. Romito, Measurement-induced phase transition in interacting bosons from most likely quantum trajectory, (2025), arXiv:25xx.xxxx .

[236] A. Nahum, S. Roy, B. Skinner, and J. Ruhman, *Measurement and entanglement phase transitions in all-to-all quantum circuits, on quantum trees, and in landau-ginsburg theory,* PRX Quantum **2**, 010352 (2021).

[237] E. V. H. Doggen, Y. Gefen, I. V. Gornyi, A. D. Mirlin, and D. G. Polyakov, *Generalized quantum measurements with matrix product states: Entanglement phase transition and clusterization,* Phys. Rev. Res. **4**, 023146 (2022).

[238] Y. Fuji and Y. Ashida, *Measurement-induced quantum criticality under continuous monitoring,* Phys. Rev. B **102**, 054302 (2020).

[239] K. Yokomizo and Y. Ashida, Measurement-induced phase transition in free bosons, (2024), arXiv:2405.19768 [quant-ph] .

[240] S. Coleman, *Quantum sine-gordon equation as the massive thirring model,* Phys. Rev. D **11**, 2088 (1975).

[241] D. Boyanovsky, F. Cooper, H. J. De Vega, and P. Sodano, *Evolution of inhomogeneous condensates: Self-consistent variational approach,* Phys. Rev. D **58**, 025007 (1998).

[242] Y. D. Van Nieuwkerk and F. H. L. Essler, *Self-consistent time-dependent harmonic approximation for the sine-gordon model out of equilibrium,* J. Stat. Mech: Theory Exp. **2019**, 084012 (2019).

[243] T. Karmakar, P. Lewalle, and A. N. Jordan, *Stochastic path-integral analysis of the continuously monitored quantum harmonic oscillator,* PRX Quantum **3**, 010327 (2022).

[244] A. Serafini, *Quantum continuous variables: a primer of theoretical methods* (CRC press, 2023).

[245] G. Adesso and F. Illuminati, *Entanglement in continuous-variable systems: recent advances and current perspectives,* J. Phys. A: Math. Theor. **40**, 7821 (2007).

[246] K. Audenaert, J. Eisert, M. B. Plenio, and R. F. Werner, *Entanglement properties of the harmonic chain,* Phys. Rev. A **66**, 042327 (2002).

[247] L. D. Faddeev and V. E. Korepin, *Quantum theory of solitons,* Phys. Rep. **42**, 1 (1978).

[248] F. Iemini, R. Fazio, and A. Sanpera, *Floquet time crystals as quantum sensors of ac fields,* Phys. Rev. A **109**, L050203 (2024).

[249] D. Gribben, A. Sanpera, R. Fazio, J. Marino, and F. Iemini, *Boundary time crystals as ac sensors: Enhancements and constraints,* SciPost Physics **18** (2025).

[250] L. Viotti, M. Huber, R. Fazio, and G. Manzano, Quantum time crystal clock and its performance, (2025), arXiv:2505.08276 [quant-ph] .

[251] G. M. Vaidya, S. B. Jäger, and A. Shankar, *Quantum synchronization and dissipative quantum sensing,* Phys. Rev. A **111**, 012410 (2025).

[252] A. Shankar, J. Cooper, J. G. Bohnet, J. J. Bollinger, and M. Holland, *Steady-state spin synchronization through the collective motion of trapped ions,* Phys. Rev. A **95**, 033423 (2017).

[253] Y. Yang, B. Yadin, and Z.-P. Xu, *Quantum-enhanced metrology with network states,* Phys. Rev. Lett. **132**, 210801 (2024).

[254] D. Cilluffo, L. Ferialdi, G. M. Palma, G. Calajó, and F. Ciccarello, Multimode-cavity picture of non-markovian waveguide qed, (2024), arXiv:2403.07110 [quant-ph] .

[255] V. Link, K. Müller, R. G. Lena, K. Luoma, F. m. c. Damanet, W. T. Strunz, and A. J. Daley, *Non-markovian quantum dynamics in strongly coupled multi-mode cavities conditioned on continuous measurement,* PRX Quantum **3**, 020348 (2022).

[256] K. Sinha, P. Meystre, E. A. Goldschmidt, F. K. Fatemi, S. L. Rolston, and P. Solano, *Non-markovian collective emission from macroscopically separated emitters,* Phys. Rev. Lett. **124**, 043603 (2020).

[257] T. Ramos, B. Vermersch, P. Hauke, H. Pichler, and P. Zoller, *Non-markovian dynamics in chiral quantum networks with spins and photons,* Phys. Rev. A **93**, 062104 (2016).

[258] H. Pichler and P. Zoller, *Photonic circuits with time delays and quantum feedback,* Phys. Rev. Lett. **116**, 093601 (2016).

[259] H. Pichler, S. Choi, P. Zoller, and M. D. Lukin, *Universal photonic quantum computation via time-delayed feedback,* PNAS **114**, 11362 (2017), https://www.pnas.org/doi/pdf/10.1073/pnas.1711003114 .

[260] P. Calabrese, J. Cardy, and E. Tonni, *Entanglement negativity in quantum field theory,* Phys. Rev. Lett. **109**, 130502 (2012).

[261] V. Eisler and Z. Zimborás, *Entanglement negativity in the harmonic chain out of equilibrium,* New J. Phys. **16**, 123020 (2014).